Fabrication and Characterisation of a Nanocrystal Activated Schottky Barrier Solar Cell

Philippa Kate Hardy

Submitted in accordance with the requirements for the degree of

Doctor of Philosophy

as part of the integrated MSc/PhD in Low Carbon Technologies

The University of Leeds
Energy Research Institute
School of Process, Environment and Materials Engineering

Doctoral Training Centre in Low Carbon Technologies

November, 2014

The candidate confirms that the work submitted is her own, except where work which has formed part of jointly authored publications has been included. The contribution of the candidate and the other authors to this work has been explicitly indicated below. The candidate confirms that appropriate credit has been given within the thesis where reference has been made to the work of others.

Chapter 4, 5 and **6** includes the following work;

Philippa Hardy, Robert Mitchell, Ross Jarett, Richard Douthwaite and Rolf Crook, *Nanocrystal Activated Schottky Barrier PV Cell*, Proceedings from PVSAT-9, Wales, UK, 9-11th April 2013.

The work detailed within this paper was all the candidates own with the guidance of Dr Rolf Crook, with the exception of the following; Ross Jarett who produced the silver nanowires, Robert Mitchell and Richard Douthwaite who produced the CdS and CdSe nanocrystals.

Chapter 5 includes the following work;

Philippa Hardy and Rolf Crook, *A Nanocrystal Test Bed for Excitonic Photovoltaic Cells*, Proceedings from PVSAT-7, Edinburgh, UK, 6-8th April 2011.

The work detailed within this paper was all the candidates own with the guidance of Dr Rolf Crook.

Acknowledgements

This PhD has been the longest and most difficult journey I have ever embarked on and would simply not have been possible without the time, support and help from many people. Thanks must start with my supervisor, Dr Rolf Crook, for all the meetings, answering my endless questions and demanding high quality research, this PhD definitely would not have been possible without your help and guidance. Thanks to my secondary supervisors Professor Rik Brydson and Dr Tim Foxon, for being available to meet and guide me with certain aspects of the project. Thanks to Professor Paul Williams, James McKay and the DTC for selecting me as one of the lucky six, funding me through this adventure and for the extra opportunities - I've very much enjoyed being part of the DTC. There are many other people that provided academic support, resources and time, including; Dr Chandra Malvi and the staff at MITS for the research project in India, Li Chen for evaporating my samples, the Mechanical Engineering workshop for saving me from hand-sawing anymore titanium, Ross Jarrett for making silver nanowires, the LEMAS team – John, Stuart and Richard - for training and impromptu support, Dr Jay Wadhawan and Yan Zhou at the University of Hull for the silver electrodepositing placement, Robert Mitchell and Richard Douthwaite from the University of York for providing nanocrystals and Matthew Booth from Physics at the University of Leeds for providing nanocrystals. Thanks also to the solar group - Graham, Dave, Ross and Chris – I can't begin to imagine what the lab would have been like without all of you. Finally thanks to PVSAT for the paper award.

I would also like to especially thank the first cohort and my very good friends, Hannah, Sam, Gilli, Tom (and honorary members Z and Joel) for being in it together. Thanks for making me challenge myself, inspiring me, and your endless support - I thoroughly enjoyed all the hours spent crying and laughing and I would do it all again. A special thanks to my Zen Shem for everything, I can't put into one sentence exactly how much of an amazing friend, teacher, councillor and partner you've been over the last few years and I don't think one thank you here will ever cover it. Thanks also to the rest of the DTC who have made my working environment for the last 4 years very stimulating and an exciting place full of personal and world change.

Thanks is also due to all of my friends outside of the PhD world for putting up with my hippy ways, supporting me and always being there, I'm very happy to have you all in my life, in particular Emma, Alexis and the aviation boys, Nicky & Veena, Ed, Emma & Lucy. Last but not least thanks to my family for their everlasting love and support – Mum, Dad, Vic & Lee, Ness and Dom.

Abstract

Climate change is a reality and a move away from fossil fuels to renewable energy technologies is an essential part of mitigation efforts. Photovoltaics (PV) provide a way to generate clean and renewable energy from a ubiquitous source. Despite this, fossil fuels are still deeply entrenched in the global energy system, in part due to their low cost. Silicon solar cells currently dominate the PV market, however, their levelised cost is relatively high compared to other energy technologies. Therefore, if PV is to achieve its full potential, there is a need to develop low cost solar cells to enable global uptake of this promising technology.

The aim of this research was to demonstrate a nanocrystal (NC) activated Schottky barrier solar cell fabricated using relatively ambient processes. Ti film was anodised or thermally oxidised and the Schottky barrier was subsequently formed at the interface between TiO_2 and the noble metal, Au, Ag, or Pt, which were sputtered, evaporated or dropcast in nanowire (NW) form. In the absence of activating nanocrystals, the Schottky barrier functions as an efficient cell but only for UV light due to the wide band gap of TiO_2. Nanocrystals with a narrower band gap were deposited on the Schottky barrier to extend the response into the visible region.

The cells fabricated with Ag NWs and Pt provided the largest Schottky barrier heights of 1.02 eV and 1 eV respectively. The Pt device obtained the largest UV photoresponse of 390 μAcm^{-2} and 721 mV at 330 nm, and external quantum efficiency (EQE) of 18% at 330 nm. The Pt and AgNW cells were subsequently activated with CdS, CdSe, CuO, $CuInS_2$ and CdTe NCs. The CdS-NC/Pt, CdS-NC/Ag-NW, and $CuInS_2$-NC/Ag-NW devices, in particular, provided proof-of-concept, generating a UV photoresponse from the TiO_2 and a visible photoresponse from the NCs consistent with the respective band gaps. The optimum EQE measured for the CdS-NC/Pt device was 0.04% at 470 nm. Hence, this work demonstrates the NC activated Schottky barrier solar cell and provides a possible low cost fabrication route for future development.

Table of Contents

List of Tables

List of Figures

Appendix

Chapter 1

An Introduction to Photovoltaics

There is a large drive towards using low carbon and renewable energy sources for energy generation globally due to increasing concerns and awareness of climate change. It is well known that atmospheric concentrations of greenhouse gases (GHG) have increased since 1750 exceeding pre-industrial values, as a direct result of increased fossil fuel consumption due to human activities. This has led to climate warming, which has been observed through increases in global average air and sea temperatures, snow and ice melting, and rising global average sea level [1]. The interlinked problem of increasing fossil fuel consumption and global warming highlights the need for a low carbon future.

One of the largest emission intensive industries in the UK is the power sector accounting for 40% of CO_2 emissions [2]. With global energy demand forecasted to increase by 45% by 2030 [3], electricity generation needs to be dramatically decarbonised if we are to meet our 2050 target of a reduction in GHGs by 80% from 1990 levels and avoid dangerous climate change [4]. The UK is further legally bound to provide 15% of the UKs energy demand from renewable sources by 2020 [5]. This further emphasises the scope for low carbon and renewable energy generating technologies to help meet these targets.

The solar resource is a clean, ubiquitous and renewable source of energy, with approximately 10,000 times the current total human energy consumption globally reaching the earth each day [6]. It is clear that the potential for solar technology is huge. If solar energy generation met just 1% of the UKs electricity demand 1.5 million tonnes of GHG per annum could be avoided [7]. Furthermore, solar power alone is capable of meeting all worldwide 2050 targets by installing solar technology on as little as 0.4% of land globally [6].

There has been a rapid uptake of solar PV over the last few years, due in part to government financial initiatives, such as the Feed in Tariff. However currently solar technology only accounts for 0.4% of the UKs electricity generation [8]. For solar technology to become a feasible contender for energy generation a number of technological barriers must be explored, including its high levelised cost, high life cycle emissions, and limited photoconversion efficiency. It is therefore worth exploring alternative novel solar cell technologies in an attempt to reduce solar cells cost as well as increase efficiency.

1.1 Current solar cells - room for improvement

Silicon solar cells currently dominate the market with a 90% share, the remaining 10% attributable to thin film technologies [9]. This large market share is mainly due to economics, with China producing very cheap cells, enabled by technology maturity, reliability and abundance of raw silicon. Silicon is an ideal material for use in PV cells due to its 1.1 eV bandgap which absorbs visible light. However, there are many disadvantages with first generation silicon solar cells including high life cycle emissions, high manufacturing cost and high levelised cost compared to other renewables and fossil fuels. Despite its technological advantages, silicon solar cells also have a theoretical efficiency limit. It has been indicated by many that investigating alternative materials or technologies can provide a route to further enhance this efficiency limit [10].

1.1.1 Life cycle emissions

Life cycle emissions of low carbon technologies are an important consideration for our future energy mix. Despite having a clean fuel source the life cycle emissions of first generation solar cells are the highest of the renewable technologies family, estimated to be between 1 – 218 gCO_2-eq/kWh, with a mean of 49.9 g CO_2-eq/kWh across a review of PV life cycle assessments [11]. It has been estimated that 71% of these emissions are produced by the energy intensive extraction, processing and fabrication of the cell. Sengul and Theis [12] carried out a comparative life cycle assessment between current silicon cells and future nanocrystal solar cell technology. Their study estimated silicon solar cell life cycle emissions to be 20-30 g CO_2-eq/kWh whereas their proposed nanocrystal solar cell architecture achieved 5 g CO_2-eq/kWh. The proposed cell used an aluminium substrate, CdSe nanocrystals, alumina and ITO and was assigned a comparative efficiency of 14%. It is clear therefore that the type of solar cell technology and its processing techniques considerably affect its life cycle emissions. Moreover moving to nanocrystal solar cell architectures could potentially reduce the life cycle emissions of solar cells.

1.1.2 Solar cell production cost

As well as an energy intensive production process, crystalline silicon cells require costly manufacturing due to the purity and thickness of silicon required [13-15]. Manufacturing in china has recently led to a sharp decrease in cost, with a price crash from €1 to €0.46 /Wp. However, this has led to negative profits and many bankrupt businesses, hence not a true reflection of the cost of silicon solar cells [16]. Despite these cost reductions solar cells still account for about 40% of the overall cost of an installed system [9]. Therefore there is a need to explore alternative materials to reduce cell production costs and allow flexibility of resources. It is possible to reduce cell production costs by using alternative architectures, as demonstrated by thin film cell technology. However, thin films operate at a lower efficiency for this cost reduction. Further developments should therefore concentrate on decreasing cost whilst maintaining or increasing efficiency.

1.1.3 Levelised cost of PV

Many events and supporting government policies have led to a dramatic increase in the use of PV over the last decade. Notable are the temporary silicon shortages between 2004 – 2008, after which silicon prices fell dramatically, the recent cost reductions due to China's rapid cell manufacturing growth, combined with increasing electricity prices and coherent Feed-in-Tariff (FiT) schemes in over 50 countries worldwide. However, PV remains expensive compared to many renewable and fossil fuel technologies, with an average levelised cost of £290/MWh [9, 17]. Therefore, looking into alternative materials could potentially reduce the levelised cost for PV.

1.1.4 Efficiency

Silicon is an ideal material for PV with a bandgap of 1.1eV, which absorbs mainly the visible part of the spectrum. Ultraviolet and infrared radiation do not have enough energy to excite an electron and are instead absorbed as heat or reflected by surface coatings [18]. If the UV and IR radiation can be converted into useful electrical energy, cell efficiency can potentially increase. The maximum theoretical efficiency from silicon solar cells is 30%, the Shockley-Queisser limit [19, 20]. However, current commercial module efficiency lies between 12-21%, depending on the manufacturing process and technology used [9]. Silicon technology is limited to this theoretical efficiency limit, whereas other technologies employing architectures different to the p-n junction can enhance efficiency above 30%. A few second generation technologies such as multi-junction cells and concentrator cells have demonstrated this, see 1.2.

1.1.5 Future development

There has been continued development into silicon solar cells, for example developing cheaper materials, such as multi- and poly-crystalline silicon, streamlining the production process, and achieving a commercial cell efficiency of 21% [21]. However, first generation silicon cells are close to reaching their improvement limit, so future developments are focused towards developing new cell architectures and incorporating nanomaterials to explore new avenues to reduce cost and life cycle emissions and increase efficiency [22].

1.2 Alternative solar cell technology

There have been significant advances in solar cell research, with the main cost reductions and efficiency increases to date arising from thin film and multi-junction concentrator solar cells respectively [15, 23]. Second and third generation solar cells explore new solar cell architectures and materials to overcome some of the barriers faced by first generation solar cells, such as high cost, high life cycle emissions, brittleness and limited theoretical efficiency. The research focus of second generation technology was to create solar cells at a lower cost, excepting a compromise in efficiency. Second generation solar cells have been commercialised, with thin film solar cells accounting for approximately 10% of the market [9]. Third generation solar cells generally encompass research solar cells that focus on incorporating nanotechnology into solar cell architectures, with the overall aim being to increase cell efficiency by taking advantage of nano-related phenomena. By using nanomaterials third generation solar cells can also potentially reduce material use, cost and life cycle emissions.

1.2.1 Second generation solar cells

Second generation solar cells exhibit a lower efficiency to first generation devices, but also have a lower cost [13]. This reduced cost comes from a different manufacturing process and the use of thin films, which reduces the amount of materials required. Second generation technology makes use of alternative semiconductors, generally amorphous silicon, CdTe, and CIGS, which have gained popularity due to their desirable energy gaps for solar applications, in the visible and IR range [24]. CIGS thin film solar cells are currently the most efficient with efficiencies of around 18% [25]. An advantage of thin film technology over silicon is that they can be flexible, which overcomes the brittle nature of silicon wafers. The disadvantage with thin film technology is that they are slightly less efficient because they suffer from structural defects [21]. A secondary controversial issue with thin films are that the semiconductors employed contain toxic and rare elements, making them less favourable material candidates compared to silicon.

1.2.2 Third generation solar cells

Despite development first and second generation solar cells are near to reaching their improvement limit, in terms of lowering cost and increasing efficiency, so developments in solar cell technology are now focused on novel third generation cells incorporating nanotechnology [13, 21, 22]. Third generation solar cells currently being researched include hot carrier, multi-junction, quantum well, tandem and excitonic solar cells. Some of these technologies are more advanced than others. In particular the triple junction tandem cell which has achieved ~41% efficiency under concentrated light, the highest efficiency of any solar cell to date [26]. Tandem cells involves stacking cells on top of each other, each with varying materials and hence bandgaps, harnessing photons of light from a broader array of wavelengths [21, 22]. It has been suggested that multi-junction type solar cells can theoretically harness an efficiency of 66% [18]. The drawback with this type of sophisticated technology is that it is very expensive to produce [13].

Solution processed nanocrystals provide an opportunity to help reduce the cost and increase the efficiency of third generation solar cells [12]. There are a multitude of different excitonic solar cell architectures suitable for use and manipulation with solution processed nanomaterials, these include depleted heterojunction, thin absorber, hybrid, bulk heterojunction, nanocrystal sensitised, and Schottky solar cells [10]. Advances in solution processed nanocrystal solar cells to date have led to efficiencies of up to 5.1% AM1.5 power conversion efficiencies [27]. Excitonic solar cells using solution processed nanocrystals are therefore worth exploring further.

1.3 The use of nanotechnology for solar cells

Incorporating nanomaterials in solar cells provides many advantages including the potential to use lower cost processing methods, decrease the quantity of materials used and potentially increase efficiency through nano-related phenomena. The use of nanotechnology provides a significantly flexible approach to producing PV cells, since various nanomaterials can be incorporated into a range of different cell architectures.

1.3.1 Life cycle emission reductions

Lower life cycle emissions have been calculated for a proposed CdSe QDPV, averaging 5 gCO_2-eq/kWh, which is significantly lower than silicon, thin film and dye sensitised solar cells. The main reason for this is that nano-solar cells inherently require fewer raw materials and can be processed using less energy intensive processes. Similar low life cycle emissions can therefore be expected for other nanocrystal architecture. Further reductions of life cycle emissions can also be realised from using alternative transparent conductive electrodes to replace traditionally used bulk aluminium or ITO [12]. This could include nanowires, nano-doped materials or nano-composite membranes.

1.3.2 Reduced manufacturing cost

It has been postulated by many that solar cells incorporating nanomaterials have the potential to reduce high manufacturing costs [7, 10, 12, 19, 28, 29]. This is mainly because nanomaterials can be processed via low cost solution processing. Reduced manufacturing costs can also be realised due to the use of less materials. As well as benefitting from a reduced cost, solution processing is also useful for integration of nanomaterials into various types of solar cell architecture [10]. Since cultivation and manufacturing account for a large proportion of the overall solar PV cost, as discussed earlier, it is clear that using nanomaterials can help to reduce this cost, which will ultimately also reduce the levelised cost for PV.

1.3.3 Increasing efficiency

There are many ways that nanomaterials can be used to increase the theoretical efficiency of conventional solar cells, including multiple exciton generation (MEG), hot electron generation and doping nanomaterials to create mid states [30]. MEG relates to multiple excitons produced from a single photon, which can raise the theoretical efficiency limit to 44% and higher with light concentration [31, 32]. Furthermore, using nanocrystals in solar cells provides a high surface area that increases internal reflections and hence increases the probability of light absorption [30]. Higher efficiency cells are of interest as they can reduce the amount of materials required for an equivalent energy production which further decrease the overall cost and life cycle emissions of solar cells [12, 14, 27].

As well as inherent properties and nano-related phenomena, nanomaterials can be manipulated and controlled to engineer certain properties such as the bandgap, size, shape and composition of nanocrystals, enabling manipulation over electronic and optical properties. However, one of the main problems with NC solar cells is the extraction of photo-generated charge from the point of generation to the external electrodes, which can be limited by energetic, kinetic and structural constraints [33].

1.4 Nanocrystal-activated Schottky barrier solar cell

As discussed in 1.3, third generation solar cell technologies seek to reduce solar cell cost and life cycle emissions by utilising nanomaterials. Nanomaterials also hold promise to potentially increase cell efficiency, although this is more of a longer term aim. There are many different possible nanocrystal solar cell architectures that can be explored further. This research focuses on a nanocrystal activated Schottky barrier solar cell.

A Schottky barrier solar cell provides a low cost and robust architecture that can be enhanced with nanocrystals. Incorporating nanocrystals plays a crucial role in potential efficiency enhancement and can also further reduce costs due to solution processing and the use of fewer materials. McFarland and Tang [34] and Tang [35] have previously reported a photo-active Schottky solar cell, using a merbromin dye and CdS/CdSe nanocrystals respectively, with promising results. No other study to date has built on this work. This work aims to fill this research gap and show that a wide range of semiconducting nanocrystals are suitable for activating the Schottky barrier solar cell.

1.4.1 Research aims and objectives

This research presents a proof of concept for a nanocrystal activated Schottky barrier solar cell which explores avenues for low cost processing and widening the diversity of materials that can be used with the potential to increase efficiency in the future. The research at this stage is fundamental and will therefore not be competitive with first or second generation solar cell technology at present.

Aim: Proof of concept and understanding of underlying physics of a nanocrystal activated Schottky solar cell.

The main objectives are to;

- Fabricate and characterise a Schottky barrier solar cell using a variety of low cost processing techniques.
- Explore a range of transparent conductive electrodes to demonstrate flexibility of the architecture and provide low cost processing routes for the future.
- Activate the Schottky solar cell with a range of semiconducting nanocrystals to show visible absorption of the complete nanocrystal-activated Schottky barrier solar cell. Compare with the Schottky solar cell to prove the concept of this nanocrystal solar cell architecture.
- Characterise the completed cells using current-voltage and photoresponse data and analyse the results to inform the underlying physics of the nanocrystal activated Schottky solar cell.

1.5 Outline of thesis

This work involved experimental research into the fabrication and characterisation of a nanocrystal activated Schottky barrier solar cell. The following provides a breakdown of the content of each chapter.

Chapter 2 provides a brief physical background of a number of solar cell architectures, starting with the most common p-n junction and then discussing alternative research architectures which incorporate nanocrystals for future solar cell development. A detailed discussion of Schottky solar cells, the architecture selected for this work, and the physical processes related to metal-semiconductor junctions are presented. Analysis into previous work is discussed and an outline of the research gap into nanocrystal activated Schottky barrier solar cells is demonstrated. This chapter concludes with the detailed aims and objectives for this research.

Chapter 3 explains the methods used for the fabrication and characterisation of the nanocrystal activated Schottky solar cell. This includes manual and electro-polishing of a titanium substrate, anodisation and oxidation to create titanium dioxide, deposition of noble metals by sputtering, evaporating, electrodepositing and the deposition of nanowires, and the selection, deposition, and post deposition treatment of nanocrystals. The motivation is given for each material and technique selected with reference to previous studies.

Chapter 4 presents I-V, Schottky barrier heights and photoresponse results for Schottky solar cells fabricated with sputtered and evaporated platinum, gold and silver films and compares this to similar studies in the literature, analysing and accounting for any differences of results. An in-depth discussion of Schottky barrier physics with reference to the I-V results is given.

Chapter 5 presents sheet resistance, SEM, I-V, Schottky barrier heights and photoresponse for alternative Schottky solar cells fabricated with electrodeposited silver and dropcasted silver nanowires instead of bulk metal films. Similar to Chapter 4 an in depth analysis of Schottky barrier physics is given. Comparisons are made between these alternative transparent conductive metal films and the more traditional approach of evaporating given in Chapter 4.

Chapter 6 presents the experimental results for the Schottky barrier solar cell activated with CdS, CdSe, CuO, $CuInS_2$, or CdTe nanocrystals. The nanocrystals were deposited onto the optimum Schottky solar cells only, which were platinum sputtered and silver nanowire deposited cells. This chapter presents mainly photoresponse measurements to indicate the success of the nanocrystal-activated Schottky solar cell and uses measurements from the Schottky solar cell without nanocrystals to verify whether or not the nanocrystals are operational.

Chapter 7 summarises the work, providing main conclusions and suggestions for future work.

Chapter 2

Background on PV Technology Developments

Silicon solar cell technology currently dominates the PV market yet their high levelised cost and life cycle emissions as well as efficiency limitation has prompted research into alternative solar cell architectures that incorporate nanotechnology. The use of nanomaterials in solar cells has the potential to reduce cost and increase efficiency of the next generation of solar cells. This chapter gives an overview of some nanocrystal solar cell architectures currently being investigated. For this work a Schottky barrier solar cell was selected for further research, therefore the background physics on the mechanisms of this device are discussed. Enhancements to this device in the form of activating the surface layer for visible absorption can be undertaken by a dye or layer of nanocrystals. These enhancements are discussed, along with mechanisms for the addition of an activating layer. This chapter concludes with the direction of the rest of this research.

2.1 PV architecture

Nanocrystals (NC) are receiving increased attention due to their application for low cost solar cells and their potential to increase the Shockley – Queisser limit [36, 37]. Nanocrystals can be produced by solution processing which can significantly decrease the overall cost of the cell as well as simplifying their integration into various types of solar cell architecture [7, 10, 19, 28-30]. In addition a variety of low cost, abundant and wide bandgap semiconductors, which would otherwise be unsuitable for PV applications, can be used due to bandgap tuning [10, 27]. Modifying the size and shape of wide bandgap nanocrystals can tailor their absorption properties to match the solar spectrum. Due to the wide range of materials and architectures that can be used, resource dependency and exhaustion is less likely.

Incorporating nanotechnology into solar cells has the potential to increase the efficiency, through the exploitation of quantum phenomena such as multiple exciton generation and hot electron carriers [30]. Moreover nanocrystals provide a higher surface area that increases internal reflections and hence increases the probability of light absorption. As well as inherent properties, nanomaterials can be engineered by controlling their size, shape, composition and bandgap to alter their electrical and optical properties [10, 33].

One of the main problems with using NCs in solar cells is the extraction of photo-generated charge from the point of generation to the external electrodes, which can be limited by energetic, kinetic and structural constraints. Other disadvantages include the fact that it is difficult to determine the intrinsic properties of the active NC as their electrical, optical and structural properties will change due to the chemical or physical treatments. More research is needed to gain a better understanding of NC energy levels and charge transfer mechanism in order to enhance the effective extraction of photogenerated charges across NC interfaces [33].

Nanocrystal solar cells work differently to the current silicon p-n junction solar cells described in 2.1.1 which is dictated by their structure and the materials used. There are many research solar cells that are currently under investigation to contribute to the issues of cost, resource diversity and increased efficiency of current silicon cells. Those most relevant to this research include the hot carrier, depleted heterojunction, quantum dot sensitised, and Schottky solar cells.

2.1.1 P-n junctions

A p-n junction is formed between a semiconductor with an excess of electron acceptors or holes (p-type) and a semiconductor having an excess of electron donors or free electrons (n-type). When p and n – type semiconductors come into contact there is a large gradient of electron and hole concentrations. As a result charge transfer occurs at the interface, where excess electrons in the n-region diffuse to the p-region and excess holes in the p-region diffuse to the n-region, which continues until the Fermi energies are equal. This charge transfer induces an electric field at the interface from the n- to p-regions, creating a space charge region, which results in band bending at the semiconductor interface [38, 39]. Figure 2-1 displays the p-type and n-type semiconductors and the p-n junction formation, as described above.

When a photon of light is absorbed with energy equal or higher than the bandgap an electron is promoted from the valence band into the conduction band, leaving a ‘hole’ in the valence band, also known as an electron – hole pair. An electric field is formed which prevents the recombination of electron-hole pairs [18].

The maximum theoretical efficiency of a p-n junction cell, 30 % for a 1.1 eV energy gap, is the Shockley–Queisser limit [20].This theoretical value is limited due to loss mechanisms, shown in Figure 2-2. One of the main losses is due to the energy of incident photons. Photons with energy lower than the bandgap will not be absorbed, and photons with higher energy are wasted as heat (carrier thermalisation) [40, 41]. Other losses include surface reflection, carrier recombination, below and above bandgap photons, contact voltage drop, and junction voltage drop [18, 42].

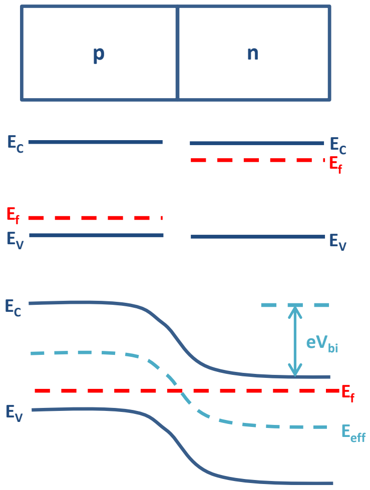

Figure 2-1: P-n junction formation schematic, illustrating the energy band diagrams of the semiconductors and the p-n junction in thermal equilibrium, showing the conduction band E_c, valence band E_v, Fermi energy E_f and built in potential eV_{bi}, adapted from [24, 39].

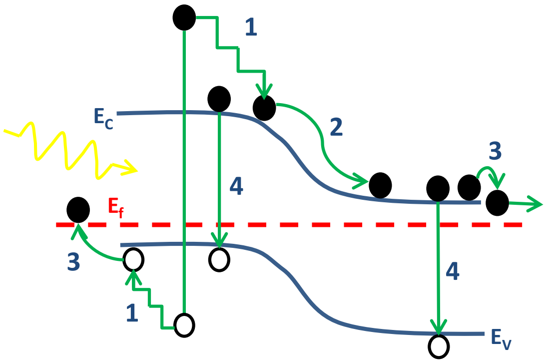

Figure 2-2: Efficiency Losses in a solar cell - (1) thermalisation loss, (2) junction loss, (3) contact loss, (4) recombination loss, adapted from [42].

Silicon p-n junctions currently dominant the PV market, however it is evident from Figure 2-2 that there is room for improvement. Alternative architectures, such as the Schottky barrier solar cell, can reduce recombination due to being a majority charge carrier device. Nanomaterials can be incorporated into many different solar cell architectures and will have different roles depending on the design of the cell. The next few sections will introduce the current research architectures incorporating nanomaterials.

2.1.2 Hot carrier solar cell

The main loss mechanism in a p-n junction solar cell is due to carrier thermalisation, as shown in Figure 2-2. The hot carrier solar cell (HCSC) addresses this problem. The main concept of the HCSC is to reduce the rate of photoexcited carrier cooling, so that carriers can be collected whilst they are still at high energies or ‘hot’. This allows higher voltages to be obtained from the cell [43].

Hot charge carriers are generated by photons with energies above the semiconductor bandgap but these cool very quickly, about 1 pico-second, limiting the amount of energy that can be captured from them. Therefore, extracting carriers at elevated temperatures requires a delay in carrier cooling, which happens in an absorber [44]. The absorber reduces thermalisation and allows enough time for carrier extraction. The absorber is a semiconductor material with a small bandgap that maximises photon absorption by slowing down the rate of carrier relaxation by a phonon bottleneck effect. This effect has mainly been observed in bulk absorbers at extremely high illumination intensities (i.e. equivalent to 2500 suns) [45]. Quantum dot superlattices and many other nanostructures are currently under investigation for use as an absorber as they have the potential to reduce carrier relaxation at lower light intensities due to quantum confinement [46].

Another key aspect of the hot carrier solar cells is the energy selective contacts (ESC), which act like an energy filter to only allow a narrow energy range to pass through to the metal contacts [47]. The ESC has energy states for electrons within a certain energy interval and provide a contact to the hot electron distribution in the absorber. This transmitting contact is generally a large bandgap n-type semiconductor for electrons and a p-type semiconductor for holes [48]. High energy carriers with energies outside of this prescribed range are reflected back to the absorber where they are normalised to lower energies via scattering and then re-emitted to the ESCs [47]. The lower band edge of the ESC prevents cold carriers from reaching the hot absorber, which would decrease the average energy of carriers [43]. Figure 2-3 shows a schematic and energy band diagram of the HCSC to illustrate the absorber and ESC.

Together the absorber and the energy selective contacts ideally allow isentropic cooling, which avoids energy losses. This controlled cooling of electrons and holes does not alter their concentration or energy distribution. The advantages of this solar cell is that it can have almost any value depending on the energy of the electrons and holes withdrawn in the energy selective contacts [48].

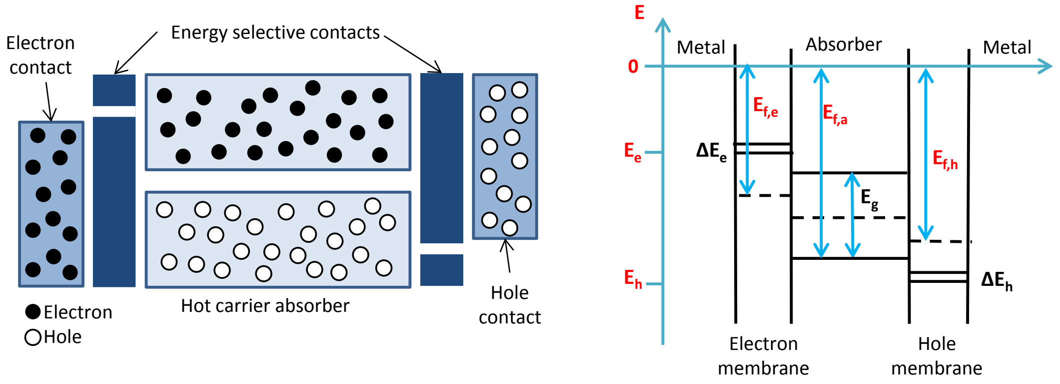

Figure 2-3: Hot carrier solar cell schematic and energy diagram, adapted from [47, 48].

If the energy in 'hot carriers' could be captured then efficiencies could theoretically increase up to 66% [40, 47]. These efficiencies are realistic if scattering of the photo-excited electrons and re-absorption of photons in the conduction band is faster than hot carrier cooling and transfer of hot carriers to the ESC in the narrow energy window [40]. A disadvantage with this device is that some excess energy can be lost when the hot carriers come into contact with the cold metal electrodes [47].

Hot electrons can cool in a number of ways, including scattering, cooling by phonon emission, radiative and non-radiative recombination. These relaxation processes can be altered by quantization effects, which occur when hot carriers are confined to spaces that are smaller than their de Broglie wavelength, around 10 – 50 nm [46]. Hence nanomaterials have a large potential to increase the feasibility and efficiency of the hot carrier solar cell, via reduced carrier cooling and enhanced extraction of hot carriers [40, 49]. In addition to this, nanocrystals can increase carrier generation through enhanced impact ionisation [46]. Impact ionisation is an important phenomena in nanocrystals whereby a photon with light above the energy gap can excite a high energy electron-hole pair which can in turn generate two electron-hole pairs [50]. Slowed carrier cooling has previously been reported for semiconductor nanocrystals [51-53]. Furthermore nanocrystals offer total energy selection and they can be tuned to optimise carrier collection by controlling the size of the nanocrystals [47].

The hot carrier solar cell architecture is currently in the research stage. Previous studies have offered discussions of concepts and materials [44] and modelling of ESC [45], and the absorber [49], however no studies to date have demonstrated a fully operational hot carrier solar cell. The progress in this field is at proof of concept stage – a study using silicon nanocrystals as an ESC has been shown by Conibeer et al in [54] and [43] and again by Shrestha et al [47]. In addition Tisdale et al [40] show that hot carrier transfer is possible from PbSe nanocrystals to a TiO_2 electron acceptor, and it is suggested that the same can be expected from other semiconductor nanocrystal materials.

2.1.3 Depleted heterojunction solar cell

The depleted heterojunction (DH) solar cell architecture comprises of a p-type semiconducting nanocrystal absorbing film sandwiched between a wide bandgap n-type semiconductor and a metal electrode, shown in Figure 2-4 [55]. In this device the purpose of the semiconductor is to transport electrons. Minority carrier separation exists due to the transparent electron accepting semiconductor being on the illuminating side of the cell. An in-built depletion region exists due to charge transfer from the electron accepting contact to the colloidal quantum dot (CQD) film, indicated in the energy band diagram in Figure 2-4, hence back electron transfer from the TiO_2 to the CQD film is prevented. In addition, there is a large potential barrier in the valence band for hole injection to the electron-extracting electrode [10, 27].

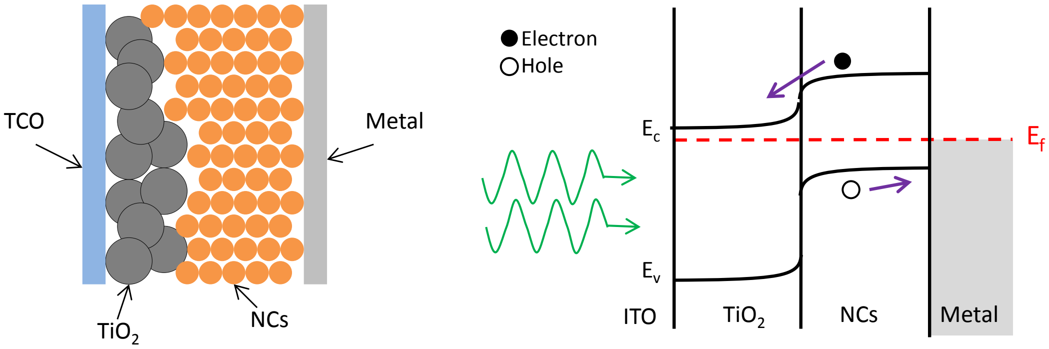

Figure 2-4: Depleted heterojunction solar cell schematic and energy band diagram, adapted from [27].

The DH architecture is different from the standard p-n heterojunction, since the bandgap and size of the QDs can be varied in DH cells to alter the absorbing ability and open circuit voltage respectively. Moreover the CQD provides a low cost processing route. The DH architecture combines the advantages of the Schottky and QD sensitised solar cells, see next two sections, which allows this design to obtain higher FF, V_{oc} and J_{sc}. Improved open circuit voltage can be obtained due to better charge separation at the CQD/TiO_2 interface [10, 27]. Nanocrystals are a vital part of the depleted heterojunction architecture since they allow passivation of the semiconductor/QD interface, which means they overcome surface defect states at the interface due to being solution phase deposited and hence do not suffer from Fermi level pinning. Furthermore, the DH cell has good charge transport functionality and can employ many monolayers of light absorbing CQDs, which could further add to the efficiency of the device [27].

There have been many demonstrations of DH solar cells, in particular Luther et al [56] obtain a photoconversion efficiency (PCE) of 2.9% for PbS and ZnO nanoparticles, Ju et al [57] obtain a 3% PCE using PbS/TiO_2 nanoparticle, Pattantyus-Abraham et al [27] achieve 5.1% PCE using PbSe-QD /TiO_2 and Tang et al [58] achieve the highest efficiency to date of 6% with a PbS/TiO_2 DH cell.

2.1.4 Quantum dot sensitised solar cells

The working principle of the quantum dot sensitised solar cell (QDSSC) is similar to the dye-sensitised solar cell (DSC) which have reached efficiencies of up to 10% [59]. The main difference between these two architectures is that the QDSSC uses a combination of two or more nanostructures instead of a dye. A larger variety of materials and different configurations can be used in the QDSSC and therefore a specific configuration may enhance performance, for example the type of electrolyte can shift energy bands and affect surface traps, whereas the density of QDs in the cell can affect recombination mechanisms [60].

The QDSSC is composed of a wide bandgap semiconducting mesoporous nanostructure (generally TiO_2), sensitised by a CQD monolayer and a liquid or solid electrolyte fills the free space between the nanostructures. The nanostructure can be in any form including films, rods, tubes, or wires and provide a larger surface area than the equivalent absorber in the DSC. The CQD layer can be very thin, in the region of a monolayer, since QDs have a higher absorption coefficient than organic dyes and the light will travel past hundreds of these monolayers [60, 61].

Light is incident on the transparent conductive electrode, as demonstrated in Figure 2-5, and QDs absorb light and inject excited electrons into the conduction band of the semiconductor nanostructure by diffusion. Oxidised QDs are then rejuvenated by the redox electrolyte [60]. Using quantum dots to replace the dye molecules enables optical tuning through semiconductor material and size selection. Similar to the other nanocrystal devices described previously, nanocrystals can reduce the cost by low cost processing techniques and enhance efficiency by multiple exciton generation [62]. Moreover the nanostructured absorber and nano-sensitizer overcomes losses associated with bulk film or nanoparticle films which suffer from recombination loss at grain boundaries due to charge trapping, which leads to higher open circuit voltages compared to other architectures [33, 60].

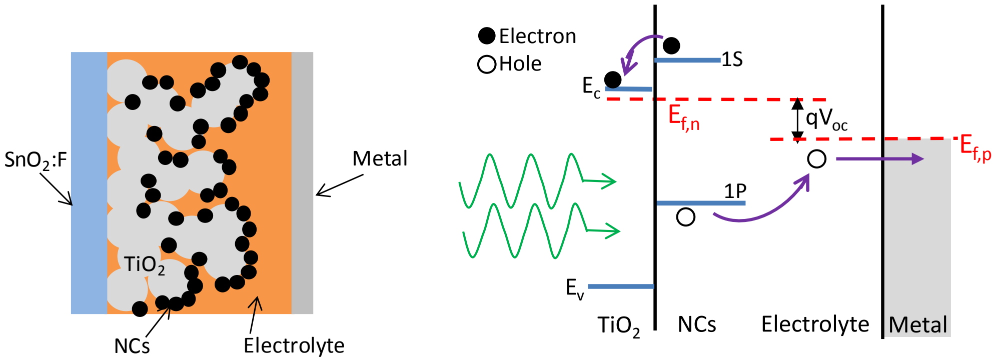

Figure 2-5: Colloidal quantum dot sensitised solar cell schematic and energy band diagram, adapted from [27].

The main disadvantages with this architecture include the fact that colloidal nanocrystals are likely to damage the ordered array of nanowire/nanocrystal combination and molecule linkers are likely to cause barriers to charge transfer. Therefore, more understanding is needed at this interface and between the substrate surface to improve QDSSCs [62].

A fully operational QDSSC has been demonstrated in many studies. The largest power conversion efficiency (PCE) achieved to date is 4.22% for co-sensitisation of CdS/CdSe nanocrystals on a TiO_2 nanocrystalline film [63], followed by a 4.15% PCE for CdSe sensitised TiO_2 nanotube Peng [64] and 2.3% PCE for PbS/CdSe sensitised nanostructured TiO_2 [65]. Many other studies in QDSSC have obtained a 0.4–2.3% PCE using nanostructures of CdS/TiO_2 [66], CdSe/TiO_2 [61, 67, 68], PbS/TiO_2 [69], nitrogen doped TiO_2/CdSe [70], CdSe/ZnO [71] and CdS/graphene incorporated TiO_2 [72].

2.1.5 Schottky solar cells

A Schottky solar cell is one of the simplest solar cells that can be fabricated, see Figure 2-6. The cell has a robust design making use of a transparent conductive electrode, coated with a nanocrystal or bulk film semiconductor and then a metal contact [73]. This cell works by band bending caused at the interface between the metal and semiconductor creating a depletion region due to charge transfer, described in detail in section 2.2. The efficiency of these cells depends on how effectively carriers can be extracted before recombination, however this relies on the built-in potential of the work function and so depends on the type of materials used in the cell [10].

Advantages of the Schottky solar cell are that they can incorporate solution processed nanocrystals, making this design particularly low cost [10]. Colloidal nanocrystals can be adhered easily to the surface by spray-coating or through inkjet printing requiring only a very thin absorber layer of approximately 100nm. Both the processing and use of less material is therefore beneficial in reducing the cost of this solar cell architecture, compared to a p-n junction [74]. Similar to the other architectures described previously, the incorporation of nanocrystals can enhance the overall device performance due to engineering certain optical properties and nanomaterial related phenomenon, such as multiple exciton generation.

Extensive research into Schottky barriers has shown that the barrier created can suppress recombination if materials are suitably matched, for example a high work function metal with a semiconductor, for example TiO_2 [75]. Furthermore, noble metal deposition onto TiO_2 can shift the Fermi level to more negative potentials which leads to better charge separation and therefore reduces recombination of photo-generated electron-hole pairs, which in turn enhances efficiency. This has been demonstrated in Ag/TiO_2 [76] and Au/TiO_2 [77] Schottky barriers.

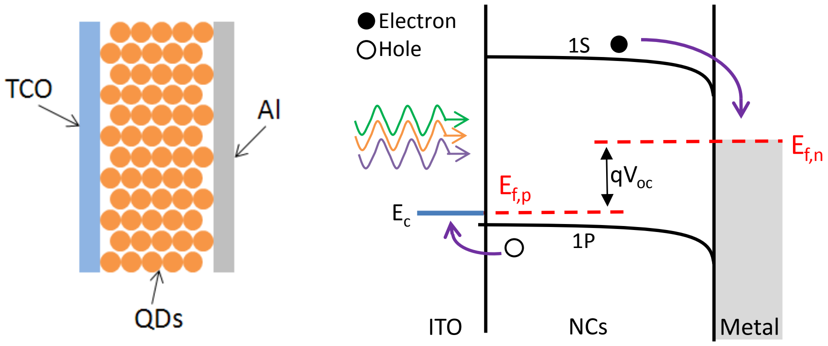

Figure 2-6: Schottky barrier cell schematic [left] and energy band diagram [right], adapted from [27].

In this architecture light absorption occurs at the Ohmic side of the cell, which means that excited electrons must travel the thickness of the semiconductor to the Schottky barrier and hence are more prone to recombination before reaching the electrode. Interfacial states and defects are inherent in Schottky barriers, which leads to interfacial oxide formation and Fermi level pinning [74]. These defects consequentially limit the open circuit photovoltage and fill factor to below their potential [10, 27].

Research into Schottky barrier solar cells has slowed in the last decade due to these fundamental material challenges [74]. However, previous studies of Schottky barrier solar cells using the structure shown in Figure 2-6 have obtained photoconversion efficiencies up to 3.3% and 3.4% using PbSe QDs [33, 78] and 3.6 % with PbS QDs [79]. As discussed, most studies to date use colloidal semiconducting nanocrystals in the cell for electron transport and formation of the Schottky junction, using nanocrystals as a photoactive layer has been less well studied.

Table 2-1 presents a concise review of a range of recent Schottky solar cells. Many different semiconductors have been trialled, including polymers, organic materials and nanostructures. A substantial number of the devices use a semiconducting nanocrystalline film, due to the low cost fabrication and requiring fewer materials to reach equivalent or higher efficiencies. As is evident from the table, the most popular materials for the Schottky devices centralise on utilising Si, PbSe, CdTe and PbS, producing mainly p-type Schottky barriers and utilising infrared absorbing materials. The most popular substrate for the Schottky barriers is a transparent conductive oxide, namely ITO, with fewer being based on metals such as titanium or stainless steel. Silver and aluminium are the most commonly used metal contacts.

Most of the devices presented in Table 2-1 absorb in the UV and/or Infrared region due to the use of small bandgap semiconducting nanocrystals or wide bandgap bulk semiconductors. The highest power conversion efficiency from this review is 5% for the Al/CdTe/ITO Schottky barrier device. More novel developments by McFarland and Tang [34] and Tang et al [35] have incorporated a photoactive dye and nanocrystals, respectively, to enhance the visible absorption of the Schottky barrier device, but have so far not exceeded this top efficiency for a Schottky barrier device. This highlights the scope to further develop visible active Schottky barrier devices for use as a low cost and potentially high efficient solar cell.

The next sections 2.2 and 2.3 will give a more detailed discussion of the physics and mechanisms of Schottky barrier solar cells before investigating progress and scope of a nanocrystal-activated Schottky barrier solar cell.

Table 2-1: Review of Schottky barrier solar cells.

Schottky Cell Details	Fabrication method	SBH	R_S/R_L	I_S/n	J_{SC}/V_{OC}	Efficiency/ Fill factor	Comments	Reference
Al/CdTe/ITO	Thin films of 360 nm CdTe nanorods are spin cast on to ITO and then coated with cadmium chloride, sintered at 400°C and rinsed in hot water to remove remaining $CdCl_2$. Aluminum contacts are evaporated on top of the cell.	~1eV	-	-	20.4 mA cm^{-2}	PCE = 5%	Pathway to ultra-thin and highly efficient nanocrystal devices. Less material and cheap processing techniques used. P-type Schottky barrier formed. Sintering CdTe nanocrystals was necessary to enhance optical absorption. $CdCl_2$ treatment causes red shift to absorption due to loss of quantum confinement. Short circuit current densities are comparable to much thicker CdTe films. Further improvements can be achieved by more sintering and improved contacts.	Olson et al [80]
			-	-	540 mV	45.5%		
Al or Ag/PbS/ ITO	PbS prepared by colloidal synthesis. PbS nanocrystals were layer by layer deposited on to ITO and then annealed in air at 90°C for 5mins. Electrodes were thermally evaporated on top at pressure.	-	157 – 669 Ω	-	<7.8 mA cm^{-2}	EQE = 24.5 – 38.1 % MPCE = 0.78 – 4.1 %	Devices stored in ambient conditions. Ag device was more stable and had a much longer lifetime than the Al device; however Al obtained a larger V_{OC}. Device losses are caused by degradation of the Schottky barrier and oxidation. Introducing a LiF interface layer in the Al/PbS device enhanced stability and performance.	Tang et al [81]
			752 – 4590 Ω	-	0.24 - 0.42 V	27 – 48%		
Mg, Al, Au, Ag/PbSe/ITO	PbSe spin coated on to ITO and then immersed in a solution of benzenedithiol in acetonitrile for 10-30 minutes. A second layer of nanocrystals were	-	-	-	-	EQE = 37% IR and 70% visible	P-type Schottky barrier formed. Device was stable in air for 10 days. Evaporated contacts failed to show a photoresponse until PbSe was chemically treated. Replacement of long	Koleilat et al [82]

	deposited to ensure a densely packed film. The top and bottom contacts were evaporated. Long oleate chains surrounding nanocrystals were replaced with shorter organic ligands.					PCE = 3.6% IR and 1.1% at AM1.5 IQE = 90% IR	organic chains enhanced charge transport. Diffusion found to be the main charge transport mechanism.	
			-	-	-	-		
Al/PbSe/ITO	60 – 300 nm monodispersed, spherical PbSe nanocrystals formed on a patterned ITO substrate are dip coated in a layer by layer coating method from a hexane solution, followed by washing in 0.01 M EDT in acetonitrile to remove oleate ligands. Al contacts are evaporated onto the PbSe.	-	-	-	24.5 mAcm^{-2}	EQE = 55-65% visible, and 25% IR. IQE = 80% visible PCE = 2.1%	Schottky barrier is at the back rather than the front contact, so thin cell is required, which makes light absorption for higher efficiencies a difficulty. The diode becomes a resistor when exposed to air for several minutes. Surface oxidation of the nanocrystals leads to device degradation.	Luther et al [83]
			-	-	239 mV	0.41		
Dye/Au/TiO$_2$/Ti	250nm Ti layer evaporated on a Ti foil. 200nm TiO$_2$ produced by thermal oxidation at 500^{0}C. 10-50nm Au films electrodeposited. Substrate was immersed in photoactive merbromin to adsorb it to the substrate and then rinsed in water.	0.9 eV	-	-	10 - 18 µA cm^{-2} at 100 mWcm^{-2}	IQE = 10%	Aim to produce a durable low cost cell that can use a variety of materials. Dye used as a photoreceptor, having an energy level above the barrier. Barrier height not measured experimentally. Internal electron emission is the dominant mechanism. Does not require a reducing agent in the electrolyte for charge transport. Photo-oxidised dye is reduced by transfer of thermalized electrons from Au Fermi level.	McFarland and Tang [34]
			-	-	600 - 800mV at 100 mWcm^{-2}	0.63		
Al/Si NCs/ITO	Silicon NCs were synthesized by a plasma reactor under a vacuum. Si NCs were spin	-	-	-	0.148 mAcm^{-2}	PCE = 0.02% IPCE = ~4% in UV	Nanocrystals do not require post treatment. No ligand exchange, removal or attachment was undertaken for the Si nanocrystals, which could reduce fabrication cost. Device performance	Liu and Kortshagen [84]

	cast onto ITO and repeated several times. Al was then deposited on top.		-	-	0.51V	0.26	was poor due to poor absorption and recombination.	
Mg/PbS/ITO	ITO was dip coated in a 4% volume solution of ethanedithiol in acetonitrile and then into a dilute solution of PbS-nanocrystals. This dip coating was repeated 3 times. The devices were all annealed in air/vacuum at 110°C, 130°C, and 150°C for 3 hours. Mg was deposited by thermal evaporation.	-	-	-	-	PCE = 2% EQE = 18% at infrared	Results show that air annealed PbS NCs perform better than vacuum treated. Ligand exchange carried out to replace strongly bound long oleic acid ligands with a butylamine ligand which reduces the spacing between particles and improves conductivity. Absorption spectra of nanocrystals indicate quantum confinement and that the nanocrystals had not been sintered into an amorphous film.	Klem et al [85]
			-	-	100-425 mV at infrared	-		
Pt/Si-NW/n-Si/Al	Polished n-type Si wafers were etched with 35 mM $AgNO_3$ and 15 mM HF to produce Si nanowires (NWs). Si-NW samples were treated in a 5% aq HF solution to remove silicon oxide, then passivated by hydrogen. Pt nanoparticles were deposited by electroless plating in a K_2PtCl_6 solvent. Ohmic Al contact evaporated on the back.	0.93 eV	1.99 kΩ	-	-	-	Tridimensional Schottky barrier diodes using nanowires. Microstructure of the Pt/Si-NW affects the electrical characteristics. Pt NCs formed by an electroless plating method. Device parameters found by Cheung's functions. Series resistance decreases with increasing plating of Pt, leading to a continuous layer. Large ideality factor attributed to interfacial layer, barrier inhomogeneity or barrier height lowering due to image force lowering.	Zhu et al [86]
			-	11.58 eV	-	-		
Au/MoS_2/ITO	Mo layer was deposited on to Si/SiO_2 by electron beam evaporation. N-type doped molybdenum disulfide (MoS_2) nano-membranes were synthesized by chemical vapour deposition of sulphur and annealed at 1000°C for 1 hour. MoS_2 films were transferred to ITO via wet chemical etching in KOH. 50 nm of Au	1 eV	-	-	2.52 - 5.37 $mAcm^{-2}$	PCE = 0.7 - 1.8 % EQE = 41-52% at 600 nm	Layered MoS_2 semiconductor leads to fewer interfacial traps hence less recombination of majority carriers. The MoS_2 nano-membrane increases photonic absorption in the range 350 -950 nm. The thickness of the MoS_2 nano-membrane is determined by the thickness of Mo film. The defect density is insensitive to the nano-membrane thickness.	Shanmugam et al [74]
			-	-	590 -597 mV	0.48 - 0.55		

	was deposited by electron-beam evaporation.							
Al/NiPc/Ag	100 nm of Al and Ag were deposited on clean glass substrates by thermal vacuum evaporation. 170 nm of Nickel Phthalocyanine (NiPc) was then deposited thermally between the electrodes.	1.12 eV	24.6 MΩ	1.67 x 10^{-9} A	-	-	Organic semiconductor Schottky device. Device parameters calculated from I-V and C-V characteristics and verified with Cheung's function. Forward I-V characteristics suggest traps in the organic material bandgap. Barrier height calculated from C-V was highest.	Shah et al [87]
			310 MΩ	50	-	-		
Al/PEDT	1 µm of p-type Poly 3, 4-ethylenedioxythiophene (PEDT)/ polystyrenesulfonate (PSS) was spin coated on to a silicon substrate, followed by annealing at 120°C for 5 minutes. 150 nm Al film was deposited on the PEDT/PSS by thermal vacuum evaporation. Reactive ion etching formed the polymer Schottky diodes.	0.97 eV	7.34Ω	-	-	-	Polymer based Schottky diode. A modified Norde function was used to find parameters of the device. Excessive series resistance obtained due to the low conductivity of the polymer.	Liang and Varahramyan [88]
			-	1.42	-	-		
Al/PbS-NC/ITO	100 – 300 nm thick PbS NC films were spin coated onto ITO coated glass from a 150 mgmL^{-1} octane solution. A stack of 0.7 nm LiF/140 nm Al/190 nm Ag were deposited by thermal evaporation to form the Schottky barrier. A methanol treatment was used to remove long organic ligands from the PbS NCs.	-	-	-	12.3 mAcm^{-2}	PCE = 1.8% AM1.5 and 4.2% at IR IQE = 90% EQE = 13-37%	P-type Schottky barrier formed with solution processed nanocrystals. Architecture incorporated simple planar and stackable nanocrystal layers. Spin coating of nanocrystals gave smooth and densely packed arrays. Long oleate ligands removed as much as possible so to improve charge transport in nanocrystal films.	Johnston et al [89]
			-	-	0.17 – 0.31 V	42-49%		
Al/OG/n-Si/AuSb	An AuSb ohmic contact was evaporated onto the back of the substrate and annealed at 420°C for 3 minutes in	1.02 eV	154 kΩ	-	-	-	Organic Schottky barrier solar cell. Charge transport is mainly governed by space charge limited current mechanism. Compares the	Gullu et al [91]

	nitrogen. The native oxide on n-Si substrate was removed in aq HF. 4 µL of orange-G (1, 3-naphthalenedisulfonic acid, 7-hydroxy-8-(phenylazo)-, disodium salt) (OG) was deposited onto the n-Si wafer and then dried for 1 hour. Al was evaporated on the OG.		-	4.2	-	-	calculation of Schottky barrier device using thermionic emission theory, a method by Cheung and Cheung [90], the Nordes function and C-V. Good agreement between the Cheung and Norde methods. The Norde function provided the highest Schottky barrier.	
Au/TiO_2/Ti	250 nm Ti was deposited by electron beam evaporation onto a clean Ti foil. Annealing at 500ºC for 8 hours formed TiO_2 on the Ti. Au was deposited by galvanostatic electrodeposition for 2 minutes, using a solution of AuCn, KCN and aqueous KOH with a Pt counter electrode. Samples were rinsed with deionised water and dried.	1.1 eV	-	-	-	-	Large area, 10-30 nm thick and electrically continuous Au films were produced by electrodeposition. The Au films were interconnected Au islands. Conduction found deviated significantly from ideal thermionic emission theory. The barrier heights found were higher than equivalent Au films prepared by evaporation.	Tang et al [35]
			-	2.1	-	-		
Au/CdTe/SS	1 µm n-type CdTe films were electrodeposited on to a clean stainless steel substrate. 100 nm Au dots were evaporated through a mask onto the CdTe, forming a Schottky barrier.	0.7 eV	4.11 kΩ	2.39×10^{-8} A	-	-	I-V characteristics were measured as a function of temperature. Ideality factor found to be >1. Both ideality factor and series resistance increase with decreasing temperature. Thermionic emission diffusion main charge transport mechanism.	Pattabi et al [92]
			-	1.85	-	-		

__Abbreviations:__ SBH – Schottky barrier height, R_S – series resistance, R_L – leakage resistance, I_S – saturation current, n – ideality factor, J_{SC} – short circuit current, V_{OC} – open circuit voltage, PCE – power conversion efficiency, EQE – external quantum efficiency, IQE – internal quantum efficiency (all efficiencies were measured at AM1.5 unless otherwise stated).

2.2 Schottky solar cell physics

In Section 2.1 a selection of research solar cell architectures incorporating nanotechnology were discussed. For this study the Schottky barrier architecture was selected for further research due to the opportunity of incorporating visible active components to make this device comparable to other research nano-architectures. It was evident from the review in Table 2-1 that there is scope for further development of a Schottky barrier device in this way. With this enhancement a nanocrystal-activated Schottky barrier solar cell can provide a novel way to reduce the cost of fabrication as well as the quantity of materials needed. Past studies on dye and nanocrystal activated Schottky barrier solar cells and research opportunities will be discussed fully in Section 2.3. This section concentrates on the basic principles of metal-semiconductor junctions as background for the rest of this report.

2.2.1 Metal – semiconductor junctions

Metal semiconductor (M-S) junctions can behave as rectifying (Schottky barrier) or non-rectifying (Ohmic) contacts, which is dictated by the characteristics of the interface and the work function of the materials. A Schottky barrier, established by W. Schottky [93], is formed when the Fermi level (E_f) between an n-type semiconductor and a metal is equalised. Before contact the Fermi level in the semiconductor is above that in the metal, as shown in Figure 2-7. For the Fermi level to be constant throughout the interface, in thermal equilibrium, electrons from the conduction band (E_c) of the semiconductor (having higher energy than the electrons in the metal) flow into the lower energy states in the metal, until the Fermi level is balanced on both sides. As electrons move out of the semiconductor the concentration of free electrons reduces. With decreasing concentration of electrons the separation between the conduction band edge and Fermi level increases, leading to conduction band bending. This leaves positively charged ‘holes’ or donor atoms in the semiconductor, creating a space charge region, a high resistance region depleted of mobile carriers and an electric field from the semiconductor to the metal [38, 39, 94, 95].

Since the energy gap of the semiconductor does not change by contact with the metal the valence band (E_v) will also bend parallel to the conduction band. The electron affinity of the semiconductor is assumed to remain unchanged in an ideal Schottky barrier hence the vacuum level will remain parallel with the conduction band and also bend. The amount of band bending will be equivalent to the difference between the metal and semiconductor vacuum levels, since it must remain continuous across the interface. This is also equivalent to the difference between the work functions of the metal and semiconductor, given by $qV_i = (\phi_m - \phi_s)$ in Figure 2-7 where qV_i is the in-built junction potential.

The shape of the barrier is determined from the distribution of holes in the semiconductor. The Schottky theory assumes this is uniform throughout the semiconductor and up to the metal interface, which gives a constant charge density in the depletion region. The Schottky barrier (a parabolic barrier at the interface) is then a result of the electric field strength of the depletion region which rises with distance from the edge of the space charge region.

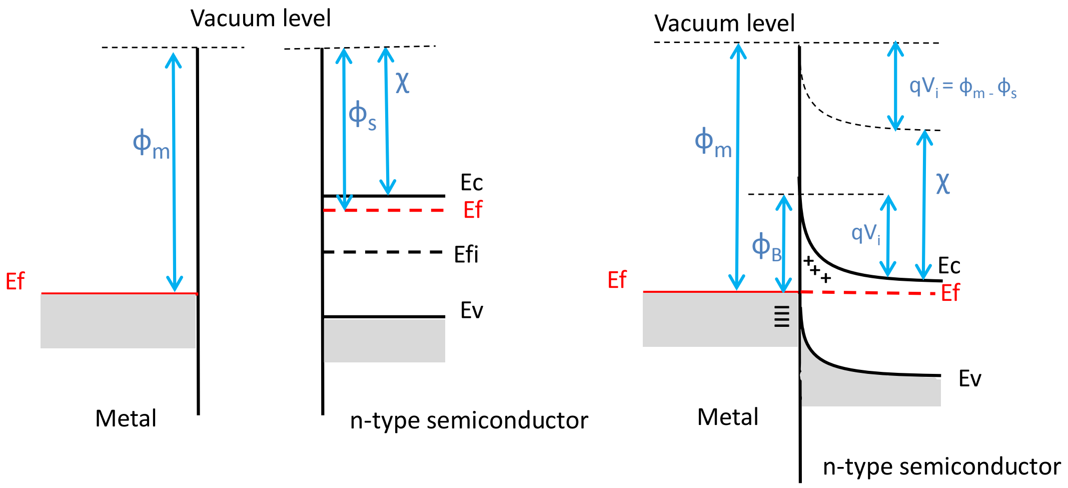

Figure 2-7: Energy bandgap diagram of an ideal metal-semiconductor contact, where the work function of the metal (ϕ_m) is higher than the work function of the semiconductor (ϕ_s), before contact [a] and after contact [b]. E_{fi} is the intrinsic Fermi level. Adapted from [39, 95, 96].

The Schottky - Mott theory [93, 97] states that the potential barrier is a result of the different work functions of the two materials. The work function is the minimum energy above the Fermi level needed for an electron to escape from the metal. The Schottky barrier height can therefore be described as the potential barrier which electrons in the semiconductor moving into the metal must overcome. The Schottky barrier height (ϕ_B) is ideally governed by Equation 2-1, where ϕ_m is the metal work function and χ is electron affinity.

$$\phi_B = (\phi_{m} - \chi)$$

Equation 2-1

It is clear from this relationship that the barrier height for an n-type semiconductor will increase for metals with a higher work function.

2.2.2 Rectifying contacts

When voltage is applied to the Schottky barrier, the barrier and energy levels will alter due to the changing potential across the depletion region. A rectifying contact, where current can flow in one direction only, generally exists If $\phi_m > \phi_s$ for an n-type semiconductor. The Shockley ideal diode equation, in Equation 2-2, gives the I-V characteristics of an ideal diode with applied forward bias, where I is the diode current, I_S is the saturation current, q is electron charge, V is applied voltage, k is the Boltzmann constant, T is temperature and n is the ideality factor. For ideal diodes, the ideality factor, n is equal to 1, for non-ideal diodes, n is larger than 1.

$$I = I_s \left[exp \left(\frac{qV}{nKT} \right) - 1 \right]$$

Equation 2-2

Figure 2-8 illustrates the energy band diagrams for a rectifying M-S contact. In thermal equilibrium, no current flows as there is a balance between the rate of electrons crossing over the barrier from the semiconductor into the metal and the rate of electrons crossing the barrier in the opposite direction, as discussed previously. Due to the depletion region, the resistance in the semiconductor is very high. Applying a voltage alters this equilibrium by changing the potential drop across the depletion region and therefore band bending occurs.

Applying a forward bias (making the semiconductor more negative than the metal) reduces the depletion region width (W) and the voltage across this region. This means that the electrons in the semiconductor now see a reduced barrier, therefore electron flow increases above its equilibrium value from the semiconductor to the metal. However in the metal the barrier remains unchanged since no voltage drop occurs, thus electron flow remains unchanged from the metal to the semiconductor with respect to the equilibrium level. This flow of electrons from a semiconductor to a metal causes a net current flow in the opposite direction. For a forward biased junction, current increases exponentially with voltage.

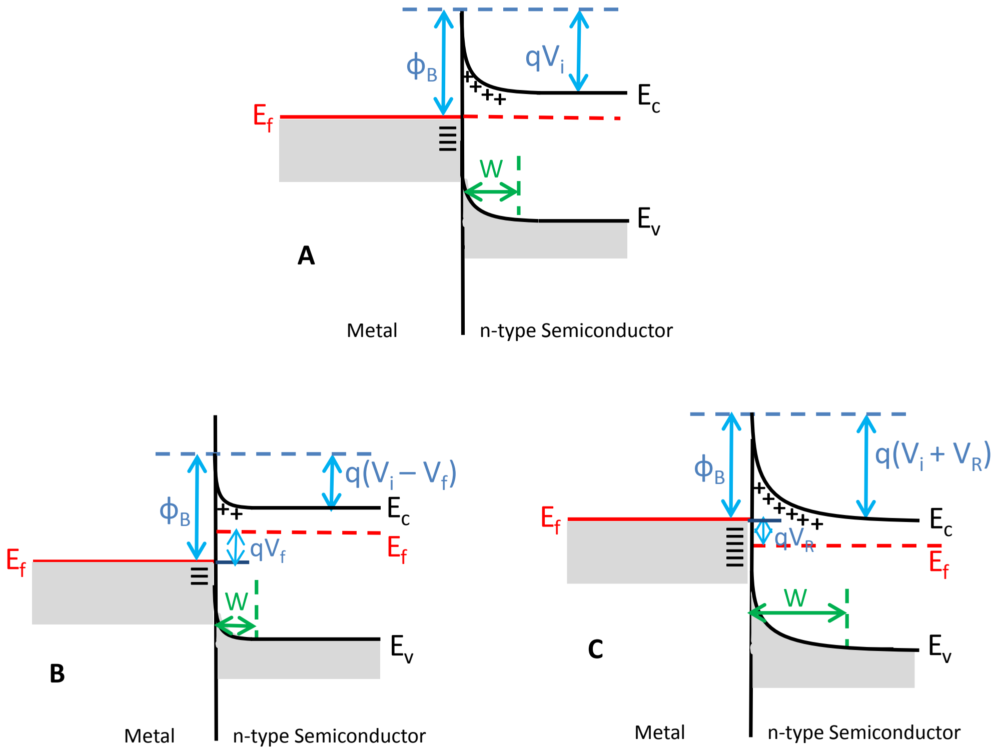

Figure 2-8: Energy band diagrams of a rectifying M-S contact in thermal equilibrium [A], forward bias [B] and reverse bias [C], adapted from [95].

For a reverse biased junction, the semiconductor is made positive compared to the metal. Here the voltage drop across the depletion region is increased and the electron flow from the semiconductor to the metal is reduced below its equilibrium level. The electron flow from the metal to the semiconductor remains unchanged, hence current flows from the semiconductor to the metal. This current flow is very small compared to the forward bias scenario, therefore creating a rectifying M-S contact [95].

2.2.3 Non-rectifying contacts

A non-rectifying, or Ohmic, contact is a low resistance junction where electrons can flow in both directions, depicted in Figure 2-9. Generally an Ohmic contact is created if $\phi_m < \phi_s$ for an n-type semiconductor. In this instance electrons will flow from the metal in to the conduction band of the semiconductor, leaving holes in the metal and an increased amount of electrons in the semiconductor, until the Fermi level in the semiconductor is raised to meet the Fermi level in the metal. This positive build-up of charge in the metal causes a surface charge due to the concentration of electrons in the metal being very large. The accumulation of electrons in the semiconductor is limited, hence, only a surface charge is produced. Therefore no depletion region exists and hence there is no potential barrier in either direction. Since the concentration of electrons is increased around the M-S interface, the region of highest resistivity is in the bulk semiconductor. When an external load is applied it will therefore affect the bulk semiconductor region rather than the interface. Thus it is evident that the current is independent of the bias direction, meaning that current can easily flow in two directions. The current is instead dependant on the resistance of the bulk semiconductor [39, 94, 95].

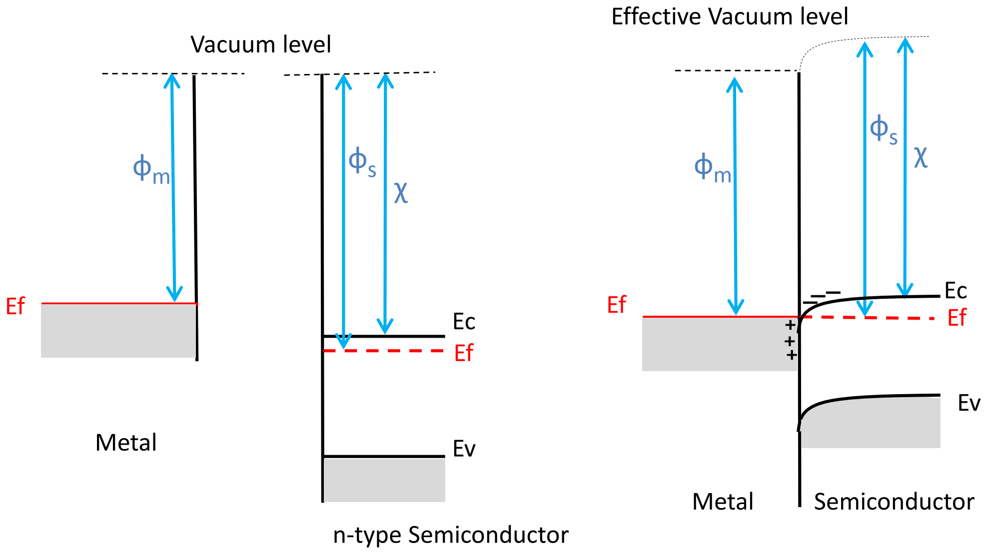

Figure 2-9: Electron energy band diagram of a metal with a lower work function than the semiconductor [left] and the formation of a non-rectifying, or Ohmic, junction formed under thermal equilibrium [right] adapted from [95].

Figure 2-10 illustrates graphically the different I-V characteristics expected from a rectifying and non-rectifying junction. Clearly the Ohmic junction obtains a linear I-V response where current can easily flow under forward and reverse bias. An ideal rectifying junction, or Schottky barrier, displays a forward bias current response which exponentially increases with voltage. A very small leakage current in reverse bias exists.

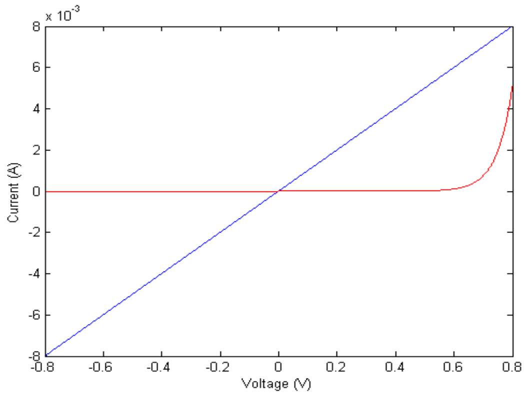

Figure 2-10: I-V Illustration to show the different electrical characteristics of a rectifying (red) and non-rectifying (blue) junction.

2.2.4 Transport mechanisms in a rectifying M-S junction

As discussed above, current flows due to charge transport at the M-S junction. Charge transport occurs through a number of mechanisms, including thermionic emission, quantum mechanical tunnelling, carrier generation and recombination, illustrated in Figure 2-11. Thermionic emission over the barrier is the main charge transport pathway in an ideal Schottky barrier, hence the other mechanisms are responsible for non-ideal characteristics [95]. Thermionic emission occurs via electrons moving through the depletion region from the semiconductor by drift and diffusion. Furthermore, the density of available states in the metal controls the emissions of electrons from the semiconductor into the metal.

Quantum mechanical tunnelling occurs in heavily doped semiconductors where the depletion region is very thin and the Fermi level lies above the conduction band. Due to this thin depletion region, electrons at low temperatures with energy close to the Fermi level can tunnel from the semiconductor to the metal. Tunnelling can also take place at higher temperatures (thermionic field emission), where a larger number of electrons are able to rise above the Fermi level where there is a lower, thinner barrier. These electrons can tunnel into the metal before getting to the top of the barrier.

In thermal equilibrium, the number of electron-hole pairs generated in the depletion region is equal to the amount of recombination. Depending on the applied voltage, there will be an increase in either carrier generation or recombination. For a reverse bias, electron-hole pairs above the thermal equilibrium will be generated in the depletion region and moved by the electric field causing a reverse current. For a forward bias the electrons and holes will be injected into the depletion region by the semiconductor and metal respectively. In the depletion region these excess carriers will recombine giving a net forward current. Recombination centres, or traps, are most effective when their energy levels are mid bandgap of a semiconductor.

An additional recombination mechanism is due to inherent defects in non-ideal semiconductors. These defects lead to the formation of additional electronic energy states in the bandgap, which act as recombination sites, as explained by the Shockley–Read-Hall theory. This theory also outlines four processes by which electrons and holes can recombine due to these defects;

1. An electron from the conduction band is captured by a neutral trap.
2. Emission of an electron to the conduction band that is initially trapped in the extra energy state.

3. A hole from the valence band is captured by a negatively charged trap.
4. Emission of a hole from a neutral trap into the valence band.

Compared to a p-n junction, recombination occurs faster in the metal of the Schottky barrier [94].

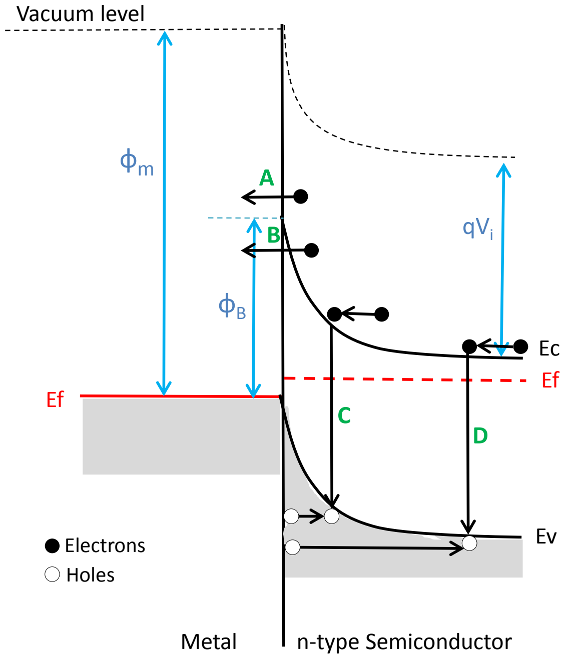

Figure 2-11: Transport mechanisms of a forward bias Schottky barrier, showing A) Thermionic emission, B) Tunnelling, C) Recombination in the depletion region, D) Hole injection from the metal, adapted from [95].

Similar to the recombination processes described above, hole injection from the metal to the semiconductor also causes recombination in the semiconductor. This generally occurs under forward bias where the barrier height is more than half the bandgap energy of the semiconductor. In this situation an n-type semiconductor at the interface has a large concentration of holes, making it p-type. With a forward bias applied, electrons flow from the semiconductor to the metal, allowing the holes to diffuse to the neutral region of the semiconductor, which causes injection of holes from the metal to the semiconductor. The injected holes recombine with electrons as they diffuse into the semiconductor.

2.2.5 Metal – Semiconductor junction interfaces

The interface between an M-S junction can vary depending on how the junction has been formed. Moreover, the properties of the resultant interface can vary the dependence of the barrier height on the work function of the metal. Generally the type of interface can be described by one of the following four categories [95];

1. Ideal Schottky barrier – the metal is physisorbed on to the semiconductor and the barrier height varies directly with work function.
2. Bardeen Barrier – the metal makes a weak chemical bond with a semiconductor but does not react with it to form a bulk material and the barrier height can become independent of the work function.
3. Opposite to 2 in that a strong chemical bonding exists between the metal and semiconductor interfaces with the barrier height being dependent on reactions at the interface.
4. An interfacial layer exists (commonly a thin native oxide film) between the interfaces due to surface preparation which prevents absolute contact between the M-S contacts – commonly witnessed in experimental barriers. The barrier height is unaffected as electrons can easily tunnel through a thin interfacial layer.

There are many parameters that can affect the M-S interface structure including surface roughness, grain size and defects [98]. Surface states exist in imperfect semiconductors since the crystal lattice ends abruptly at the surface which results in a distribution of allowed energy states in the bandgap, as well as the discrete energy states described above. These additional energy states in the bandgap have an effect on electron and hole behaviour by modifying the charge in the depletion region. For experimental M-S junctions the Schottky barrier can sometimes be dictated by the localised surface states and hence changing the linear relationship with ϕ_m [95].

When there is intrinsically a high density of surface states in the semiconductor a potential barrier can be formed in the absence of a metal contact. This means that when a metal is bought into contact the equalisation of charge occurs largely between the metal and the surface states of the semiconductor, leaving the depletion region unaffected. Intrinsic surface states can lead to Fermi level pinning at the surface above the valence band in the bandgap. Furthermore, the surface states can create a charge that is so large that the semiconductor becomes less affected by the metal work function. It is also known that oxides at the interface produce surface states, which are largely unaffected by the presence of the metal. Deep traps may also exist in imperfect semiconductors, which will also have an effect on the barrier properties. Deep traps refer to energy levels in the depletion region that exist due to intrinsic lattice defects or impurities [95].

2.3 Recent developments of Schottky solar cells

It is well known that a Schottky barrier solar cell is not as efficient as other alternative architectures and cannot currently compete with current silicon technology. However, enhancing a basic Schottky solar cell, as described in 2.1.5 and 2.2, can provide a pathway to increasing device performance, whilst using a low cost solar cell architecture. This section describes previous work by McFarland and Tang [34] on the introduction of a dye-activated Schottky barrier solar cell as a way to improve the Schottky barrier solar cell. The origins of this research on a nanocrystal–activated Schottky barrier solar cell, initiated by Tang et al [35] are then outlined, leading onto a discussion of device mechanisms. As well as taking advantage of a low cost design, these enhancements are very flexible, since a variety of materials are suitable for use. In addition to this the nanocrystals used for activating the cell can provide many advantages relating to device performance as described in 2.1.

2.3.1 Dye - activated Schottky barrier solar cell

The conventional solid state p-n junction solar cell described in 2.1.1 involves the creation of electron-hole pairs in the semiconductor by light absorption and then separation and collection of the pairs via the semiconductor's electric fields. McFarland and Tang [34] outlined an alternative design in which photon absorption occurs in photoreceptors deposited on an ultra-thin metal-semiconductor Schottky barrier. The use of the semiconductor in the hot electron device serves for charge transport and separation, which is different to conventional solar cells.

McFarland and Tang [34] fabricate their solar cell using an Au/TiO_2 Schottky barrier on a Ti substrate with an organic dye photoreceptor. The Schottky barrier at the Au/TiO_2 interface is essential for irreversible electron injection into the TiO_2 layer. Figure 2-12 presents a process schematic for their dye-activated Schottky barrier solar cell. The photon-to-electron conversion takes place in 4 steps;

1. Light is absorbed in the photoreceptors (dye), producing energetic electrons. A merbromin dye is used as a photoreceptor to ensure that the photoexcited donor level is sufficiently above the bandgap.
2. These 'hot' electrons are injected into the conduction band of the adjacent metal and travel ballistically through a 10-50 nm thick Au film above the Fermi energy. Ballistic travel occurs because at energies of ~1eV above the Fermi level, electrons in noble metals have very long mean free path lengths, allowing a large fraction of the electrons to be collected.

3. Internal electron emission will occur in the semiconductor if the energy of the electron in the metal is higher than the Schottky barrier height, with a sufficiently long mean free path length compared to metal thickness, allowing the electrons to enter the conduction levels of the semiconductor (200 nm thick TiO_2). Steps 2 and 3 give rise to the photocurrent in the device.
4. The electron conducts through the semiconductor to the Ti at the back of the cell where a photovoltage is produced from the remaining excess electron energy. The Schottky barrier is estimated to be approximately 0.9V at the metal-semiconductor interface, due to material choice.

The device shown in Figure 2-12 obtains a 10% internal quantum efficiency (electrons measured per photon absorbed), open circuit photovoltage of 685 mV, short circuit photocurrent of 18 μAcm^{-2} and 0.63 FF. The small photocurrent is due to only a monolayer of dye harvesting light. Before the dye deposition the Schottky barrier gave a weak visible photoresponse of 325 mV and 0.9 mAcm^{-2}. It was suggested that this is caused by excitation of defect levels in the thermally oxidised TiO_2.

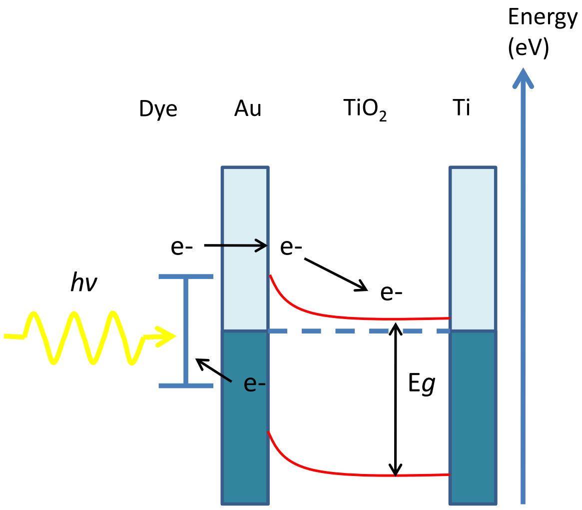

Figure 2-12: Principles of the dye-activated Schottky barrier solar cell, adapted from [34].

The efficiency of this solar cell assembly depends on the favourable dissipation process. The main and desired process is the production of ballistic electrons in the metal. Other dissipation pathways that could occur include dissipation by heat and scattering. McFarland and Tang [34] found that electron transfer of energetic electrons from the photoexcited state into the unoccupied conduction states of the metal was the main dissipation pathway, followed by intermolecular de-excitation with coupling to the conduction electrons. Both dissipation pathways produce hot electrons that have sufficient energy and momentum to traverse the Schottky barrier, giving photocurrent in this particular device. Dissipation of electronic excitation energy as heat is the main competing process to this. However the device can overcome this competing process as long as the conducting metal is thin enough so that the majority of the injected electrons will reach the Schottky barrier. The ballistic mean free path of Au and other noble metals is very long (between approximately 20-150 nm) so this is very possible when using noble metal layers under 50 nm [99].

The disadvantage with this device is that the Schottky barrier height significance is increased. However, the device takes advantage of ballistic electron transport and internal electron emission, therefore making the bandgap and semiconductor thickness less important, since the semiconductor is not used for photon absorption. Similar to dye sensitised solar cells, the dye-activated Schottky cell separates the photon absorption process from charge separation and transport, however it has the added advantage of not requiring a reducing agent in an electrolyte for intermolecular charge transport [34]. In addition, this structure can provide a durable and low cost solar cell that may use a variety of materials. Maximum photovoltage and photocurrent can be achieved by choice and preparation of the device materials to control and match the Schottky barrier height, semiconductor conduction band positions, and the nanocrystal donor/acceptor levels.

Further work by Koole et al [100] and Taylor et al [101] have contributed to the dye-activated Schottky barrier solar cell architecture. Koole et al [100] have replicated McFarland and Tangs [34] work, confirming the findings of a visible photoresponse for the merbromin dye-activated Schottky barrier cell which confirms electron injection into the TiO_2 conduction band. However, they indicated that the deposition of a dye decreased the Schottky barrier and had a negative effect on the photovoltage of a device, indicating that the electrical characteristics of the merbromin/Au/TiO_2/Ti device is very sensitive to the chemistry at the Au/TiO_2 interface. Hence higher cell efficiencies can be obtained if the photoreceptors do not disturb the TiO_2 surface chemistry. Under ambient conditions a stable photovoltage of 600 – 700 mV was obtained for the dye-activated device. In addition to the TiO_2 surface chemistry determining the electrical characteristics of the Schottky barrier, the testing atmosphere was also found to have an effect on electrical characteristics; non-rectifying I-V characteristics were obtained for the device in a closed cell filled with oxygen, air or argon, however rectifying features were recovered after exposure to ambient conditions.

Taylor et al [101] contributed towards the dye activated Schottky barrier cell by fabricating a bi-isonicotinic acid/Au/TiO_2/Ti cell. An organic ligand was used instead of a dye because the ligand is important for anchoring a variety of dye molecules to the TiO_2. Taylor et al [101] agree with main transport mechanisms of the cell outlined by McFarland and Tang [34], but proposed two additional transport mechanisms. Firstly, there is the possibility of energy transferring from the dye to excite Au electrons, which are then subsequently injected into the semiconductor conduction band. Secondly the dye or organic molecules may interact directly with the TiO_2, since the gold sputtered layer forms islands on the TiO_2 rather than a continuous layer, also suggested by Koole et al [100]. Hence in addition to the ballistic travel indicated previously, dye molecules may also interact with the Au islands and the TiO_2 substrate.

2.3.2 Nanocrystal - activated Schottky barrier solar cell

Many studies have displayed successful creation of a Schottky barrier with a variety of materials; see Table 2-1, including using bulk and nanocrystal semiconductors and metal contacts. The idea of using a photoreceptor to activate a Schottky barrier has been trialled in very few studies. As discussed above, McFarland and Tang [34] used a dye to activate a Schottky barrier, however this dye can be replaced with nanocrystals. Nanocrystals offer many advantages over dyes for use as photoreceptors, since they have tuneable optical properties and bandgaps, due to quantum confinement, and are resistant to photo-bleaching, unlike dyes [35, 102]. Moreover, dyes on top of a Schottky barrier have been shown to decrease the height of the Schottky barrier [100]. Another advantage of using nanocrystals over dyes is that they can potentially take advantage of nano associated phenomena, such as multiple exciton generation (MEG). MEG is a mechanism for using excess photon energy, by creating multiple electron-hole pairs, or excitons, for each incident high energy photon. It is based on the Coulomb-interaction theory, which states that the greater the proximity of an electron-hole pair the more likely it is that a photon with twice the bandgap energy will create two electron-hole pairs with the same energy as the bandgap**.** This decreases energy losses, since without Coulomb-interaction an electron-hole pair would otherwise have excess energy above the bandgap [22]. MEG works best in nanocrystals and can reach efficiencies of 44%, meaning that nanocrystals can theoretically exceed the Shockley–Queisser limit [19, 21, 50, 103].

Extracting the extra excitons to produce electricity is a major hurdle for MEG in nanocrystals because of Auger recombination, a competing process that leads to a fast decay of multiple excitons. Therefore harnessing this extra exciton energy from MEG before decay is experimentally difficult, due to the time resolution of hundreds of picoseconds [104]. Moreover, certain chemical coatings hinder the movement of nanocrystals. However close and regularly packed nanocrystals could make it easier for the movement of electronic charges [22]. Evidence of MEG has been reported in PbS, PbTe, PbSe, CdSe, and Si nanocrystals [10]. Furthermore, Pijpers et al [104] demonstrate that MEG can achieve up to seven carriers per photon in nanocrystals.

Tang et al [35] is one of the few studies that demonstrate using semiconductor nanocrystals as a photoreceptor to activate a Schottky barrier cell. In their study CdSe/CdS nanocrystals were deposited on to Au/TiO_2/Ti Schottky barrier. The method for the Schottky barrier involved depositing Ti onto a clean and polished Ti foil by electron beam evaporation. TiO_2 was formed by anodisation at 70 V for 5 seconds with a 0.5 M H_2SO_4 aqueous electrolyte followed by annealing in air at 550 ^oC for 8 hours and 12 nm of Au was evaporated on top. 4 - 10 nm diameter CdSe/CdS NCs were synthesised following the method outlined in [105]. The Au layer was modified with SAM molecular linkers by 2 mM ethanol solution of MPA under argon, followed by rinsing and drying. The NCs were then assembled on the modified device by using an aqueous solution of CdSe/CdS NCs for 4 hours under argon. The best device obtained a photoresponse under AM 1.5 with an open circuit voltage of 140 mV, short circuit current density of 55 μAcm^{-2} and a 0.5 FF. They found an absorption peak at 545 nm, which was consistent with the NC absorption peak. Comparing this device with the dye activated Schottky barrier above, it is evident that the dye activated Schottky barrier gains a higher open circuit voltage of 685 mV and fill factor of 0.63, but a lower short circuit current density of 18 μAcm^{-2}.

In their study on a dye-activated Schottky barrier, Koole et al [100], also referred to a CdSe/Au/TiO_2 Schottky barrier cell they had fabricated. They found that the rectifying current−voltage characteristics of the Schottky barrier became Ohmic after nanocrystal deposition, indicating deteriorating of the Schottky barrier due to the nanocrystals. Furthermore, Koole et al [100] indicated that the deposition of a dye or nanocrystals had a negative effect on the photovoltage of a device and recommend that higher cell efficiencies can be obtained if the photoreceptors do not disturb the TiO_2 surface chemistry.

It is important to understand the transport mechanisms in the device, since they will dictate the I-V and photoresponse gained from the solar cells. The possible transport mechanisms in the NC activated Schottky barrier cell are illustrated in Figure 2-13.

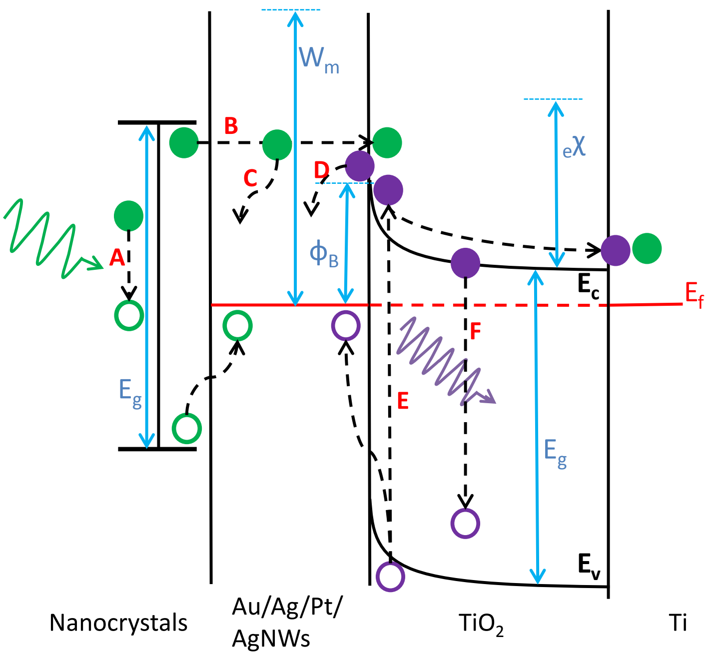

Figure 2-13: Transport and energy loss mechanisms in the nanocrystal - activated Schottky barrier solar cell. Electrons are presented as solid circles and holes are white circles. The green arrow represents visible light absorption in the nanocrystals and the green electrons and holes demonstrate the subsequent kinetics. Likewise the purple symbols represent UV absorption in the TiO_2. Dashed lines represent electron and hole kinetics.

The main mechanisms depicted in Figure 2-13 are;

A. **Recombination in the nanocrystal layer**. Photons are absorbed by the nanocrystals but electrons quickly lose this energy and recombine in the nanocrystal layer before escaping to the metal layer. This could be due to insulating features of the nanocrystals which make electron travel more difficult. Recombination in the NCs and through surface states is likely to be a major loss mechanism.

B. **Ballistic travel** of electrons from the NC through the metal to the semiconductor.

C. **Electron relaxation**. Electrons excited in the NC layer may not have enough energy to ballistically travel through the metal and instead scatter inside the metal and lose energy.

D. **Reverse or back recombination**. The barrier is not high enough and recombination occurs from the semiconductor to the metal. When the device is illuminated and develops a forward bias this mechanism will become more likely.

E. **UV absorption**. An electron is excited across the bandgap in the semiconductor and is collected at the back contact whilst the hole is collected in the metal contact.

F. **Recombination in the semiconductor**. After being excited over the Schottky barrier electrons, the majority carriers, may lose energy and recombine in the semiconductor before reaching the conductive back contact. Recombination of majority carriers in this device should be negligible.

G. **Recombination due to surface states**. Likely to be a major loss mechanism.

A more in-depth discussion of transport mechanisms and more non-ideal transport mechanisms are discussed later in 4.3.

Very limited work has been carried out on the nanocrystal activated Schottky barrier cell. McFarland and Tang [34] discovered the dye activated Schottky barrier cell and Tang [35] went on to replace the dye with nanocrystals, initiating the nanocrystal activated Schottky barrier cell. Aside from these introductory studies, very few studies have built on this work, hence there is scope to confirm previous findings. The aim of this work is therefore to contribute to this field by fabricating and characterising the architecture shown in Figure 2-12, using a nanocrystal activating layer, keeping in mind the need to use low cost materials and techniques. As well as limited work in this area, the studies discussed above are brief and all use similar materials and techniques. All of the studies outlined are based on an Au Schottky barrier cell and use CdSe/CdS nanocrystals. Hence, there is an opportunity to test different noble metals in the Schottky barrier, with higher conductivity and work functions, such as silver and platinum, which may improve the device. Furthermore, there are a whole host of alternative semiconducting nanocrystals that could be tested including CdTe, CuO and $CuInS_2$. In addition to varying materials and techniques, there is a need to analyse and confirm the physical mechanisms in the cell since Koole et al [100] and Taylor et al [101] indicated mechanisms not previously outlined by McFarland and Tang [34], such as the electrons (from the photoreceptors) interaction with TiO_2 and Au and the degradation of the device due to deposition of photoreceptors. It is clear that there is much potential to contribute to the field of nanocrystal activated Schottky barrier solar cells.

2.4 Aim and objectives

Schottky barrier solar cells provide a low cost fabrication route to reduce production costs of solar cells in the future. Furthermore, incorporating nanotechnology plays a crucial role in potential efficiency enhancement, due to nano-related phenomena, and can also further reduce costs due to solution processing and the use of fewer materials. McFarland and Tang [34] and Tang [35] have previously reported a photo-active Schottky solar cell, using a merbromin dye and CdS/CdSe nanocrystals respectively, with promising results. Subsequent work by Koole et al [100] has replicated both the dye and nanocrystal activated Schottky barrier cells and Taylor et al [101] analysed the dye activated Schottky barrier mechanisms through the use of an organic ligand. Both studies confirmed that the architecture is functional. However, Koole et al [100] outlined that the photoreceptors decrease the Schottky barrier height and photovoltage, and the TiO_2 surface chemistry had an important role in determining the electrical characteristics. Whereas Taylor et al [101] proposed other transport mechanisms in the cell. No other studies to date have built on this work. This indicates the large potential to enhance progress in this field.

Aim: Proof of concept and underlying physics of a nanocrystal activated Schottky barrier solar cell.

The aim of the thesis will be met by the following objectives:

- Fabricate and characterise a Schottky barrier solar cell using low cost processing techniques, compared to the literature, to provide a device for comparison.
- Analyse each fabrication stage of a Schottky barrier solar cell to understand the effects of surface preparation techniques on the subsequent cell.
- Show that a range of noble metals and deposition techniques are suitable for use in Schottky barrier solar cells.
- Explore novel transparent conductive electrodes (TCE) - silver nanowires and electrodeposited silver - for use in the Schottky solar cell to provide potential pathways for lowering cost and enhancing performance. Compare results with the more traditional approaches.
- Provide an optimised Schottky solar cell based on a comparison of numerous different approaches, techniques and materials.
- Show how the physical background of Schottky barrier solar cells links to the results found in the experimental work.
- Activate the characterised Schottky barrier with a range of suitable semiconductor nanocrystals to allow the solar cell to absorb in the visible range.
- Characterise the nanocrystal activated cell and compare to the Schottky barrier to prove the concept.
- Analyse the physics of how the nano-activated Schottky barrier solar cell works on a practical level and explain in terms of the results obtained from the devices.
- Make further recommendations based on experience.

Chapter 3

Device Fabrication and Characterisation

This chapter details the methods used to fabricate a nanocrystal-activated Schottky barrier solar cell, depicted in Figure 3-1, along with the motivation for each method selected. The method is sequential from the Ti substrate to the top photo-active nanocrystal (NC) layer. To create a reproducible and controlled substrate the Ti was prepared by manual polishing then electropolishing, which gave a uniform finish with a surface roughness of less than 10 nm. The TiO_2 layer was created by chemically anodising or thermally oxidising the Ti substrate. A variety of metals were trialled as conductive layers, including gold, platinum, silver films and silver nanowires, deposited by sputtering, evaporation, electrodeposition and drop casting. After electrical characterisation of the Schottky barrier created between the metal/TiO_2 interfaces, the NCs were drop cast and annealed onto the device. Current–voltage (I-V) and photoresponse characterisation were carried out at all stages to infer information about the Schottky barrier formed and the cells response to light. Other additional characterisation for some parts of the work involved sheet resistance, SEM analysis and UV visible spectroscopy.

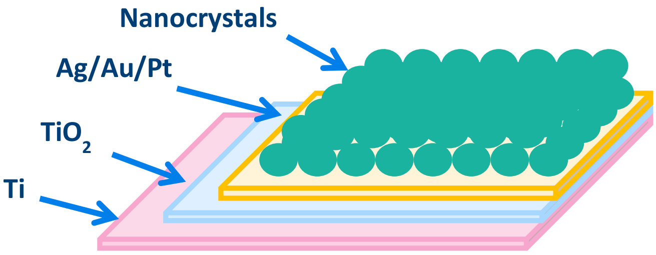

Figure 3-1: Schematic of the nanocrystal activated Schottky barrier solar cell

3.1 Device structure and materials choices

The main selection criteria for materials to fabricate the nanocrystal-activated Schottky barrier solar cell encompassed requirements for the finished device to be low cost in terms of fabrication and materials, to be scalable for future development, as well as meet the required properties for the specific layer of the device as described in 2.3.2. The device is based on previous work by McFarland and Tang [34] and Tang [35], as discussed previously in 2.3.1, hence material selection required to expand this work takes their material choices into account as well. The materials selected along with a summary of required properties for each layer is presented in Table 3-1.

Table 3-1: Summary of the purpose and properties of each layer with subsequent material selection and criteria for the nanocrystal-activated Schottky barrier solar cell.

Device layer	Purpose of the layer	Required properties	Material selected	Layer thickness
Substrate	Base for the cell.	Rigid base, provide electrical contact, good adhesion to the semiconductor and an Ohmic contact to the semiconductor.	Titanium	0.25 – 1.5mm
Semiconductor	Formation of a Schottky barrier with the noble metal and efficient electron transporter.	Wide bandgap n-type semiconductor required to form a Schottky barrier.	TiO_2	<100 µm
Noble metal	Schottky barrier formation, allow ballistic travel and provide an electronic contact.	High conductivity and thin for ballistic electrons, transparent to UV light, high work function to form a large Schottky barrier. Does not readily form an oxide. Adheres well with the semiconductor.	Gold, Platinum, silver and silver nanowires	10-100 nm
Nanocrystals	Absorb visible light.	Semiconducting with a ~1eV bandgap to absorb in the visible range. Dispersed in solution for easy deposition and storage. Uniform size distribution. Conduction band higher than the Schottky barrier for band alignment.	CdS, CdSe, CdTe, CuO, and $CuInS_2$	5-10 monolayers or ~100 nm

Many materials were considered for selection for each layer, including ITO, steel and other metal substrates for the rigid base; zinc oxide, silicon and nanocrystalline semiconductors; copper, palladium or aluminium for metal contacts; PbS, PbSe and other semiconducting NCs. The Ti/TiO_2 substrate/semiconductor combination was selected as it provides a rigid base, a well adhered semiconductor, and a route to easily fabricating and controlling the oxide. Platinum, gold and silver were selected as they have the highest work functions and conductivity. These materials are expensive however only a minimum of 10 nm is required, which greatly reduces this cost. The techniques used to deposit noble metals can be costly and require special environments, so alternative techniques were trialled to further reduce the fabrication cost. Alternative techniques included depositing colloidal nanowires and electrodeposition using silver only as it has the highest conductivity. Many nanocrystals are suitable for use in this device, however only cadmium sulphide (CdS), cadmium selenide (CdSe), cadmium telluride (CdTe), copper indium sulphide ($CuInS_2$) and copper oxide (CuO) were selected. These nanocrystals were chosen as they all absorb in the visible range 400 – 700 nm, can be produced with uniform size distribution and have conduction band edges above the Schottky barrier. Moreover, CdS/CdSe NCs were used previously by Tang [35], hence the findings in this work could be compared. All nanocrystals were produced by colloidal synthesis and drop-casted, both of which are low cost techniques which can be scaled up in the future. The thickness of the layers were estimated from the previous work specifically on this device, see 2.3, as well as other literature which will be discussed further in the subsequent sections.

The rest of this chapter describes in detail the methods used for substrate processing, semiconductor formation, metal and nanocrystal deposition, as well as further justification and comparisons with literature for each technique used.

3.2 Substrate processing

Commercially pure titanium (CpTi) foil with 99.99% purity and a thickness of 0.5 mm and 0.25 mm were sourced from Sigma Aldrich. Initial studies used titanium recycled samples that were approximately 1 mm thick. The purity of these recycled Ti samples was unknown but assumed to be lower than the CpTi. Prior to creating a TiO_2 layer, the substrate is mechanically then electrochemically polished to provide a control surface with a surface roughness of approximately 10 nm. The surface roughness was confirmed by Atomic force microscopy (AFM), presented later in Figure 3-3.

The purpose of polishing the substrate is three fold:-

1. To produce a uniformly flat control surface that is reproducible across devices.
2. To enable ease of electrical characterisation with a probe system, since a textured substrate is more likely to be damaged or changed.
3. To enable comparison between different devices with more confidence and accuracy.

3.2.1 Mechanical polishing

Mechanical polishing was carried out by hand using micro-grit wet/dry silicon carbide paper starting with a p240 grit size and using 3 finer grit sizes to an ultra-fine grade of p2500. The p- numbers are related to the size of the particles in the silicon carbide paper and hence indicate the level of surface roughness attained by the different papers, displayed in Table 3-2. The substrates were manually polished for 2-3 minutes per grade. However, some substrates were recycled and these required more manual polishing than the unused titanium substrates.

Table 3-2: Polishing grades of mechanical polishing, taken from [106].

Grade of sand paper used	Average grain size (µm)
p240	58.5 ± 2
p400	35 ± 1.5
p1200	15.3 ± 1
p2500	8.4 ± 0.5

Mechanical polishing alone has been shown to lead to uneven growth of a subsequent oxide film, whereas electropolishing ensures reproducibility of subsequent further processing, such as the formation of well-structured oxide crystalline lattices [107]. However, mechanical polishing prior to electropolishing can lead to a lower surface roughness after electropolishing [108]. A comparison of substrates that were manually polished against those that were manually and electrochemically polished was undertaken and it was found that the substrates that had undergone both types of polishing reproducibly gave better results in terms of I-V and UV response after semiconductor formation. Therefore both mechanical polishing and electropolishing were required.

3.2.2 Electrochemical polishing

Electrochemical polishing (EP) is a process whereby a metal surface is smoothed by anodic polarization in an appropriate electrolyte. The metal to be polished, titanium here, is the anode and when a current is applied the electrolyte surrounding the substrate becomes polarized and allows diffusion of metal ions from the substrate to the cathode. There are two distinct parts of the electropolishing process, anodic levelling and anodic brightening or macro- and micro- smoothing. Macro-smoothing results from high current density areas at the peaks of a surface profile leading to locally higher dissolution rates. The rate of anodic levelling is equal to the difference in the dissolution rate between peaks and troughs. Micro-smoothing occurs after macro-smoothing once the influence of the surface profile on the dissolution process is suppressed. Anodic dissolution is limited by the mass transport of Ti^{4+} ions diffusing from the anode to the electrolyte [109, 110]. Figure 3-2 demonstrates this anodic levelling.

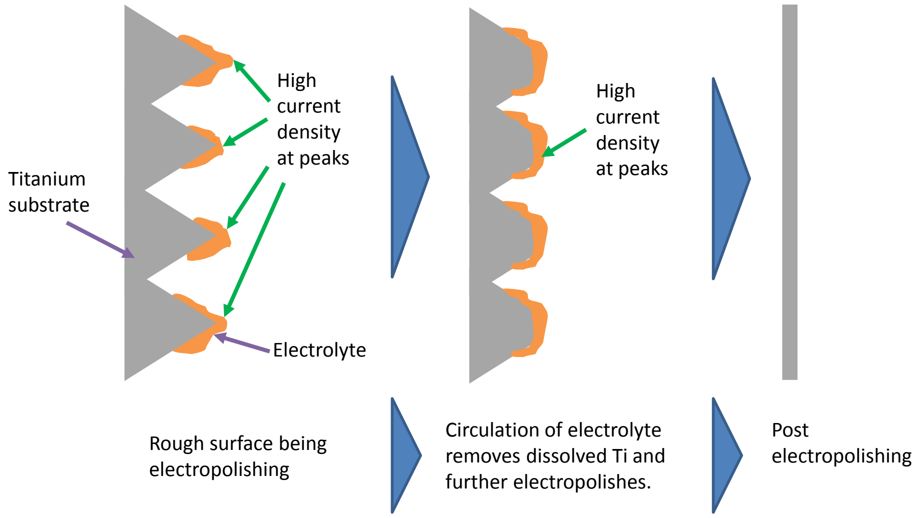

Figure 3-2: Electropolishing Schematic. Microscopic peaks and troughs exist on an unpolished surface. These peaks are removed at a greater rate than the troughs since they have higher current densities.

The electrolyte forms a viscous film around the metal which limits diffusion, due to the transport–limited mechanism. Constant agitation exposes peaks and replenishes the electrolyte at the metal surface. Increased electrolyte flow due to agitation by an electronic mixer was found to create smoother surfaces, further indicating that the mechanism of electropolishing was mass transport limited. Problems with EP include inconsistent polishing over surfaces and oxide or other unwanted compound formation on the surface that can suppress the mechanisms of EP. Moreover the surface finish depends on a number of factors including the extent of mechanical polishing, time, temperature and current density. Increasing these variables tends to lead to a more polished finish [108].

3.2.2.1 Electrochemical polishing electrolytes

Electrolytes for electropolishing titanium typically involve acids, as they can achieve uniformly polished substrates with low surface roughness. Many studies have demonstrated EP of Ti using acid electrolytes, for example Mahe and Devillers [107] used a methanol/butanol/perchloric acid electrolyte to get reproducible low surface mean roughness of 0.089 nm. Kuhn [111] provides a review of acid based electrolytes, including sulphuric and perchloric acid, that achieve a low average surface roughness between 0.057 and 0.008 µm. Piotrowski et al [112] have demonstrated the use of a methanol and sulphuric acid electrolyte to reduce the hazards associated with perchloric acid.

Alternative electrolytes for EP have been studied to avoid using hazardous and toxic acids. Fushimi and Habazaki [113] demonstrated electropolishing of titanium with ethylene glycol (EG) achieving an average surface roughness range of 0.2 – 0.4 µm. EG is atoxic and therefore reduces the hazards associated with acid electrolytes. However, EG electrolytes cause pitting and generally result in a higher surface roughness than the acid electrolytes. Through trial experiments using EG by colleagues, this method was found to result in high surface roughness and pitting, hence would require much more further development before use, which was outside the scope of this research.

Another alternative to both acid and EG electrolytes are chloride/alcohol based electrolytes. Chloride electrolytes can pose hazards but these are significantly reduced compared to acid electrolytes [114]. Furthermore, the surface roughness obtained from chloride electrolytes is generally comparable to acid electrolytes and better than EG. This is due to the fluoride or chloride ions, since they can facilitate attack on the passive oxide layer [115]. Tajima et al [114] used an ethanol, isopropanol, zinc chloride and aluminium chloride electrolyte, and obtained a 0.03 - 0.67 µm surface roughness. The main disadvantage with chloride/alcohol based electrolytes is that they generally have a low water content, so water ingress or content leads to increasing stability of the passive oxide layer, whereby anodic dissolution in this case would lead to pitting rather than polishing [109, 115].

For electropolishing Ti a chloride/alcohol based electrolyte was selected since a low surface roughness, equivalent to that obtained by an acid electrolyte can be achieved with less toxic and hazardous chemicals.

3.2.2.2 Electrochemical polishing method

Electropolishing to achieve a mirror finish and surface roughness of less than 10 nm was carried out following the method in Tajima et al [114]. The alcohol electrolyte used, with a transport rate limiting step, consisted of 42ml ethanol, 18ml isopropanol, 3.6g aluminium chloride and 15g zinc chloride. Mixing the chemicals in the solvents to form the electrolyte caused an exothermic reaction. The temperature of the solvent when dissolving the chloride powders was limited by slow addition of the chloride powders into the solvents and allowing the electrolyte time to cool. This was an important step to prevent degradation of the electrolyte performance. It was found that adding the zinc chloride to the alcohol and allowing it to dissolve before adding the aluminium chloride improved the dissolution rate and hence performance of the electrolyte. Dissolving the aluminium chloride powder into the solvent first increased the temperature of the electrolyte more and reduced the dissolution rate of the zinc chloride. The temperature of the electrolyte increased most when the aluminium chloride was added to the electrolyte. Zinc chloride is highly hygroscopic and was stored in a desiccator to prevent it deteriorating. To aid dissolving the chloride powders the electrolyte was placed in an ultrasonic bath at ambient temperature.

Before electropolishing the mechanically polished substrates were washed in acetone rather than deionised water as suggested in [114], since anhydrous solvents were used to provide a higher quality electrolyte for better surface finishing. As discussed previously an electrolyte with a higher water content leads to oxidation and pitting. This was demonstrated through a comparison between electrolytes produced with anhydrous versus hydrous ethanol. The cathode and anode were both 0.8 mm diameter titanium wires, with the anode attached to the titanium sample. It was found that using a cathode with a larger surface area (a coiled Ti wire rather than a straight wire) improved the substrate finish. The electrode separation was maintained at approximately 35 mm and a magnetic stirrer was used at 5 revolutions per second to refresh the electrolyte around the sample. Agitation was essential as it removes viscous layers from the surface of the titanium substrate, hence refreshing the electrolyte around the substrate and providing a better surface finish, as indicated by Tajima et al [114].

A power supply was used in constant current mode at 1A, this typically related to a voltage ranging between 30 – 60V. All of the samples were electropolished for a maximum of 5 minutes. Some samples were stopped before reaching 5 minutes due to attaining high temperatures (65°C), since it was considered unsafe operating at higher temperatures given the boiling point of ethanol at 78°C. A water bath surrounding the electrolyte was used to prevent it from overheating, which was changed between each sample. During electropolishing the electrolyte temperature ranged between 25-65°C. It was found that smoother surfaces were obtained on substrates when the electrolyte had warmed up a little and maintained mid-range temperatures around 45-60^{0}C. At consistently high temperatures signs of pitting and black films, probably titanium chloride, on the substrate surface became apparent. To avoid this, the electrolyte was allowed to cool between electropolishing each sample. This cooling period was particularly important when higher temperatures were obtained as without cooling, the temperature increased more rapidly for subsequent substrates. In some instances black films were produced without reaching a high temperature. This was generally found after the electrolyte had been used to EP many substrates, and was due to water ingress through condensation or exhaustion of the chloride ions. In these instances the substrate was recycled and a new electrolyte was used for further processing. All substrates were cleaned in acetone and propanol afterwards using an ultrasonic bath.

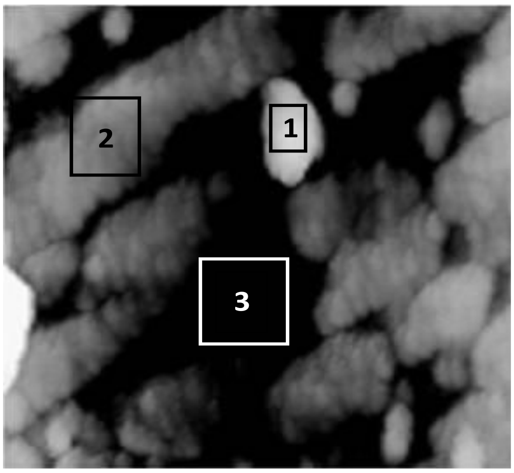

Position	Surface roughness R_a (nm)
Whole image	9.29
1. High	4.36
1. Middle	1.07
1. Low	3.10

Figure 3-3: AFM image of electropolished Ti. The numbered boxes relate to surface roughness measurements, shown in the table. Image and measurements courtesy of Mr Graham Smith, University of Leeds [116].

The surface finish of the titanium varied depending on the type of substrate. As mentioned previously in 3.2 the substrates varied between 1 mm thick recycled titanium, and 0.25/0.5mm CpTi. Furthermore, all samples were recycled to produce subsequent devices. The difference between the finish of the old and the new titanium substrates can be explained by making assumptions about the microstructure of the substrates. The new CpTi substrates were assumed to be less rough than the recycled substrates, meaning that the new samples had a more uniform surface area, with less peaks and troughs and therefore obtained a lower surface roughness when electropolished. The recycled Ti was assumed to have a rougher surface initially, hence having more peaks across the surface, which provides a much smaller surface area for electropolishing. Despite these differences a typical surface roughness of less than 10 nm was achieved, as illustrated in Figure 3-3. This was obtained by measuring the average roughness profile across a typical electropolished Ti using atomic force microscopy (AFM).

3.3 Semiconductor formation

The Ti/TiO_2 substrate was chosen as it presents a low cost, wide bandgap, rigid base that can form a strongly adhered semiconductor, which can be manipulated to control the thickness. Furthermore, this combination can easily be scaled up to industrial applications, for example solar active metal coatings for integration in commercial buildings are currently being commercialised at Specific Innovation Centre, Wales.

TiO_2 is a promising semiconductor for PV as it is inexpensive, abundant, and has good photostability. Despite these advantages, TiO_2 has a large bandgap of 3.2 eV, capable of absorbing the UV part of the solar spectrum only (<5% of the solar spectrum) [117, 118]. For

PV applications many studies use materials with a bandgap of less than 2 eV to absorb visible light and hence view TiO_2 as unsuitable. Alternatively TiO_2 can be used as a UV absorbing base and electron transporter and nanocrystals can provide visible light absorption, as in the proposed design. TiO_2 has been well studied showing that it is easy to process and is intrinsically n-type due to an excess of holes [40, 121-123].

Titanium dioxide has three crystalline polymorphs, anatase, brookite and rutile [124]. Rutile and anatase have tetragonal crystal structure, containing six and twelve atoms per unit cell, whereas brookite has a more complicated orthorhombic crystal structure [125]. Rutile is the most common and stable form and is generally yielded from most crystal-growth techniques [125, 126]. Oshida [127] provides a review of which techniques lead to the different crystal structures. He summarises that dry oxidation at temperatures between 300 – 1000^{o}C forms rutile TiO_2, whereas wet oxidation or anodising can form rutile or a mixture of rutile and anatase and physical deposition forms anatase only. The type of TiO_2 produced via the methods used here will be discussed in the appropriate sections.

Thermal oxidation and chemical anodisation are well established techniques for creating TiO_2 on Ti. Both processes were piloted and found to produce similar reproducibility of oxide layers. The TiO_2 produced by oxidation was found to produce fewer short circuits in the device indicating that fewer conduction pathways across the oxide existed, compared to the anodised TiO_2 which created a porous layer that experienced more short circuits. Due to this and the fact that thermal oxidation does not involve harsh chemicals this method was used for the bulk of the devices. Both oxidation processes are discussed below.

3.3.1 Chemical anodisation

Anodisation, or anodic oxidation, is an electrochemical process whereby an oxide layer can be formed on a metal using an aqueous acid electrolyte. The mechanisms for anodisation are still under discussion, however, it is generally accepted that when a voltage passes through a metal in an electrolyte an electric field forms across the natural oxide layer [128]. Due to this electric field a large current density exists, allowing metal ions to migrate through the natural oxide layer and react with oxygen, or hydroxyl ions, produced at the anode from the aqueous electrolyte. The anodic oxide film produced comprises of a relatively uniform barrier layer next to the metal, a thin non-porous inner oxide similar in composition to the passivating oxide, and a thick porous outer layer [129, 130]. Masahashi et al [131] found this inner oxide layer on a Ti substrate to be 200 nm.

At the anode, anodisation occurs due to diffusion of metal ions from the metal and oxygen atoms towards the metal. Film growth continues until the resistance of the film prevents the current from reaching the metal. As the surface oxide increases in thickness the current density decreases and chemical dissolution of the oxide occurs due to the electrolyte, making the oxide porous. This leads to a higher current flow which then allows further internal oxidation. Hence during anodisation there exists a competitive process between oxide formation and dissolution dictated by the electrolyte and the temperature. Simply, the outer oxide forms by the breakdown of the inner oxide film, whilst simultaneously the inner oxide forms when the outer oxide is under chemical attack by the electrolyte. When the rate of oxide growth equals the rate of dissolution the thickness of the oxide film produced then remains constant. This diffusion limiting reaction consequently means that the oxide layer will have a maximum thickness attainable depending on the electrolyte, concentration and temperature used [128-130].

Applied voltage is also an important consideration for oxide formation, in addition to other experimental variables. It is known that the thickness of a TiO_2 layer produced by anodisation is directly proportional to the potential applied, hence higher potentials lead to thicker oxide films [126, 132]. The thickness of the oxide can be determined directly from the applied voltage, which for titanium is 2 nm/V [133].

The colour of the oxide produced by anodisation can be indicative of the thickness of the TiO_2 produced, due to the light interference effect occurring at the interfaces [132]. Due to interference, the oxide filters out light waves producing a colour that can be related to the oxide thickness on the titanium [134]. The order of colours of increasing thickness are yellow–purple–blue–light blue–silver–yellow–pink–violet–cobalt blue–green–yellow/green –pink–green [132].

It is important to consider anodisation conditions carefully since etching rather than anodising can occur if strong acids, high currents, or long durations are used [114]. Aqueous sulphuric acid has been used extensively as an electrolyte, initially for anodising aluminium but now also for titanium. Table 3-3 shows a review of titanium anodisation studies, to compare the parameters used against the thickness of oxide achieved.

Table 3-3: Review of anodisation of commercially pure titanium in sulphuric acid electrolytes.

Electrolyte	Voltage/current density	Time	Temperature (°C)	Further processing	TiO_2 thickness	Colour of TiO_2	Comments	Reference
0.5 – 1 M H_2SO_4	10 - 140 V 200 – 800 $mAcm^2$	-	-	-	107 and 178 nm	Yellow/green/blue	Oxide is completely amorphous. Oxide growth shows a linear dependence on applied voltage. Bright and uniform colours obtained.	Diamanti et al [132]
0.5 M H_2SO_4	5 – 50 $mAcm^2$	-	25	-	35 nm	-	Ti substrates electropolished first. Very reproducible Ti/TiO_2 produced with a low surface roughness.	Mahe and Devilliers [107]
0.05 M H_2SO_4	1.5 – 6.5 V 0.1 – 1 mV/s sweep rates 3 – 20 μAcm^2	-	-	-	5–23nm (3.5nm/V)	-	Substrates electropolished first. As the oxide growth rate increased the films structure became more homogeneous. Rutile TiO_2 produced.	Kozlowski et al [135]
1M H_2SO_4	Up to 100 V 5 V/s sweep rate	-	-	-	105-170nm (2nm/V)	-	Carbon and hydrogen contamination found at the metal – oxide interface. Oxide produced is multi-layered; inner dense layer, central porous layer and outer dense layer.	Jaeggi et al [133]
1M H_2SO_4	50 V voltage drop 100 - 6100 Am^{-2}	1 min	25	-	-	Yellow and blue.	Oxide reproduces grain structure of Ti substrate. Growth mode affects oxide structure. Oxide film is contaminated with carbon and sulphur.	Deplancke et al [136]

0.05 M H_2SO_4	Sweep from 0 - 50 Vat a rate of 5 mVs	-	-	Annealed at 675 ºC for 1 hour in air.	50-60 nm	Blue/ grey/yellow after annealing.	TiO_2 has a rough topography. Annealing changed the surface significantly. Annealed TiO_2 was rutile. Bulk defects in TiO_2 are removed by annealing.	Koole et al [100]
1M H_2SO_4	5 – 15 V	4 – 180 min	6 – 36 ºC	Dried at room temperature for 1 day.	(1.4 – 2.9nm/V)	-	Lower growth constants found for lower temperatures. Oxide thickness is linearly dependant on voltage. No cracks in TiO_2 for polished Ti surfaces.	Capek et al [128]
1M H_2SO_4	20 – 130 V 5 – 40 $mAcm^2$	2.5 – 156 s	14-42 ºC	-	54.3 - 361.5 nm (21.7 - 2.3 nm/V)	22 V – dark purple 60 V – blue/yellow 100 V – green	Higher voltage obtained thicker oxides. Galvanostatic anodic oxide films demonstrate TiO_2 interference colours.	Sul et al [137]
0.002 M H_2SO_4	50 mA/cm^2, until 210 V reached.	30 min	-	Annealing at 723K for 5 hours in air.	0.3 µm	-	Glassy anodised oxide with submicron pores which are inhomogeneous distribution, size and shape.	Masahashi et al [131]
1.2 M H_2SO_4	50 mA/cm^2, until 210 V reached.	30 min	-	Annealing at 723K for 5 hours in air.	7 µm	-	Coalescence of homogeneous pores in the oxide. No micro-cracks.	Masahashi et al [131]

3.3.1.1 Titanium anodisation method

For the device, electropolished Ti was anodised in a weak aqueous 0.002M sulphuric acid (H_2SO_4) electrolyte adapted from the method outlined in Masahashi et al [131]. The anode comprised of a Ti clip which held the Ti sample and carbon rods were used as cathodes. Each sample was anodised with a constant voltage of 50 V for 30 seconds, with a current limit of 1 A. The current rapidly falls after the first 5 seconds where most of the anodisation occurs. However it was found that a slightly higher voltage (60 V) or longer duration (up to 1 min) can also be used to produce a thicker oxide. The majority of the oxide layer was formed within the first 3 seconds, where a distinct colour change was observed. After each process the anode Ti wire clip that held the substrate was manually filed to remove any oxide in preparation for the next sample. After anodisation the samples were washed in deionised water.

The changes in colour of the TiO_2 substrates once anodised could be categorised into two distinct groups, blue or golden yellow. Thickness and purity of the titanium substrates were the only two factors that were varied and so must have had an effect on the oxidation colour and hence thickness. Generally the thicker, recycled Ti substrates were golden yellow and the pure, thin Ti substrates produced a blue coating. Both blue and yellow are common in the literature, as indicated in Table 3-3, and relate to approximately 100 nm thick oxide layer. At a constant voltage of 50 V, using the relationship 2 nm per volt [133], we would expect to obtain a 100 nm layer also.

As well as various thicknesses obtained, indicated by the different colour changes observed, anodic TiO_2 layers may also contain impurities originating from the H_2SO_4 electrolyte. Unlike anodisation thermal oxidation will produce a more stoichiometric TiO_2 layer that can be more easily controlled by experimental variables [124]. Furthermore, thermal oxidation does not require any chemicals, which reduces impurities and hazards and can potentially result in cost and resource savings at the fabrication stage. The next section will discuss the thermal oxidation of titanium.

3.3.2 Thermal oxidation

Titanium is highly reactive and oxidizes in air within nanoseconds to create a stable and well adhered surface oxide layer. The natural oxide produced is approximately 1.5 – 10 nm, but varies depending on the substrate composition, the environment and time [124, 126, 128, 137]. Oxidation of titanium has many stages, with oxide layers progressively becoming higher oxides as oxidation develops and temperature increases, leading to a graded material. The sequence of titanium oxidation in air is as follows; Ti + O → Ti (O) (O dissolved as interstates in Ti lattice) → Ti_6O → Ti_3O → Ti_2O →TiO→ Ti_2O_3→ Ti_3O_5→ TiO_2. TiO_2 is the most stable and common surface and TiO/Ti_2O_3 are the dominant oxide phases [124, 126].

The oxidation rate of titanium is highest in the initial stages of thermal oxidation, decreasing quickly with time, and is dependent on the temperature and duration of oxidation [134, 138]. The rate of oxidation slows as the oxide layer increases, since a thicker oxide limits the diffusion of oxygen and hence the rate of further oxidation. Gemelli and Camargo [138] demonstrated that the oxidation rate of titanium increased with temperature between 300 – 700°C, with most of the oxide growth occurring in the first 10-20 minutes. Revie et al [134] suggested that below 500°C the oxidation rate of titanium is low and decreases with time, whereas exposures over 650°C and longer durations lead to oxide ‘scale’ cracking and rapid oxide growth, quadrupling in thickness between 538 and 649°C.

Adhesion of TiO_2 to Ti can also vary depending on the conditions used. Oshida et al [124] showed that TiO_2 adhesion to titanium is greater for oxidation in air than pure oxygen, however adhesion of oxide layers decreased as the thickness of the oxide layer and temperature increased. It was also found that TiO_2 does not show any phase transformation up to its melting point of 1885^{o}C, however Ti allotropically transforms at 885^{o}C, changing from a hexagonally close packed crystalline structure to a body centred cubic crystalline structure. Hence, increasing past this temperature may create weaker bond strength between Ti and TiO_2.

After considering the literature on the various oxidation temperatures and durations, shown in Table 3-4, 700°C for 30 minutes was selected for oxidation of the titanium substrates. These parameters were selected since in the previous studies temperatures much higher than 700°C give poor adherence to the Ti substrate, longer durations gave a much thicker layer and shorter durations give a mixed anatase/rutile structure, which affects the bandgap created. The same conditions were applied to all samples to ensure controllability and reproducibility. The resultant TiO_2 was anticipated to be approximately 1 µm and rutile.

Table 3-4: Review of titanium oxidation parameters.

Substrate	Temperature (°C)	Duration (hours)	Atmosphere	Layer thickness	Colour	TiO_2 type	Adherence	Ti/TiO_2 interface	Reference
CpTi SMAT& CG	500	1	-	0 nm	SMAT – blue CG – tawny	-	-	-	Wen et al [139]
CpTi SMAT & CG	600	1	-	4.8 µm for SMAT 0 nm CG	SMAT – light golden CG – sky blue	Rutile and Ti_3O_5	-	-	Wen et al [139]
CpTi SMAT & CG	700	1	-	8.5 µm for SMAT 5.6 µm for CG	SMAT – dark grey CG – grey	Rutile	-	-	Wen et al [139]
Ti foil	600	0.5	Air	~1 µm	-	Multiphase - rutile and anatase	Good	Ohmic	Hossein-Babaei et al [122]
Ti foil	700	0.5	Air	~1 µm	-	Rutile	Good	Ohmic	Hossein-Babaei et al [122]
Ti Foil	800	0.5	Air	~1 µm	-	Rutile	Poor	Ohmic	Hossein-Babaei et al [122]
CpTi	500	8	Air	-	-	Amorphous and rutile	-	Ohmic	Tang et al [120]
CpTi	500	-	-	200 nm	-	Rutile	-	Ohmic	McFarland and Tang [34]
CpTi 0.2mm	700	0.5	Air	1 µm	-	Rutile	Strong adherence	Ohmic	Hossein-Babaei and Rahbarpour[140, 141]
Ti evaporated	846	0.5	Air	-	-	Amorphous	-	-	Wang et al [142]

CpTi	200 – 800	48	Air	-	-	<276ºC - anatase <457 ºC - anatase/rutile >718ºC - pure rutile	More stable layer at high temperatures	-	Gemelli and Camargo [138]
CpTi	750	-	0.1 atm	32 nm	Purple blue	Rutile	Good	-	Adachi et al [143]
CpTi	1000	-	0.1 atm	1 µm	-	Rutile	Poor	-	Adachi et al [143]

Acronyms: CpTi – commercially pure Ti, SMAT – surface mechanical attrition treated, CG - coarse grain.

3.3.2.1 Titanium thermal oxidation method

Following electropolishing, Ti substrates were thermally oxidised in air, in an oven, which heated up to 700°C in 3-4 minutes. The sample was placed in the oven and timed for 30 minutes once 700°C was reached, after which the oven was switched off and the sample was left to cool in the oven with the door open. Since thermal oxidation of titanium is a common process, in depth characterisation was not carried out. As indicated above a maximum of 1 µm rutile layer is expected. The majority of the oxidised rutile produced was light blue.

An average profile roughness of 15 nm was found across a representative electropolished and thermally oxidised substrate surface, by AFM analysis, as depicted in Figure 3-4. This is important since if the oxide created had a high surface roughness it could potentially cause the noble metal film to crack during electrical characterisation (see section 3.6.1).

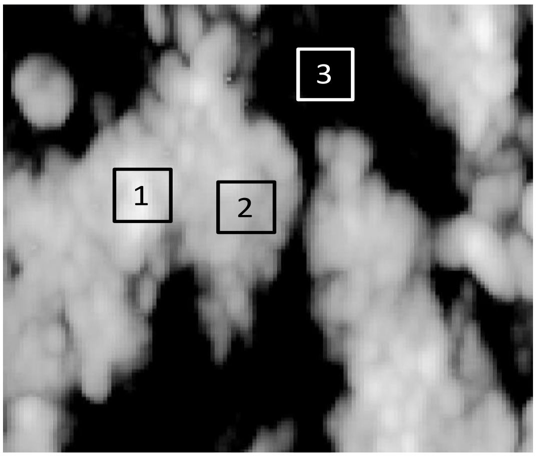

Position	**Surface roughness R_a (nm)**
Whole image	14.8
1. High	2.64
2. Middle	3.14
3. Low	5.30

Figure 3-4: AFM image of a typical Ti substrate electropolished with H_2SO_4 and thermally oxidised at 700°C for 30 minutes. The patchiness of the image is due to the high contrast settings to find peaks and troughs of the oxide layer formed, since the oxide produced was continuous across the surface, verified by I-V characterisation. The numbered boxes relate to surface roughness measurements, shown in the table. Image and data courtesy of Mr Graham Smith, University of Leeds[116].

It was found by Gemelli and Camargo [138] that thermally oxidised Ti resulted in TiO_2 films that were crack free and had a uniform averaged surface roughness profile (R_a) of 0.8 - 1.35 µm for oxidation at 600 – 650 °C for 48 h. The same R_a measurement in this works shows a considerably lower value for thermally oxidised Ti, at 700°C for 30 minutes. Comparing the thermally oxidised substrate averaged surface profile roughness to the electropolished sample given in Figure 3-3 gives a 5 nm difference. This indicates that electropolishing the sample first provides a control base for a uniform TiO_2 layer to form.

3.4 Metal deposition

For the nanocrystal (NC) activated Schottky barrier cell a transparent and conductive metal layer is needed for transporting electrons across the Schottky barrier. Gold, silver and platinum are all ideal materials due to their high work functions and long electron ballistic mean free path lengths (see Table 3-5). This means that electrons have negligible electrical resistivity, due to scattering, and hence the average distance an electron can travel without being obstructed is increased [120]. The conductivity of a metal affects the ballistic transport, since a highly conductive metal will enable an electron to more easily move through it. High work functions are desirable as they create a larger Schottky barrier when combined with an n-type semiconductor, discussed further in 2.1.5. Furthermore, platinum and gold do not oxidise and silver has a low propensity to oxidation. When combined with a NC top layer the metal-NC interface is affected by the work function since lower work function metals are known to rapidly oxidise and may adversely react with the capping agent or ligands surrounding the NCs [81].

Table 3-5: Work function and mean free path of metals used in device [146, 147].

Metal	Work function (eV)	Electron inelastic mean free path Å (10^{-10} m) with electron energy of 50 eV	Conductivity σ (S/m at 20°C)
Platinum	5.12 – 5.93 (5.65 [39, 148, 149])	5.0	9.4×10^6
Gold	5.31 – 5.47 (5.1 [39])	5.1	4.1×10^7
Silver	4.52 – 4.74 (4.26 [39])	6.1	6.3×10^7

When depositing very thin metal layers, resistance is an important consideration as it affects electron transfer. It has been shown by Fang et al [144] that as Pt film thickness increases from 2 nm to 415 nm its sheet resistance decreases. However, it was also found that equally high energy conversion efficiencies can be obtained and the charge transfer resistance presented no change due to Pt thickness of the Pt electrode in the dye-sensitised solar cell in this study. The study also showed that the conductivity of a Pt coated FTO electrode improved as the thickness of Pt increased up to 100 nm, after which further deposition gave no significant improvement [144, 145]. This suggests that the metal layer should be no thicker than 100 nm but can produce an electrically continuous layer if only 2 nm are deposited. This synchronises well to the criteria for a 10 – 50 nm metal layer required for the device. Using a thinner metal layer will also help to reduce the overall cost of the device.

There are many established industrial processes for applying metal layers, such as evaporation and sputtering. Silver in particular is widely used in industry due to its high conductivity, abundance, ease to process, and lower cost in comparison to gold [76]. For this research a few different techniques have been trialled to provide the conductive metal layer required, these include sputtering gold and platinum, evaporating silver, electrodepositing silver and drop casting silver nanowires. The following sections will discuss all of these techniques.

3.4.1 Sputtered and evaporated films

Sputtering is a well-known tool for applying continuous metal layers to many types of surfaces and making poorly conducting surfaces more conductive. Sputtering with a gold loaded target was undertaken to produce a well adhered, continuous and uniformly thin gold layer on to the TiO_2/Ti substrate. An EM-Scope sputtering system was used at 20 mA and 0.05 torr, between 2-8 minutes to gain gold layers of 10-40 nm respectively. A schematic for the gold sputtering is shown in Figure 3-5.

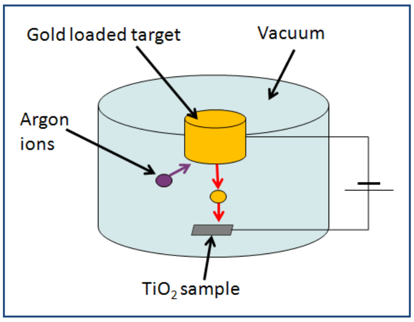

Figure 3-5: Schematic of the sputtering system.

Gold was used initially, to coat the TiO_2/Ti substrate, since it is an established material for sputtering. However, it was soon realised that the gold layers produced were not reproducibly continuous. This was thought to be caused by a disruption with the argon gas supplied to the machine and also an issue with system reliability, rather than a problem with the substrate and electrical testing. These problems were evident since the gold sputterer would intermittently produce different thicknesses despite using the same set up conditions. Sometimes this was due to an argon gas supply problem but at times when the argon gas was being supplied properly, the non-reproducible films were explained as a system problem. To overcome the problem of non-continuous layers the thickness of the gold layer was increased to between 40 - 80nm to provide the continuity needed, however this decreased the photocurrent due to the reduced transparency of the gold layer.

The growth mechanisms of the film during sputtering could have impacted on the continuity of the metal films. The growth mechanisms include an initial nucleation phase followed by lateral growth. Sputtering on to a semiconductor may have elongated this nucleation stage, due to the insulating semiconductor properties, and hence for thin layers a continuous film may not have been established. Re-sputtering generally increased the continuity of the layers deposited, indicated by an increase in exponential features, however it also reduced the transparency of the layer. Slepicka et al [150] agree that metal layer thickness is affected by the metal nucleation on to the substrate surface. Furthermore, Koole et al [100] also found that sputtered gold layers between 15-50 nm formed interconnected patches rather than a continuous film on the TiO_2.

Figure 3-6 shows an SEM image for a typical gold and platinum sputtered sample. The Au layer was 40 nm thick and the Pt layer was 10 nm thick. The Au layer appears to form islands that have agglomerated to form an electrically continuous layer on top of the TiO_2, so much so that the TiO_2 layer cannot be seen. The thinner Pt layer shows similarities in that Pt islands have agglomerated to create an electrically continuous film, but we can also see through to the TiO_2 since less Pt was sputtered. For a thicker sputtered layer these gaps are anticipated to decrease. SEM images across the surface of the device showed the same results, confirming the continuity of the sputtered film across the surface.

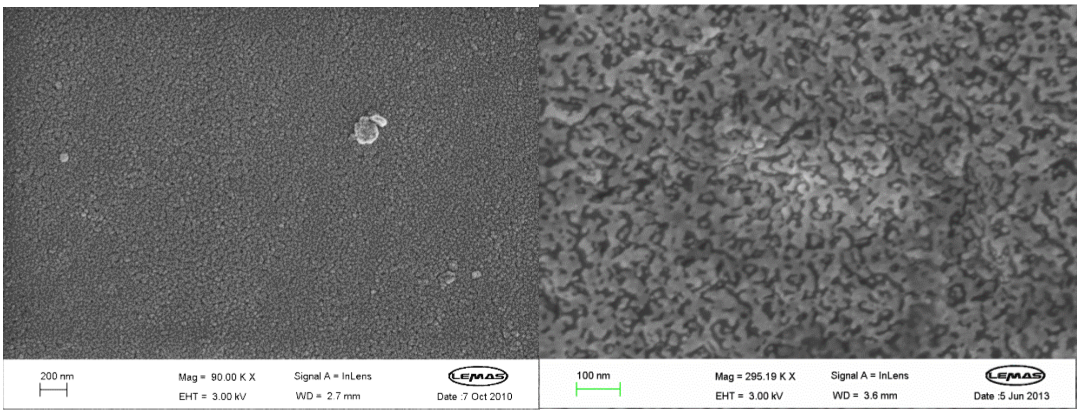

Figure 3-6: SEM Image of a typical gold (left) and platinum (right) sputtered TiO_2 (Sample 10 and 502 respectively).

An Agar Scientific system was used for platinum sputtering. A specific thickness was programmed into the machine rather than a duration, which gives more confidence in the films produced. The samples were placed in the sputtering column, the lid was replaced and an argon vacuum was applied to 0.05 torr. Once the system had flushed and leaked, the thickness was set. When the vacuum of 0.05 torr was reached the machine was started and automatically finished when the pre-set thickness was reached. Despite being a newer machine, some variations in the Pt thickness on TiO_2/Ti were observed via glass slides that were sputtered simultaneously to the substrates. It was found that for the same pre-set thickness the transparency of the glass slides varied. Despite this discrepancy the layers were more reproducible than the gold, since less Pt devices created short circuits compared to the Au films.

Silver was evaporated on to 6 substrates to provide a control sample for comparison with the silver nanowire samples. Like sputtering, evaporation is a well-established technique and due to being used on a limited number of samples further discussions is considered unnecessary.

3.4.2 Silver electrodeposition

Electrodeposition is widely used in industry for many coating applications. It is a low cost, scalable process, where small manipulations in current can have large effects on surfaces created. The mechanism of electrodeposition follow $M^+_{(aq)} + e^- \rightarrow M_{(s)}$, where a charged metal cation, from an electrolyte containing dissolved metal salts, deposits on a cathode by an electric current [151]. Generally electrodeposition produces well adhered films, however, problems are known to occur when noble metals are deposited on a less-noble metal substrate [152]. This is because electrodeposition requires an electrically conductive substrate; hence a semiconductor substrate with insulating properties can inhibit the electrolysis process. Cyclic voltammetry can be used to deposit and then re-dissolve the material, or ‘strip’, from the electrode to produce well-adhered metal deposits on a substrate. This ‘stripping’ phase removes loosely adhered and agglomerated deposits, which allows more efficient electrolysis on to the substrate in subsequent deposition cycles [153].

Previous work on electrodeposition of noble metals on to semiconductor substrates include the electrodeposition of Cu [154-156], Au [35, 156-158] and Pt [156] on silicon, Pt on n-GaAs [159], Ag on TiO_2 [160, 161] and TiO_2 nanotubes [162, 163]. A number of studies have reported electrically continuous gold films via electrodeposition resulting in a higher Schottky barrier height compared to a bulk gold film on TiO_2 [120], n-GaAs [164] and on silicon [158]. There have been a number of studies that have looked at electrodepositing different forms of silver on to many different surfaces, for example silver nanoparticles [161-163]. Many studies have also looked into different techniques to deposit silver on to TiO_2 including doping [123], photochemical impregnation [76] and vacuum deposition [122]. Only a few studies have looked at electrodeposition of silver on to TiO_2, including Boskovic et al [160] and Poroshnov and Gurin [165]. Boskovic et al [160] form a composite TiO_2/Ag film, by electrodepositing and anodising a Ti substrate simultaneously through an electrodeposition process. They report that silver formed either dendritic or nanoparticles on the substrate. Poroshnov and Gurin [165] electrodeposit silver on to TiO_2 and similarly obtained spherical particles and dendritic structures. Very few, if any, studies to date have looked at the electrodeposition of silver on to a TiO_2 substrate to gain an electrically continuous film for solar cell applications. In addition to this research gap, silver was also selected for electrodeposition on to the TiO_2/Ti substrates over the other noble metals because of its higher conductivity.

Two electrodepositing techniques were used, a ‘standard’ technique, undertaken at the University of Hull with Dr Jay Wadhawan, and ‘strike electrodeposition’. The standard electrodeposition technique used a nickel coil cathode, a potassium chloride/mercury reference cell, and the TiO_2/Ti substrate as the anode. An air tight, plastic cell holder was used to secure the sample in place. The back of the substrate was filed to remove the oxide layer and then coated with silver epoxy to ensure good electrical contact with the copper plate in the cell holder, which was connected to an external circuit. The top of the plastic holder was then securely fastened to provide an air tight cell. Wax covered the remaining exposed copper between the sample and the cell holder. The cell was filled with the electrolyte and then degassed with argon gas at 0.5 Bar. A potentiostat using GPES software recorded the potential versus the current at different scan rates. Depositing and stripping cyclic voltammetry controlled the growth of the silver film on the substrate. Verification that the stripping and depositing of silver was taking place can be confirmed by the I-V curve produced, a typical example of which is shown in Figure 3-7. The curve clearly shows a positive stripping phase and a negative deposition phase, as indicated.

The strike electrodeposition method has been shown to obtain better results for deposition compared to evaporation and sputtering techniques, in the context of a higher Schottky barrier in [120]. The strike electrodeposition technique differed from the standard approach as it used a palladium plate cathode and incorporated ‘strikes’ in addition to depositing and stripping regimes. The electrolytes used for this technique were all aqueous. The strike method was adapted from Tang et al [120] and involved pulsing a current of 200 mA/cm^2 for 20 ms to create strongly adhered silver nucleation islands from which further lateral deposition could proceed. The periodic pulse train current used was -1.7 mA/cm^2 to +0.2 mA/cm^2 (the effective area being 0.25 cm^2) with a 50% duty cycle and

5 ms period. Generally this technique uses 1 strike and a growth phase of 2 - 8 minutes afterwards, however up to 10 strikes and sometimes no continuous growth phase were trialled to test the effect of different deposition rates. After electrodeposition all samples were rinsed with deionised water to remove any larger agglomerated particles that were not adhered to the surface.

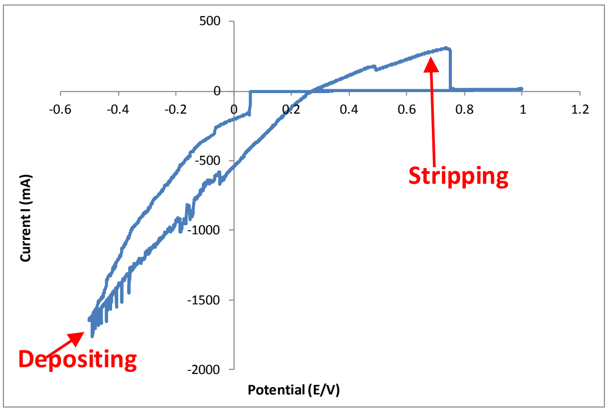

Figure 3-7: Typical depositing and stripping curve for electrodeposited silver Schottky devices.

Various electrolytes and scan rates were experimented with to find an optimum for well adhered silver deposits, presented in Table 3-6. Both dimethyl sulfoxide (DMSO) and deionised water solvents were used. DMSO is a highly miscible, non-toxic, organic solvent that is often used in electrochemistry as it is resistant to oxidation and reduction, and can provide a wide voltage range. Its aprotic nature means that it can easily dissolve organic salts to provide a homogenous electrolyte which is necessary for uniform electrodeposition. DMSO has a high boiling point of 189°C and a high dielectric constant of 46.7, meaning that solution resistance is reduced which can minimise Ohmic losses. Water has a higher dielectric constant than DMSO of 81 and a high boiling point. Moreover, water provides higher charge mobility than organic solvents due to fast solvent proton exchange, a phenomenon that does not exist in aprotic solvents, and therefore increases mass transfer in the electrolyte. Water is known to hydrolyse at high voltages, however only relatively low voltages were used. Both solvents have a low viscosity which is desirable for facilitating mass transport by diffusion [151].

Tetra-butyl-ammonium perchlorate (TBAP) and tetra-butyl-ammonium-tetra-fluoroborate ($Bu_4N^+BF_{4-}$) are commonly used at large scales with DMSO as supporting electrolytes and have been thoroughly reviewed in the literature. The tetrafluoroborates are safer than perchlorates, although in this work neither present a particular hazard due to the ambient conditions. The supporting electrolytes main function is to provide a conducting medium, reduce resistance and enhance mass transport, since both solvents are non-conducting. Tartaric acid was used as a supporting electrolyte in water solvents as a less toxic alternative [151]. Silver acetate and nitrate were both used in the solvents on an experimental basis to find which provided the most continuous layer.

Table 3-6: Silver electrodeposition techniques, scan rates and electrolytes

	Scan rates	Electrolyte composition	Observations
Standard electrodeposition	Deposition: Depositing scan rate ranged between 5 – 10 mVs^{-1}. Stripping: Stripping scan rate ranged between 100 – 400 mVs^{-1}. Scans were repeated between 1 – 5 times before starting a different scan rate.	1mM silver nitrate 0.1M $Bu_4N^+BF_4^-$ 100ml DMSO	$Bu_4N^+BF4^-$ did not dissolve fully - precipitation and discolouring observed in the electrolyte. No obvious stripping peak - concentration of nitrate deemed too weak.
		50mM silver nitrate 0.1M TBAP 100ml DMSO	Clear stripping and deposition peaks but very noisy at all scan rates. At faster scans the stripping peak is not visible. Silver deposits observed on TiO_2 but easily wipe/rinse off.
		50mM silver acetate 100ml deionised water	No visible depositions on substrate.
Strike Electrodeposition	Strike; 1-10 strikes at 200mA/cm^2 for 20ms. Growth phase; Continuous pulse train current -1.7mA/cm^2 to +0.2mA/cm^2 (effective area of 0.25cm^2) with a 50% duty cycle and 5ms period for 1-8 minutes.	0.02M silver acetate, tartaric acid and deionised water.	Higher concentrations of silver acetate did not dissolve in water. No deposition visible. On one substrate silver deposition was visible, but was not adhered as easily wipe/rinsed off.
		0.1M silver nitrate, tartaric acid and deionised water.	Silver nitrate is fully dissolved in water before experiments. No visible deposition

Abbreviations: DMSO - dimethyl sulfoxide, TBAP - tetrabutylammonium perchlorate, $Bu_4N^+BF_{4-}$ - tetrabutylammoniumtetrafluoroborate.

Prior to selecting the electrolytes in Table 3-6, silver acetate and sulphate were also trialled with DMSO but caused a reaction where precipitate formed in the solution, and were discounted from further study with DMSO, however it was found that silver acetate dissolved in water and this was tested as an electrolyte. Likewise $Bu_4N^+BF_4^-$ did not dissolve adequately in the solvent and hence tetrabutylammonium perchlorate (TBAP) was used instead and proved to dissolve well in the solvent.

3.4.3 Silver nanowire synthesis and deposition

Silver nanowire meshes are currently a large area of research since they provide a good alternative to more traditional electrodes offering excellent transparency, conductivity, electrical robustness and flexibility at a lower cost [166]. Nanowires have been used in many silicon based p-n and p-i-n junction solar cells to increase device efficiency [167-169]. Silver nanowires have also been used as a top electrode generally in polymer or organic solar cells [170-174], however it is not immediately evident that anyone has used silver nanowires as a top electrode in a Schottky solar cell.

The nanowires can enhance photo-conversion by enhanced absorption and light trapping, increased tolerance of defects and improved bandgap tuning [175, 176]. These improvements come from surface plasmon resonance (SPR), an effect associated with metal nanostructures [173]. Surface plasmons are charge density oscillations confined to metal nanostructures. When light is absorbed at a wavelength where resonance occurs, a surface plasmon is excited, resulting in light scattering and an increased local electromagnetic field. The intensity and frequency of the surface plasmons depend on the type, size and shape of the material as well as the environment [177]. In the NC-activated Schottky cell the use of nanowires also provide the added benefit of enhanced charge transfer efficiency due to the nanocrystals being closer to the TiO_2 substrate.

Despite these advantages, nanowires are not expected to increase the maximum efficiency of a device. However, nanowires provide further benefits in that the quantity and quality of material can be reduced to gain equivalent efficiencies, presenting a further option to lowering costs in comparison to sputtering. Chemical vapour deposition and patterned chemical etching are two of the most common techniques to fabricate good quality nanowires of a variety of materials [176]. However a more simple, rapid and low cost process to produce nanowires has been suggested in [178-180], which involves chemical synthesis and nanowire production using the polyol method.

3.4.3.1 Nanowire synthesis

The silver nanowires were produced using the polyol method, given by Korte et al [178], in which silver nitrate is reduced at 150^oC under ambient atmosphere using ethylene glycol as both a solvent and reducing agent. The process utilises poly-vinyl-pyrollidone and copper chloride for kinetic growth control. The silver nanowires used in this work were synthesised by Ross Jarrett (University of Leeds, Doctoral Training Centre in Low Carbon Technologies, Energy Research Institute).

3.4.3.2 Nanowire filtering

The silver nanowires were filtered before deposition. This was carried out by pulling 2 ml of unfiltered silver nanowires in solution through a syringe, then attaching a 0.45 µm filter paper in a metal housing to the syringe and forcing the unfiltered nanowires through the filter. To wash the nanowires 1 ml of acetone was pulled through the filter and pushed back out slowly, this was repeated 3 times. Further washing with water was carried out after acetone, but this was repeated 15 times. After washing the nanowires, the syringe was removed and filled with air, then reattached and slowly pushed to remove excess solvents which may have been trapped in the metal housing. The filter was then carefully removed, placed in a glass vial with 1 ml of ethanol and then put in to the ultrasonic bath to remove the nanowires from the filter. After 10 minutes the filter was removed from the vial, leaving the nanowires suspended in ethanol. After filtering the nanowires were used immediately, but they were also found to produce similar results after a couple of months in solution. The filtered nanowires were kept in air tight sealed containers in an ambient environment. All of the different nanowire batches used were characterised using the SEM and resistance measurements were carried out to ensure electrical continuity of the deposited films.

3.4.3.3 Nanowire deposition

The nanowires with an average concentration of 1.55 ± 0.14 mg/ml were drop cast in stages on to the substrate using a micropipette, with total mass varying between 3 and 40 µL. It was realised that larger mass deposits (over generally 15 µL) were required to produce a Schottky barrier with the TiO_2/Ti substrate and a photoresponse. After deposition all samples were annealed in air at 180°C for 20 minutes, following the duration and temperature suggested by Lee et al [171]. Longer annealing times have been found to increase resistance and reduce conductivity [181, 182]. The mass of nanowires in a particular solution was found by evaporating the solvent and weighing the mass left. Variations across different batches were found, despite being synthesised following the same method. Experimental variables were thought to account for these changes.

3.5 Nanocrystal deposition

An advantage of the Schottky barrier solar cell is that a large variety of semiconductor nanocrystals (NCs) can be deposited on top of the cell to enhance visible light absorption. CdTe, CdS, CdSe, $CuInS_2$ and Cu_2O nanocrystals were drop cast on to the metal/Ti/TiO_2 devices. Nanowire and nanocrystal devices were also produced, but due to the experimental parameters used for the nanowire deposition (see 2.4.3), the nanocrystals had to be deposited first. Various volumes and concentrations of NCs were trialled in order to obtain a visible photoresponse from the nanocrystals. Surface treatments to remove the capping agent were also considered.

3.5.1 Nanocrystal selection

The main criterion for nanocrystal selection for the device was the ability to absorb visible light. Another important consideration was band edge positioning in respect to TiO_2, since the band edge positions of a semiconductor dictate its ability to undergo electron transfer [183].

The space charge region at the interface between nanocrystals and a semiconductor or metal oxide is not well understood. Loef et al [37] show that n-type semiconductor NCs show p-type behaviour at a TiO_2 interface, therefore forming a Schottky barrier between the semiconductor NCs and the noble metal layer. However, there is some disagreement over band bending in nanoparticles, some argue that band bending is negligible in small nanoparticles of <6nm [184] but can exist in nanocrystals >20nm [185]. In the NC-activated Schottky cell the mechanism for electron transport from the nanocrystals into the TiO_2 is via ballistic travel through the noble metal layer, this means that we wouldn’t expect a Schottky barrier to form between the semiconductor nanocrystals and the metal layer. This rules out the need to consider doping the semiconductor NCs (i.e. p- or n-type), leaving only band alignment affects to be considered.

It has been suggested by Linsebigler et al [183] that for nanocrystals to be able to conduct electrons to a n-type semiconductor the donor potential level needs to be above the valence band of the semiconductor, so that the electrons can be donated to the empty hole. For this to occur, the acceptor species must have a potential level below the conduction band of the semiconductor. However, due to ballistic travel through the metal in the nanocrystal activated device the semiconductor will be accepting electrons from the NCs and so the conduction band of the semiconductor needs to be lower than the conduction band of the NCs. This is in agreement with Lee et al [63] who fabricated a CdS/TiO_2 device, where the CdS has the higher conduction band edge which is suitable for the injection of excited electrons from CdS to TiO_2. Figure 3-8 shows the band alignment of TiO_2 with respect to the variety of nanocrystals that were considered. We can see that CdS and CdTe look favourable with regards to their conduction band being slightly above that of TiO_2.

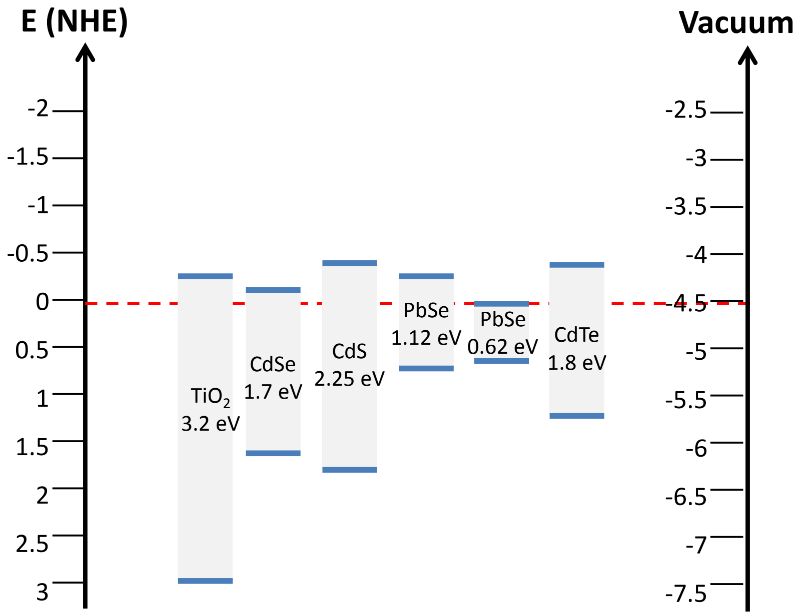

Figure 3-8: Energy levels of TiO_2 and selected nanocrystals, with reference to the flat band potentials in a contact solution of pH =1, adapted from [183, 184, 186]. The vacuum level here is the energy of a free electron that is outside of any material and used as an energy reference [187]. Inclusion of PbSe NC energy levels from details given in [40], where PbSe 1.12eV relates to d = 3.4 nm and 0.62 eV relates to d = 6.7 nm. CdTe nanocrystals taken from [188].

As illustrated in Figure 3-8 the bandgap of CdS limits its absorption range to around 500 nm, whereas the absorption range of CdSe can extend further to 730 nm. However the conduction band edge of CdSe is below that of TiO_2, hence electron injection efficiency will be reduced in comparison to CdS [63]. On the other hand, it has been suggested in [189] and [102] that CdSe conduction band can increase above the conduction band of TiO_2 with decreasing particle size and increasing bandgap energies, therefore could be suitable for injecting electrons into TiO_2. This applies to other NCs since when NC size reduces, the effective bandgap increases and hence NCs conduction band potentials can increase with respect to TiO_2, enabling more effective electron injection [40, 183].

Despite the effect of NC size on conduction band potential level, Tisdale et al [40] showed that electron transfer from the lowest excited state of PbSe to TiO_2 is unfavourable energetically, at NC sizes between 3.3 – 6.7 nm. Moreover, PbS and PbSe are strongly IR absorbers, and would provide more of an obstacle when characterising as the arc lamp used for photoresponse measurements is limited to a wavelength range of 260-800 nm. For these practical and theoretical reasons PbS and PbSe were not considered any further. CdS and CdTe were sourced initially due to their favourable compatibility with the device.

3.5.2 Nanocrystal sourcing

The nanocrystals were sourced from various locations, see Table 3-7, including a mixture of commercially and laboratory synthesised nanocrystals. All of the nanocrystals were delivered in the concentrations shown and required no further processing, apart from the CdTe. The CdTe came in powder form and was dissolved in deionised water to the concentration shown below before use. As described above, only CdS and CdTe were initially sought, however CdSe was supplied with the CdS and so experimentation was undertaken. It is in the interest of the future solar cell market to use low cost and less toxic materials and so $CuInS_2$ and Cu_2O were also sourced as alternatives to CdS and CdSe.

Table 3-7: Nanocrystal specification and sourcing

Nanocrystal	Size (nm)	Solvent	Concentration (mgml^{-1})	Produced by	Synthesis Reference
CdS	3	Toluene	2.37	Robert Mitchell, Chemistry Department, University of York.	[190]
CdSe	5	Toluene	3.48	Robert Mitchell, Chemistry department, University of York.	[191]
CdTe	2 - 7	Deionised water	4.7	EmFutur (online provider)	-
$CuInS_2$	2.9	n-hexane	0.01	Matthew Booth, Physics department, University of Leeds.	-
Cu_2O	350	Ethanol	15	Sigma Aldrich (online provider)	[192]

Cu_2O - copper (I) oxide/cuprous oxide

3.5.3 Nanocrystal deposition technique

There are many deposition techniques for nanocrystals including spin coating, evaporating, drop-casting, submerging and layer by layer (LBL) deposition. LBL is often used instead of dropcasting or spin coating, as it is found to avoid formation of cracks and other defects in the film that make a reproducible solar cell difficult to achieve [193].

All nanocrystals were drop cast on to the Schottky devices in a layer by layer fashion, whilst stationary and on a flat surface. Drop casting was employed due to its low cost and since this study was focussed on proof of concept rather than optimisation. LBL was used to ensure that there was sufficient coverage of nanocrystals on the surface of the device. The nanocrystals in solution were measured and dropcasted using a 1-10µL finnpipette which was bought as close to the device as possible, without touching, before the nanocrystals were released, to prevent the nanocrystals leaking over the sides of the device. Between 1 - 30 µL of nanocrystals were deposited onto the surface and this was repeated until the required amount of NCs was deposited. The viscosity of the nanocrystals was such that when depositing up to 5µL, a ~4 mm diameter circle was formed on the device that did not flow over the sides.

The volume of nanocrystals required was approximately calculated to ensure that the right order of magnitude of nanocrystals was being deposited. This involved making some assumptions on the formation of a nanocrystal layer on the Schottky devices. These assumptions included that the nanocrystals would form a 2D single layer of hexagonally close packed NCs with a hexagonal packing fraction of 0.91, 5-10 monolayers were required, and the nanocrystal diameter and density were found from freely available resources. The area, volume and mass of a single nanocrystal were calculated. From this the number of nanocrystals required, total mass required and therefore the volume required were calculated for the given area of the device. For the CdS and CdSe with concentrations of 2.37 and 3.48 mg/ml respectively this gave a volume required of 0.2 µL. The smallest quantity that can be deposited was 1 µL due to the specification of the Thermo Scientific finnpipette used. For the CdS and CdSe this would give approximately 5 monolayers of nanocrystals, which was as required. A variety of NC concentrations and volumes up to 30 µL were experimented with in order to harness a large visible photoresponse from the NCs.

3.5.4 Nanocrystal surface treatment

Electrically insulating organic ligands, commonly oleic acid, are used to cap colloidal NCs when processing to prevent further growth and maintain NC properties. However if not removed these ligands can reduce exciton separation, decrease charge carrier transport, maintain insulating properties, produce surface charging and change the band alignment of the NCs [102, 188, 194]. Organic ligands can be removed by thermal or chemical treatment which will convert NC solids from insulators to conductors and can improve electronic coupling to the Schottky device. Chemical treatment such as ethanedithiol (EDT), hydrazine (HYD) or amine treatments, involve substituting the long chained organic ligands with smaller molecules that can decrease the inter-NC spacing, passivate surface traps and chemically dope the films. Thermal treatments involve complete removal of organic chains surrounding the NCs [40, 193, 194].

However all post deposition treatments are problematic as they can cause volume loss due to the removal of organic ligands which causes macroscopic cracks that could short circuit the cell, re-depositing NCs layers rarely overcomes this [194]. Treatments can also leave excess bonds on the NC surface which could lead to scattering and increase electron cooling in the NCs [40]. Moreover some chemical treatments, particularly EDT is suggested to make the film vulnerable to attack by oxygen and moisture [81].

Table 3-8 outlines the different chemical and thermal treatments that have been used in other studies and the results obtained. It is evident from Table 3-8 that there are advantages and disadvantages to both chemical and thermal treatments. It has recently been suggested that sintering NCs is an effective way to overcome the issues of post treatment as it creates a polycrystalline film which can improve optoelectronic properties of NCs leading to a highly efficient PV device that overcomes surface defects that trap charge carriers, which will otherwise degrade performance, and is a low cost manufacturing route [195-198]. Furthermore, the sintered films lead to a red shifted photoresponse which can further enhance absorption in the visible and IR range [80, 194, 199].

Table 3-8: Comparison between chemical and thermal NC surface treatments

Treatment type	Treatment details	Aim of treatment	Nanocrystal	Results and comments	Reference
Chemical	Substrates dipped into a solution of EDT - 0.1M 1,2 ethanedithiol (EDT) in acetonitrile for several minutes, removed and dried.	Quantitative replacement of oleic acid (OA) with EDT, oleate removal and decrease inter-NC spacing.	PbSe	After OA removal NCs move closer together, the lattice becomes disordered and the films crack, but the NC size is unchanged by EDT treatment. OA estimated to account for 30-40% of the initial film volume. EDT replaces OA, shown by the presence of sulphur within the treated NC film. Absorbance and conductivity of NCs was enhanced. EDT treated films rapidly oxidised in air.	Luther et al [193]
Chemical	NC films were submerged in 0.1M EDT in acetonitrile for 30s at room temperature then dried in argon.	Remove or substitute oleate with shorter molecules.	PbSe	EDT quantitatively replaced OA, as shown by the presence of sulphur in the NC film. Treatment enhances electronic coupling to TiO_2 substrate and within the film. EDT passivated the NCs which slow hot electron relaxation. Hot-electron transfer was observed for all NC sizes.	Tisdale et al [40]
Chemical	NC films were submerged in 1 M hydrazine (HYD) in acetonitrile for 20 minutes at room temperature and then dried in argon.	Remove oleate without changing PbSe size or chemical properties.	PbSe	Treatment resulted in nearly complete removal of OA. After treatment NC spacing decreased and individual NCs remain distinct, but they cannot be spatially resolved. HYD treatment showed stronger electronic coupling to the TiO_2 substrate than EDT. HYD left dangling bonds at the nanocrystal surface which act as scattering sites and accelerate electronic cooling.	Tisdale et al [40]
Chemical	NC substrates were immersed in 3- 5 mL of 1M HYD in acetonitrile.	Remove oleate.	PbSe	OA removed and not substituted. HYD removed 2-7% of oleate and created an n-type conductive semiconductor, without a substantial increase in NC size. A small decrease in inter-NC spacing was observed. All chemical treatments ruined the superlattice order of the NC film. Substantial volume loss and microscopic cracks short circuited the cell. Further NC deposition did not eliminate these problems.	Law et al [194]
Chemical	NC substrates were immersed in either 3 – 5 mL of 1M HYD, 1M Methylamine (MET) or 1M pyridine (PYR) in ethanol. Alternative treatments included soaking NC films in pure 31M HYD and 12.4M PYR treatment.	Remove oleate.	PbSe (offered some analysis on CdSe, ZnSe)	Ethanol treatments preserved NC size, removed more OA, decreased inter-NC spacing, but had extensive film cracking and ruined the NC superlattice. HYD removed 85-90% of OA, MET removed 80-85% of OA, PYR removed 18-22% of OA. PYR was no more effective than washing NC films in pure ethanol. HYD/ethanol treatments showed greater OA removal than HYD/acetonitrile. Pure HYD removed 70% of OA and pure PYR removed 95% of OA, however both caused significant NC growth.	Law et al [194]

				HYD converted some of the PbSe film to Pb. OA remnants were detected in ZnSe and CdSe NCs.	
Chemical	NC films were dip coated in 0.01M EDT in acetonitrile. Process involved 25-40 dip coating cycles.	To replace electrically insulating oleate ligands.	PbSe, PbS and CdSe	Large crack free and conductive NC films produced. NCs were partially coated in the adsorbed EDT. CdSe devices had better air stability than PbSe devices. PbSe NC films had poor air stability. EDT treatment enhanced performance but supressed MEG.	Luther et al [83]
Chemical	Methylamine (MA)	Remove the oleate.	PbSe, PbS and CdSe	Similar results to EDT. MA treatment required twice as many dip coating cycles as EDT to obtain a similar optical density.	Luther et al [83]
Chemical	Octylamine exchanged NCs were spin coated on to ITO and then treated with a solution of benzenedithiol (BEN) in acetonitrile (3.5 mM) for 10 – 30 minutes. This was repeated twice.	Replace oleate ligands (2nm) with shorter octylamine ligands (1nm).	PbSe	Photoresponse was only obtained after the BEN treatment. Treated NC films were stable in air for 48 hours. Two layers of NCs were deposited separately to avoid pin holes and provide densely packed NC layer. NC films retained quantum size effects and inter-NC spacing was reduced. Electron mobility was high due to BEN conductor molecules providing a pathway for electron transfer.	Koleilat et al [82]
Chemical	OA capped NCs were subjected to ligand exchange with N-2, 4, 6-trimethylphenyl-N-methyldithiocarbamate (TPMC) for 4 hours in ambient conditions.	Displace OA with shorter ligands.	PbS	TPMC chosen to be strongly bound to the NCs, unlike other ligand replacements which are weakly bound and allow oxygen and water ingress. TPMC treated NC films obtained a blue shifted and broadened absorption peak. Inter-NC spacing was reduced from 2.5 nm to 1 nm after ligand exchange. Devices were stable in air for 0.5 hours.	Debnath et al [79]
Chemical	Ligand exchange with n-butylamine (BUT) and then washing in methanol to remove BUT.	Displace OA with shorter ligands.	PbS	Decreased inter-NC spacing achieved. Conductance after ligand exchange was low, but increased by two orders of magnitude when washed in methanol. Open circuit voltage increased without compromising efficiency. Lower density of surface traps at the interface due to ligand exchange.	Johnston et al [89] and Konstantatos et al [200]
Thermal	NC films heated on a hot plate in a nitrogen atmosphere between 200- 500°C for 1 hour.	Remove OA.	PbSe	NCs were thermally unstable at temperatures below that required for OA removal. NCs begin to grow at ~200°C and triple in diameter at 250°C. Ligand chains decreased as a function of temperature until all OA has been pyrolyzed at ~350°C, just leaving the PbSe film. NC absorption red shifted due to increased NC size after heat treatment. Higher temperatures are shown to remove all excitonic features due to sintering. Sintered NC films form highly conductive p-type bulk films and have a large hole density.	Law et al [194]

Thermal	NC films heated on a hot plate in a nitrogen atmosphere at 500°C for 1 hour.	Remove oleate.	ZnSe	NCs did not increase in size during high temperature treatments. Thermal treatment thought to depend on the NC type.	Law et al [194]
Thermal	NC film annealed in a nitrogen environment in a cryostat at 673 – 683°C for ~35 minutes.	Improve electrical transport and remove OA.	PbSe	Thickness of the capping layer decreases from ~2 nm to ~1 nm after annealing. NC lattice becomes more disordered, evident from TEM. Prior to annealing the current through the NC film is not measurable, after annealing the conductance increases by six orders of magnitude.	Mentzel et al [198]
Thermal	NC films were annealed in a vacuum inside a cryostat at 110°C. For temperatures >110°C samples were annealed in a 95% nitrogen and 5% hydrogen environment on a hotplate. Highest temperature was 430°C. Annealing time was 1 hour.	Investigation of transport properties and removal of organic capping agent – trioctyphosphine oxide (TOPO).	CdSe	Capping agent prevented large potential barrier for electrons moving between NCs. Temperature selected was below the melting point of NCs. Separation between the NCs decreased after annealing. Optical absorption of NC films red shifted and the peaks broaden. Dark current and photocurrent were significantly enhanced, due to the enhanced tunnelling caused by decreased inter-NC spacing and chemical changes in organic capping agent reducing the barrier height. NCs remained distinct and their size did not change after annealing. Clear excitonic features visible in spectra after annealing.	Drndic et al [199]
Thermal	Co deposited films are annealed for 1 hour at 400°C.	Removal of OA.	Co	Annealing altered the NC superlattice and reduced Inter-NC spacing from 4 nm to 2 nm, which caused film shrinkage. Annealing was found to reduce the surface oxide layer formed during handling. Numerous monolayers of NCs deposited to overcome volume loss.	Black et al [201]
Thermal	Devices were annealed in ambient air at 150°C for 20 mins.	Altering the microstructure of the device and increasing efficiency.	CdS nanorods	After annealed the interfacial pyridine was removed, which decreased inter-nanorod spacing and allowed electron transport. Annealed devices obtained a decrease in recombination pathways and higher energy conversion efficiency than devices that were not annealed.	Huang et al [202]
Thermal	Review of sintering techniques – typically 500 – 530°C.	Desorb or decompose organic ligands.	CdTe, CIGSe, CZTS	Sintering resulted in larger dense grains and higher device efficiencies compared to untreated NC films. Some ligand removal and desorption occurs, but decomposition can lead to carbon – rich layers. Sintering created a polycrystalline NC film.	Bucherl et al [196]
Chemical/ Thermal	NCs were spun cast on to ITO, heated at 150°C for 2 min, dipped in $CdCl_2$ and then sintered at 350°C for 30 seconds in air. Process repeated 4 times.	Reduce the cost of NC film fabrication and increasing device efficiency	CdSe/CdTe	Sintering created large structural defects in the NC films which short circuited the devices. Layer by layer fabrication overcame this problem. Large grain growth due to sintering found. Extended NIR response obtained with efficiencies up to 7.1%. Multi-layered NC films demonstrated.	MacDonald et al [197]

Chemical/ thermal	Sequential spin casting of PYR capped CdTe and CdSe onto ITO, briefly annealed at 200ºC for 15 minutes, washed with $CdCl_2$/methanol and annealed at 400ºC for 15 minutes in oxygen.	Reduce the cost, increase device efficiency and obtain air stable devices.	CdTe-NC and CdSe-nanorods	Bulk polycrystalline NC films created. Devices were stable in air. Sintering found to reduce high surface trap areas, increase carrier transport and enhance device performance. NC films were insulating in the dark but achieved two orders of magnitude enhancement in photoconductivity after sintering. Broad spectral response obtained after sintering.	Gur et al [203]
Chemical/ Thermal	CdTe nanorods are spin cast onto ITO, coated with $CdCl_2$ and sintered at 400ºC and then rinsed in hot water.	Facilitate grain growth and enhance optical absorption.	CdTe nanorods	Sintering with $CdCl_2$ resulted in grain growth, which removed energetic barriers at grain boundaries improving carrier transport. Optical absorption red shifted and amplified and an increase in trap distribution were observed. Devices were less reproducible due to the sintering effect on the ITO substrate. Over treating the NC film lead to shunting.	Olson et al [80]
Chemical/ thermal	Interlayer chemical and thermal treatments. Pyridine capped NCs spun cast onto ITO, dipped in $CdCl_2$ and annealed on a hot plate in air between 150 – 450ºC. Process repeated to increase film thickness.	Produce reproducible and defect free NC films.	CdTe	Defect free NC films obtained with large grain size (critical for higher performance). Higher temperatures obtained ~100 nm crystals. High temperatures suitable for glass and metal foils. PYR capped NCs that had no chemical treatment show loss of excess ligand and reduced crystal growth at 380ºC and residual OA and PYR found up to 400ºC, suggesting ligands remained bound to NCs above their BP which prevented large scale growth. $CdCl_2$ treated NCs removed all ligands.	Jasieniak et al [204]

Very few studies have looked into sintering and annealing NCs for PV, so further research in this area is needed. Due to this as well the simplicity, availability and scaling up cost of the technique, thermal treatment was selected to run initial trials of NC post deposition treatment. If more time was available a chemical treatment would have been undertaken and compared to the thermal treatment for the nanocrystals used in this work.

The annealing times and durations used are shown in Table 3-9. The annealing parameters for CdS and CdSe were advised from the University of York as a trialled and tested method. Similarly Cu_2O annealing parameters were taken as an average of those in Zhang et al [192]. The annealing parameters for $CuInS_2$ and CdTe were estimated from the boiling point of the capping agent used in the nanocrystals, since this seemed to be the general pattern seen in Table 3-9.

Table 3-9: Annealing durations and temperatures for nanocrystal deposition.

Nanocrystals	Solvent	Time (hours)	Temperature (°C)	Capping agent	Capping agent boiling point (°C)
CdS	Toluene	1-4	400	Oleic acid	360
CdSe	Toluene	1-4	400	Oleic acid	360
CdTe	Deionised water	1-4	300	Thio-carboxylic acid (HS-R-COOH)	280
$CuInS_2$	n-hexane	1-4	280	Dodecanethiol	270-280
Cu_2O	Ethanol	1.5	500	Sodium Borohydride	500

Since the nanocrystals require a higher temperature and longer residence times for annealing compared to the silver nanowires, they were deposited on the Schottky device first for the nanocrystal/nanowire (NC/NW) devices. Once the nanocrystals were annealed to the surface the nanowires were then drop cast and annealed, following the same procedure outlined in 3.4.3.

3.6 Electrical characterisation

Characterisation of the devices was carried out mainly by I-V and photoresponse measurements. From the I-V measurements the Schottky barrier height, ideality factor, series resistance and leakage resistance can be calculated, this is explained in detail in 4.4. For the nanocrystal and nanowire devices, SEM was used to analyse the device surface for continuity and structure of the layers deposited.

3.6.1 Current – voltage and photoresponse measurements

A probe station was constructed to carry out I-V and photoresponse measurements. Over the course of this project the equipment, instruments and software for data collection has gradually evolved and improved. The method referred to here is the most up to date version of the characterisation tools, previous versions are not discussed.

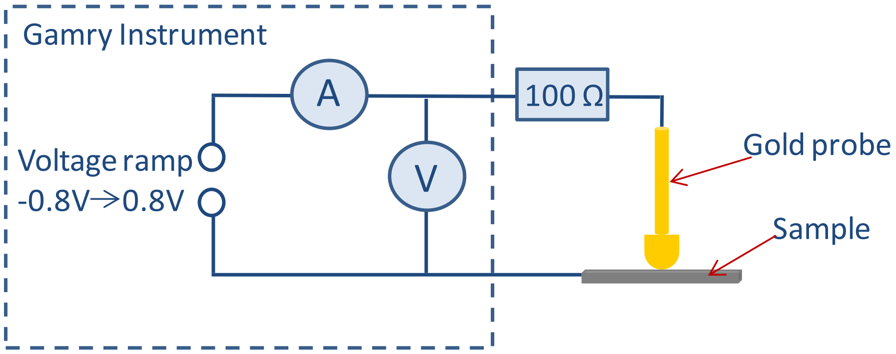

Figure 3-9: Schematic of I-V characterisation measurement.

The I-V probe station (shown in Figure 3-9) worked by gently bringing the probe on to the top surface of the device, whilst making an electrical connection at the back of the sample. To create this electrical contact the back of the substrate was filed to remove any existing oxide, silver paint was then applied to the back of the substrate to adhere it to the bottom conductive contact. The circuit incorporates a 100 Ω resistor to protect the sample from damage. The probe station is connected to a Gamry cyclic voltammetry instrument which provided a voltage ramp that was set at -0.8 V to 0.8 V and collected current data.

Before testing any device a control I-V curve was always taken to ensure that the equipment was connected properly. This control should produce a short circuit, which in terms of the I-V features resembles an Ohmic contact with a current of -8 mA at -0.8 V and 8 mA at 0.8V, due to the 100 Ω resistor in series. The I-V characteristics were measured throughout the creation of each device, i.e. before and after depositing noble metal films, nanowires and nanocrystals to ensure consistency and to detect short circuits or anomalies early.

To measure the photovoltage and photocurrent, the same probe station was used but it was connected to a multimeter instead of the I-V circuit, which via a link to a computer recorded the data, as shown in Figure 3-10. An arc lamp with a UV/visible 260 – 800 nm wavelength range illuminated the sample. The light tube was held stable by stationary fixtures. Due to the position of the probe the sample was illuminated at an angle. To prevent a reduced photoresponse the light pipe was positioned as close to the sample as possible. The wavelength was controlled by a C+ program which varied the speed, wavelength steps and direction of the scans (forward or reverse). All samples were initially scanned across the whole wavelength at 5 or 10 nms^{-1}. When samples had a good initial response more scans at 2 nms^{-1} were undertaken and these were repeated for reproducibility. A further extension to this was holding each 2nm step for 5 seconds to take a rolling average, which gave a higher resolution for the photocurrent and photovoltages measured.

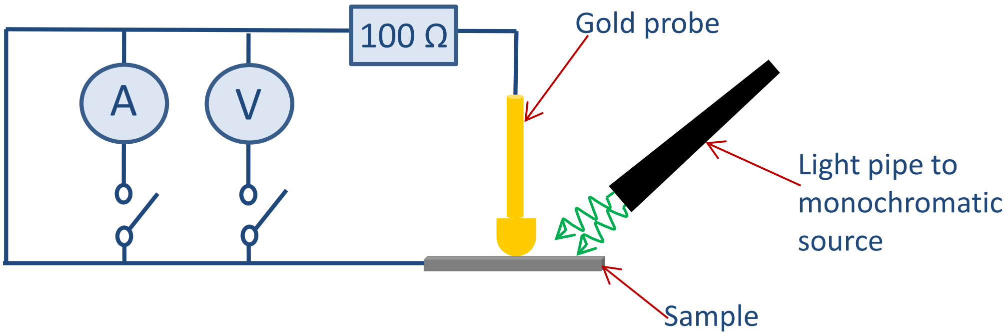

Figure 3-10: Schematic of illumination using 2-point probe set up

A transconductance amplifier was used when the photocurrent was very small to amplify the signal and to enable distinction of smaller features. Two amplifiers were used, a more sensitive amp 0.1µA > 2V and a less sensitive amp 1µA > 2V. With both transconductance amplifiers voltage was recorded and then converted to current, and if a background voltage was present this was subtracted. The background voltage was caused by resistance in the circuit and varies between samples. This background voltage was clearly displayed by the multimeter whilst the amplifier was connected and the sample was not being illuminated.

3.6.2 Resistance measurements

Resistance measurements were carried out to analyse the silver electrodeposited and gold sputtered samples only. The resistance measured indicated whether the layers were continuous over the TiO_2. In this technique two gold probes were brought gently into contact with the top surface of the sample. A voltage of 1.5mV (V_{rms}) and frequency of 18.64Hz was then applied to the circuit and a voltage reading was obtained from the lock in amplifier which was used to calculate the resistance across the surface. The idea being that if the noble metal layer is continuous then a circuit is made and the resistance will be low, however if the surface is not continuous an open circuit is created and the corresponding resistance will be much higher. Ti and TiO_2 control samples were also measured to verify this technique. The silver electrodeposited samples were cleaned around the edges (leaving exposed TiO_2) to ensure that a short circuit was not made between the silver and Ti substrate. Figure 3-11 and the following calculations indicate the assumptions made in the circuit and how resistance was calculated from this technique.

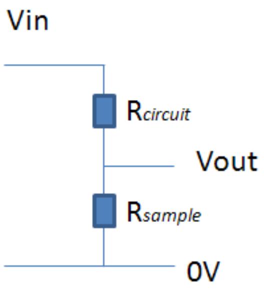

Figure 3-11: Schematic of the gold probe circuitry to aid equation explanation.

To calculate the resistance over the surface of the metal layer, Ohms law is used;

$$I = \frac{Vin}{R}$$

There are 2 resistors in series as shown in Figure 3-11 (Rc is the resistance in the circuit, which is a 10kΩ resistor and Rs is the resistance of the sample – what we are trying to calculate);

$$I = \frac{Vin}{Rc + Rs}$$

Substitute out current as all readings are in voltage;

$$Vout = \left(\frac{Rs}{Rc + Rs}\right) Vin$$

$$Vout = \left(\frac{V}{Rc + Rs}\right) Rs$$

If Rs<<Rc (which we expect it to be due to using a large resistor in the circuit);

$$Vout = \frac{Rs}{Rc}\ Vin$$

Adding the value of Rc = 10kΩ into the equation to get the final Resistance value gives,

$$Rs = \frac{Vout}{Vin} 10{,}000\ \Omega$$

3.6.3 Scanning electron microscopy (SEM)

A Leo 1530 (Carl Zeiss) field emission gun scanning electron microscope (FEGSEM), with EDX, was used for surface imaging of the silver nanowire devices mainly, in addition to the sputtered and nanocrystal samples, to indicate the continuity of surfaces.

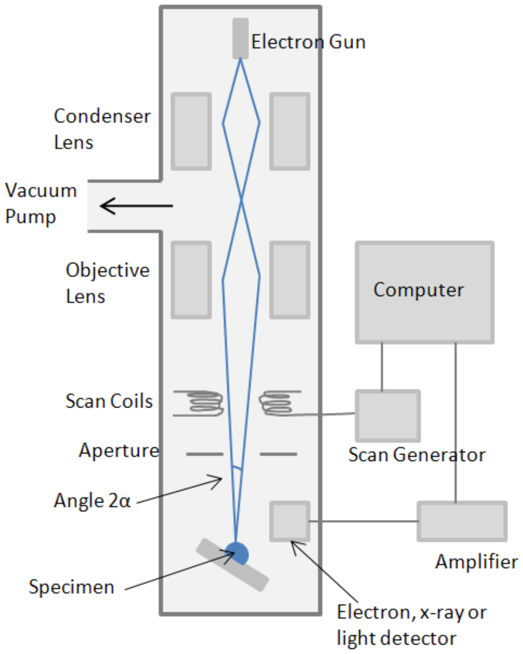

Figure 3-12: Schematic of a SEM adapted from [205].

The schematic shown in Figure 3-12 indicates how an image is gained from the SEM. In the SEM the condenser lenses are used to de-magnify the crossover from the gun; the objective lens focuses the electron beam onto the sample, giving between 2-10 nm for the final probe diameter; and the aperture limits the angular spread of the electrons. The focused beam is then scanned across the surface in 2-dimensional raster fashion with the beam passing through the optic axis at the objective lens whilst a detector monitors the secondary, backscatter electrons and/or x-rays as they are emitted at each point from the specimen surface. At the same time and using the same scan generator, a beam is scanned across the recording monitor to produce an image, for which the intensity of each point on the monitor is controlled by the amplified output of the detector, which is directly related to the emission intensity at the selected point on the surface. The magnification is the ratio of monitor raster size to the specimen raster size, which involves no lenses [205]. A FEG SEM differs slightly in that it can image nanostructures at high resolution due to the small source size from the gun [205].

Images are created by electron-specimen interactions, in the SEM secondary and backscattered electrons are the main interactions that allow the SEM to produce images of the surface. Secondary electrons are electrons that escape from the substrate with kinetic energies below 50 eV. They are generally from atoms at the surface of the sample where an electron has been ionised, gained a small amount of kinetic energy and have managed to escape. Alternatively secondary electrons can be primary electrons which have lost their energy through scattering and have just reached the surface. Secondary electrons are very abundant and are the main process for imaging in the SEM. Backscattered electrons are primary electrons that have undergone large deflections and exit the surface with very little change to their kinetic energy. Backscattered electrons are largely dependent on atomic number as they are caused due to Rutherford backscattering from the nucleus [205]. Emitted X-rays also results from specimen-electron interactions following ionisation which leads to secondary electron production, but have been used less in the characterisation of the samples.

All of the samples that were analysed by SEM were prepared by adhering the samples to metal stubs via adhesive graphite pads and then coating the uncovered pads and sides of the samples with carbon paint. A small drop of carbon paint was placed on the corner of the top surface to ensure that the conductive top layer was connected to the stub for imaging. Images were obtained by secondary electron imaging. Some EDX was carried out across representative samples to confirm the presence of certain materials and nanomaterials on the surface. Since EDX was undertaken for validation purposes only it will not be discussed any further.

This chapter has sequentially explained and examined the motivation and method used for the nanocrystal activated Schottky barrier device, considering each layer of the device individually. The next three chapters analyse the results for the devices.

Chapter 4

Schottky Barrier Devices Fabricated With Sputtered and Evaporated Metal Films

The first stage of the nanocrystal activated Schottky barrier solar cell requires fabrication and characterisation of an operational Schottky barrier solar cell, since the Schottky barrier will affect the performance of the final device. This chapter presents the results for three types of Schottky barrier cells - platinum, gold and silver coated TiO_2.

To obtain a reproducible Schottky barrier, transparent and conductive metal films of platinum, gold and silver were sputtered and evaporated on a TiO_2/Ti substrate, as outlined in 3.4.1. TiO_2 was formed on the Ti substrate by thermal oxidation or chemical anodisation, as described in 3.3. The effect of substrate preparation is discussed in this chapter, as well as the possible physical mechanisms at play across the Schottky barrier that may affect the current-voltage (I-V) response.

A probe station was constructed, as described in section 3.6, and the I-V characteristics and photoresponse of the Schottky barriers were measured. From the I-V measurements the Schottky barrier height (SBH), an important parameter to characterise the device, was calculated following the thermionic emission ideal diode relationship. This method is extended to account for non-ideal behaviour, for example additional resistance and alternative transport mechanisms that may be occurring in the devices. Device photoresponse, variation and yield are also presented. Comparisons are made between the three different metals used, showing that overall the Pt/TiO_2/Ti device outperformed the Au and Ag devices. A total of 90 devices were fabricated 37 of which were gold, 11 were silver and 42 were platinum coated TiO_2/Ti.

4.1 Yield of Schottky barrier devices

The yield of the devices, shown in Figure 4-1, indicates the reproducibility and success of the fabricated Au, Pt and Ag M-S devices. It is worth highlighting that the Au devices were the first devices to be fabricated and characterised, evident from the 70% that were inactive in producing a photoresponse. The main failure of the Au devices was due to a short circuit, indicated by the 65% of devices with linear I-V characteristics. This is not uncommon in the literature, where 1 in 5 devices created short circuits in a study by Liu et al [206].

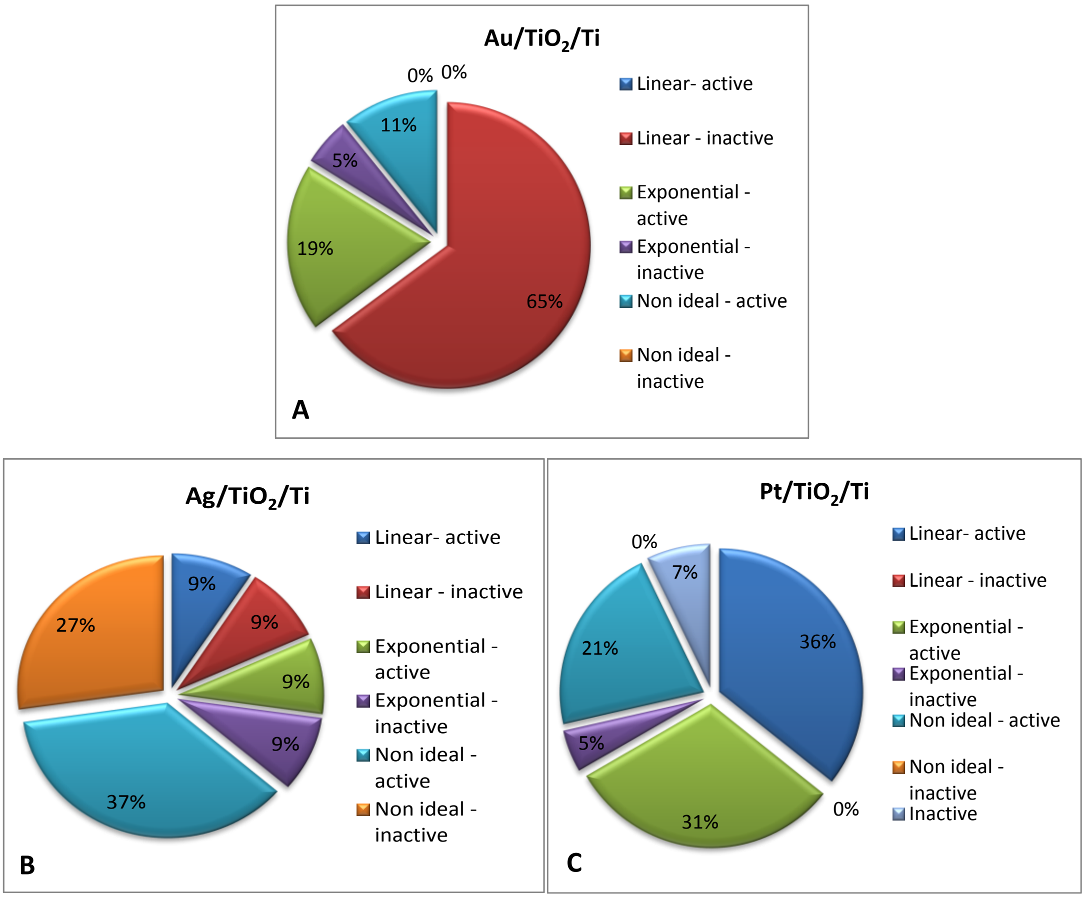

Figure 4-1: Yield of M-S devices, including sputtered gold [A], evaporated silver [B] and platinum [C] on TiO_2/Ti substrates. I-V features are described by 'linear', 'exponential' and 'non-ideal'. 'Active' and 'inactive' describe whether the device provided a photocurrent and photovoltage or not. The plots include all results from the very start of experimental work, a total number of 90 devices.

This high failure rate was due to the fact that most of the experimentation to optimise the device was carried out with the Au devices. For example, the TiO_2 layer was produced by three different techniques (anodisation, oxidation or a combination of the two), as described in 3.3. Before the optimum technique was found the TiO_2 produced may have been thin or porous which could have enabled a short circuit. In addition, different Ti substrates (Cp-Ti or recycled Ti with a higher impurity level) were used, as described in 3.2, and the electrical probe testing technique improved over time to prevent sample destruction. Hence there are a number of different pathways that could have led to a short circuit. Other physical mechanisms thought to lead to a short circuit, such as defect levels and charge hopping, are described later in 4.3. For the gold devices the 'non ideal' parameter describes devices that mainly have linear features up to 0.4 V then a small exponential section and have a sometimes symmetrical reverse bias response.

The Ag/TiO_2/Ti devices also show a poor performance with 45% of devices inactive in providing a photoresponse. This was possibly due to the thickness of silver evaporated on the substrate, since inactive devices generally had 10 nm of silver, whereas all other devices were sputtered with 20 nm. There were two exceptions to this that were inactive despite having a 20 nm layer; one of these samples was evaporated on two separate occasions to produce the 20 nm layer and the other was a recycled substrate. It was thought that the thinner evaporated layer would have been more susceptible to cracking during characterisation with a probe. Moreover cracks in the film could have been caused by the TiO_2 surface roughness, approximately 15 nm, due to microscopic peaks on the substrate surface. Unlike the gold and platinum devices, the ‘non-ideal - active’ parameter relates to devices that had a small and shallow exponential forward bias, but a large and sometimes linear reverse bias response and sometimes gave symmetrical features. This suggests that the silver devices were more Ohmic. Fuke et al [207] agree that an Ohmic contact is likely to be created with silver on TiO_2 due to its low work function of 4 eV. Moreover, this lower work function and hence barrier height could have been the cause for the lower yield of ‘exponential – active’ devices compared to the gold and platinum devices.

In contrast to the gold and silver devices the platinum devices had a higher yield with 31% of devices obtaining exponential I-V characteristics, indicating diode behaviour, and producing a photoresponse. Furthermore, only 5% of devices did not produce a photoresponse. The Pt device may have proved more successful due to its high work function, making a Schottky barrier relatively easier to achieve with TiO_2 under experimental conditions. It is also evident from Figure 4-1 that many more devices showed ‘linear-active’ I-V features compared to the other devices, suggesting additional series resistance. An additional field of ‘inactive’ was used to describe three of the devices which completely failed. This was because of contamination with a new steel mask that was trialled to attempt to make multiple devices out of a single substrate. The mask appeared to oxidise in the argon environment of the sputtering system, creating rust on the mask and a brown film on the titanium. Similar to the gold devices, the ‘non ideal – active’ field describes devices that had linear features and a small exponential section at higher voltages, with symmetrical reverse bias response, as shown later in Figure 4-3B. Appendix A gives a breakdown of all the Schottky barrier devices fabricated for more information.

4.2 Effect of TiO_2 preparation on the Schottky barrier

As indicated above, the preparation of Ti substrates and the creation of TiO_2 onto these substrates was found to be an important step in initial studies with Au sputtered devices. The purity of the Ti, the type of substrate preparation and the technique used for creating TiO_2 all impacted the yield of the Schottky devices.

4.2.1 Sourcing of Ti substrates

Initial devices were fabricated using 1 cm thick pieces of Ti that had been processed and recycled many times (recycled substrates will be noted as r-Ti). When sputtered with gold these devices consistently produced Ohmic I-V features and gave no photoresponses. To compare the effect of Ti purity, 99.97% commercially pure Ti foil was sourced (Cp-Ti).

The different Ti substrates were found to have a large effect on device performance. For r-Ti, the yield of devices was found to be 1 in 6, whereas Cp-Ti substrates yielded 100%. The yield here refers to devices giving a forward bias I-V and a photoresponse. The r-Ti consistently achieved short circuit currents or an Ohmic I-V and no photoresponse, which may be due to the higher contamination expected in the r-Ti, when compared to Cp-Ti. This suggests that the impurities in the Ti had a large effect on the TiO_2 layer produced. The physical mechanism associated with impurity doping is discussed later in 4.3.

4.2.2 Ti surface polishing

As described in 3.2, Ti substrates were manual polished and electropolished to recycle substrates, remove contaminants and provide a reproducibly low surface roughness. To ensure that both manual polishing (MP) and electropolishing (EP) were essential gold was sputtered on MP only TiO_2/Ti devices and devices which had been MP and EP.

For the r-Ti samples, the only device that produced a photoresponse had undergone MP and EP. The Cp-Ti MP-only samples were all successful, yielding a higher short circuit current (J_{SC}) and a smaller photoresponse. The samples that had a higher surface roughness (MP-only) did not produce any advantages in terms of I-V or photoresponse performance, which might be expected due to re-absorption of light and scattering due to more peaks on the surface. Further to this, new Cp-Ti substrates had a visibly smooth surface (i.e. mirror finish) and it was thought that manual polishing in these instances would increase the surface roughness, so these samples were EP-only which also had no negative effect on the results.

4.2.3 Anodisation versus oxidation

Chemical anodisation, using H_2SO_4, and thermal oxidation in air were both used to grow a TiO_2 layer from the Ti foil. Initial I-V characterisation once sputtered with Au suggested that oxidation provided a more reproducible and robust TiO_2 film, since during I-V testing all anodised TiO_2 films gave a short circuit or Ohmic response and failed to produce a photoresponse. Once the optimum temperature and time for Ti oxidation was found, 700^{o}C for 30 minutes, the reproducibility of Schottky I-V curves and photoresponses from devices was considerably higher. This is presented in the yield of devices for Au devices, above in Figure 4-1, where the 'linear' and 'inactive' devices are generally all those that were anodised, or oxidised at temperatures and durations before the optimum criteria were found. This interpretation is supported by the difference between the techniques. In 3.3.1 it was explained that anodising can etch into the surface due to the chlorides in the electrolyte, whereas thermal oxidation does not damage the surface, it is instead known to create well adhered oxide layers. The anodised TiO_2 layer could therefore have microscopic cracks which have led to short circuit currents.

4.3 I-V characteristics of Schottky barrier devices

As described in 3.6.1, I-V measurements were taken for all devices after noble metal layer deposition and prior to any further processing. Figure 4-2 shows a typical I-V curve from an optimal device. This type of curve has been referred to as 'ideal' since it aligns with the diode properties expected for an ideal Schottky barrier, rectifying forward bias and saturated reverse bias. Generally the devices did show good rectifying features, see yield of devices in Figure 4-1. However, there were many devices that diverted from the ideal diode characteristics, as shown in Figure 4-3. These 'non-ideal' features included having an unsaturated reverse bias current, Ohmic forward and reverse bias current, or a shallow exponential forward bias current gradient.

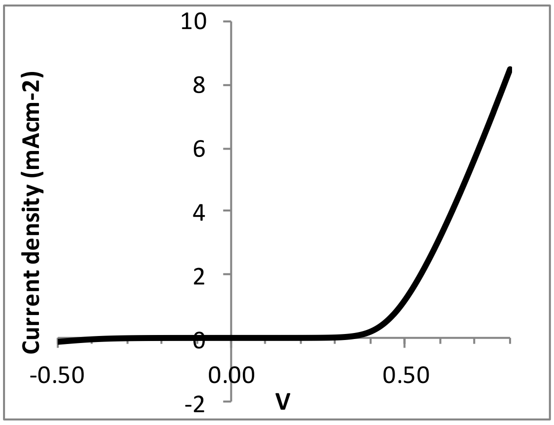

Figure 4-2: Ideal I-V characteristics, showing rectifying forward bias and saturated reverse bias (sample 505 – a Pt device).

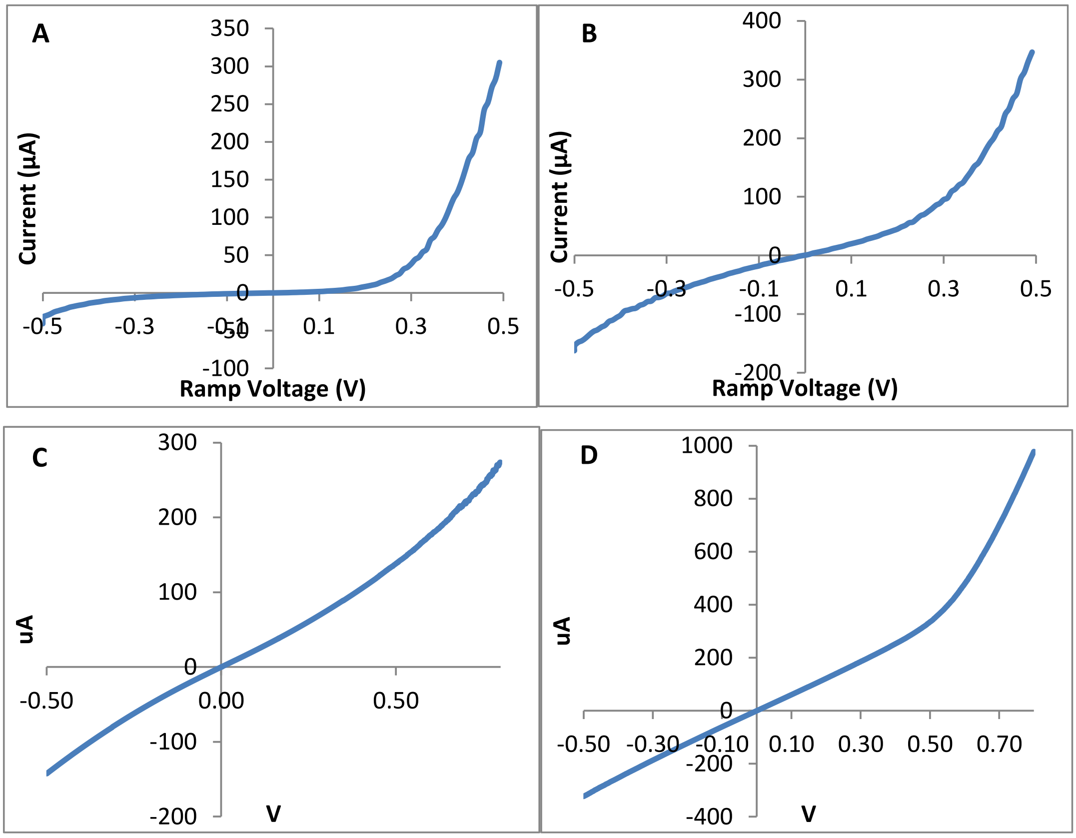

Figure 4-3: Typical 'non-ideal' I-V characteristics, showing general features across all non-ideal M-S barriers, including a small exponential reverse bias response (Sample 015) [A], a significant exponential reverse bias response (Sample 013) [B], linear sections (Sample 306) [C] and a mix of linear and exponential features with a forward and reverse bias (Sample 504) [D].

Non ideal features exist due to the devices diverting from thermionic emission theory. The I-V characteristics suggest that the applied voltage is being dropped across the diode as well as additional components, such as series and leakage resistors. Moreover different transport mechanisms, other than thermionic emission, such as tunnelling, hopping and recombination may be responsible for electron transport. The rest of this section will discuss mechanisms whereby a Schottky barrier may not follow thermionic emission theory.

4.3.1 M-I-S interface

A practical Schottky contact generally has a small ~10-20 Å insulating layer of oxide on the surface of the semiconductor, shown in Figure 4-4. This layer is so thin that electrons can tunnel through it quite easily and the voltage drop over this layer is negligible, hence the M-S interface relationship does not change. An insulating layer occurs when M-S interfaces have been prepared under poor vacuum conditions or the semiconductor surface is contaminated, therefore it is relevant to consider for the devices in this work [208].

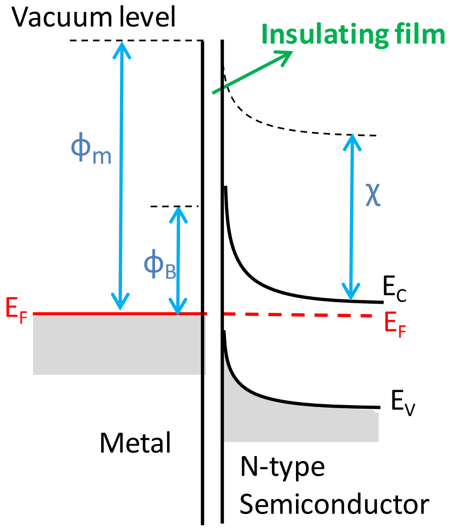

Figure 4-4: M-I-S structure, adapted from [208].

An interfacial layer can decouple the M-S interface so that the interface states at the semiconductor – oxide interface are not influenced by the metal. The metal can also chemically react with the interfacial oxide layer which can create a mixture of different phases at the interface. The interfacial layer can enable extra physical mechanisms in the device, such as additional tunnelling, through the interfacial layer to the metal, of electrons captured by interface states from the conduction band of the semiconductor, which reduces the current. This is not a significant mechanism and is only additional if electron tunnelling would not occur otherwise (tunnelling is discussed later in 4.3.8). Furthermore, an increase in minority carrier injection under forward bias occurs because hole current is unaffected by the presence of an interfacial layer and is controlled by diffusion into the neutral region of the semiconductor. A thicker interfacial layer results in more holes being able to tunnel from the metal to the semiconductor due to major band realignment [208].

The presence of this interfacial layer is a common cause of soft reverse bias I-V features, since the interfacial layer causes the Schottky barrier height (SBH) to decrease with increasing reverse bias and hence the reverse current does not saturate. Therefore a thicker insulating layer will provide a larger reverse current [208]. However, an interfacial oxide layer was shown to have only a small effect on a Cd/p-Si Schottky contact [209].

4.3.2 Leakage and series resistance

Leakage and series resistance can cause deviations to the ideal I-V characteristics expected from a Schottky barrier. Leakage or shunt resistance can be caused by short circuits in the device, created by interface states in addition to more obvious external short circuits. Liu et al [206] suggest that a linear type I-V response is caused mainly by a small leakage resistance leading to an increase in electron-hole recombination. They further stipulate that this mechanism can be caused by surface traps which act as recombination centres, which will be further discussed in 4.3.5.

Series resistance is inherent in the device due to the bulk resistance of TiO_2 and will vary throughout the device due to the different materials used. Further series resistance exists due to the resistance of the electrical wires, the titanium electrodes and high work function metal contacts. To limit the series resistance during characterisation low resistance contacts were used, including a gold probe, silver paint and low resistance wires. However, contact resistance is usually small and masked by the large resistance of the bulk semiconductor [210]. O'Hayre et al [211] show that for thick TiO_2 films, a large series resistance dominates charge transport characteristics. The physical mechanisms that contributed to the series resistance in their TiO_2 device included interparticle junctions and associated charge hopping transport, caused by shallow traps, deep traps and a high donor density.

Resistance varies across the whole device, as shown by the Pt/TiO_2/Ti resistance profile in Figure 4-5. Due to the potential barrier created between the TiO_2 and the high work function metal a large series resistance exists. TiO_2 bulk resistance contributes significantly whereas a low resistance is found between the Ti/TiO_2 interfaces, indicating an Ohmic contact [212]. It has been shown in many other studies that a Ti/TiO_2 interface forms an Ohmic contact [210, 213, 214]. In these studies the interfaces were fabricated using various techniques, some of which were similar to the techniques used in this work. The devices in this work are therefore expected to have a similar resistance profile.

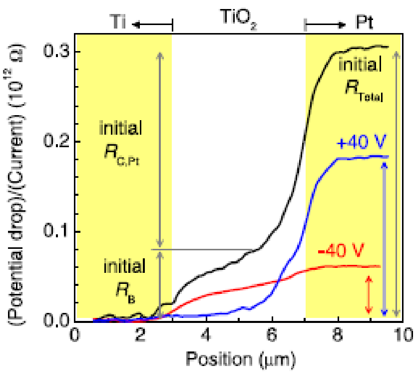

Figure 4-5: Resistance profile of a Pt/TiO_2 Schottky device, taken from [212]. The black line shows the initial resistance across the device, the red and blue lines show the resistance under electrical stress of -40 V and +40 V respectively.

The total series resistance in the device is the sum of all resistors in series and the resistance of the semiconductor in the direction of current flow, thus in a logarithmic I-V plot this is seen as curvature at high current [215, 216]. Aydin et al [209] experimentally demonstrated that series resistance between the Ohmic contact and the depletion region dominated at higher voltages, between 0.3-0.6 V, but had no affect at low voltages less than 0.3 V. The effect of series and leakage resistance on the I-V curves is demonstrated in Figure 4-17. A high leakage resistance leads to highly rectifying I-V curves whereas a decrease in leakage resistance leads to more linear I-V current gradients and a higher forward and reverse bias current. High series resistance leads to a reduction in forward bias current and a low series resistance has the opposite effect, greatly increasing the forward bias current.

4.3.3 Carrier recombination

Carrier recombination can contribute to the forward bias current. At zero bias electron-hole generation is balanced by recombination in the depletion region, which is in thermal equilibrium. With an applied forward bias electrons and holes are injected into the depletion region from the semiconductor and metal respectively. Excess electrons and holes will recombine to give a forward recombination current. Carrier recombination in the depletion region can occur via three mechanisms, as shown in Figure 4-6. The Shockley – Hall – Read (SHR) [217, 218] process explains recombination via recombination centres which arise because of defects or impurities in the semiconductor, which result in additional energy levels in the bandgap. The recombination rate is therefore proportional to the density of additional defect states in the bandgap. The SHR theory indicates that the most effective recombination centres are those that are central in the bandgap. Other mechanisms of recombination include radiative and Auger recombination. These processes are similar since they are both intrinsic, meaning that an electron directly recombines with a hole. The energy produced through recombination is emitted as a photon in the radiative process and is transferred to a different carrier in the Auger process [95].

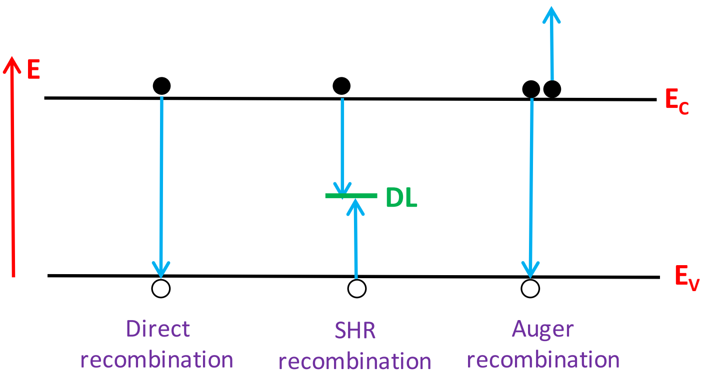

Figure 4-6: Band diagram for the three main recombination mechanisms – 'DL' is defect level and 'SHR' is Shockley-Hall-Read recombination.

Recombination is known to be a common cause of non-ideal behaviour in Schottky diodes especially for high barriers, low forward biases and low temperatures [208]. Konenkamp and Henninger [219] demonstrated recombination in TiO_2 diodes due to the capture of carriers in localised states. Where recombination is an active physical mechanism, the Ideality factor (n) varies between 1 and 2. Recombination is a dominant process in indirect semiconductors, but less dominant in direct semiconductors, unless very low carrier densities. Although there is some confusion over whether TiO_2 is a direct or indirect bandgap semiconductor [220, 221], it is generally considered and shown experimentally as having a direct bandgap [125, 222]. Thermal excitation of electrons from the Fermi level to the conduction band will occur, however thermally excited minority carriers will be very rare between the valence and conduction bands due to the large bandgap of TiO_2. Saehana et al [223] highlights that TiO_2 prevents recombination due to its wide bandgap and a large potential barrier when in contact with noble metal. Therefore recombination is probably not a major contributing transport mechanism in this device.

4.3.4 Carrier generation

Carrier generation, also generation current, is a common cause of unsaturated reverse current. This mechanism is the opposite of recombination in the space charge region and refers to electron-hole pair generation in the depletion region which contributes a current that is directly proportional to the width of the depletion region (W). W varies as $(V_i+V_R)^{1/2}$, thus current generation increases with the square root of the reverse bias. Carrier generation is important for large barrier heights, low dopant concentration, low temperature and carrier lifetime. However, carrier generation generally occurs in replacement of barrier lowering and tunnelling, due low donor density [95, 208].

4.3.5 Hopping transport

Charge hopping transport, also known as conduction hopping, was first established by Mott [224]. He described two hopping transport mechanisms, the first involved thermally activated hopping from one localized state to another and the second mechanism is hopping transport by excitation across an energy gap where the density of states is too low for tunnelling to occur. Localised states are due to dangling bonds or defects in the bulk semiconductor [225]. Hopping transport can occur across all temperature ranges but it is known for its low or room temperature effects. Hopping transport occurs due to impurities or localised states near the Fermi level and enables conduction through a M-S device which leads to Ohmic I-V characteristics and hence a low series resistance [224]. Figure 4-7 displays charge hopping transport across an M-S interface.

In addition to Mott, many studies have experimentally shown charge hopping transport to be significant in semiconductors at low temperatures [219, 225-227]. It is known that low temperature fabrication leads to a high degree of structural disorder, creating interface states which enable hopping transport [228]. Low temperature hopping transport can also be caused by impurity doping [224]. Since the Ti foil was 99.99% pure and oxidation was carried out in air, impurities are expected to exist in the devices, which will have led to interface states. Moreover TiO_2 is highly doped due to oxygen deficiencies at the surface and surface states exist due to the lack of periodic termination of surface atoms.

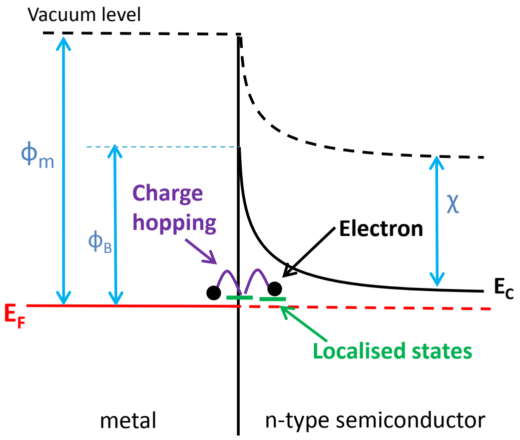

Figure 4-7: Band diagram showing charge hopping transport.

Hopping transport has been shown to be independent of semiconductor film thickness and can reduce tunnelling through the barrier [226, 227]. It is a feature of a bulk semiconductor due to the density of states in the bandgap, however, altering the surface for example by annealing has been shown to reduce the density of dangling bonds, hence decreasing the localised states and hopping transport [225]. Deposition and post deposition treatment of metals onto the semiconductor may therefore have an impact on hopping transport.

4.3.6 Fermi level pinning

The Schottky-Mott theory indicates that the SBH depends entirely on the work function of the metal. This is very rarely the case for practical Schottky devices. Fermi level pinning (FLP) describes the insensitivity of the SBH to metal work functions. FLP is a natural consequence of interfacial bonding and can be further enhanced by the presence of interface states. Bardeen [229] first described FLP by demonstrating that electronic states on the surfaces of semiconductors within the bandgap altered the resulting Schottky interface characteristics.

When the periodic structure of the crystal lattice of a semiconductor is terminated at the surface, electronic states are created which ‘pin’ the Fermi level position of the semiconductor, see Figure 4-8. These surface states are filled from the lowest energy states up to the Fermi level which creates a charge in the surface region. This charge will be negative if the Fermi level is above a central level defined by the surface states, called the charge neutrality level (CNL), since there will be an excess of electrons. Likewise if the Fermi level is lower than the CNL, the surface region will be positively charged since electrons are filled to a point short of the neutral level [96].

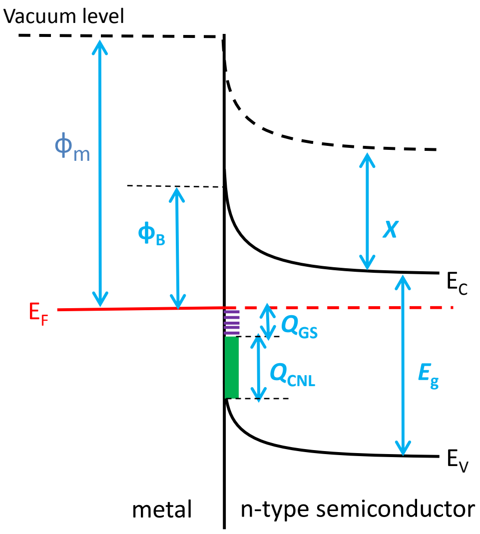

Figure 4-8: Fermi level pinning band diagram, adapted from [96]. Q_{CNL} is the charge neutrality level and Q_{GS} is the charge due to the gap states.

The occupancy of the interface states is determined by the Fermi level, which is constant throughout the barrier, hence states are filled up to the Fermi level and empty thereafter.

The barrier height is therefore pinned by these interface states. Hence the Fermi level in the semiconductor will align with the surface state occupation with or without the metal contact and therefore is not affected by the metal induced gap states (MIGS) [208]. FLP is not thought to be a dominant mechanism in TiO_2 since it belongs to a group of polar semiconductors, which are known to exhibit a low level of FLP [230, 231].

4.3.7 Heine tails

Volker Heine [232] demonstrated that the tail end of metal electron states extend into the semiconductor bandgap, as shown in Figure 4-9. Hence, states that are forbidden in the semiconductor are allowed at the surface due to altering the wavefunctions of electrons in the semiconductor, caused by metal deposition. The Heine theory suggests that the shape of the barrier can be significantly modified because of the high charge density in the metal wavefunction tail [233]. Figure 4-9 shows significant downward bending of the semiconductor conduction band at the M-S interface due to Heine tails.

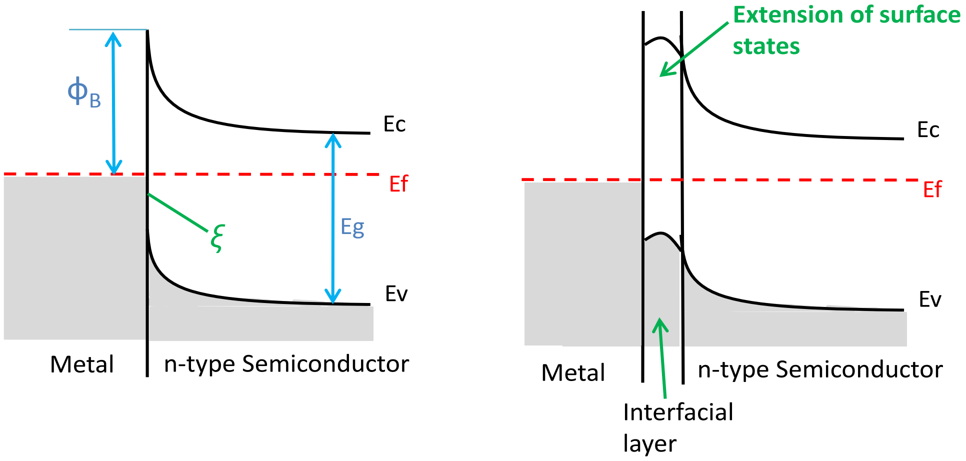

Figure 4-9: Effect of Heine tails on a Schottky barrier [left] and the effect on the potential barrier with the inclusion of an interfacial layer [right]. ξ represents a metal wave-function.

Heine tails behave in a similar manner to interface states in the semiconductor bandgap, both of which cause barrier lowering which can lead to more Ohmic I-V features due to a decreased potential barrier, hence also reducing series resistance. Hope and Bard [234] finds that Pt interdiffusion in TiO_2 was the predominant cause for Ohmic contacts across a Schottky barrier and this effect was exasperated by annealing the Pt/TiO_2. Low energy current pathways can short circuit the device. This could be the explanation why so many devices failed. However if Heine tails are not significant enough to short circuit the device, since they are normally angstroms in length, they could lead to a higher leakage current which causes a reduction in leakage resistance and a reduction in series resistance in the bulk TiO_2.

4.3.8 Tunnelling

Quantum mechanical tunnelling occurs when electrons with energies below the top of the barrier can penetrate through the barrier, instead of passing over the barrier. Tunnelling can occur via field emission (FE) or thermionic field emission (TFE). FE tunnelling occurs at low temperatures when electrons have energies close to the Fermi level in the semiconductor. TFE occurs at higher temperatures, exciting electrons to higher energies above the Fermi level where they see a thinner and lower barrier that they can tunnel through. If electrons are excited further they will pass over the barrier via the ideal thermionic emission mechanism [208].

Tunnelling can occur under forward and reverse biases, see schematic in Figure 4-10. Under forward bias tunnelling generally occurs in heavily doped semiconductors, such that the Fermi level sits above the conduction band. Due to high dopant concentrations the depletion region is very thin, allowing electrons to tunnel from the semiconductor to the metal. Tunnelling is a more significant mechanism under reverse bias and for materials with lower doping levels, causing 'soft' reverse bias I-V features. An applied reverse bias causes the potential barrier to become thin near the top of the barrier, as shown in Figure 4-10. This enables electrons near the top of the barrier to tunnel from the metal into the semiconductor via TFE. This phenomenon becomes very important at the edge of the metal contact where the electric field is enhanced by barrier curvature which reduces the barrier height in this region, therefore enabling a larger current to flow through the edge. Metals tend to be heavily doped which enables FE tunnelling even into semiconductors that may not be doped [95, 208].

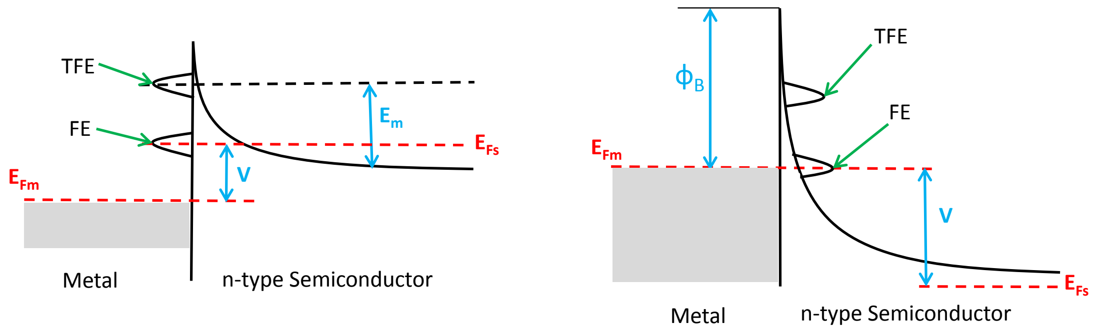

Figure 4-10: Tunnelling energy band diagram under forward bias for a heavily doped semiconductor [left] and reverse bias [right], adapted from [208]. *V* represents the difference in energy between the Fermi levels and E_m is electrons with energy above the bottom of the conduction band.

Tunnelling can affect the forward and reverse bias current at the same time or affect the reverse bias current independently leaving the forward current unaffected [235]. Konenkamp and Rieck [230] finds tunnelling a significant issue in their Pt/TiO_2 device, which was thought to arise because of defect states. It is known that defect states, as well as localised, MIGS and interface states, can aid tunnelling since a low current pathway and barrier lowering are established [219]. Moreover, it is thought that electrons from the conduction band can be captured by interface states and these can then tunnel directly from the interface states to the metal via an interfacial layer. This is only an additional mechanism if the electron would otherwise not be able to tunnel without the additional interface state present [208]. Interfacial oxide vacancies in TiO_2 have also been shown to contribute to electron tunnelling [236]. Furthermore, Padovani and Stratton [237] find that FE and TFE at forward and reverse biases were responsible for excess currents in highly doped semiconductors. The effects of tunnelling are non-linear, hence tunnelling leads to exponential features in an I-V curve for forward and reverse bias currents with increased series resistance due to the kinetics of the mechanism.

4.3.9 Barrier lowering

Image force barrier lowering (IFBL) refers to a lowering in the potential barrier that an electron has to jump over at the M-S interface, as depicted in Figure 4-11. This barrier lowering is caused by the field produced by an electron near the top of the barrier in the semiconductor conduction band. When an electron is at a certain distance from the metal surface it experiences an equal and opposite 'image' force attracting it towards the surface of the metal, giving the electron a negative potential energy. The resultant lowered barrier due to the image potential energy is displayed in Figure 4-11. Holes are also attracted to the metal by an image force, having the effect of an increasing upward bend of the valence band, hence reducing the energy gap of the semiconductor [208].

For IFBL the barrier height depends on the electric field in the depletion region and therefore the applied bias. Hence barrier lowering can occur at forward and reverse biases, but is more significant for reverse bias. Since the barrier height is a decreasing function of the electric field, an increasing reverse current will be observed with increasing reverse bias, due to an increase in the electric field and hence a decrease in barrier height. Generally IFBL alone can only account for a very small reverse bias current [208].

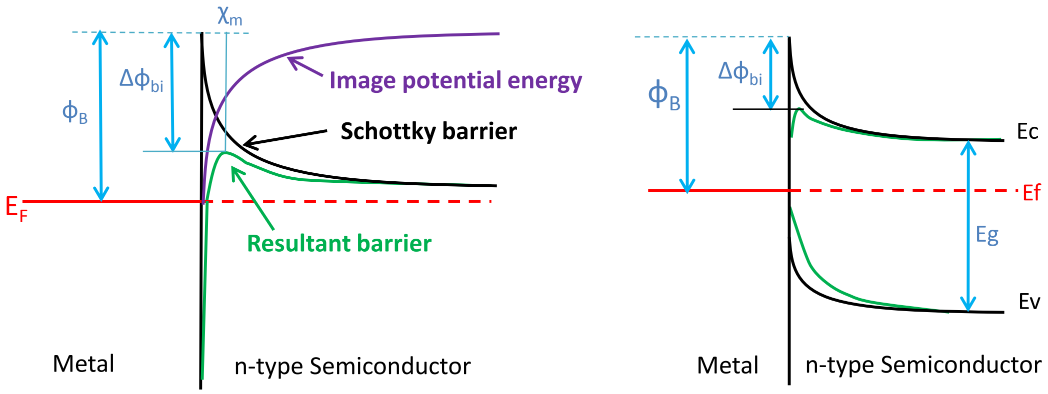

Figure 4-11: Image force barrier lowering mechanism [left] and barrier lowering at the conduction and valence bands [right]. X_m **is the maximum potential energy where the electric field in the image force is equal and opposite to the field in the depletion region.**

The IFBL mechanism can occur without the presence of an interfacial layer, however, an interfacial layer or Heine tails in clean contacts can contribute to barrier lowering. If an interfacial layer is present the potential barrier formed by this layer may also be decreased by IFBL [208]. Lee et al [236] showed that IFBL combined with Tunnelling occur in TiO_2. If IFBL was apparent in an M-S device similar effects on the I-V curve to tunnelling would be expected. However, a lower series resistance would be prevalent since electrons do not have to tunnel through the barrier, instead the barrier is lowered and the electrons can jump over at lower energies.

4.3.10 Summary of mechanisms in Schottky barrier devices

Since the mechanisms affecting Schottky devices are central to this research a summary of those mechanisms that are likely to affect the devices fabricated in this work are provided below.

- **Thermionic emission** - is the dominant mechanism for most Schottky devices created in this work. However this transport mechanism is affected by additional series and leakage resistance and is sometimes supported by a secondary transport mechanism.
- **Leakage and series resistance** – Leakage resistance is expected due to interface states in the device and series resistance is expected in bulk TiO_2 and at the interface with the noble metal, due to the potential barrier. In the devices leakage resistance dominates at low/sub-zero voltages (-0.8 - 0.1 V) and series resistance dominates at high voltages (<0.5 V).
- **Charge hopping transport** – Impurities, doping density of TiO_2, inherent localised states, and low temperature fabrication can all lead to interface or defect states that

will enable hopping transport. This is evident in non-ideal devices with linear I-V curves.

- **Tunnelling** – Localised, interface and defect states near the M-S interface will enable tunnelling at forward bias currents. Tunnelling leads to exponential I-V features and without SBH and resistance calculations it is difficult to distinguish between thermionic emission and tunnelling for forward bias currents. Soft reverse current features are often observed and larger reverse bias tunnelling currents have been observed in non-ideal devices. Image force barrier lowering is likely in the device, but will be largely overshadowed by tunnelling, since it has a similar effect on the I-V characteristics.
- **Heine tails** – The slight lowering in leakage resistance at forward and reverse biases is thought to be due to Heine tails or defect states which provide low energy current pathways through the device.
- **Recombination and Fermi level pinning** are not significant in the devices.

4.4 Schottky barrier height calculation and I-V simulation

The Schottky barrier height (SBH) is an important parameter in determining the rectifying behaviour of the Schottky barriers devices. The SBH can be calculated from either the capacitance–voltage (C-V), current-voltage (I-V), or photoresponse of the device [87, 208, 233, 238]. SBHs calculated from C-V profiles consistently give larger barrier height than those measured by I-V or photoresponse. This is partly due to C-V measurements giving the flat band barrier height rather than the zero bias barrier height. Using the ideality factor '*n*' in the I-V calculation can give a similar barrier height to those calculated by C-V [95]. To avoid over estimating the Schottky barrier height, I-V data was used to calculate the SBHs of the devices.

As discussed in 2.2.1 the Schottky barrier height, $\phi_{B,}$ can be expressed by Equation 4-1;

$$\phi_B = \phi_m - \chi_s$$

Equation 4-1

For an ideal Schottky barrier, ϕ_m is the work function of the metal and $\chi_s$is electron affinity of the semiconductor. The ideal SBH for the Pt/TiO$_2$/Ti, Au/TiO$_2$/Ti and Ag/TiO$_2$/Ti devices range between 0.84-2 eV, as presented in Table 4-1.

The ideal SBH is theoretical and so assumes that materials are defect free and the barrier created has no unwanted interfacial layer, hence the actual SBH will vary largely depending on the materials and techniques used [95, 96]. It is well known that the SBH is actually not dependant on the work function of the metal and this has been shown experimentally many times [233].

Table 4-1: Maximum ideal Schottky barrier height of M-S barriers based on the relationship; $\phi_B = \phi_m - \chi_s$. The work function of the metals are maximum values taken from Table 3-5.

Device	ϕ_m(eV)	χ_s(eV)	ϕ_B (eV)
Pt/TiO$_2$/Ti	5.93	3.9 [230, 239]	2.03
Au/TiO$_2$/Ti	5.47		1.57
Ag/TiO$_2$/Ti	4.74		0.84

Table 4-2 provides a summary of relevant Schottky barrier devices found in the literature. There is clearly a large deviation of Schottky barrier heights between studies, which can be linked to the processing techniques, materials and SBH measurement methods used. For Pt/TiO$_2$ and Au/TiO$_2$ Schottky devices the SBH found are lower than the theoretical case given in Table 4-1, as anticipated. However the Ag/TiO$_2$ studies show a higher barrier height. This may be due to the use of silver nanoparticles rather than a bulk film. It is possible for nanoparticles to have different properties to their bulk counterpart, due to quantum confinement. For metal nanoparticles this could lead to an increased work function which will give a higher Schottky barrier, this is discussed further in 5.2.5 [240]. This highlights the inaccuracy and limitations of the theoretical SBH relationship in Equation 4-1.

Table 4-2: Review of Schottky barrier heights of Pt, Au, and Ag, with TiO$_2$.

M-S	SBH	Method for TiO$_2$	Method for metal	Comments	Reference
Pt/TiO$_2$/Ti	1.2-1.3eV	Sol-gel.	Electron beam evaporation in a high vacuum.	The barrier height is experimentally shown to be the difference between the work function of the TiO$_2$ and the Pt.	Dittrich et al [228]
Pt/TiO$_2$/Au	1eV	Reactive DC magnetron sputtering deposited 150nm TiO$_2$.	Electron beam evaporation.	The interfacial roughness is linked to the electron flow.	Park et al [98]
Pt/TiO$_2$/SnO$_2$	1.7eV	Colloidal suspension of nanoporous TiO$_2$ films deposited via sol-gel. Spin	Vacuum evaporation of 3nm Pt dots.	-	Konenkamp [239]

		coated substrate, annealed and sintered.			
Pt/TiO$_2$/SnO$_2$	0.3 - 1.7 eV	Colloidal suspension of nanoporous TiO$_2$. 1µm TiO$_2$ films spin coated deposition and annealed at 450^{o}C.	150 Å Pt deposited by vacuum evaporation.	-	Konenkamp and Rieck [230]
Ag/TiO$_2$/Ti	1.5eV	Thermal oxidation for 30 minutes at 700°C in air.	Ag nanoparticles deposited by printing a suspension of silver particles and sintering at 350°C in air.	-	Hossein-Babaei and Rahbarpour [140]
Ag/TiO$_2$/Ti	1.8eV	As above.	Not given	-	Hossein-Babaei and Rahbarpour[141]
Ag/TiO$_2$/Ti	1 eV	As above.	Thermal evaporation and annealed at 200^{o}C in air.	Annealing the device altered the morphology of the silver layer.	Hossein-Babaei et al [122]
Ag/TiO$_2$/Ti	1.8 eV	Titanium foil was oxidised in air at 750^{o}C for 10 – 90 min, obtaining 100 – 250 nm TiO$_2$ thickness.	Partial sintering of silver particles at 400^{o}C to form a porous silver aggregate. Average silver particle size was 70 nm.	-	Hossein-Babaei et al[241]
Au/TiO$_2$/Ti	0.9eV - 1.1eV	Thermal oxidation at 500°C for 8 hours.	Galvanostatic electrodeposition.	-	Tang et al [120]
Au/TiO$_2$/Ti	0.9 eV	Thermal oxidation at 500^{0}C.	Electrodeposition.	Improvements can be made by reduced metal thickness and an engineered larger surface area for larger photon absorption.	McFarland and Tang [34]
Au/TiO$_2$/Ti	1.5eV	Thermal oxidation of Ti for 30 minutes at 970K in air to produce a 1µm TiO$_2$. And electron beam evaporation.	Not given.	Annealing the samples at the end of the fabrication process stabilises the device parameters.	Hossein-Babaei and Rahbarpour [141]

The next section outlines and analyses a more accurate approach, following thermionic emission theory, for calculating the SBH from the experimental I-V data for the Schottky barrier devices fabricated in this work. This approach was then extended to give a more comprehensive analysis of all I-V characteristics including series and leakage resistance variables. This involved using an ideal diode equivalent method (IDM) and an extended diode equivalent method (EDM).

4.4.1 Ideal diode equivalent circuit method (IDM)

The Schottky barrier height of an ideal Schottky barrier, that follows thermionic emission, can be calculated from the forward bias current by the following equations [208]. Since thermionic emission is generally the dominant mechanism in the devices fabricated in this work, this method was thought to be suitable to use for SBH calculation.

The current as a function of applied forward bias when $V > 3kT/q$, which at room temperature (292 K) is 0.08 V, gives;

$$I = I_s \, exp\left(\frac{qV}{nkT}\right)$$

Equation 4-2

Where I_s is the saturation current, q is elementary charge 1.6 x 10^{-19} C, k is Boltzmann's constant 1.38 x 10^{-23} m^{2}kgs^{-2}K^{-1}, T is temperature (K) and n is the ideality factor which is 1 for an ideal barrier and higher for non-ideal barriers. Since thermionic emission is governed by an exponential term, a route to calculating the SBH is to take a log-linear plot. The saturation current, I_s, and ideality factor, n, can then be obtained from extrapolation of the linear section of a log I-V plot since $y = mx + c$, see Equation 4-3.

$$\begin{tikzcd}
 & lnI = lnI_s + \left(\frac{qV}{nkT}\right) \arrow[dl] \arrow[d] \\
c = lnI_s \arrow[d] & mx = \frac{qV}{nkT} \arrow[d] \\
I_s = e^c & n = \frac{q}{mkT}
\end{tikzcd}$$

Equation 4-3

The Schottky barrier height ϕ_B can then be found from Equation 4-4 [208].

$$I_s = AA^{*}T^2 \, exp\left(\frac{-q\phi_B}{kT}\right)$$

Equation 4-4

Rearranging for $lnI_s$to find ϕ_B gives;

$$\phi_B = \frac{kT\ (lnAA^{*}T^2 - ln\, I_s)}{q}$$

Equation 4-5

A is the area of the devices 0.125 cm^2, A^* is the effective Richardson constant 1200 A/k^{2}cm^2 [120, 122, 140, 141], and *T* is the temperature in the laboratory 292 K.

In instances where the I-V curves of devices appear to follow thermionic emission, the barrier height was extracted using Equation 4-5. An example of this is given in Figure 4-12. Only positive current values at voltages above 0.1 V were considered from the log data and fitted to a linear line, since the ideal diode equation is only valid for voltages above 0.08 V, as shown above, hence below 0.1 V a large gradient is observed as displayed in Figure 4-13 D. This large gradient at low voltages is dominated by leakage resistance, as discussed previously in 4.3.

For Figure 4-12 a linear fit of the logged current is shown to be close, with the R^2 value of 0.999 giving an indication of a very good fit. The saturation current (I_S) can be found by extracting the intercept of -5.702 and using Equation 4-3 to get 3.34 x 10^{-9} A. Calculation of the Schottky barrier using Equation 4-5 then gives 0.9 eV.

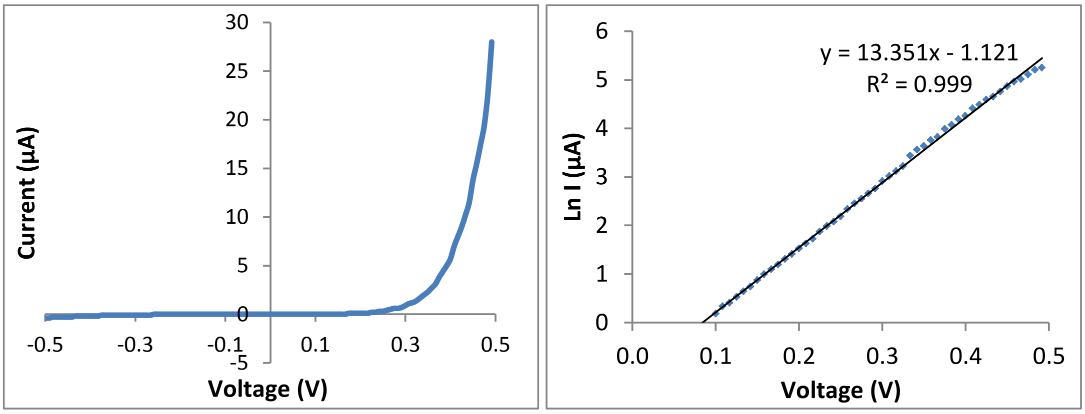

Figure 4-12: Typical Schottky barrier from sample 202 (Pt/TiO$_2$) showing an exponential I-V [Left], Ln (I) against V between 0.1 – 0.5 V [Right].

In some instances exponential I-V curves with ideal diode features, see Figure 4-13 A and C, obtained a poor fit from the IDM. This is due to the effects of additional resistance and transport mechanisms in the devices, outlined in Section 4.3, which are not considered in the IDM.

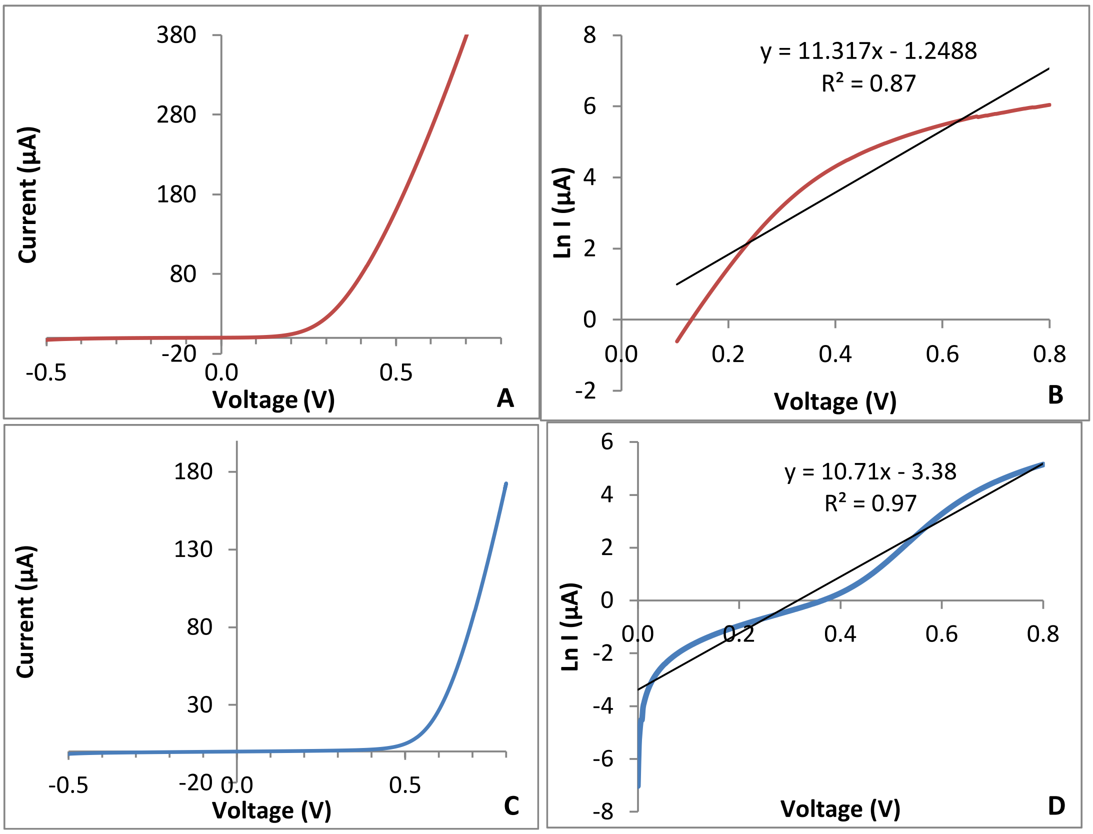

Figure 4-13: I-V curves [A and C] and IDM fit [B and D] for Pt/TiO_2 Schottky barriers, showing a poor fit. The effect of leakage resistance at voltages between 0 – 0.1 V is displayed in [D]. [A-B] Sample 501 and [C-D] Sample 302.

The largest deviations in fit in both Schottky barriers in Figure 4-13B and D is at 0.4 V and again at 0.8 V. Sample 501, in Figure 4-13 A and B, is affected by series resistance due to the dip at 0.8 V and a reduced leakage resistance due to the dip at 0.1 – 0.2 V. Furthermore, an additional transport mechanism is responsible for the fit deviation and increase in Ln (I) around 0.4 V. Tunnelling under forward bias is likely to be the cause, as this would also lead to an increase in series resistance and reduced leakage resistance whilst maintaining exponential I-V features, as discussed in 4.3.5. Similarly, Sample 302 in Figure 4-13 C and D has a better fit of 0.97 but the deviation around 0.4 V affects the anticipated linear relationship. Again, defect assisted tunnelling may be responsible for this aberration, however it is clear that the magnitude of this mechanism is reduced in comparison to sample 501. In both cases it is clear that tunnelling is secondary to thermionic emission, since they both have a rectifying characteristics.

The SBH for 'non-ideal' devices were also found using IDM. Figure 4-14 shows an example of this across Pt and Au Schottky devices. It is evident from Figure 4-14 A and B that the more linear I-V curve obtains the poorest fit, as expected since a linear fit is being applied to a logarithmic result. On the other hand, Figure 4-14 D and F show a good fit despite an obvious reduction in leakage resistance in the corresponding I-V curves in C and E. The best fit is observed for sample O13, Figure 4-14 C and D, since the leakage resistance has only had a small impact on the I-V curve in C, compared to sample 504, Figure 4-14 E and F, where the leakage resistance has decreased significantly to the extent that the I-V curve in E is linear between 0 – 0.5 V.

In addition to thermionic emission, charge hopping transport and tunnelling are thought to be dominating in these devices. Samples 017 and 504 have quite linear features which are conducive to charge hopping transport via defect states from impurities in the TiO_2. Tunnelling is thought to be dominating in sample 013 due to the exponential features in both the forward and reverse bias currents and reduced leakage resistance.

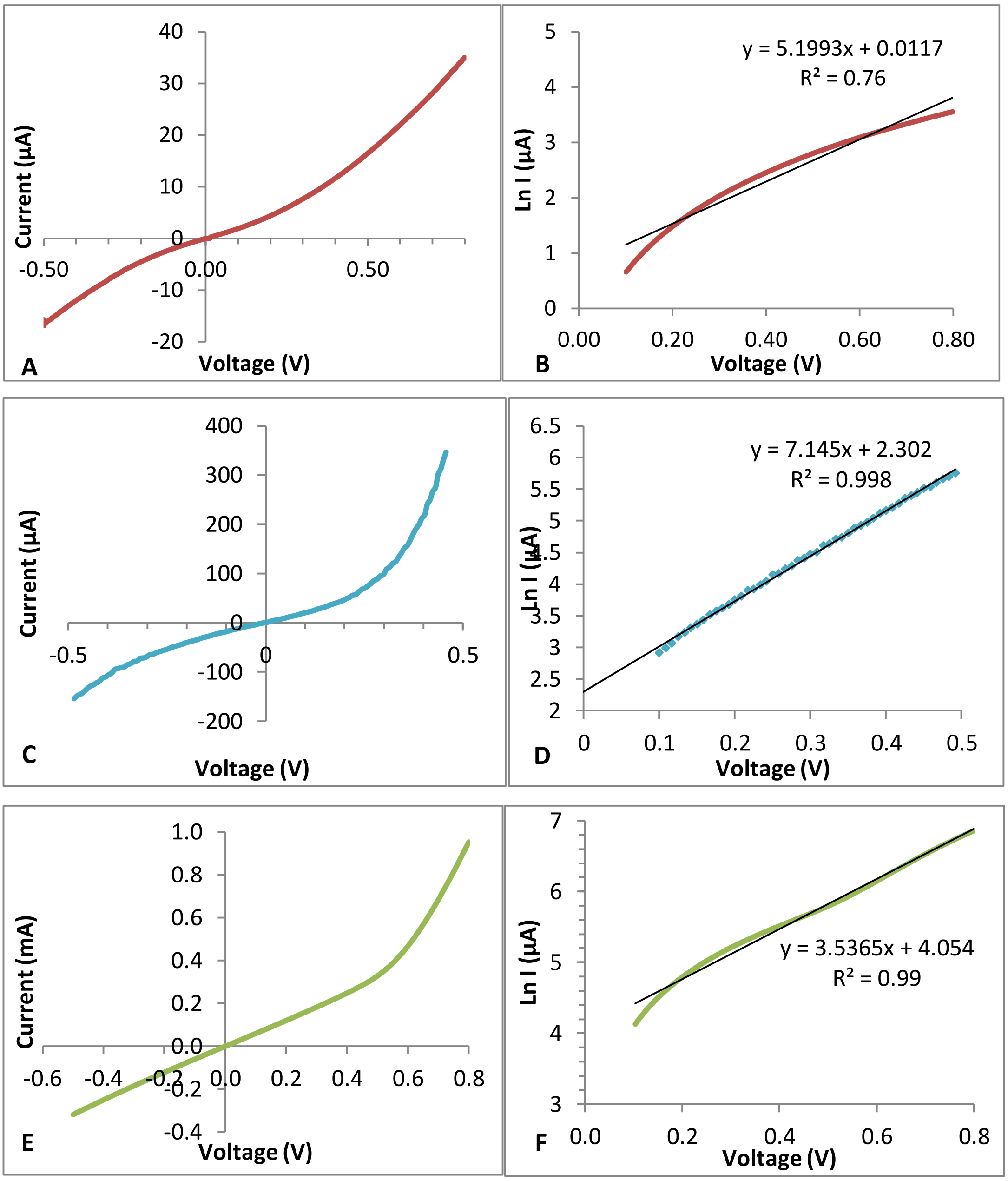

Figure 4-14: Examples of non-ideal I-V curves with respective linear fit curves for extraction of Is and n. [A-B] Sample 017 Pt/TiO$_2$, [C-D] Sample 013 Au/TiO$_2$ and [E-F] Sample 504 Pt/TiO$_2$.

Table 4-3 presents the Schottky barrier heights calculated by IDM for all of the Schottky barrier devices fabricated in this work. All I-V curves, including exponential and non-ideal, were subjected to the same calculations given Equation 4-5, as explained above. The resultant range of Schottky barrier heights calculated are compared against the theoretical and experimental Schottky barrier heights from the literature.

The SBHs calculated in this work has a large range of 0.26 eV, 0.16 eV and 0.3 eV for the Pt/TiO$_2$, Au/TiO$_2$ and Ag/TiO$_2$ devices respectively. The non-ideal devices could account for this large range, since the calculation of ϕ_B as described above should only be used to model thermionic emission, i.e. 'ideal' Schottky barriers. The non-ideal I-V curves generally obtained a lower SBH, which could be due to the additional transport mechanisms and resistance or because of the unsuitability and hence inaccuracy of the IDM for these devices. Regardless of the cause, it is expected that a less ideal device will have a lower SBH and be a poorer Schottky device. This is further confirmed by the general correlation found between a low SBH and a low photovoltage, shown in Figure 4-23. The large range of SBHs in other studies demonstrates the variation due to different techniques, materials and calculations being used, which is discussed in detail below.

Table 4-3: Calculated Schottky barrier heights and average standard deviation for all Schottky barrier devices fabricated in this work, using IDM which follows thermionic emission theory. These are compared to the Schottky model values and Schottky barrier heights from the literature.

Schottky barrier	Calculated ϕ_B range (eV)	Schottky model values ϕ_B (eV) from Table 4-1	Literature ϕ_B (eV) from Table 4-2
Pt/TiO_2/Ti	0.69 – 0.95 (+/- 0.09)	2.03	1– 1.7
Au/TiO_2/Ti	0.67 – 0.83 (+/-0.05)	1.57	0.9-1.5
Ag/TiO_2/Ti	0.61 – 0.91 (+/- 0.10)	0.84	1.5-1.7

For the Pt and Au Schottky devices it is evident from Table 4-3 that the SBHs calculated in this work are lower than the theoretical values and are only comparable to the lower limits of the SBHs measured in other studies. The higher SBH for the Pt/TiO_2 Schottky devices reported in other studies can be explained by the use of porous TiO_2 structures and calculation of the SBH under high temperature conditions [228, 239]. The porous nature of TiO_2 and the use of gaseous phases can significantly modify the SBH [228]. Moreover high temperature measurements reduce the effect of tunnelling and hence barrier lowering, which leads to higher SBHs. At room temperature the same device was found to have a significantly lower SBH of 0.3 eV [230]. This suggests that the Pt devices in this work are actually performing very well in comparison, since the SBHs are calculated from room temperature I-V measurements and are significantly higher than 0.3 eV. Furthermore, the SBHs in the other studies were calculated using a diffusion transport model [230, 239] and photoresponse data [228], which differ from the method used in this work and will have also impacted the SBHs achieved.

The highest Au/TiO_2 SBHs in Table 4-3 have been calculated following thermionic emission theory, hence only physical differences can account for the differences in SBH to this work. Similar to the Pt/TiO_2 devices, the SBH of 1.5 eV in the literature was calculated at high temperature, 573 K, and hence a higher effective SBH is anticipated [141]. The second highest SBH of 1.1 eV is from an electrodeposited gold layer. Electrodeposition of metal layers has been found to increase the SBH due to chemical composition changes and interfacial chemical reactions. There are two main theories that explain the higher SBH obtained from electrodeposition. The first suggests formation of an interfacial dipole layer in the Au because of the presence of oxygen in the electrolyte and the second suggests that the Au has stabilised the oxygen vacancies at the interface between Au and the TiO_2. Both mechanisms are thought to lead to increased SBHs [120].

Unlike the Au and Pt Schottky devices, the SBHs calculated for the Ag devices in this work are significantly lower than the SBHs found in other studies. The higher SBHs in the literature can be accounted for by annealing silver on to the TiO_2/Ti substrates after deposition [122, 140]. It is indicated that oxygen species were chemisorbed on to the silver electrodes during annealing, which remained stable at room temperature. Oxygen adsorption can increase the work function of silver between 1.2 - 5.8 eV which will therefore obtain a higher SBH [140, 141]. This difference does not appear to depend on the type of silver used as it has been demonstrated for both silver nanoparticles and thermally evaporated silver [122, 140].

Table 4-3 also presents the average standard deviation of SBHs across all devices. As already discussed in 4.1 the Pt device sample size was the largest, followed by Au and Ag devices, hence the standard deviation for Pt devices will be more accurate. Despite this it is evident that the variation about the mean is quite similar across all devices, regardless of sample size. This suggests that the number of samples does not have a large impact on variation and that there is approximately a 10% variation in device fabrication.

In addition to finding the saturation current and the SBH, the IDM was used to calculate the ideality factor (n), as described in Equation 4-3. Series and leakage resistance were also estimated from the I-V curves. Table 4-4 displays the IDM parameters found for a representative selection of exponential I-V and photoactive devices (E-A) and non-exponential I-V and photoactive devices (N-A) for each of the metals. These devices are compared later to the extended diode method (EDM) in 4.4.2. The series resistance was found by the gradient of the current between 0.6 – 0.7 V (or 0.4 – 0.5 V where 0.5V was the highest voltage reached, since earlier samples were only tested up to 0.5 V). The leakage resistance was found by the gradient of the current at 0.1 V. For the E-A device a larger leakage resistance is generally found, compared to the N-A devices which had a smaller leakage resistance. The series resistance appears to be very variable across all devices whether E-A or N-A. For the E-A devices a small series resistance is representative of the inherent resistance in the bulk TiO_2 and at the potential barrier with the noble metal. A higher series resistance in E-A devices however could indicate tunnelling. Where series resistance is small for N-A devices, hopping transport via localised states could be the dominant mechanism as this leads to more conductive behaviour through the device. N-A devices with large series resistance are likely to be due to a combination of mechanisms including tunnelling and image force barrier lowering.

Table 4-4: IDM calculated I-V parameters for series resistance (R_S), leakage resistance (R_L), saturation current (I_S), R-squared indicator of fit (R^2) and Schottky barrier height (SBH) for a representative sample of exponential – photoactive (E-A) and non-ideal – photoactive (N-A) Schottky devices.

Sample	Metal	I-V type	IDM					
			R_S	R_L	I_S	*n*	R^2	SBH
505	Pt	E-A	250	5.13E+06	1.09E-08	2.38	0.932	0.87
501			1040	2.03E+05	1.09E-06	4.41	0.897	0.76
104			3690	8.62E+05	3.36E-08	3.87	0.981	0.86
302			1615	5.71E+05	3.31E-08	3.45	0.979	0.86
502			470	4.12E+07	9.76E-10	2.14	0.973	0.94
503			285	1.00E+06	2.33E-08	2.73	0.968	0.85
504		N-A	251	1.53E+03	5.81E-08	11.24	0.991	0.66
306 Re			2174	3.98E+03	2.59E-05	12.56	0.964	0.68
811			719	4.50E+03	2.13E-05	9.63	0.981	0.68
AG5	Ag	E-A	25	6.45E+03	2.35E-08	5.54	0.917	0.85
AG4			90	1.83E+04	3.00E-09	4.02	0.966	0.90
AG3x1		N-A	6410	8.06E+06	2.04E-07	2.76	0.765	0.91
102			54	2.28E+03	3.03E-05	7.12	0.995	0.67
O26	Au	E-A	2570	5.00E+05	7.09E-08	2.87	0.997	0.83
O21			1032	5.26E+04	5.18E-07	3.71	0.991	0.78
O25		N-A	1273	4.05E+03	1.64E-05	7.11	0.985	0.70
O13			467	4.63E+03	1.07E-05	5.56	0.999	0.70

It was mentioned earlier in Equation 4-2 that the ideality factor (*n*) is 1 for ideal Schottky barriers and higher for those that deviate from the ideal diode behaviour. Equation 4-3 demonstrates how the ideality was calculated for the IDM. It is clear from Table 4-4 that none of the devices have a value of n=1, with the lowest n value being 2.14. Other studies show that in laboratory air conditions (i.e. the presence of water vapour) n has been estimated to be ~2.5 for Pt on nano-porous TiO_2 [230, 242]. The characterisation of devices in this work was carried out in ambient laboratory conditions so would also be in humid air. As discussed in 4.3.5 an ambient processing environment can lead to structural disorder and interface states, causing a departure from ideal diode behaviour due to FLP, tunnelling, barrier lowering or hopping transport. Tang et al [120] further confirms this by obtaining n = 2.1 for an electrodeposited Au/TiO_2 and n = 1.8 for vacuum electron beam evaporation Au/TiO_2. In this work, the ideality factor correlates well with the type of Schottky barrier created, since non-ideal diodes mostly have much higher ideality factors, further indicating the departure from thermionic emission to other transport mechanisms.

The closeness of fit (R^2) of the IDM to the I-V data shown in Table 4-4 ranges from 0.765 – 0.999. Figure 4-15 shows the correlation between the SBH found and the R^2 value for the devices. The lower R^2 values were generally devices which had non – ideal I-V curves, as shown in Figure 4-14. The fact that this method does not lead to consistently high fit values further indicates the need to modify the method to improve the accuracy of the SBH calculated from the devices.

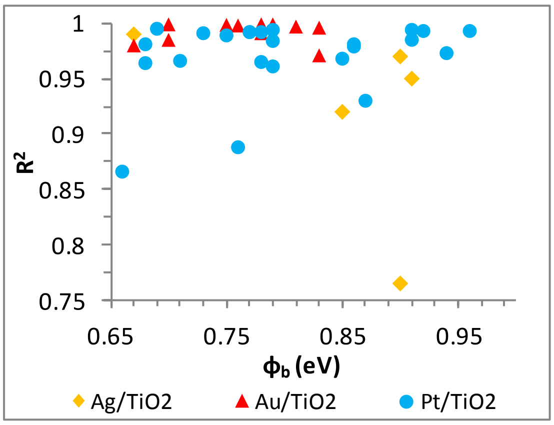

Figure 4-15: Schottky barrier height (ϕ_B) calculated from the IDM against the goodness of fit (R^2) for Ag, Au and Pt Schottky devices.

The IDM has many limitations, including the assumption that current is limited only by thermionic emission over the barrier, therefore neglecting diffusion, recombination, hopping transport or tunnelling effects. Series and leakage resistance are also not included in the SBH calculation and are only estimated broadly from the I-V curves. There is evidently large series and leakage resistances, see Table 4-4, therefore integrating both resistance values in a SBH calculation could lead to more accurate resultant SBHs. The range of R^2 values found for the IDM indicates that there is room for improvement. The next section outlines the extended diode equivalent circuit model (EDM), which builds on the IDM by including additional resistances.

4.4.2 Extended diode equivalent circuit method (EDM)

The extended diode equivalent circuit method (EDM) aims to improve the IDM and provide more accurate SBHs and other related diode variables. Figure 4-16 shows the equivalent circuit assumed in the IDM compared to that in the EDM. Using the more comprehensive equivalent circuit, two EDMs were created to fit the I-V curves to more accurately measure the saturation current (I_S), series resistance (R_S), leakage resistance (R_L) and ideality factor (n). The first method was based on an iterative error reduction approach (EDM1) and the second method was based on a gradient descent approach (EDM2), both using the least squares fit method to minimise errors. The codes for both of the EDMs were provided by Dr Rolf Crook, University of Leeds, and can be found in Appendix B and C.

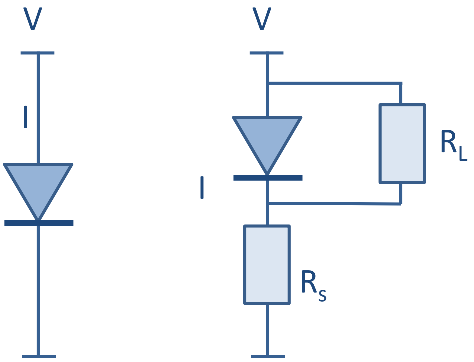

Figure 4-16: Equivalent circuit diagrams for SBH calculation. [Left] IDM assumes a single diode in series, [Right] EDM assumes a diode in series with a resistor and in parallel with a leakage resistor.

Before the EDMs were run the code was analysed to see how the different parameters were affecting the I-V curves. The code allowed different parts of the equivalent circuit in Figure 4-16 to be modelled separately and in combination. This allowed a more thorough analysis of the effect that series and leakage resistance has on a Schottky barrier. Figure 4-17 displays a selection of plots to show how the four main parameters, I_S, R_S, R_L and n effect the I-V characteristics. It is clear that the saturation current affects the shape of the exponential curve, with a smaller saturation current delaying an exponential current response to higher voltages and a larger saturation current producing an exponential curve at low voltages. When n becomes larger, the current reduces in a similar way to I_S. When the leakage resistance is much larger than the series resistance, expected for a rectifying device, the leakage resistance sets the gradient at low voltages and the series resistance at high voltages. If the leakage resistance is small the devices become Ohmic. This is expected since a reduced leakage resistance suggests a short circuit in the barrier.

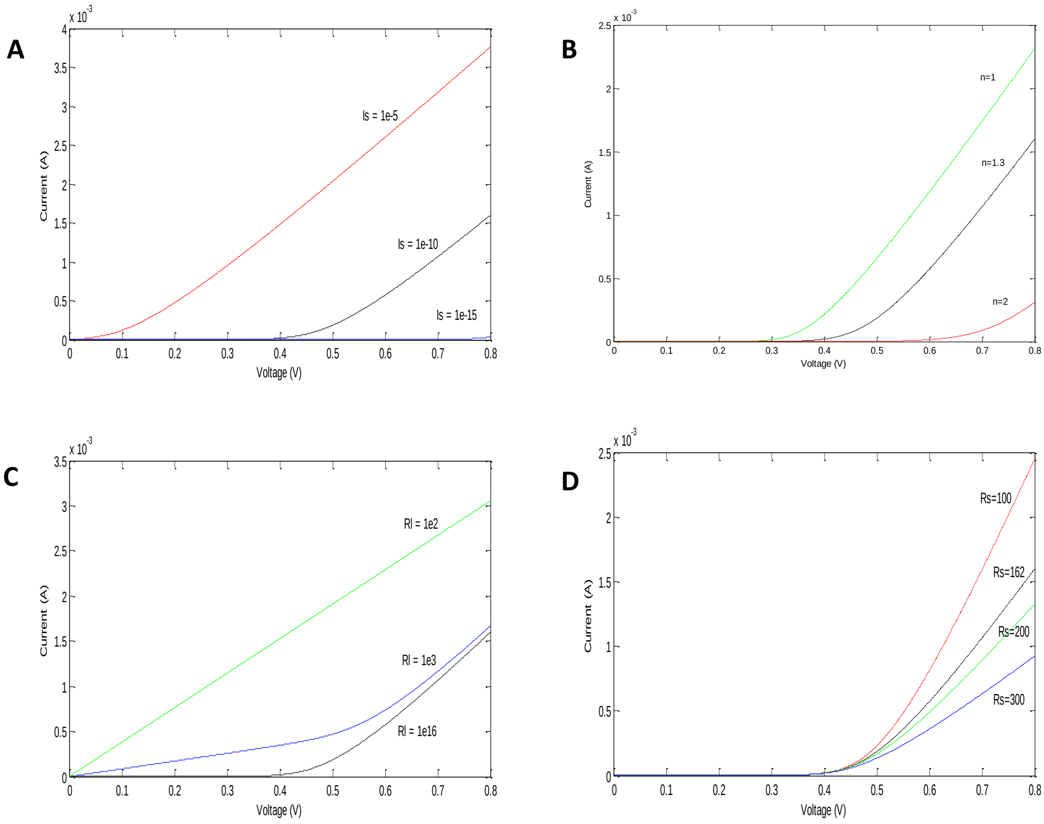

Figure 4-17: Matlab simulation of parameters which affect the I-V characteristics of a Schottky barrier, based on the extended equivalent circuit, showing variations in [A] I_S [B] n [C] R_L [D] R_S.

4.4.2.1 EDM 1: Iterative error reduction

EDM 1 uses an iterative error reduction process with least squares fit to fit the I-V data. This technique was selected since the least squares fit method can find an approximate solution for a function in which there are more equations than unknowns, which was the case here. In this method iterative refinement was used to find the best fit, which was found when the iterations minimized the sum of squared residuals. A residual here is the difference between the actual current and the fitted current. Figure 4-19 displays a flow chart to demonstrate the code for EDM 1.

This approach suffered from false minima effects. This was evident during Matlab operation where sometimes the variables did not converge, or very unrealistic values for the four key parameters were obtained. Moreover, this code could produce quite different values for the same fit, especially for leakage resistance. Results from the IDM were used as initial starting parameters for both EDM 1 and 2, to ensure an informed estimate, to avoid the local minima affect and to ensure consistency between methods. Due to the problems with false minima, a second method, EDM 2, was created to provide more accuracy.

4.4.2.2 EDM 2: Gradient descent

EDM 2 was an alternative least squares method, using a gradient descent approach, to produce a more accurate fit to the I-V data and to overcome the problems of false minima. EDM 2 used the gradient descent algorithm to find the nearest local minimum, using the relationship in Equation 4-6, where a is the current parameter from the IDM initially, γ is the coefficient which dictates the step size and ∇ is the gradient operator.

$$b = a - \gamma \nabla F\ (a)$$

Equation 4-6

Figure 4-18 presents a schematic for the process in the gradient descent approach. This method involved estimating an initial solution of a function and taking the gradient of the function at that point. Since the function is decreasing, the solution moved in the negative direction (represented by the negative in Equation 4-6) by a predefined step and the gradient at this point is then found. This process is then repeated until convergence, minimising the gradient along the function. A zero gradient corresponds to the local minimum.

The step size is an important parameter which gives this method more stability than the least squares method in EDM 1. It represents the amount that the next point will jump to, to find a solution of the function. Therefore if the step size is too large divergence occurs and the problem of reaching a false local minimum is increased, shown by the green objects in Figure 4-18. However if the step size is too small then convergence takes too long, illustrated by the small red arrows representing step size around the starting red dot in Figure 4-18. Whilst operating this method we used an adaptive approach where the step size was continuously changed to account for divergence and convergence.

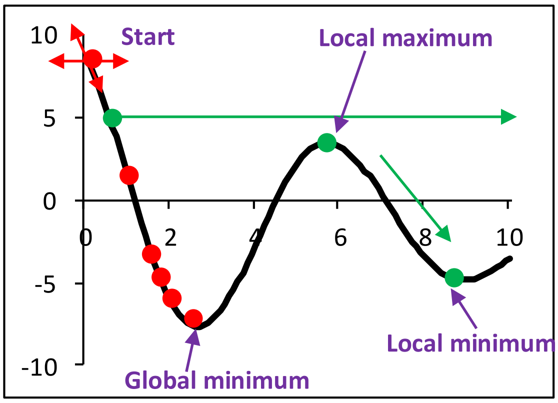

Figure 4-18: Schematic of the gradient descent method, showing the resultant global minimum and false local minimum and maximum. The arrows represent the step size γ and gradient operator ∇. The green arrows and dots illustrate the need to control the step size.

To further enhance the probability of reaching the global minimum rather than false minimum, initial values were taken from the IDM. Figure 4-20 presents a flow chart for the EDM 2 code.

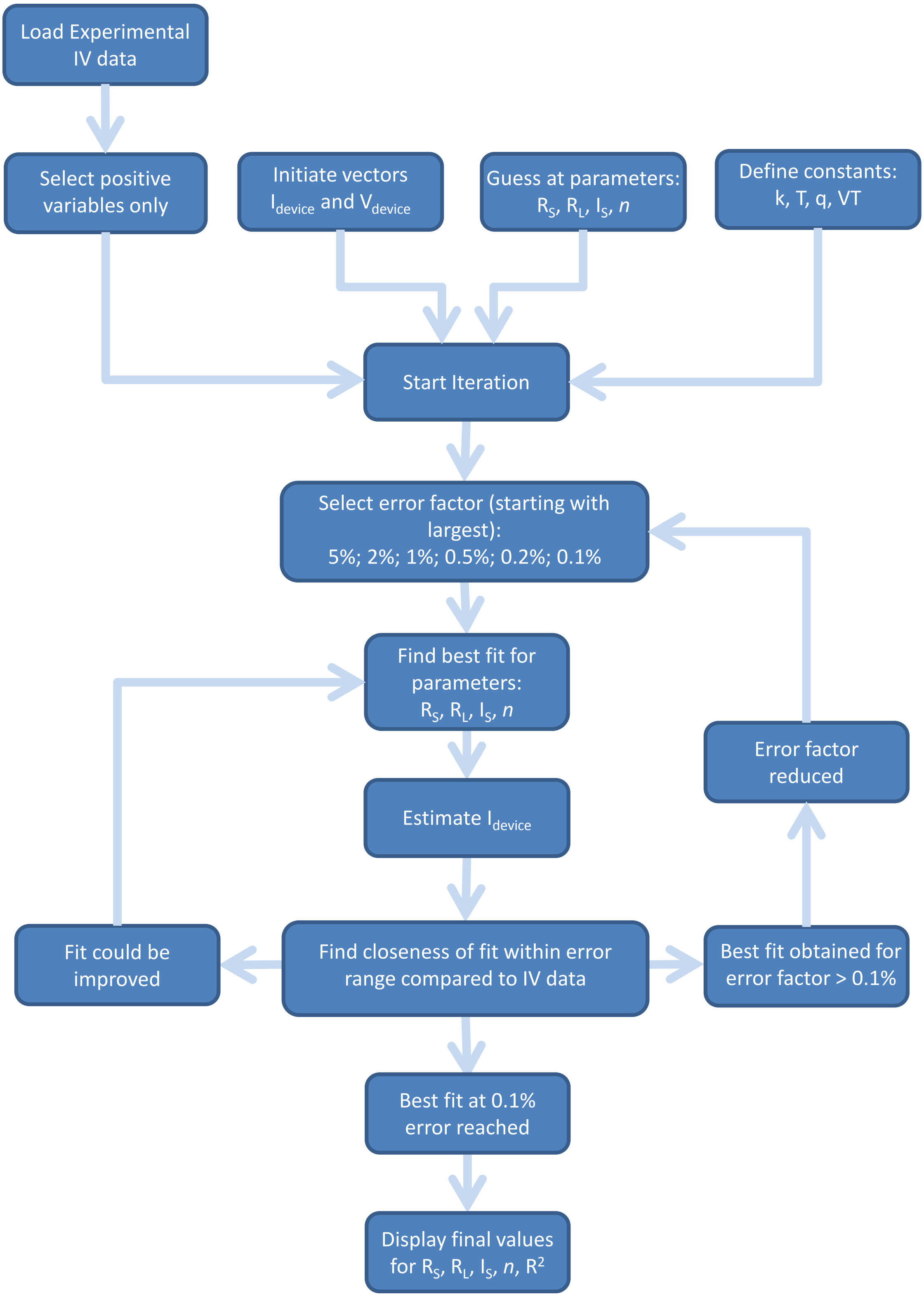

Figure 4-19: Flow chart of EDM 1 code for Matlab I-V curve fitting.

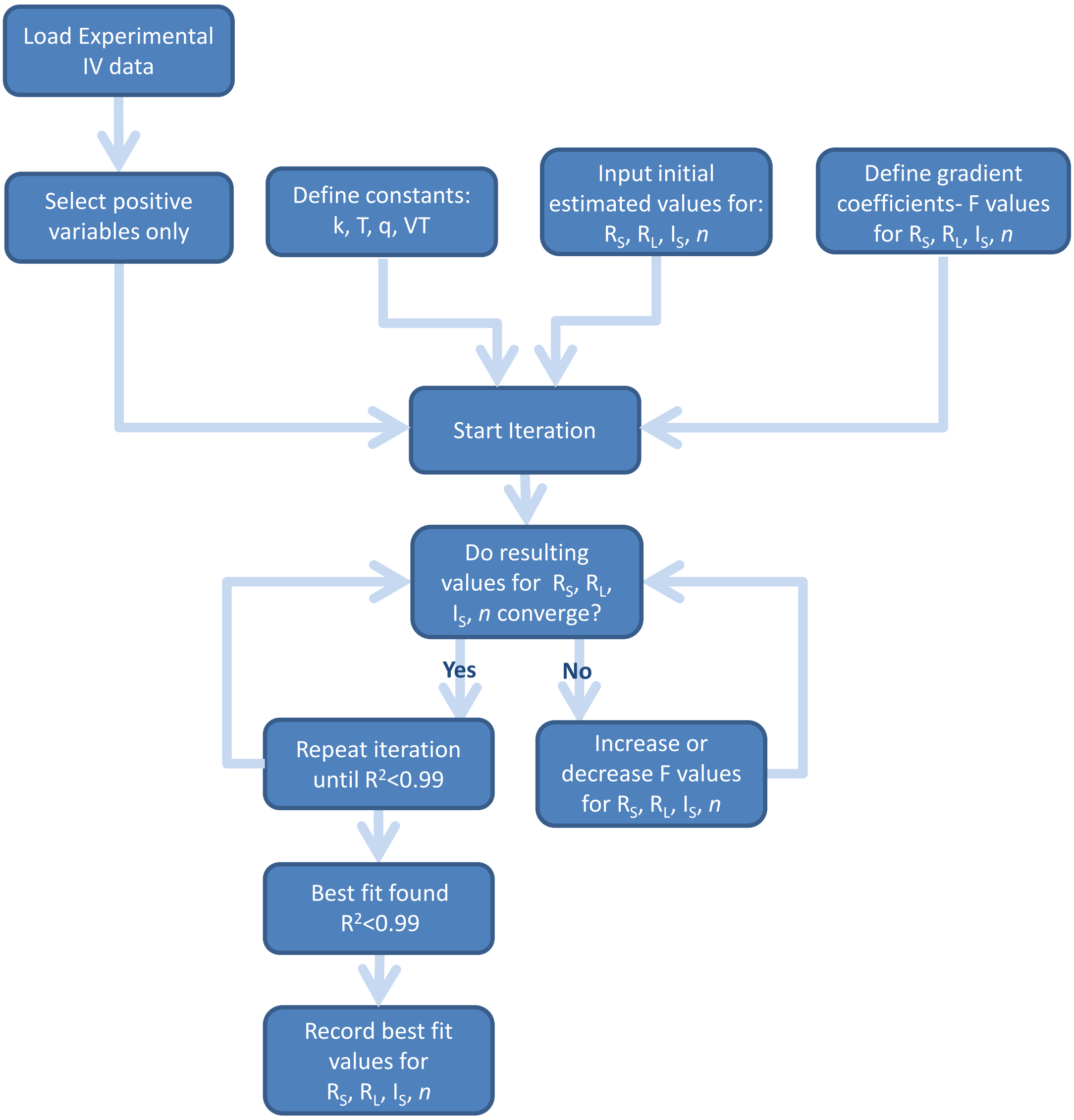

Figure 4-20: Flow chart of EDM 2 code for Matlab I-V curve fitting.

Table 4-5 shows the resultant device parameters for R_S, R_L, I_S, and n found from the two EDMs and respective indicator of fit to the experimental data (R^2). The SBH included in the table was calculated in all instances from the I_S, using Equation 4-5. Despite the local minima problem in EDM 1 where quite different parameters could be achieved for the same device, for example in sample 505 leakage resistance of $2e^5$ and $2e^{17}$ can be obtained, a good fit was obtained. Obviously this is more of a concern for large differences in saturation current or ideality factor. Comparing both EDM methods it is clear that the leakage resistances found in EDM 1 fluctuate more and reach higher values.

Table 4-6: R_S, R_L, I_S, n, R^2 and SBH for EDM 1 and 2 for I-V characterisation.

Sample	Metal	I-V type*	EDM 1						EDM 2					
			R_S	R_L	I_S	n	R^2	SBH	R_S	R_L	I_S	n	R^2	SBH
505	Pt	E-A	147	7.15E+05	1.05E-09	1.54	0.99998	0.93	145	5.66E+06	1.52E-09	1.59	0.99998	0.92
501			830	3.25E+05	3.91E-08	1.73	0.99968	0.84	845	2.02E+05	2.49E-08	1.63	0.99969	0.85
104			2074	5.42E+05	1.25E-10	1.86	0.99996	0.99	2111	4.70E+05	7.78E-11	1.79	0.99993	1.00
302			675	5.66E+17	1.19E-10	1.86	0.99999	0.99	624	6.22E+05	2.37E-10	1.98	0.99994	0.97
502			304	4.16E+17	8.30E-11	1.53	0.99999	1.00	275	8.80E+07	5.48E-10	1.78	0.99986	0.95
503			202	2.69E+17	1.04E-09	1.68	0.99999	0.93	195	5.53E+07	1.87E-09	1.77	0.99995	0.92
504		N-A	77	1.56E+03	3.04E-07	3.27	0.99954	0.79	141	1.41E+03	1.81E-08	2.15	0.99995	0.86
306R			1518	2.82E+03	8.99E-07	2.87	0.99976	0.76	1556	2.59E+03	2.99E-07	2.30	0.99975	0.79
811			365	3.81E+03	1.06E-06	3.94	0.99939	0.76	477	3.27E+03	1.69E-07	2.72	0.99880	0.81
AG5	Ag	E-A	108	1.08E+16	2.95E-06	2.38	0.99982	0.73	123	1.76E+03	9.16E-09	1.17	0.99910	0.88
AG4			81	3.95E+16	2.99E-07	2.26	0.99897	0.79	87	1.04E+04	4.44E-08	1.81	0.99890	0.84
AG3.1		N-A	4954	4.74E+05	5.58E-09	2.75	0.98807	0.89	6353	7.74E+07	1.03E-09	2.13	0.98453	0.93
102			87	2.43E+03	1.25E-06	3.23	0.99187	0.75	138	2.00E+03	2.36E-10	1.24	0.99022	0.97
O26	Au	E_A	647	1.48E+05	6.20E-09	2.00	0.99810	0.89	728	1.33E+05	3.88E-09	1.88	0.99778	0.90
O21			260	5.23E+04	1.44E-08	2.00	0.9993	0.87	293	5.46E+04	1.20E-08	1.94	0.99926	0.87
O25		N-A	839	3.72E+03	6.74E-07	2.21	0.99944	0.77	859	3.50E+03	3.85E-07	1.97	0.99945	0.78
O13			202	4.70E+03	2.98E-07	2.26	0.99932	0.79	238	4.38E+03	1.37E-07	1.97	0.99908	0.81

**I-V type column describes the Schottky barrier in terms of I-V features and photoresponse: E-A = exponential – photoactive, N-A = Non-ideal-photoactive.*

Most of the other parameters are comparable between the two methods. The series resistance correlates well between both of the methods, with results in the same order of magnitude, and over half of the samples obtained a resistance within +/- 40 Ω of the other method. The saturation current is also similar between the two methods, but they are generally higher in EDM 2. There is a close correlation in the ideality factor between the methods with a third of the samples only having a difference of +/- 0.1 and 11 out of 17 samples within +/- 0.5 of each other. Individually, both methods produce a very good fit to the I-V data, indicated by the R^2 values generally exceeding 0.99. The calculated Schottky barrier heights from the saturated current are also comparable between the two methods. Apart from three, all of the samples have a SBH that is +/- 0.05 eV between EDM 1 and 2. Generally the SBH calculated were slightly higher in EDM 2, especially for the non-ideal I-V curves. Overall, the largest differences between the methods tend to occur for the non-exponential I-V curves.

Comparing these results to the IDM results in Table 4-4, it is evident that the results from the IDM generally differ from the EDMs. This occurs in all parameters apart from the leakage resistance which are generally very similar across all 3 methods, with EDM 1 giving the largest variations and not the IDM as might be anticipated. As explained above, this is probably due to false local minima in EDM 1. The series resistance is generally over estimated in the IDM, apart from a few exceptions. This is probably due to the fact that the EDMs use more of the data to find a more accurate series resistance, rather than the more simplistic method applied in the IDM. The significantly lower series resistance from the EDMs indicates that less tunnelling occurs in the E-A devices and it confirms that hopping transport in the N-A occurs.

The saturation current is generally lower in the IDM which is due to fitting less of the data, since only current above 0.1 V were taken into account, and the inaccuracy of linear fit to the experimental data. Equally the SBHs from the IDM are considerably lower than the SBHs calculated from EDM 1 and 2, expected due to the lower saturation current obtained from the IDM. Significantly lower ideality factors are found in the EDMs which are more comparable with other studies, especially for the Pt devices, discussed previously after Table 4-4. This also suggests that the E-A devices have not deviated much from thermionic emission, as was indicated by the ideality factors found from the IDM. The combination of the above analysis of the results indicate why the data fit (R^2) is far superior in both of the EDMs.

Since the EDMs are more accurate, the SBH for the devices can now be updated. Taking *n* values from EDM 2 the maximum SBH calculated for each device has now increased to 1 eV, 0.97 eV and 0.90 eV for Pt, Ag, and Au devices respectively, which makes them more competitive to SBH found in other studies, shown in Table 4-3.

4.5 Photoresponse of Schottky devices

After thoroughly analysing the Schottky devices I-V characteristics, the devices were illuminated to find their photoresponse, as described in Section 3.6.1. Light with a wavelength less than an absorption edge in a semiconductor will be absorbed, which is related to the bandgap energy in Equation 4-7. This is derived from the energy of a photon shown in Equation 4-8. Expressing the constants hc in terms of eVnm^{-1} gives Equation 4-9. In the following equations *E* is the energy of a photon (eV), λ is the wavelength of light (nm), *h* is Planck's constant 6.63 × 10^{-34} m^{2} kgs^{-1} and *c* is the speed of light 3 x 10^{8}ms^{-1}.

$$\lambda = 1240/Eg$$

Equation 4-7

$$E = \frac{hc}{\lambda}$$

Equation 4-8

$$hc\ \frac{1}{1.602\ x\ 10^{-19}} = 1240\ eVnm^{-1}$$

Equation 4-9

Equation 4-7 relates energy to the wavelength of a photon. For rutile TiO_2 with a direct bandgap of 3.2 eV, light with wavelengths below 388 nm should be absorbed. Figure 4-21 shows the typical photocurrent and photovoltage from the Schottky devices. The devices reproducibly absorb in the UV region between 260 and 410 nm with peak absorption at 330 nm after which the absorption tails off.

Table 4-6 displays the maximum photoresponses from the Schottky devices. Clearly the Pt/TiO_2/Ti device outperforms the other two with a maximum photovoltage of 721 mV and photocurrent density of 390 μAcm^{-2}. The theoretical maximum photovoltage for the devices can be estimated by the band bending. The difference in energy between the conduction band and Fermi level of TiO_2 is approximately 0.25 eV. Subtracting this from the maximum SBH for Pt/TiO_2/Ti (1 eV), gives 0.75eV as the maximum energy obtainable from the Schottky barrier, equating to a photovoltage of 750 mV, which aligns with the maximum photovoltage found. Using the same principles the Ag/TiO_2/Ti and Au/TiO_2/Ti devices have lower SBH and therefore a lower maximum photovoltage, approximately 720 mV and 650 mV respectively. This suggests that there is potential for the silver and gold Schottky barriers to gain higher photovoltages than those measured.

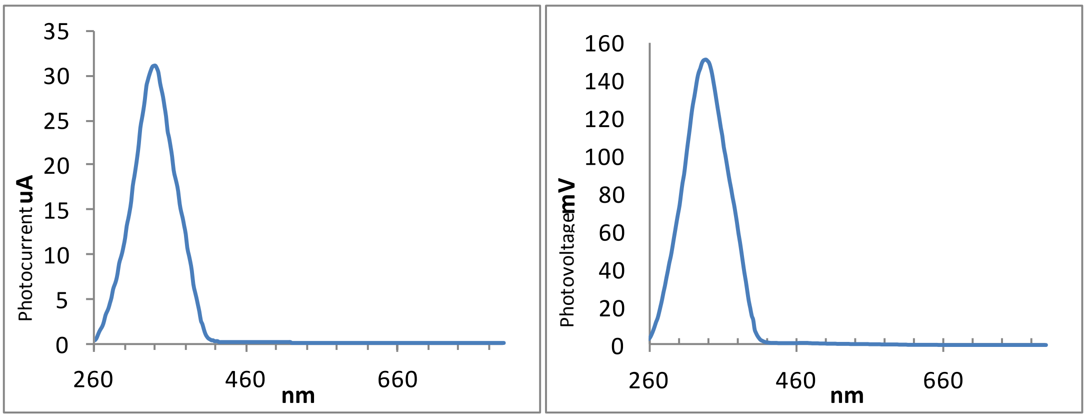

Figure 4-21: Typical photocurrent [Left] and photovoltage [Right] responses for Schottky devices. The sample shown here is Pt/TiO_2/Ti (Sample 504), gold and silver Schottky barriers showed the same features.

Under 100 mWcm^{-2} visible band illumination McFarland and Tang [34] obtained an open circuit photovoltage of 325 mV and a short circuit photocurrent of 0.9 μAcm^{-2} for their Au/TiO_2/Ti Schottky barrier. The maximum photocurrent and photovoltage in the Schottky devices in this work were measured under UV illumination at 330 nm hence a direct correlation is not possible. However from the results in this work, it is possible to suggest that McFarland and Tang may have been able to reach higher photovoltages and photocurrents if they used silver or platinum instead of gold. The external quantum efficiency (EQE) measured at 330 nm for the optimum Schottky barrier devices were 18% for Pt/TiO_2/Ti, 1.5% for Au/TiO_2/Ti and 11% for Ag/TiO_2/Ti.

Table 4-6: Maximum photocurrent and photovoltage for Schottky barriers at 330 nm.

Device	Maximum Photocurrent μAcm^{-2}	Maximum Photovoltage mV
Pt/TiO_2/Ti	390	721
Au/TiO_2/Ti	32	100
Ag/TiO_2/Ti	237	282

Figure 4-22 presents the distribution of maximum photoresponses across the three different Schottky devices. It is clear from the histograms that the most common photoresponses obtained were the lowest, up to 50 μAcm^{-2} and 100 mV. The gold devices performed the poorest with no distribution of photoresponses outside of the smallest bin, whereas the silver and platinum devices had a wider distribution. This suggests that the optimum devices were not very reproducible and that variation in device parameters had a large effect. It was shown in Table 4-3 that the SBHs calculated had an average variation of 10% hence some variation in photoresponse is therefore expected.

As discussed in 3.4.1 there were some inconsistent experimental parameters when comparing the whole range of devices. The gold devices experienced the most variation in experimental parameters due to the use of different purity Ti foils, chemical anodisation and oxidisation in air to produce TiO_2, and lastly various gold thicknesses were sputtered up to 80 nm due to problems associated with the sputtering system and the continuous nature of the gold film, see 3.4.1. All of these variations will have had an impact on the devices, for example a higher impurity density could have produced more defect states which will lower the effective SBH and hence photoresponse. The only device parameter that was altered in the fabrication of the silver and platinum devices was the thickness of the metals deposited. For silver this ranged between 10 – 20 nm and for platinum this ranged between 10 – 40 nm. In all of the devices the thickness of the metal films are a dominant parameter that has clearly affected the photoresponses, since a thicker film would transmit less light hence producing a lower photocurrent.

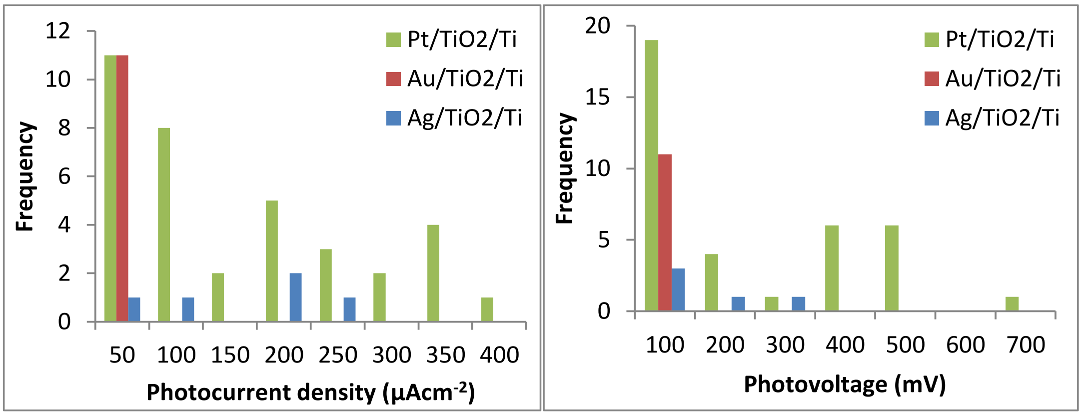

Figure 4-22: Histograms of photocurrent density [left] and photovoltage [right] distributions between devices, taking into account all samples which provided a photoresponse.

The photovoltage is directly related to the SBH for the devices since the SBH determines the maximum photovoltage that can be attained from a device [100]. This is evident from comparing the maximum SBH presented in Table 4-3 and maximum photovoltage displayed in Table 4-6. Figure 4-23 presents this correlation, showing an increasing photovoltage with a higher SBH for Pt devices. Only Pt devices were selected due to the larger number of devices fabricated. There are some outliers to the linear trend which can be explained by extra transport mechanisms, such as tunnelling and charge hopping, which can increase the photovoltage, previously discussed in detail in 4.3 and 4.4. As expected there was a general correlation between non – ideal I-V curves and low photovoltage. As discussed previously non-ideal I-V curves gave lower SBHs.

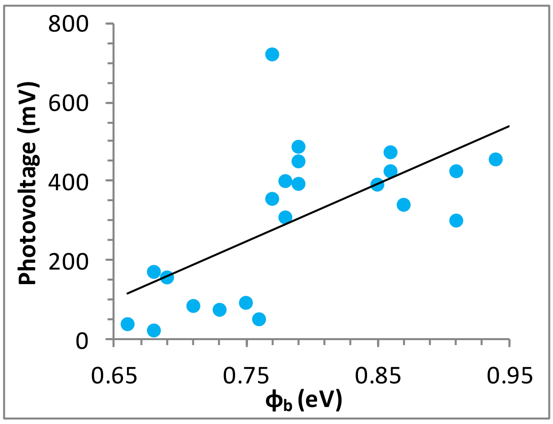

Figure 4-23: Relationship between SBH and photovoltage of Pt devices.

4.5.1 Visible light response of Schottky barriers

A visible photoresponse was found in some of the Schottky devices made with Pt, Au and Ag. The largest visible photoresponse was found in Pt devices. Figure 4-24 A clearly shows an extensive visible light photovoltage in a Pt device from 420 nm to 800 nm with a peak at 470 nm. However a much smaller visible photocurrent is observed, shown in Figure 4-24 C. This suggests that the mechanism for the very large visible photovoltage is not very efficient. Noteworthy is that the steps in the photocurrent are not a special feature, they are caused due to the resolution capabilities of the measurement equipment. The short wavelength fall in Figure 4-24 could be due to the falling output from the arc lamp, combined with the falling efficiency of the UV device as the wavelength becomes much larger than the bandgap of the material. The long wavelength onset in the UV feature is caused by absorption at the bandgap of TiO_2 with some thermal broadening. The visible response is discussed further below.

To verify the reproducibility of the visible responses found, the photovoltage and photocurrent measurements were repeated 3 times. Photovoltage decay tests were also undertaken to indicate whether any UV induced interface or bulk charging was present which could subsequently be released giving rise to a false signal in the visible wavelength region during a photoresponse scan. To measure the photovoltage decay the device was illuminated with the peak wavelength absorption, 330nm in all devices, for 1 to 2 minutes, after which the voltage of the device as a function of time was measured without illumination. The voltage decay curve in Figure 4-24 B clearly shows that there was no significant charging, indicating that the Schottky device is giving a visible response. Moreover, the photovoltage decay decreases with time whilst illuminated with the same wavelength of light, indicating that some other destructive charge transport mechanism is present in the device, such as recombination.

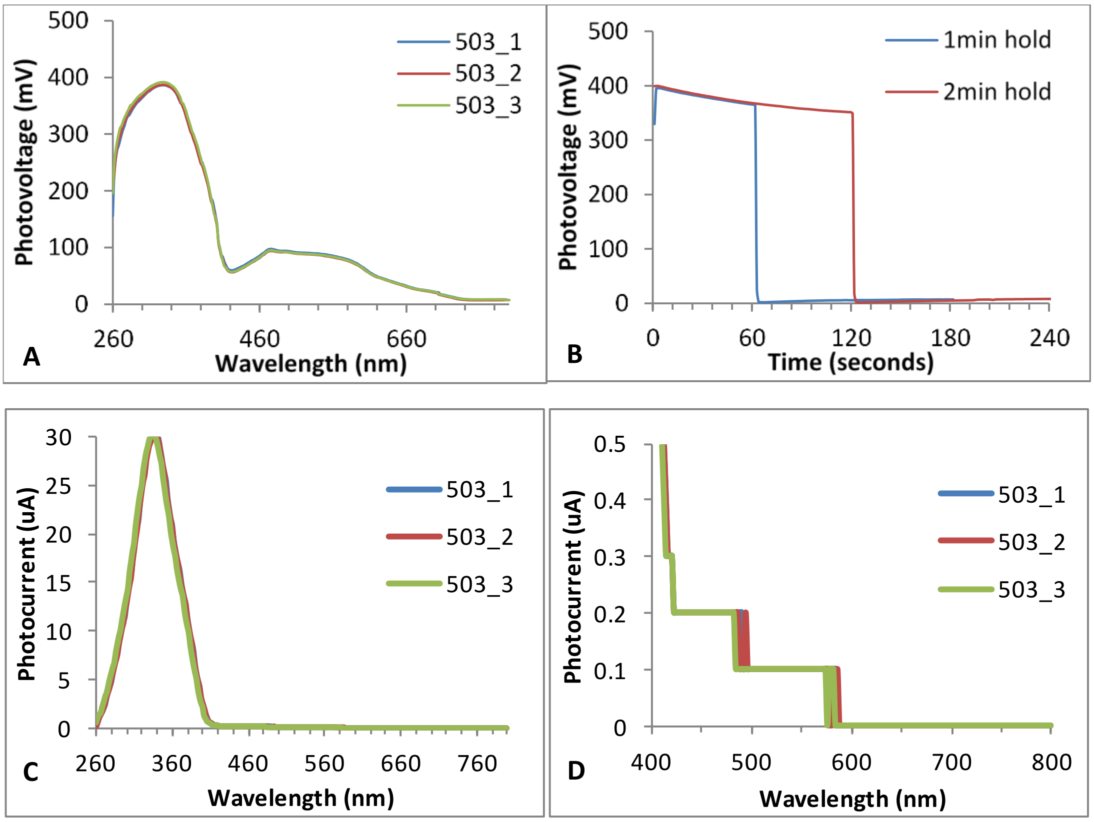

Figure 4-24: Pt/TiO$_2$/Ti photovoltage showing visible light absorption [A] with corresponding photovoltage decay [B]. Corresponding photocurrent is displayed between 260-800 nm [C] and emphasis on the visible region between 400-800 nm [D] due to low resolution (Sample 503).

Photovoltage decay tests were routinely undertaken to ensure accurate understanding of the devices and any additional charging mechanisms. The photovoltage decay test was verified by varying the scan speeds between 2 - 10 nms^{-1} and undertaking scans in both directions, from high to low wavelengths and vice versa, demonstrated in Figure 4-25. Further photovoltage decay plots will not be presented unless a voltage decay response has been found.

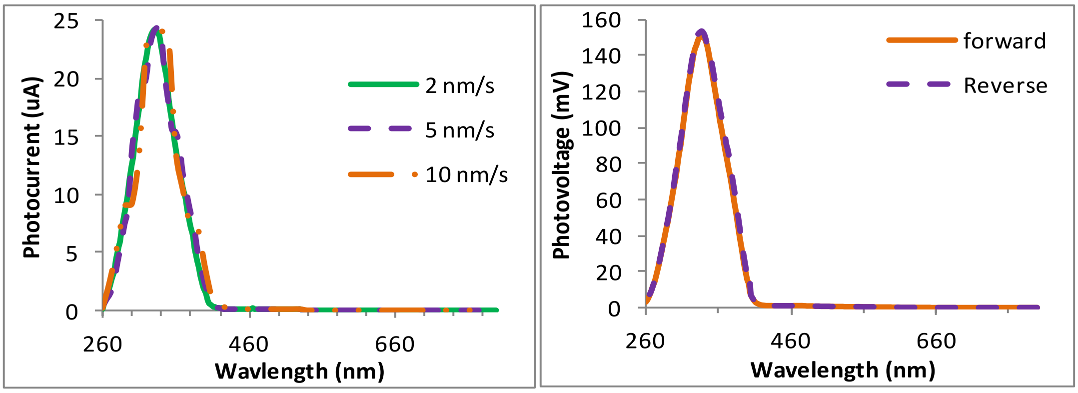

Figure 4-25: Representative photoresponse scans of different scan rates and directions. [Left] Photocurrent at 3 different scan rates – 2, 5 and 10 nms^{-1} and [right] photovoltage scanned at forward and reverse directions.

The large visible response in Figure 4-24 was rarely observed, only a total of 2 samples showed the same features. However a smaller visible photocurrent and photovoltage was found in many of the Pt/TiO_2 Schottky devices. Figure 4-26 shows the more typical visible photocurrent and photovoltage response from a Pt/TiO_2 sample. A peak at 470 nm is evident in both the photocurrent and photovoltage after close inspection on the wavelength range after 400 nm, with a visible photoresponse tail up to 600 nm. This visible response could only be seen in devices that gave a high photoresponse, indicating that the visible response is probably proportional to the UV response. It follows that devices that gave a small UV response may have produced a visible response but this was too small to detect. The fact that a small visible response is evident in a number of the Pt/TiO_2 Schottky barriers suggests that the effect is causal to the metal on the TiO_2 surface.

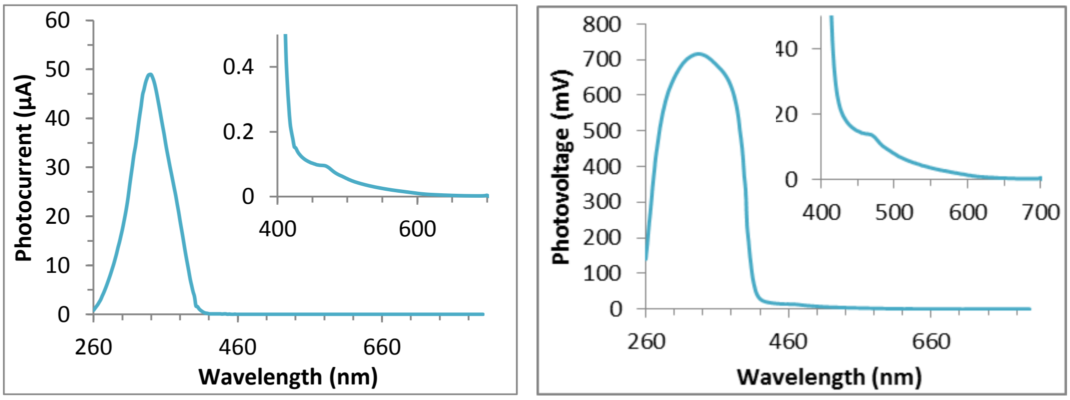

Figure 4-26: Pt/TiO_2/Ti Schottky barrier photocurrent [left] and photovoltage [right], both showing a small visible response at 470 nm (Sample 304Re).

A visible photoresponse has also been observed in the Ag/TiO_2/Ti Schottky barriers. Figure 4-27 displays the largest visible photocurrent and photovoltage found in an Ag/TiO_2 Schottky barrier. Similar to the Pt/TiO_2 samples, not all Ag devices have a visible photoresponse and only the one sample, presented here, showed a very large visible response. The visible response displayed here shows a peak at 500 nm with a visible range of 400 – 600 nm. Comparing Figure 4-24 to Figure 4-27 it is evident that the visible features differ between the Pt and Ag Schottky barriers. This further implies that the visible response is dependent on the metal deposited onto the TiO_2.

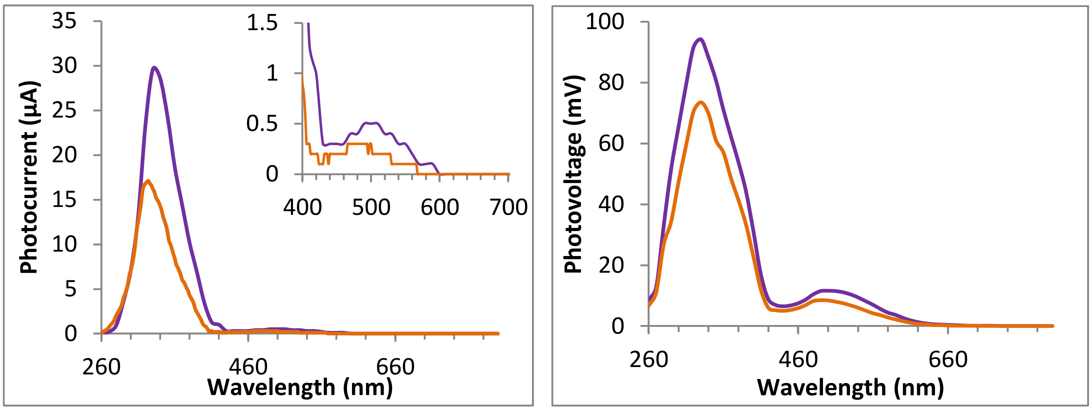

Figure 4-27: Ag/TiO_2 Schottky barrier photocurrent [left] and photovoltage [right], where different coloured lines show repeated scan (Sample AG5).

For the Au/TiO_2 Schottky barriers, a weak visible photovoltage, but no visible photocurrent, was evident in very few of the samples. Figure 4-28 shows one of the examples of this visible photovoltage. Unlike the devices above, this sample shows no clear absorption edge or feature but more of a tail from the UV response into the visible region. The fact that less Au/TiO_2 samples showed a visible response can be linked to the earlier discussion on the maximum photoresponse obtained, see Figure 4-23. Table 4-6 shows that the gold devices generally gave a lower maximum photoresponse compared to the Pt and Ag Schottky barriers.

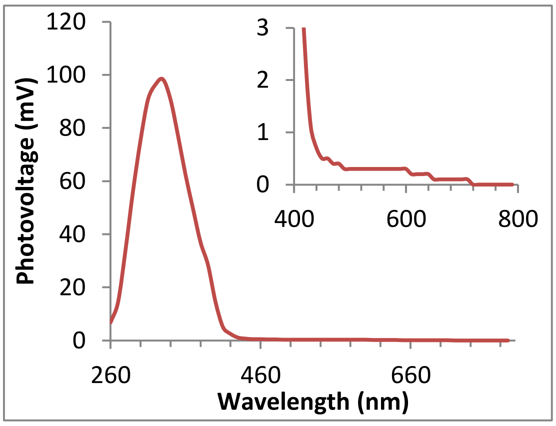

Figure 4-28: Photovoltage of Au/TiO_2 Schottky barrier, showing a weak visible response. No corresponding visible photocurrent was found (Sample O26).

It is clear from Figure 4-24 to Figure 4-28 that the metal films deposited on to the TiO_2 substrates are contributing to the visible photocurrents and photovoltages obtained. Visible photoresponses for Schottky barriers with TiO_2 have been demonstrated for Pt [75, 243-245], Ag [246] and Au [34, 247, 248]. Figure 4-29 shows two of the results from these studies which show similar features to that found for Pt and Ag devices in this work. The common explanation for this is due to defect levels in the TiO_2 which allow sub bandgap absorption, as depicted in Figure 4-30.

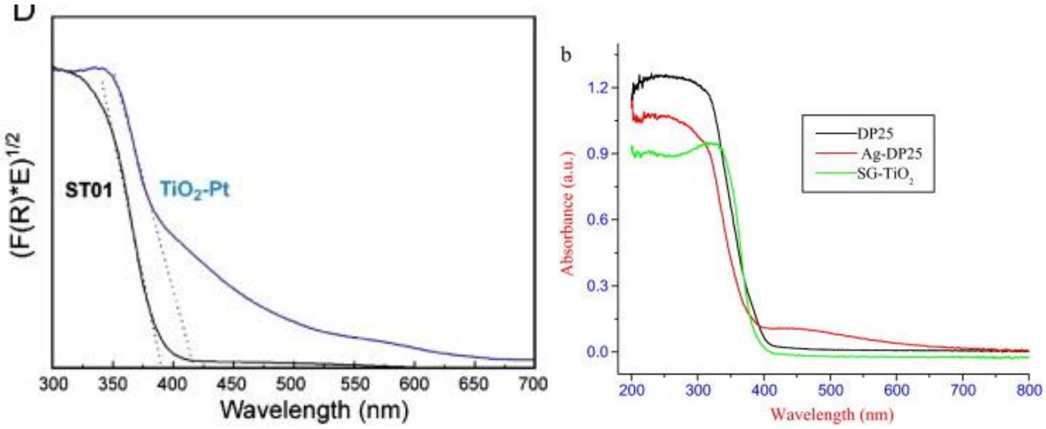

Figure 4-29: [Left] Pt/TiO_2 visible photoresponse taken from Tseng et al [243]. [Right] Ag/TiO_2 absorbance taken from Devi and Reddy [246-248].

Defect levels effectively create new energy levels below the conduction band which creates a secondary bandgap much smaller than that of TiO_2 hence making visible absorption possible. These defect states have been attributed to titanium oxide states, interface states and metal induced defect states [249-251]. Since the visible photoresponse in this work is causal to the metal deposition, metal induced defect states in the TiO_2 are thought to be the dominant mechanism.

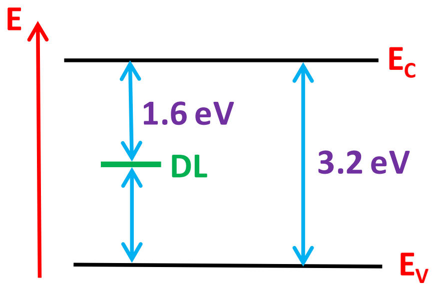

Figure 4-30: Energy band schematic of a semiconductor showing visible light absorption capabilities due to a defect level (DL) half way between the conduction and valence band.

4.6 Summary of main findings

This chapter has presented results and discussions on Schottky barrier devices fabricated with TiO_2 and sputtered or evaporated noble metal films of Pt, Ag and Au. The yield of devices indicated that the platinum devices outperformed the gold and silver devices in terms of ideal I-V features and photoresponses obtained. The gold devices performed poorly due to experimental variables and the silver devices also obtained a low yield, possibly due to the low work function of silver which makes it more likely to produce an Ohmic contact. Thermionic emission is the dominant transport mechanism for most of the ideal Schottky devices created in this work. However in some devices additional series and leakage resistance is evident, which is sometimes supported by a secondary transport mechanism, mainly charge hopping transport and tunnelling due to localised states. Charge hopping leads to more linear I-V features, whereas tunnelling leads to exponential features, both of which are observed in the devices. The main causes of non-idealities are probably due to the low temperature processing which is known to causes surface defects, inherent impurities and defect levels in the TiO_2 and diffusion of metal particles into the semiconductor.

The SBH, ideality factor, series and leakage resistance calculated by EDM 2 provided higher accuracy, observed by a significantly better fit to the data, compared to the thermionic emission calculation (IDM) which was very limiting. The highest SBH found was 1 eV for a Pt/TiO_2 Schottky barrier, which is comparable to previous studies. The Pt Schottky devices also obtained the highest photocurrent and photovoltage which was expected due to the higher SBH found, since the SBH dictates the magnitude of the photovoltage. Visible photoresponses were obtained from some of the Schottky devices with Pt, Au and Ag. The Pt devices gained the highest visible response, the magnitude of which was proportional to the UV response. The visible response is due to the metal diffusing into the semiconductor causing defect levels in the bandgap, which provide additional lower energy levels that can excite electrons under visible illumination.

Chapter 5

Schottky Barrier Devices Fabricated With Electrodeposited Silver Films and Silver Nanowires

The previous chapter presented I-V and photoresponse results of Schottky barriers with sputtered and evaporated platinum, gold and silver films on TiO_2/Ti substrates. It was found that the yield of devices obtaining exponential features and producing a photoresponse was generally quite low. Therefore it is necessary to explore different and more novel transparent and conductive metal films to obtain an increased performance. In this chapter metal films produced via chemical synthesis were trialled to attempt to improve the Schottky barrier features. In addition to the potential for increased device performance, chemical synthesis approaches can also lower device fabrication cost. Silver is a highly conductive material, more so than both gold and platinum and was shown in the last chapter to obtain comparable SBHs to platinum and gold films, hence was selected for further research. Electrodeposition of silver and deposition of silver nanowires were selected for producing the thin, uniform and electrically continuous metal film required. Silver electrodeposition has previously been used in Schottky barrier cells [160, 165], however, neither electrodeposited silver or silver nanowires have been used as part of a nanocrystal-activated Schottky barrier device.

The first half of this chapter analyses SEM and surface resistance measurements of electrodeposited Ag/TiO_2 Schottky barriers, following standard and strike electrodeposition as detailed in 3.4.2. The second half of this chapter presents I-V, sheet resistance and photoresponse results from the deposition of silver nanowires on to TiO_2/Ti substrates, which were synthesised and deposited as described in 3.4.3. The variation, degradation and yield of silver nanowire devices are also presented. Only the silver nanowires were successful in creating a conductive film on the substrate, hence at the end of this chapter the silver nanowire devices are compared to the Schottky barrier devices presented in Chapter 4.

5.1 Silver electrodeposition

Electrodeposition is an attractive technique for metal deposition, for use in the nanocrystal activated Schottky barrier solar cells, as it is low cost compared to sputtering and evaporation, it can be used for large areas and more complex geometries and offers more flexibility since less stringent deposition criteria are required. Moreover it has been found in a number of studies that electrically continuous electrodeposited metal films created higher SBHs than an equivalent sputtered or evaporated metal film [120, 156, 158, 164, 252]. As discussed previously in 4.4.1, a higher SBH can be obtained due to chemical composition changes and interfacial chemical reactions. This is thought to be due to the formation of an interfacial dipole layer in the metal or because the metal ions stabilise the oxygen vacancies at the M-S interface [120].

There have been a number of studies that have looked at electrodepositing different forms of silver on to many different surfaces, for example silver nanoparticles [161-163]. Many studies have also looked into different techniques to deposit silver on to TiO_2 including doping [123], photochemical impregnation [76] and vacuum deposition [122]. However only a few studies have looked at electrodeposition of silver on to TiO_2, namely Boskovic et al [160] and Poroshkov and Gurin [165]. Boskovic et al [160] created a composite TiO_2/Ag film by using a Ti substrate and forming the TiO_2 layer at the same time as the silver layer through electrodeposition. They report that the silver forms either dendritic or nanoparticles on the substrate. Poroshkov and Gurin [165] electrodeposited silver on to TiO_2 and similarly only obtained spherical particles and dendritic structures. No studies have been found that have looked at electrodeposition of silver on to a TiO_2 substrate to gain an electrically continuous film for solar cell applications.

Standard and strike electrodeposition of silver onto TiO_2/Ti substrates was carried out following the method outlined in 3.4.2. A number of different silver containing electrolytes were trialled to source an optimum electrolyte for uniform and continuous silver electrodeposition, outlined in Table 3-6. Scanning electron microscope (SEM) images and surface resistance measurements indicated the continuity of the surface and these results are presented below. A total of 23 electrodeposited Ag/TiO_2/Ti Schottky barriers were fabricated, 7 of which were made by standard electrodeposition and 16 used strike electrodeposition.

5.1.1 SEM of silver electrodeposited substrates

SEM was used to characterise the silver electrodeposited on to the TiO_2/Ti substrate as it can clearly indicate the continuous and uniform nature of the film. The results have been presented to reflect and make comparisons between the two different electrodeposition techniques and the various electrolytes used. The SEM images presented below are representative of the devices fabricated from the different electrolytes.

Figure 5-1 shows SEM images from 2 samples which were made from a DMSO electrolyte with silver nitrate and TBAP. It is evident from the images that crystalline, spherical silver particles have been formed on the TiO_2/Ti substrate. It is also clear from [A] that the silver deposited on the surface did not form a continuous or uniform layer over the substrate. An indication of spherical particles laterally growing into a near-continuous layer is shown in [B-D] however there are also non-uniform, large agglomerated silver particles growing out of the surface, which will increase the surface roughness. The images shown in Figure 5-1 [A] and [B] are from different areas on the same substrate (approximately $1cm^2$), which further indicates the level of discontinuity across the surface of the silver deposits. Images [C] and [D] in Figure 5-1 underwent much more growth phases at a slower rate and less stripping at a faster rate during electrodeposition than images in [A] and [B], to improve surface adhesion and increase lateral deposition. There is some improvement from image [A] to [C] and [D], but image [B] appears to be relatively comparable, in terms of continuity. Overall, it is clear from all of the images that a fully continuous silver film has not been achieved.

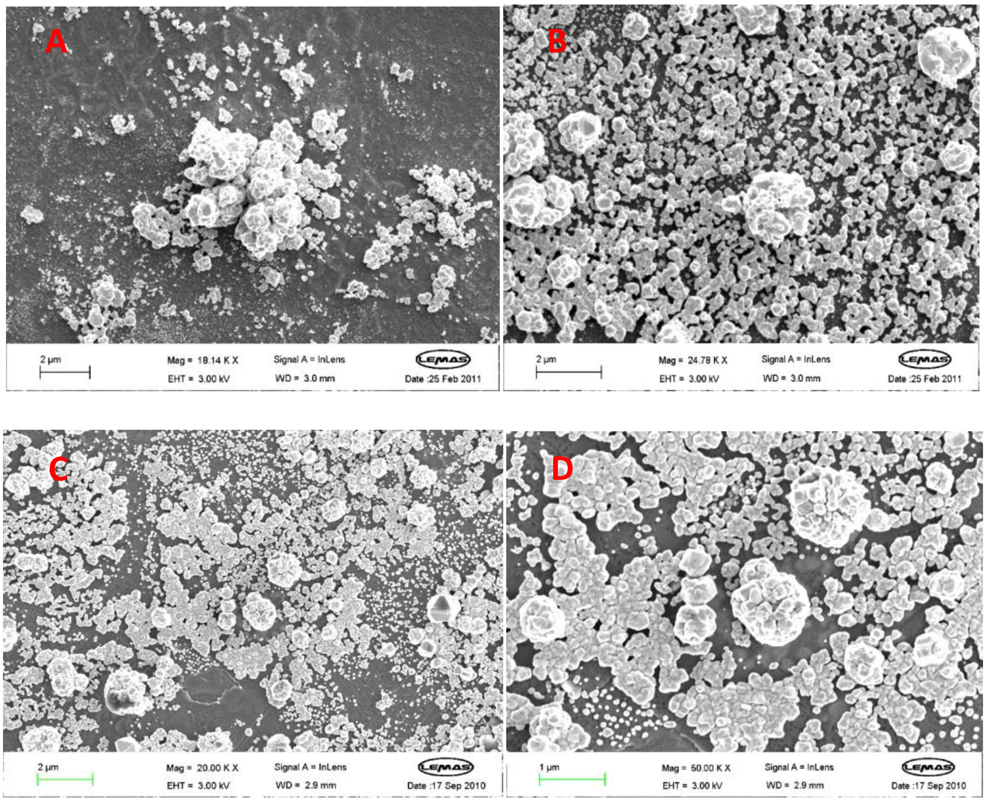

Figure 5-1: SEM image of 2 samples with silver deposited via standard electrodeposition using a DMSO electrolyte containing silver nitrate and TBAP. [A] and [B] show different areas of Sample 3, which has undergone 2 deposition phases each followed by 5 stripping scans after each phase. [C] and [D] show two different magnifications for the same area on the Sample 7 which has undergone 3 repeated deposition phases followed by 3 very fast stripping phases.

Figure 5-2 shows a representative SEM image of a device which used a silver nitrate and DMSO electrolyte but with $Bu_4N^+BF4^-$ instead of TBAP as the active agent. It was indicated in 3.4.2 that the $Bu_4N^+BF4^-$ did not dissolve fully and caused a precipitate in the electrolyte, however, Figure 5-2 shows that silver nucleation islands were still deposited successfully on the surface. It is clear from comparing the SEM images in Figure 5-2 and Figure 5-1 that the mass loading and continuity of deposits are far reduced with the $Bu_4N^+BF4^-$ containing electrolyte, despite undergoing similar electrodepositing scan rates. The depositing and stripping curves showed no obvious features, unlike the samples above, indicating an inability to create a silver layer, which is more than likely due to the electrolyte. This further justifies the discontinued use of $Bu_4N^+BF4^-$ in the electrolyte.

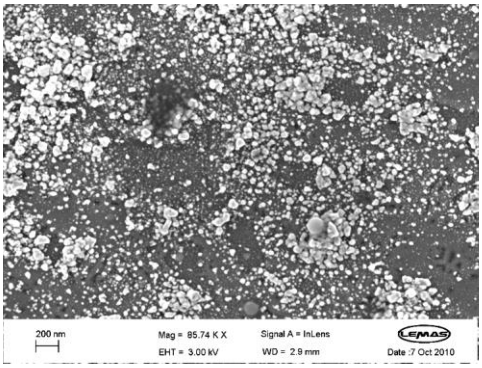

Figure 5-2: SEM image of silver deposited via standard electrodeposition using a DMSO electrolyte containing silver nitrate and $Bu_4N^+BF4^-$ (Sample 2).

As described above the standard electrodepositing approach consistently provided poor surface adhesion where silver deposits easily wiped off the surface. Strike electrodeposition is well known for better surface adhesion and so was used to create a more strongly adhesive silver layer. Figure 5-3 shows the SEM images for silver deposited from an aqueous silver nitrate electrolyte. Silver deposition is achieved using strike electrodeposition with only 1 strike, shown in [A]. The crystalline silver nucleation islands in [A] appear to be relatively large and reasonably uniform but sparsely distributed. The additional growth phases in [B] and [C] of 2 and 8 minutes respectively show a gradual increase in silver deposits with dendritic growth. Dendritic growth by silver electrodeposition has also been observed by Poroshkov and Gurin [165]. The longer growth phase, in [C], tends to lead to more agglomerated silver deposits that favour vertical growth rather than extensive lateral growth. It is evident from [C] that even after an extensive growth phase, a continuous layer of silver has not been realised, however the branch like structures may provide an advantageous structure for an electrically continuous film if this method was developed further.

Comparing both silver nitrate electrolytes presented in Figure 5-1 and Figure 5-3 show that neither electrolyte has been successful in providing a continuous film. Larger and more agglomerated crystalline silver deposition is evident in the DMSO electrolyte, whereas the aqueous electrolyte provided dendritic structures with less agglomerated growth but also less lateral growth. The branch like structures, with more experimentation into the growth kinetics, may however be favourable for creating an electrically continuous film.

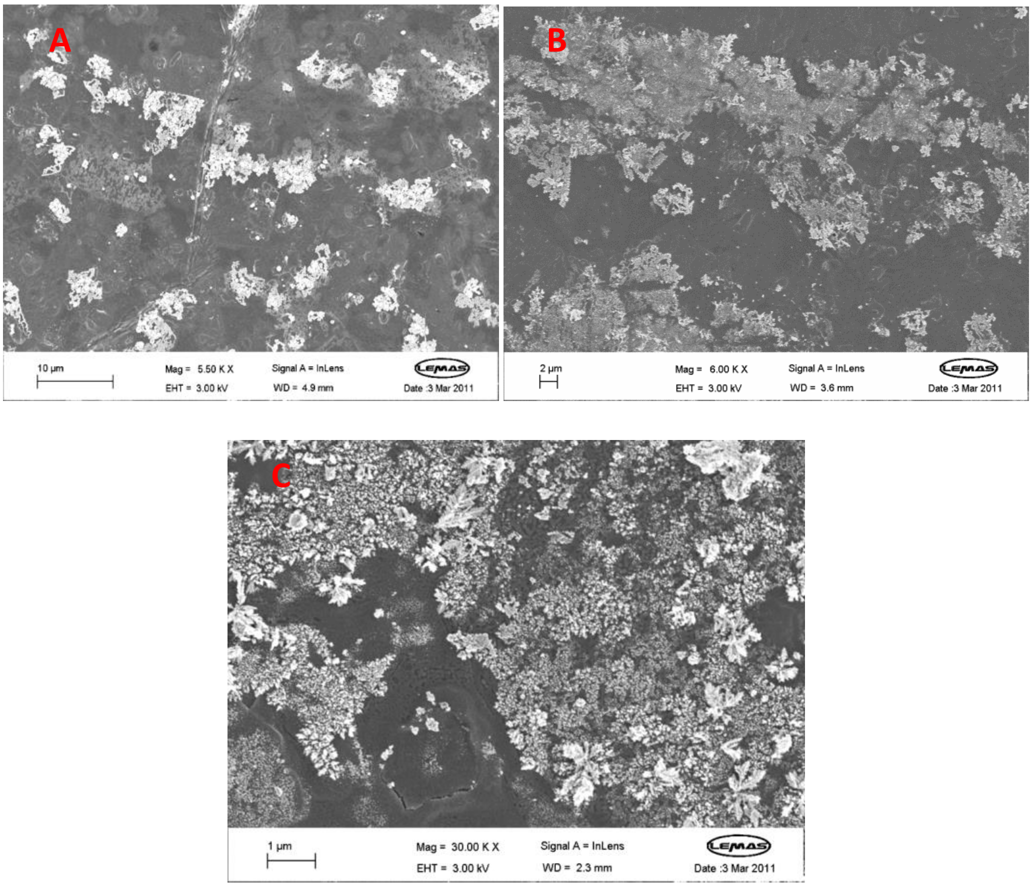

Figure 5-3: SEM images for silver deposited from strike electrodeposition using aqueous silver nitrate electrolytes. Samples have all undergone 1 strike with either no growth phase (sample 21) [A], 2 minutes (sample 22) [B], or 8 minutes (sample 24) [C] of growth.

Comparing the silver growth presented in Figure 5-2 and Figure 5-3 to that found in previous studies shows substantial similarities. Figure 5-4 shows the dendritic and spherical silver growth found by Boskovic et al [160]. Similar features were also reported by Poroshnov and Gurin [165]. Comparing the scales of the SEM images in all figures, it is clear that more extensive silver growth has been found in this work.

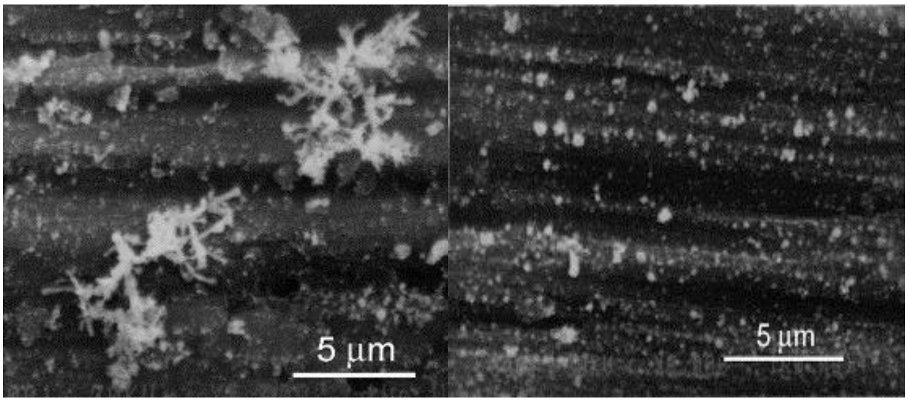

Figure 5-4: Dendritic [left] and spherical [right] silver growth on TiO_2 via electrodeposition, taken from [160].

The silver nitrate aqueous electrolyte was substituted with a silver acetate aqueous electrolyte to see if more lateral and continuous silver deposition was possible. Figure 5-5 shows a selection of typical results observed with the silver acetate aqueous electrolyte using both standard and strike electrodeposition techniques. It is evident from Figure 5-5 that there is lots of variability with the silver acetate electrolyte, with no uniformity or continuity of silver deposits between the different samples.

Figure 5-5 [A] presents the only electrolyte that did not use a control agent. The silver deposits here have formed faceted structures in horizontal and vertical directions which are clearly uncontrolled and unsuitable for the device. The samples in images [B-D] all used a tartaric acid control agent and show completely different silver structures to [A]. It is evident from images [B-D] that the silver acetate electrolyte deposits silver on the substrate very easily using the strike method, however, even with tartaric acid the growth mechanisms are clearly uncontrolled, leading to many different types of silver structures with varying degrees of agglomeration. Smooth background lateral growth, large crystalline agglomerations, dendritic and faceted structures are all visible in images [B-D].

Comparing the images across the different electrolytes where only 1 strike has been used with no growth phase, image Figure 5-5 [B] and Figure 5-3 [A], it is clear that one strike has a more profound effect using the silver acetate electrolyte, since a near continuous silver base layer exists (in the background to the faceted branch-like structures). Comparing the growth phases after the strike between Figure 5-5 [C and D] and Figure 5-3 [B and C] again shows that the silver acetate induces faster, yet more uncontrolled and agglomerated, silver growth on the TiO_2/Ti than the silver nitrate electrolyte.

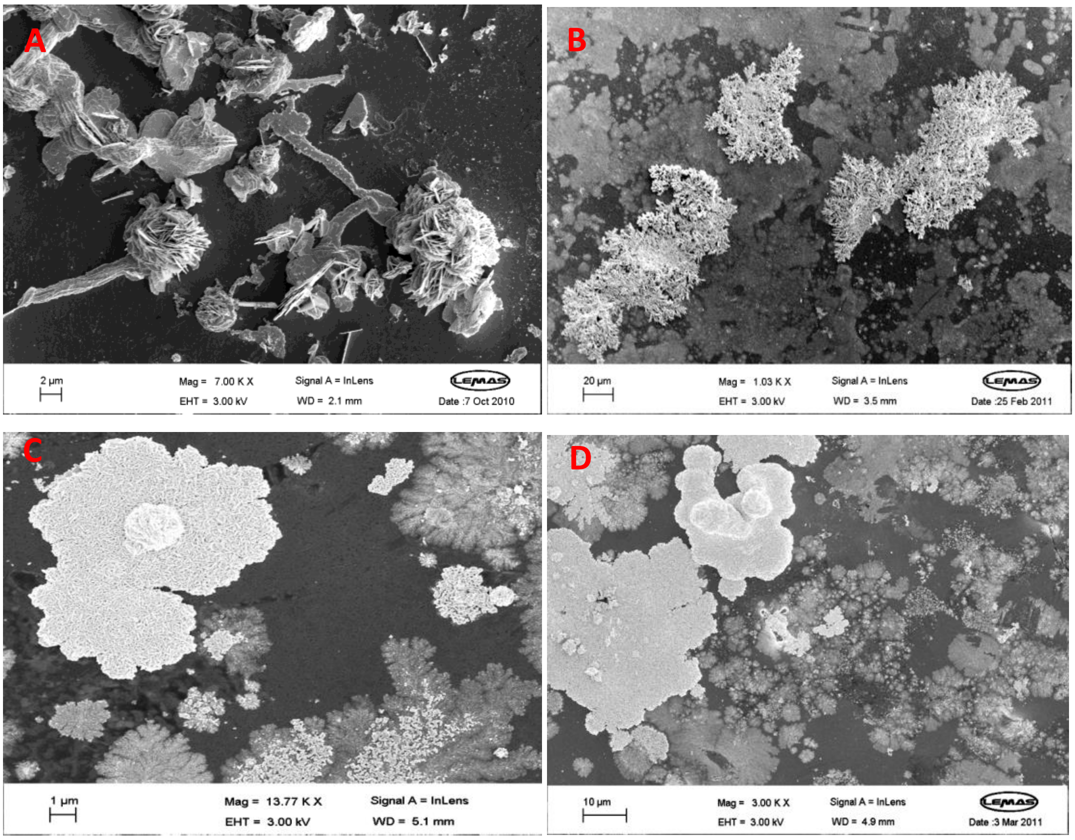

Figure 5-5: SEM images for silver deposited from standard (sample 19) [A] and strike electrodeposition [B-D] using aqueous silver acetate electrolytes. Strike samples have all undergone 1 strike, with either no growth phase (sample D1) [B], 4 minutes (sample D2) [C], and 8 minutes of growth (sample D2) [D].

Due to the extensive lateral growth found after 1 strike and no growth phase with the silver acetate electrolyte, presented in Figure 5-5 [B], 10 strikes and no growth phase were trialled since the growth phase appears to effect the vertical agglomeration of silver rather than the uniform and planar growth. The resultant images are shown in Figure 5-6. All of the SEM images in Figure 5-6 show extensive planar and uniform silver film growth where the central section of the substrate in [A and B] are near-continuous. This indicates that the continuous growth phase has less impact than the amount of strikes. This complements the growth kinetics in the strike technique since more strikes suggest greater nucleation sites and increasing silver deposits. Despite good planar growth, it is clear that the 10 strikes have led to a rather thick deposition. Moreover, the silver is not well adhered and can easily be wiped off, demonstrated in [C] where the edge has been gently wiped.

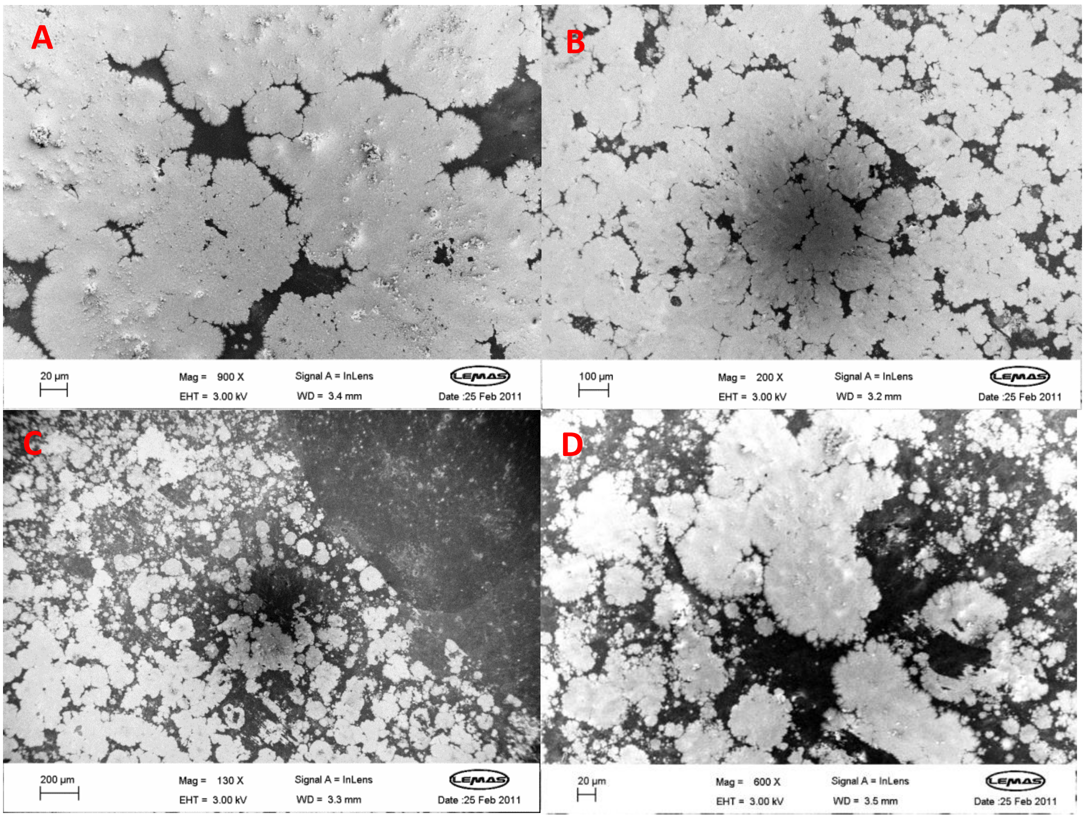

Figure 5-6: SEM images for silver deposited from strike electrodeposition using aqueous silver acetate electrolytes and 10 strikes followed by 4 minutes of growth, showing central positions on samples D3 in [A] and [B] and an edge section at different magnitudes in [C] and [D].

It is clear from the SEM images above that none of the electrolytes in either the standard or strike electrodeposition techniques provided a single continuous silver film on the TiO_2 substrate. The silver nitrate electrolytes obtained crystalline and dendritic structures but no continuity, whereas the silver acetate electrolytes gave good planar growth during strikes, but deposits were weakly bonded, agglomerated and uncontrollable. Both electrodepositing techniques are reasonably comparable, however the strike method clearly has a more dominant effect on the strike pulse. Controlling the number of strikes, analysing the growth kinetics and procuring a more optimum silver containing electrolyte could lead to a more continuous silver film. The observations from the SEM images presented above highlight the difficulty in controlling the direction and growth of silver deposits using electrodeposition. In addition to SEM images, surface resistance measurements were undertaken to verify whether the films were electrically continuous or not, the results for which are presented in the next section.

5.1.2 Surface resistance measurements of silver electrodeposited substrates

Surface resistance measurements were undertaken to infer the continuity of the silver film, as outlined in section 3.6.2. Table 5-1 shows a comparison of the average surface resistance measurements of the silver electrodeposited samples compared to two conductive and one insulating reference surfaces. The conductive references used were an Au/TiO_2/Ti Schottky barrier and an electropolished Ti and the insulating reference was a TiO_2/Ti substrate. The average surface resistance of the control samples give an estimate of the values for surface resistance expected from the silver electrodeposited samples for a continuous and non-continuous surface. It is evident from Table 5-1 that the surface resistance of the silver electrodeposited samples are similar across all electrolytes and clearly correspond to the 'insulating' control sample. This high surface resistance indicates that the surfaces are not continuous, since an electrically continuous surface is expected to have a low surface resistance. This further indicates that electrodeposition of silver needs much more refining to be suitable for the conductive and transparent film needed for the device.

Table 5-1: Resistance measurements of electrodeposited silver layers and gold sputtered surfaces in comparison to control samples of titanium and titanium dioxide.

Control sample	Average Surface Resistance (Ω)
Gold sputtered TiO_2	26
Electropolished Ti	76
TiO_2 (anodised Ti)	10155
Silver electrodeposited device (by electrolyte)	**Average Surface Resistance (Ω)**
Ag Nitrate DMSO	10170
Aqueous Ag Nitrate	10530
Aqueous Ag Acetate	10200

As mentioned previously, only two studies have been found on the electrodeposition of silver on to TiO_2 and neither of these studies form electrically continuous silver films either [160, 165].

5.1.3 Summary for electrodeposited silver on TiO_2/Ti

It is evident by visual inspection of the SEM images presented in 5.1.1 and more specifically the surface resistance measurements in 5.1.2 that none of the electrodeposited samples were successful in providing the electrically continuous and uniformly thin layer required for the Schottky barrier device. Due to the unsuccessful nature of this metal film, silver electrodeposition was not used any further in this work. Future work for this topic could involve more experimentation with the strike technique and alternative silver electrolytes. The degradation of these devices was not analysed, however this is an important issue if this work is to be developed, since the silver molecules may oxidise on the substrate surface and hence degrade performance of the device over time.

5.2 Silver nanowires as an alternative conductive electrode

Electrodeposited silver on to TiO_2/Ti substrates, presented in section 5.1, was not able to achieve an electrically continuous film suitable for the Schottky barrier. Therefore silver nanowires produced by chemical synthesis were trialled as an alternative novel, transparent and conductive layer to substitute the sputtered and evaporated metals in Chapter 4. Nanowires provide significant advantages over bulk films in many ways. Firstly they can provide an electrically continuous mesh that has the ability to enhance photoconversion efficiency because of increased transmission, increased photon absorption due to reduced reflection and light trapping, improved electron transport and electron-hole separation and increased defect tolerance. Secondly they can reduce the amount of materials needed and the quality, leading to potential cost savings [123, 176, 253]. Furthermore silver deposited on to TiO_2 has shown enhanced visible light excitation of TiO_2 [123, 254].

There has been vast and rapidly growing research in to the production of nanowires for a number of different applications. Specific to this research are those studies fabricating and characterising Schottky barriers using nanowires. A few studies have analysed semiconductor nanowires on metal substrates including Si-NW on Pt thin films [255] and ZnO nanorods with Ag contacts [256]. Ag/TiO_2 Schottky barriers using different types of nanomaterials and composites have also been studied, for example silver doped TiO_2 nanomaterials [123], Ag/TiO_2 nanocomposites [254], Ag-NW/TiO_2-nanoparticles core–shell composite nanowires [253], Ag/TiO_2 nanofiber membrane, composed of silver nanoparticles on TiO_2 nanofibers [257] and Ag-nanoparticles on TiO_2 [258]. However no study has been found that has researched silver nanowires on a bulk oxidised TiO_2/Ti substrate for a Schottky barrier or a nanocrystal activated Schottky barrier solar cell.

Silver nanowires offer advantages to electrodeposited silver, described in 5.1, because they can be produced and deposited separately, hence experimental parameters can be more easily controlled and problems highlighted between the two stages. Section 3.4.3 described the methods used for silver nanowire synthesis, deposition and post treatment. Similar to section 5.1, this section presents SEM images for visual inspection of the deposited nanowires and sheet resistance measurements to prove the electrical continuity of the silver mesh. Since the nanowires provided an electrically continuous mesh further analysis in the form of I-V and photoresponse measurements were undertaken to characterise the devices. Device yield, degradation and variability are also presented in this section. A total of 42 Ag-NW/TiO_2/Ti devices were fabricated, with some variability between mass loading and concentration as given in 3.4.3.3. A summary of all Ag-NW devices can be found in Appendix A.

5.2.1 SEM analysis of silver nanowires

Silver nanowires were characterised by SEM alongside I-V and photoresponse measurements to indicate any clear differences that account for performance between devices. Figure 5-7 shows a selection of typical features across all nanowire devices. Nanowires typically measured between 1 – 5 µm, with an average of 2.5 µm, and had a typical surface coverage of 59%. The surface coverage was estimated across 3 photo-active Schottky barrier devices, from a pixel histogram of four different sections across each sample, all of which had an average of 20 µL of deposited nanowires.

The SEM images displayed in Figure 5-7 [A] to [D] were taken from different sections of the same sample. The nanowires were generally found to be unevenly distributed across the sample [D], with extensive agglomeration of nanowires at the droplet edge [B], and sparsely distributed nanowires in central areas [C]. The accumulation of nanowires at the droplet edge is due to drop casting. On deposition the low viscosity of the nanowires suspended in solution allows the nanowires to travel across the substrate surface, evaporating faster at the edges, hence causing an internal current to move more nanowires to the edges. This leads to more accumulation of nanowires at the edges of the evaporated solution and a slightly sparser mass loading of nanowires in the centre of the device. The patchy agglomeration in [D] is possibly due to electrostatic attraction between the nanowires. Despite the agglomeration and somewhat uneven distribution, the nanowires still attained an electrically continuous mesh on the substrate.

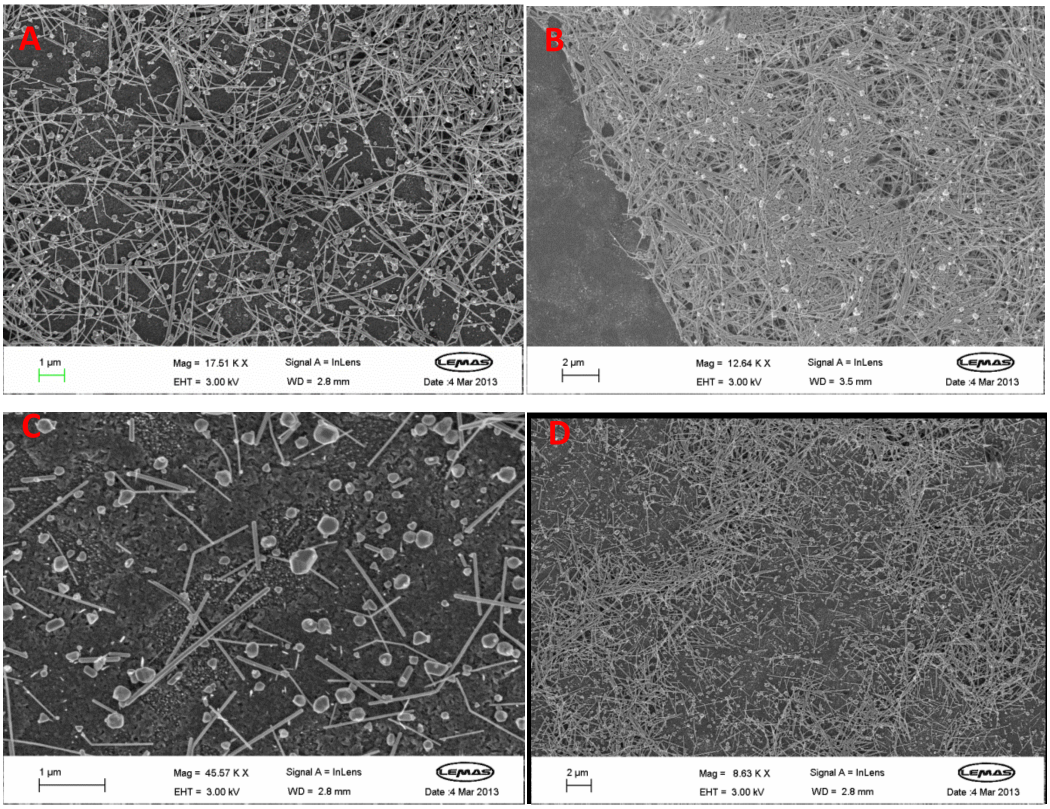

Figure 5-7: SEM images of a typical Ag-NW/TiO_2/Ti device (sample 101), with a typical surface coverage [A], agglomeration at the edge of deposits [B], a central location [C] and a lower magnitude surface distribution [D].

The adherence of nanowires to the substrate was poor and even after annealing the silver nanowires could be easily wiped off the substrate, a similar finding to the electrodeposited silver. Due to experiencing issues finding the optimum mass loading of nanowires, no additional techniques were undertaken for providing a more uniform distribution of nanowires. However spin coating was considered as an alternative technique to gain a more uniform distribution of nanowires and should be used in future work to prevent agglomeration at the edges and sparse, localised distribution across the substrate.

5.2.2 Sheet resistance measurements of silver nanowires

Sheet resistance measurements were undertaken to indicate the continuity of the nanowire mesh. A low sheet resistance was found across the silver nanowire samples, as shown in Figure 5-8, indicating that they are forming an electrically continuous mesh. This is confirmed by comparing the sheet resistance with the conductive control samples in Table 5-1. It is also evident that the resistance decreases with increasing nanowire deposits, signifying that the amount of nanowires deposited is important.

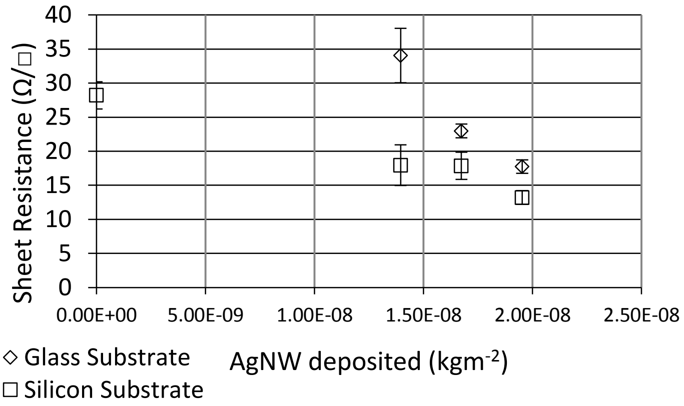

Figure 5-8: Sheet resistance of Ag nanowires on glass and silicon substrates, from Ross Jarrett, University of Leeds.

5.2.3 Yield of Ag-NW devices

The yield of the Ag-NW/TiO_2/Ti devices is shown in Figure 5-9. It is evident that about a quarter of devices failed, labelled ‘inactive’, i.e. did not give an I-V or photoresponse. The other ‘inactive’ category labels with corresponding I-V features increase this to 50% of devices fabricated failed to give a photoresponse. All of these inactive devices were made from the same batch of nanowires hence it was assumed that this particular batch was the main problem and not the deposition or post treatment of nanowires that had previously been successful. This is supported by the fact that a few different nanowire solutions were used and all of the other solutions produced devices with a photoresponse. Poor performing devices were analysed with the SEM however no distinct differences were visible. This indicates that more analysis of the nanowires is needed before use. As well as a poor performing batch of nanowires, lots of different deposition masses were trialled, those below a certain threshold failed. Through trial and error it was found that at least 15 µL of nanowires were needed on the substrate to give an I-V response, see section 3.4.3 for a more detailed description, and hence create an electrical continuous nanowire mesh.

Only 12% of devices were ‘exponential – active’, which is comparable to the evaporated silver device in Figure 4-1, however only a total of 50% of the Ag-NW devices produced a photoresponse. All of the ‘non-ideal - active’ devices, apart from two, had a forward bias exponential feature and a reverse bias response. The two exceptions to this were devices which gave an I-V response with more series and less leakage resistance, as in Figure 5-11 B. Overall, Figure 5-9 suggests that the nanowire devices are not as reproducible and have a higher variability, due to the nanowires produced, in comparison to the sputtered and evaporated films.

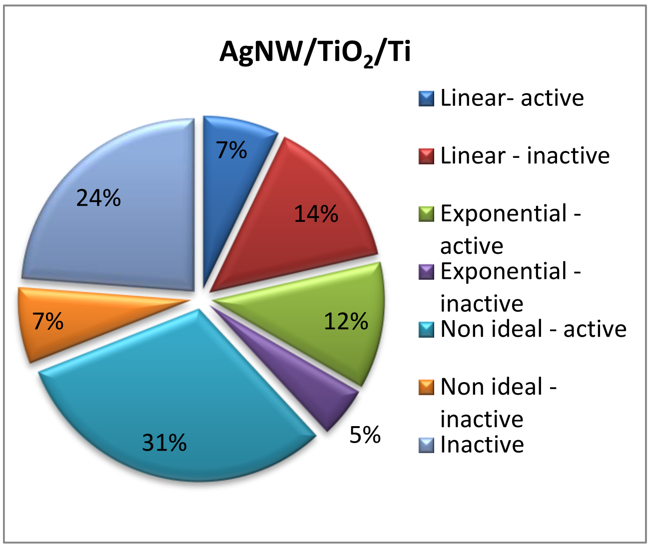

Figure 5-9: Yield of all Ag-NW/TiO$_2$/Ti devices. A total number of 42 devices were fabricated. I-V features are described by 'linear', 'exponential' and 'non-ideal'. A UV photoresponse is grouped as either 'active', i.e. giving a photocurrent and photovoltage, or 'inactive'.

5.2.4 I-V characterisation of Ag-NW devices

Similar to the Schottky devices in 4.3, I-V characterisation was undertaken to indicate the physical transport mechanisms at play in the NW devices. The method for this is outlined in 3.6.1. The results shown in Figure 5-10 and Figure 5-11 for Ag-NW/TiO$_2$/Ti Schottky barriers show similar 'ideal' and 'non-ideal' features to those presented for the M-S barriers, detailed in section 4.3. Furthermore, the Ag-NW/TiO$_2$/Ti short circuit current at 10 mAcm^{-2} is comparable to the Ag/TiO$_2$/Ti at 16 mAcm^{-2}.

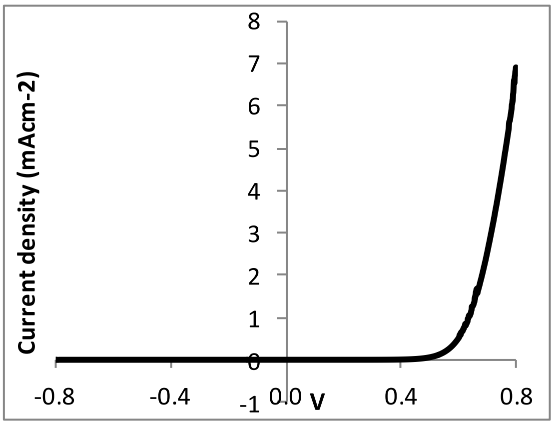

Figure 5-10: Optimum I-V characteristics, showing rectifying forward bias and saturated reverse bias in Ag-NW/TiO$_2$/Ti devices (sample 509).

Figure 5-11 presents a selection of typical non-ideal I-V features observed across the Ag-NW/TiO$_2$ Schottky barrier devices. Section 4.3 has already given a detailed discussion on the causes of some of these non-ideal features and so will not be repeated here. Noticeably different from the bulk Ag/TiO_2 devices is the presence of a large reverse bias, shown in Figure 5-11 A. This large reverse bias current displays typical tunnelling features. This feature is only observed in the Ag-NW/TiO_2 devices. The bulk metal layer devices sometimes have a reverse bias current, however the features are quite linear or a smaller exponential feature after -0.5 V (refer to Figure 4-3). Also significantly different is that the nanowire I-V curves have more 'noise', shown in Figure 5-11 A and C. This is due to the movement of nanowires under the probe tip, which confirms the presence of a conductive nanowire mesh, but also raises issues of adhesion to the TiO_2/Ti substrate. It has previously been indicated that I-V curves obtained through experiments of nanoscale diodes often deviate from that found in bulk materials [259-263].

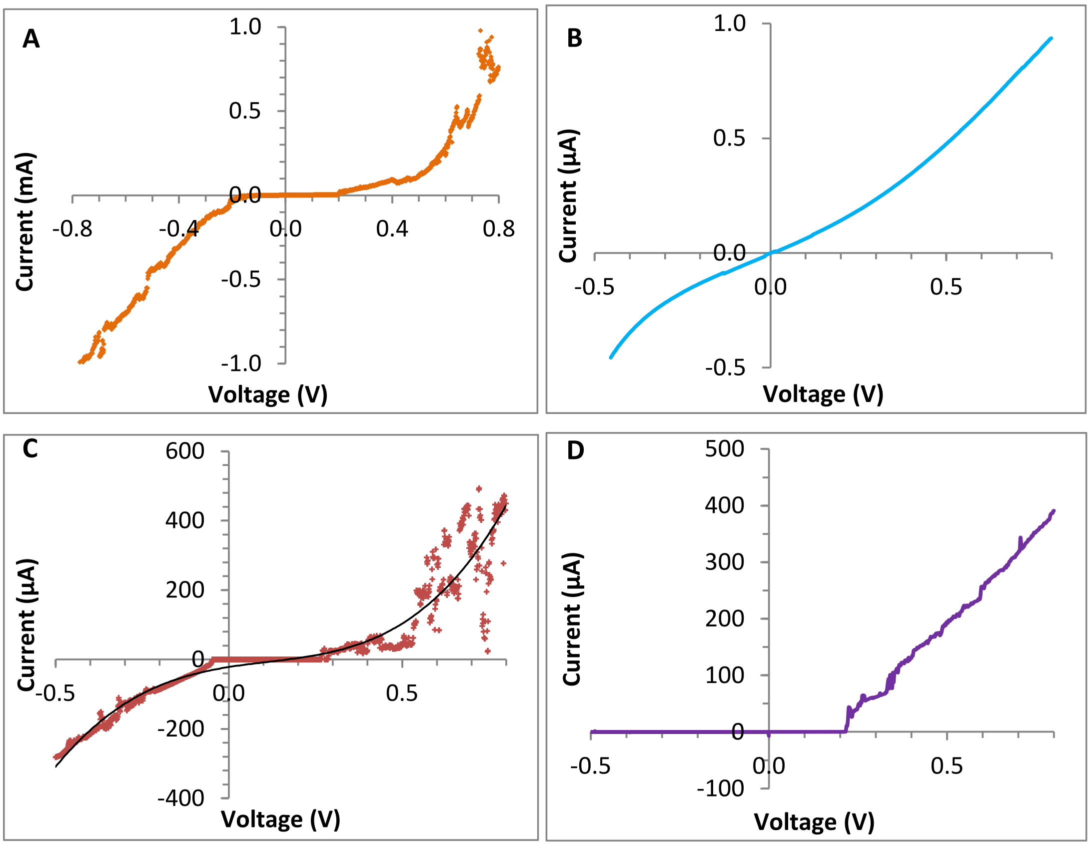

Figure 5-11: Typical non-ideal I-V features observed across Ag-NW/TiO_2/Ti Schottky barriers showing extensive reverse bias (sample 507) [A], Ohmic features (sample 301) [B], scattering of current data points (sample 601x2) [C] and a linear/exponential I-V composite (sample 101) [D].

Many studies have shown that the two main transport mechanisms in nanoscale devices are thermionic emission and tunnelling [255, 259, 260, 264]. As previously discussed in 4.3.8, the tunnelling current depends on the barrier height and thickness [259]. In nanomaterials the thickness of the barrier becomes a function of the diode and is determined by the size and shape of the diode rather than the doping level or carrier concentration. Barrier width decreases with decreasing diode size and hence a narrower barrier has been found for nanoscale Schottky devices [260]. This leads to a reduced resistance which further enhances tunnelling. Defects induced by the nanomaterials or an additional oxide layer surrounding the nanomaterials can further enhance tunnelling [255]. Since the whole device in this work was not nanoscale and the coverage area of the nanowires is shown to equate to a similar area to the evaporated films, the barrier width and thickness dependence on diode size will probably not apply, however defect assisted tunnelling, due to induced surface stress, can still occur and hence is probably the main explanation for tunnelling in the Ag-NW devices.

Tunnelling affects the forward and reverse I-V characteristics. Forward bias tunnelling will effectively reduce the leakage resistance, increase series resistance, and can lead to an increase in current. Tunnelling provides a reverse bias current which, depending on the magnitude of the current, can lead to an exponential reverse current as shown in Figure 5-12 [260]. The features associated with tunnelling are often observed in the Ag-NW devices, as is evident from a comparison of Figure 5-11 with Figure 5-12.

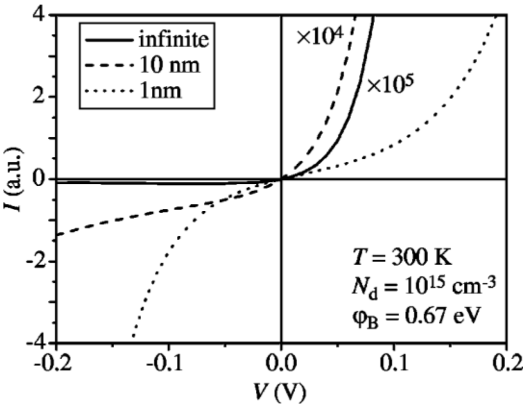

Figure 5-12: Effect of tunnelling on the I-V characteristics of nanoscale Schottky diodes, taken from [260].

Tunnelling is not dominant in all devices, as indicated by Figure 5-11 B and D, as a much smaller reverse bias leakage has also been found. Nanoscale Schottky diodes in the literature have also shown smaller reverse leakage currents [262, 263]. It has been shown previously that NCs formed on a semiconductor surface induce stress due to disorder at the interface, which creates defects [265]. This could enhance hopping transport, discussed in 4.3.5. Figure 5-11 B shows Ohmic current behaviour typical of hopping transport, which is also quite similar to that displayed in Figure 4-3 for bulk M-S devices. This indicates that hopping transport could be occurring in the NW devices. The experiments are not proof that the transport is 'hopping', to clarify this extra experimentation is needed, for example measuring the conductivity versus temperature for a device. Moreover, it is evident that similar current transport mechanisms can be found across both bulk and nanowire silver films. This is not unexpected since the TiO_2 substrate in all devices was processed in an identical way and this layer is responsible for substantial charge transport.

5.2.5 Schottky barrier height calculation of Ag-NW devices

Similar to section 4.4 an IDM and two EDMs (EDM 1: Iterative error reduction and EDM 2: gradient descent approach) were used to find the leakage resistance (R_L), series resistance (R_S), saturation current (I_S), ideality factor (n). The Schottky barrier height (SBH) was calculated assuming thermionic emission from the saturation current following the method outlined in 4.4.1 and Equation 4-5. The same methods were used for consistency and so that the Ag-NW/TiO_2 barriers can be compared against the bulk Ag/TiO_2 barriers. A more in depth discussion on these methods can be found in 4.4.1 and 4.4.2. Figure 5-13 and Figure 5-14 show representative IDM I-V curve fitting of ideal and non-ideal Ag-NW/TiO_2 Schottky devices respectively.

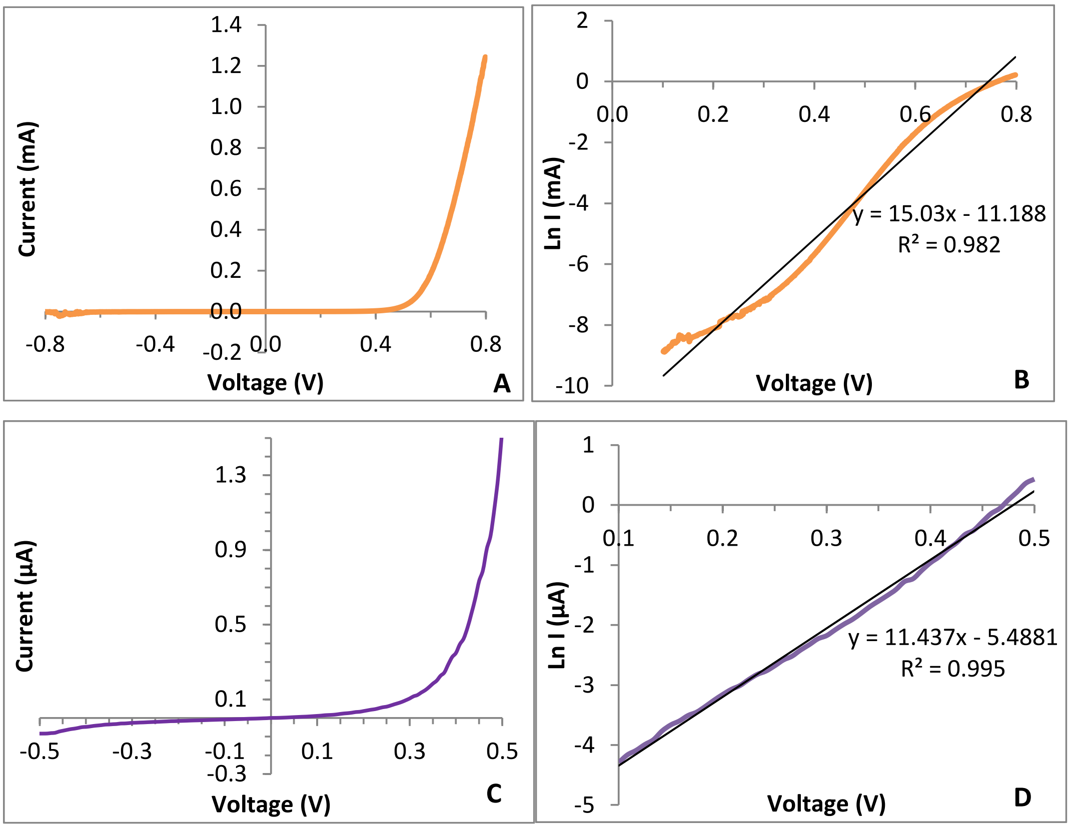

Figure 5-13: I-V curve fitting using the IDM of exponential I-V curves. [A-B] Sample 508 and [C-D] Sample 206x1.

The ideal I-V curve in Figure 5-13 A-B has a relatively poor fit between 0.2 – 0.4 V and again at 0.6V, which relates to the areas of high leakage resistance and series resistance respectively. Aside from the limitation of the IDM, previously discussed in 4.4.1, this deviation is similar to those found in Figure 4-13 for bulk films and represents electron tunnelling. The exponential curve with slightly less leakage resistance in Figure 5-13 C-D were found to have a better fit in the IDM, which suggests that thermionic emission over the barrier is the dominant mechanism in this device.

The ‘noisy’ I-V curves, mentioned previously in 5.2.4, obtained when characterising the nanowire devices caused obvious problems when curve fitting, as demonstrated in Figure 5-14 A – B. This scattering of data points is thought to be due to nanowire movement, but has previously not been shown in any other studies. It is evident that the fit for these types of curves presented a poorer fit than those with less scattering of data points. Figure 5-14 C -D shows that the IDM only accurately represents Schottky barriers with less leakage and series resistance, which agrees with the IDM curve fitting method and observations for bulk metal films in Figure 4-14.

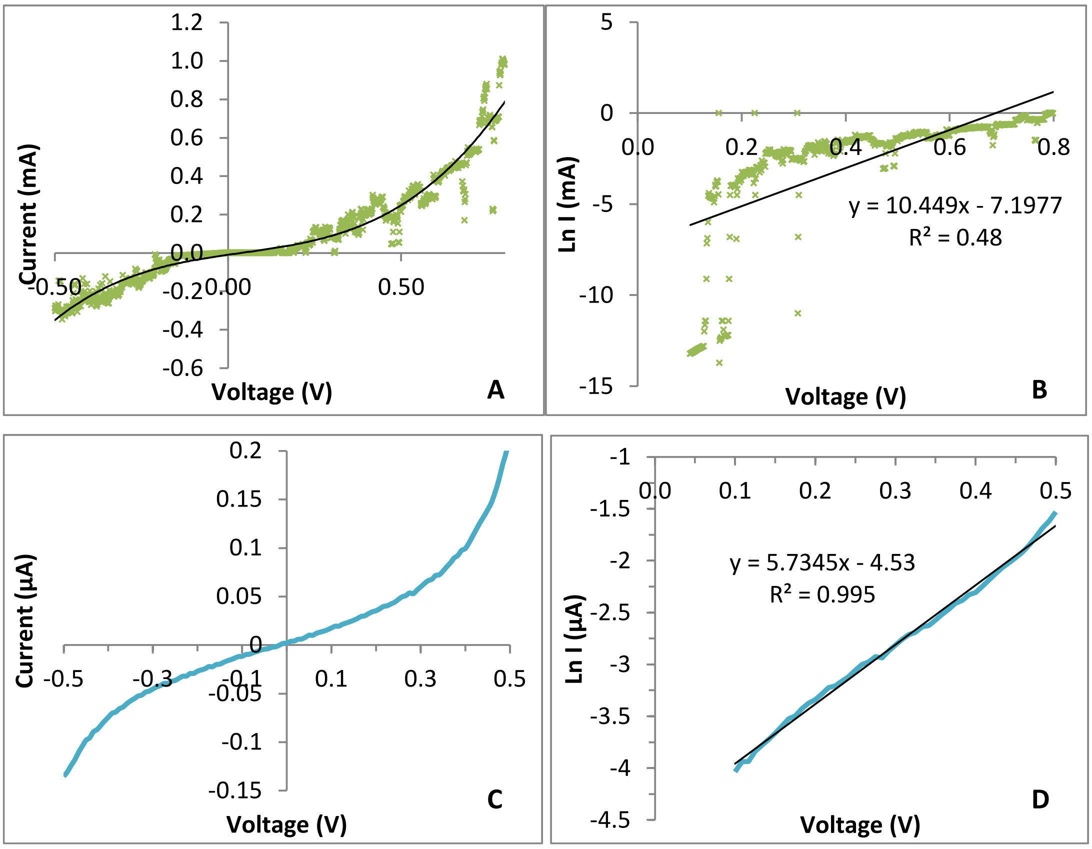

Figure 5-14: I-V curve fitting using the IDM for typical non-ideal I-V features seen across Ag-NW/TiO_2/Ti Schottky barriers showing extensive scattering (sample 601) [A-B] and less leakage resistance (sample 101) [C-D].

Table 5-2 shows the theoretical SBH calculated from the ideal relationship given in Equation 4-1, for Ag/TiO_2 Schottky barriers. Very few studies have researched the work function of silver nanowires, or more broadly silver nanomaterials. In the limited number of studies available a range of different silver nanowire work functions have been suggested. Yang et al [266] simply use the work function of bulk silver for their silver nanowires, whereas Ye et al [240] experimentally show that Ag-TCNQ (tetracyanoquinodimethane) nanowires have a work function of 5.45 eV. Hardin et al [267] alternatively suggest that the silver oxide work function (5.1 eV) can be used for silver nanowires that have been fabricated and stored in air, as is the case with the nanowires in this work, which gives a higher work function than silver. This is verified in other studies which further indicate the tendency of silver to adsorb oxygen which increases its work function [122, 140, 268]. However it has been more recently suggested that a thin layer of silver sulphide (5.32 eV) is created on the nanowire surface rather than silver oxide, over 24 weeks in ambient conditions [269]. Hence Table 5-2 represents the range of work functions and therefore theoretical SBHs for Ag-NW/TiO_2 Schottky barriers. It is clear that the SBH could be higher for Ag-NW/TiO_2 devices compared to a bulk silver equivalent device.

Table 5-2: Theoretical maximum Schottky barrier of Ag-NW/TiO_2 compared to evaporated Ag/TiO_2.

Schottky Barrier	ϕ_m(eV)	χ_s(eV)	ϕ_B (eV)
Ag/TiO_2/Ti	4.74	3.9 [230, 239]	0.84
Ag-NW/TiO_2/Ti	4.74 - 5.45		0.84 – 1.55

No study to date has compared the SBH of Ag/TiO_2 to Ag-NW/TiO_2, however a few studies have commented on the differences found between other nano and bulk metals. Table 5-3 shows a comparison between all of the Ag-NW/TiO_2 and Ag/TiO_2 Schottky barrier heights calculated from the IDM, described earlier in 4.4.1. Noteworthy is that the ‘experimental SBHs from literature’ in the table for Ag-NW devices relates to silver nanomaterials in general, since no studies to date have reported a SBH for an Ag-NW/TiO_2 Schottky device. The studies this data relates to are two studies on Ag nanoparticles sintered at 350°C on TiO_2, further details can be found in Table 4-2. Arguably the sintered nanoparticles could be considered as a bulk silver layer rather than a nanoscale layer.

It is clear from Table 5-3 that the Ag-NW devices have obtained higher Schottky barrier heights than the evaporated Ag/TiO_2 Schottky barriers. This aligns well with the higher theoretical SBH thought to be obtainable from NW devices in comparison to bulk films as described above. The differences between properties of nanoscale and bulk metals are relatively unknown, however, a few studies have demonstrated or outlined explanations for nano-metals giving higher SBHs. Landman et al [270] show that nanomaterials can achieve up to 90% higher SBH than their bulk counterparts, since nanowires have highly localised interfacial dipoles which further enhance FLP. Dag and Wang [271] agree that additional surface dipoles lead to FL lowering. Most other studies explain a higher SBH in terms of quantum confinement effects, i.e. a reduction in nanoparticle diameter gives an increasing SBH [262, 263, 265]. Hasegawag et al [265] indicate that the SBH they found for nanoscale metals were strongly dependant on the processing conditions. Processing induced disorder caused stress at the interface which created defects and disorder in the semiconductor and enhanced FLP. Furthermore, Hasegawag et al [265] found that all of the Schottky devices were inhomogeneous, giving different SBHs between devices, and this depended on the degree of induced disorder from processing. This could also explain the variation in the nanowire devices in this work.

Table 5-3: Comparison of calculated Schottky barrier heights and standard deviation for the Ag-NW/TiO_2/Ti and Ag/TiO_2/Ti devices using IDM. These are compared to the Schottky model values and Schottky barrier heights from the literature.

Schottky barrier	Calculated ϕ_B (eV)	Schottky model values from Table 4-1 (eV)	Literature values ϕ_B (eV)
Ag-NW/TiO_2/Ti	0.75 – 1.05 (+/- 0.1)	1.2	1.3 [268], 1.5 [140]
Ag/TiO_2/Ti	0.67 – 0.91 (+/- 0.1)	0.84	1 eV [122]

The Ag-NW device sample size was significantly larger than the Ag devices, hence the SD will be more accurate. Similar to the SD in Table 4-3, it is evident that the variation about the mean is similar across both device types, regardless of sample size. The variation between Ag-NW devices is 11% which is similar to the 10% average variation found for bulk films in Table 4-3. This is a significant result since there are many more possible variation pathways in the processing of Ag-NW devices, such as the chemical synthesis of the nanowires, deposition volume, area of nanowires after deposition, impact of heat treatment and further chemical changes during characterisation.

Looking at the correlation between closeness of fit and SBH it is clear from Figure 5-15 that the IDM is less suitable for the nanowire samples compared to the other devices, mainly because of the more ‘noisy’ I-V characteristics shown in Figure 5-14. Hence the EDMs were used to provide a better fit and hence more accurate measurements for device parameters.

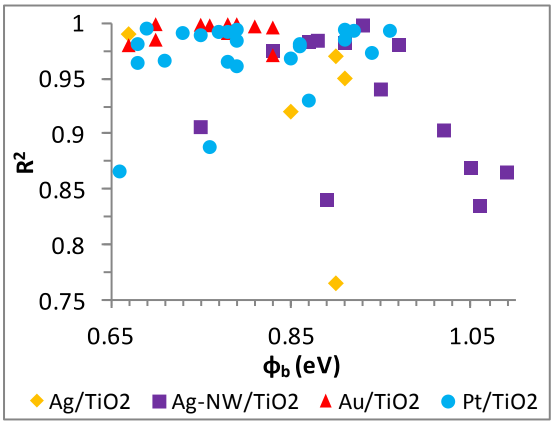

Figure 5-15: Schottky barrier height (ϕ_B) calculated from the IDM against the goodness of fit (R^2), showing the difference between Ag-NW devices and the other Schottky devices.

Similar to earlier work with the M-S devices in section 4.4, a range of representative samples from the Ag-NW/TiO_2 devices were selected to compare the parameters for R_L, R_S, I_S, R^2 and SBH between the IDM and the two EDMs. It is immediately clear from Table 5-4 that the fit of the data has improved significantly in both of the EDMs, compared to the IDM. The reasons for this have already been discussed in 4.4.1. Moreover, the EDMs do not appear to discriminate against the non-ideal I-V curves, obtaining equally high R^2 and SBHs after taking into account additional resistors. In some instances the SBHs have increased in both of the EDMs. With more accuracy in these approaches it is anticipated that these SBH are therefore more reliable. The highest SBH obtained for the Ag-NW devices has decreased from 1.05 eV in the IDM to 1.02 eV in EDM 2. This is still considerably higher than the bulk Ag/TiO_2 devices.

The series resistance in the IDM is generally over estimated, with reference to the EDMs, but it is still within the same order of magnitude indicating a good correlation between all three methods. The leakage resistance between the IDM and the EDM 2 align more closely than EDM 1 for the Ag-NW barriers. On the other hand, anything above $1e^6$ Ω generally displays the same features in both EDM 1 and 2. There are large differences in the saturation current between all methods for the Ag-NW devices, indicating the difficulty of measuring the nanowires due to the ‘noisy’ I-V curves. The ideality factors found by the EDM 1 are questionable since sample 101 obtains n = 0.74 which is incorrect as n = 1 is the lowest value possible and indicates ideality. This highlights the possible errors in EDM 1. The ideality factors found in EDM 2 are more consistent.

Table 5-4: R_S, R_L, I_S, n, R^2 and SBH for Ag-NW and Ag Schottky devices from IDM, EDM 1 and 2.

Sample	Metal	I-V type	IDM					
			R_S	R_L	I_S	n	R^2	SBH
206	**Ag-NW**	E-A	1.86E+05	8.06E+06	5.55E-09	3.38	0.982	0.91
508			80	7.19E+05	1.38E-08	2.63	0.983	0.87
509			185	1.72E+07	2.69E-10	1.98	0.985	0.97
601		N-A	339	5.68E+07	2.52E-08	1.80	0.869	1.05
101			1389	1.36E+06	2.15E-05	2.46	0.843	0.89
101x3			8.93E+05	5.13E+06	1.08E-08	4.03	0.935	0.95
AG5	**Ag**	E-A	25	6.45E+03	2.35E-08	5.54	0.917	0.85
AG4			90	1.83E+04	3.00E-09	4.02	0.965	0.90
AG3x1		N-A	6410	8.06E+06	2.04E-07	2.76	0.765	0.91
102			54	2.28E+03	3.03E-05	7.12	0.995	0.67
Sample	**Metal**	**I-V type**	**EDM 1**					
			R_S	R_L	I_S	n	R^2	SBH
206	**Ag-NW**	E-A	8.14E+04	5.87E+06	1.68E-09	2.70	0.99726	0.92
508			11	5.12E+18	1.68E-10	1.65	0.99984	0.98
509			3	2.04E+18	3.85E-10	1.95	0.99902	0.96
601		N-A	167	2.47E+03	8.49E-08	2.95	0.90797	0.82
101			1267	5.49E+17	1.34E-09	0.74	0.99638	0.93
101x3			7.17E-06	5.77E+06	1.17E-10	2.83	0.99937	0.99
AG5	**Ag**	E-A	108	1.08E+16	2.95E-06	2.38	0.99982	0.73
AG4			81	3.95E+16	2.99E-07	2.26	0.99897	0.79
AG3x1		N-A	4954	4.74E+05	5.58E-09	2.75	0.98807	0.89
102			87	2.43E+03	1.25E-06	3.23	0.99187	0.75
Sample	**Metal**	**I-V type**	**EDM 2**					
			R_S	R_L	I_S	n	R^2	SBH
206	**Ag-NW**	E-A	1.61E+05	3.05E+14	4.57E-10	1.88	0.98932	0.95
508			2	4.09E+07	1.04E-09	1.89	0.99970	0.93
509			23	1.70E+07	3.26E-11	1.64	0.99831	1.02
601		N-A	541	4.85E+07	8.93E-07	2.47	0.88582	0.76
101			1053	1.36E+06	1.10E-06	2.07	0.99305	0.76
101x3			1.12E+05	5.44E+06	3.87E-11	2.33	0.99904	1.02
AG5	**Ag**	E-A	123	1.76E+03	9.16E-09	1.17	0.99910	0.88
AG4			87	1.04E+04	4.44E-08	1.81	0.99890	0.84
AG3x1		N-A	6353	7.74E+07	1.03E-09	2.13	0.98453	0.93
102			138	2.00E+03	2.36E-10	1.24	0.99022	0.97

**I-V type column describes the Schottky barrier in terms of I-V features and photoresponse:*

E-A = exponential – active, N-A = Non-ideal-active.

5.2.6 Photoresponse of Ag-NW devices

The photoresponse of the Ag-NW Schottky barriers were tested using the same procedure explained previously for the other M-S barriers, see 3.6.1. The absorption of the Ag-NW Schottky barriers is expected to be similar to the other M-S barriers due to the TiO_2 in the device. The normalised photocurrent and photovoltage of some of the optimum devices are presented in Figure 5-16. Similar to the bulk M-S devices a peak at 330 nm is evident, see C and D, which is due to the TiO_2 bandgap absorption. Similar to the M-S devices in Chapter 4, the UV fall off at short wavelengths is likely due to a reduction in power from the arc lamp, combined with a reduction in device efficiency.

A second notch or small dip in the UV range is immediately evident. This is due to surface plasmons creating additional scattering, due to the plasmonic effect. This second dip has not been observed in the bulk silver film and so has to be attributable to the use of nanowires rather than a film. Nanoparticles are known to have a plasmonic effect - a plasmon is an oscillation of electrons in a metal which leads to resonance features in optical spectra [272]. The oscillating plasmons create high electric fields at the surface of the metal, which can lead to enhanced optical transmission due to excitation of the plasmon. It has been shown by many that surface plasmon resonance occurs with silver nanoparticles on the surface of silicon solar cells, enhancing the short circuit photocurrent up to 8 times, increasing the photocurrent below 500nm [272] or across the entire solar spectrum [273], and enhancing the overall efficiency [274]. This is because the plasmons act as a forward scattering layer and therefore enhance absorption [272, 274].

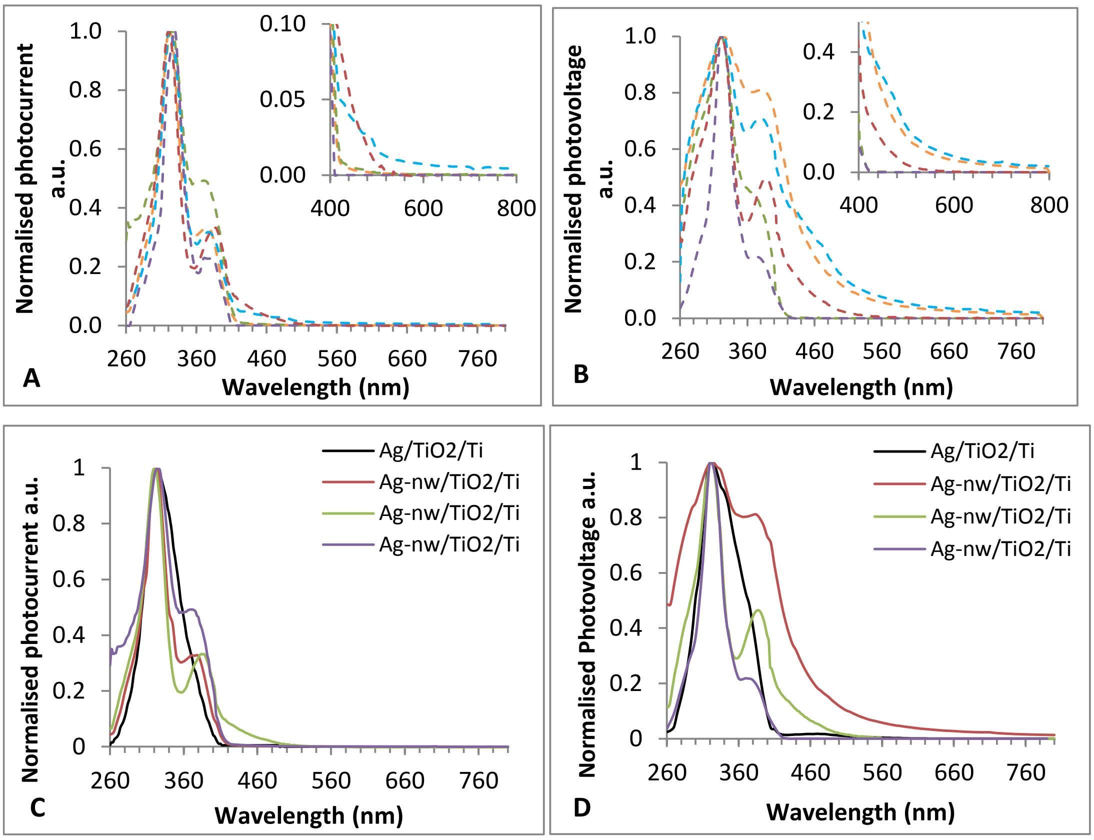

Figure 5-16: Normalised photocurrent [A] and photovoltage [B] for optimum Ag-NW/TiO$_2$/Ti Schottky barriers. The Inset graphs highlight the response between 400 – 800 nm. The photocurrent and photovoltage against a representative Ag/TiO$_2$ Schottky barrier (black line) is displayed against a selection of the Ag-NW devices in [C] and [D] respectively.

In addition to the second dip in the photoresponse discussed above, there is a significant visible photovoltage and a small visible photocurrent, as shown in the inset to Figure 5-16. Previous work has shown that TiO$_2$ coated with silver nanoparticles can absorb in the visible range, this is attributable to surface plasmon resonance [123, 254, 258, 275, 276]. For example, Veres et al [258] show absorption characteristics for their Ag-nanocrystal/TiO$_2$ Schottky barrier (see Figure 5-17) that are in-line with the photoresponse characteristics observed in Figure 5-16. An Ag/TiO$_2$ Schottky barrier has also been shown by Liu et al [76] to act as an electron trap where electrons accumulate, leading to enhanced separation of electrons and holes, and hence, increasing absorption. Therefore, the photoresponse of the TiO$_2$ in the visible range, shown in Figure 5-16, is likely due to the effect of the deposited nanowires.

Unlike the visible photovoltage, the visible photocurrent is significantly smaller in magnitude, which suggests that the mechanism for providing the photocurrent is not very efficient. Refining the nanowires, for example by additional filtering to remove spherical particles or employing a more suitable deposition method to attain a more even distribution of nanowires, could potentially result in an improved photocurrent.

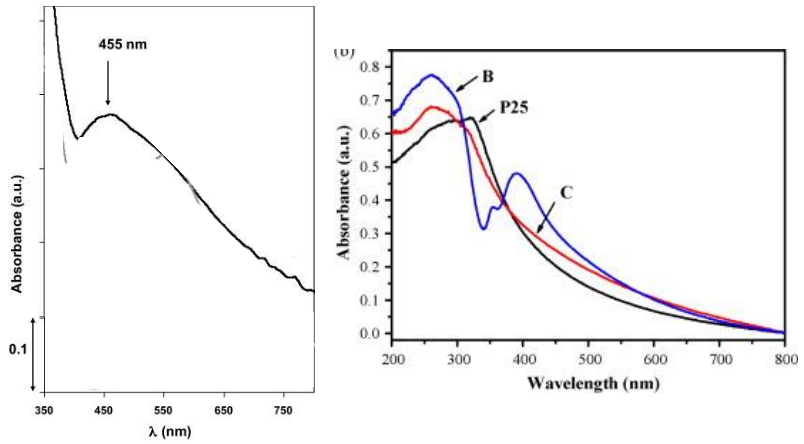

Figure 5-17: [Left] Absorbance vs wavelength of Ag-NCs photodeposited on a TiO_2 substrate, taken from Veres et al [258]. [Right] Absorbance versus wavelength of Ag/TiO_2 composite nanowires (line B) taken from Cheng et al [253].

Table 5-5 displays the maximum photocurrent and photovoltage measured at 300 nm compared to the bulk silver Schottky barriers. The Ag-NW/TiO_2 barrier has obtained a higher photovoltage but underachieves significantly with the photocurrent density. Considering the variation in nanowire loading and the non-uniform nature of the nanowire mesh, see SEM images in Figure 5-7, the lower current is probably due to inefficient charge transport through the mesh. This indicates that the nanowire mesh requires further refinement. The fact that the nanowires obtained a higher photovoltage suggests that they have a higher potential than the silver evaporated films.

Table 5-5: Comparison of maximum photocurrent and photovoltage for bulk silver and silver nanowire Schottky barriers at 330 nm.

Device	Maximum Photocurrent density μAcm^{-2}	Maximum Photovoltage mV
Ag-NW/TiO_2/Ti	18.4	397
Ag/TiO_2/Ti	237	281.6

The EQE for the optimum Ag-NW/TiO_2/Ti device was 0.43% at 330 nm and 0.08% at 390 nm (where the second shoulder was commonly found across devices).

5.2.7 Ag-NW/TiO_2 device variability

Considerable variability is experienced when characterising the nanowire substrates, since the nanowires are thought to move underneath the probe, due to poor adhesion with the substrate. I-V and photoresponse results are not always consistent over the surface of a nanowire substrate, unlike the sputtered and evaporate M-S barriers. This is due to the fact that when the probe is positioned at the edge it is in contact with a more agglomerated silver mesh than when the probe is in the middle of the sample, as displayed in Figure 5-7.

Figure 5-18 displays this variability in photoresponse during characterisation of an Ag-NW/TiO_2 sample. All measurements were recorded during the same testing period (approximately 1 hour). The probe was bought down on 3 points across the surface, including the centre, edge and mid-section. Central positions on the device tended to give reproducibly higher photoresponses, shown by position 2 in the graphs below. This suggests that the agglomerated nanowires at the edge are less efficient at transporting electrons than the sparser yet electrically continuous areas. It was generally observed that photovoltage was more variable than the photocurrent, with ~100 mV change compared with ~0.1 µA change respectively. The variability in the photovoltage is so great that some responses indicated extensive visible absorption compared to other positions on the same sample.

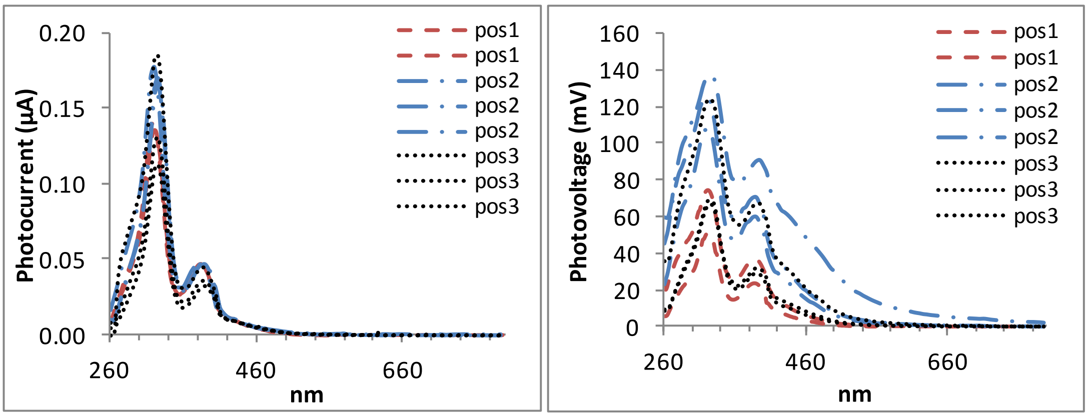

Figure 5-18: Variability within measured photocurrent [Left] and photovoltage [Right] of one Ag-NW/TiO_2/Ti device (sample 206). Legend labels relate to the position across the substrate - Position 1 = edge, position 2 = central and position 3 = is between the edge and centre.

It is evident that the variability of Ag-NW/TiO_2 simply depends on further refinement of the nanowire deposition. More reproducible results would be expected from a uniformly distributed and nanowire mesh.

5.2.8 Silver nanowire degradation

The silver nanowires were not treated or protected by a capping agent, to reduce the possibility of insulating the wires. The lifetime of the nanowires was assumed to be low because of this, since silver nanowires can oxidise in air easily, which therefore may impact the performance of the device. Hence, a degradation test was undertaken to test the response of nanowires over time.

An optimum Ag-NW/TiO_2 device with reproducible results was kept in a sealed plastic container and tested 1 week after initial testing and then again 6 months later. The results of the degradation of the device are presented in Table 5-6 and Figure 5-19. Table 5-6 presents the Schottky barrier height for an Ag-NW/TiO_2 device over the testing period. It is clear that the Schottky barrier height remains comparable within a week, with a small change of 0.01 V which is likely to be due to experimental variations rather than degradation, but the barrier height does decrease after 6 months by 8 times this initial change. This notable decrease in the barrier height will allow electrons to more easily flow over the M-S interface. This suggests that the device has become less resistive, which is confirmed by the I-V curve shown in Figure 5-19.

Table 5-6: Calculated Schottky barrier height for an Ag-NW/TiO_2/Ti device over 6 months (Sample 206).

Time period	Calculated Schottky Barrier height (eV)
Initial	0.95
1 week	0.96
6 months	0.87

It is difficult to come to firm conclusions based on the I-V curve in Figure 5-19 due to the initial measurements only being taken up to 0.5 V rather than 0.8 V. However, at 0.5 V the current for the 6 month data is 4 μA, which is ~2.5 times larger than the initial tests. A larger current at the same voltage indicates that the device has become less resistive. If the nanowires had oxidised we would expect to see more resistive features and hence a lower current. This decrease in resistivity could be due to surface states that could exist due to the nanowires which may help promote electron transport.

Figure 5-19 also shows the photoresponses for the Ag-NW/TiO_2/Ti device over 6 months. Due to the response variability described above, the minimum and maximum photoresponse values were included for the 6 month data against the maximum values for the initial tests. It can be seen in Figure 5-19 that the photoresponse for the initial and 1 week tests are comparable. The maximum photoresponse for the 6 month old device exceeds the maximum photoresponses gained previously by the same device, which indicates an improvement, however the responses are very variable. Averaging the photoresponses indicates that at the very least the device has not degraded over time and if possible an improvement has been seen. Koole et al [100] suggest that a Schottky barrier can be recovered by exposing the device to oxygen and/or water vapour, which correlates with the ambient conditions used in this characterisation. More exhaustive tests need to be carried out to conclude whether the aged device has remained stable over time.

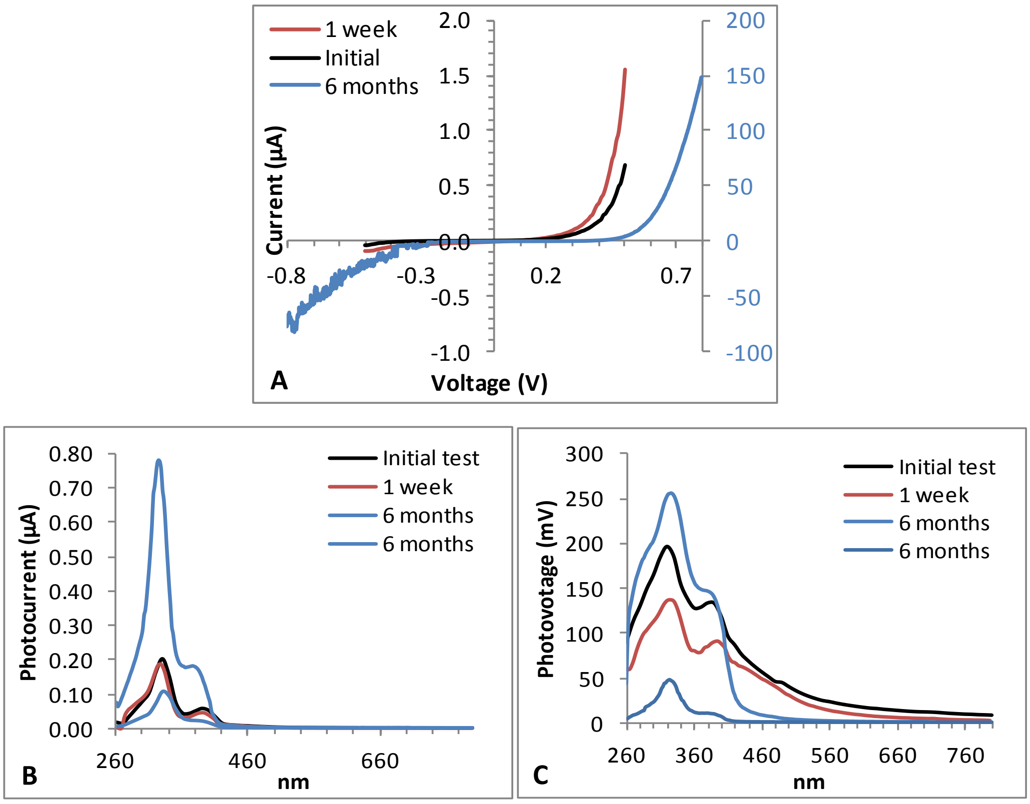

Figure 5-19: Difference in I-V characteristics and photoresponse of an Ag-NW/TiO_2/Ti Schottky barrier (sample 206) over a 6 month period. [A] I-V - 6 month curve plotted on the secondary axis. Degradation over 6 months of photocurrent [B] and photovoltage [C]. Additional 6 months test photoresponse data input due to large variability of responses. Initial and 1 week tests show the maximum values obtained.

5.3 Summary of main findings

This chapter has presented results and discussions on the use of alternative transparent and conductive thin films for the use in a Schottky barrier solar cell, to provide more reproducible metal films and further reduce fabrication costs. Firstly, silver electrodeposition on to TiO_2/Ti substrates was trialled, using various silver containing electrolytes and two different techniques – standard and strike electrodeposition. Overall, dendritic and sporadic silver growth was obtained, which was similar to other work in this area. There were some early signs of a continuous layer being produced, but this was largely uncontrollable, often also forming large silver agglomerations and was not well adhered to the surface. Due to the unsuccessful experimentation of silver electrodeposition, it was discontinued as a route to produce the electrically continuous film required.

A more successful electrically continuous film was provided by a silver nanowire mesh. Silver nanowires were produced by chemical synthesis and were subsequently dropcast on to the substrate, allowing more control during experimentation than electrodeposition. There were many similarities between the I-V characteristics and therefore transport mechanisms of the NW Schottky devices and the M-S devices in Chapter 4. The main differences were the ‘noisy’ features in the I-V curves, due to nanowire movement under the probe tip, and more extensive tunnelling, which is common to nanocrystal Schottky barriers. Ag-NW devices obtained the highest SBH of 1.02 eV in the EDM calculation which is significantly higher than all of the M-S devices in Chapter 4. This may be due to annealing which may unintentionally diffuse Ag into the surface, or due to highly localised states at the interface which leads to FLP. The photoresponse of the Ag-NW devices showed a second distinctive shoulder in the UV range extending into the visible region. This additional photoresponse is due to a plasmon effect of the nanowires. It can also be emphasised by the localised states at the M-S interface. Unlike the photovoltage, the photocurrent is significantly lower than the other M-S devices, which suggest that the mechanism for providing the photocurrent is not very efficient. The fact that the NWs have agglomerated on the surface could explain this. Using an alternative deposition method, for example spray deposition or spin casting, may overcome the problem of agglomeration to achieve a more uniform finish. Compared to the other M-S devices the NW devices experienced a much larger device variability, which indicates that further work is needed to obtain a more consistent and reproducible technique for the production of nanowires.

Chapter 6

Nanocrystal Activated Schottky Barrier Solar Cells

Chapter 4 and Chapter 5 have presented an in depth study of Schottky barriers using a variety of noble metals and techniques, for the intention of use in the nanocrystal activated Schottky barrier solar cell. The conclusions drawn from these chapters were that the sputtered Pt/TiO_2 and Ag-NW/TiO_2 Schottky devices provided the highest reproducibility and best performance in terms of a high SBH and photoresponse, than the other Schottky devices. Hence, these two devices were selected for use in the nanocrystal activated Schottky barrier device. This chapter presents the results of the deposition of a variety of visible absorbing semiconducting nanocrystals on to the Pt or Ag-NW Schottky devices, and hence the complete nanocrystal-activated Schottky barrier device. The aim of this work was to obtain a visible photoresponse from the nanocrystals, as well as maintaining the UV response from the Schottky barriers, to confirm that the complete device is operational.

The Schottky devices were fabricated as described in 3.3 and 3.4. CdS, CdSe, $CuInS_2$, CuO and CdTe semiconductor nanocrystals, with absorbing capabilities between 420 – 800 nm, were drop cast on the surface of the Schottky devices and annealed as described in Table 3-9. The motivation for nanocrystal selection and deposition are centred on low cost fabrication, bandgap alignment and visible absorption capabilities, further described in 3.5. The various concentration, mass loadings, deposition and post deposition treatment of nanocrystals are also outlined in 3.5. Optical characterisation of the nanocrystals to confirm their absorption range is given at the start of this chapter as a reference point for the rest of the photoresponse results. The first half of this chapter presents results and discussion on the NC/Pt/TiO_2/Ti devices and the second half on the NC/Ag-NW/TiO_2/Ti devices. I-V and photoresponse data are analysed to confirm the current transport mechanisms and show which nanocrystals are activating the Schottky devices. Table 6-1 gives an overview of the devices, detailing which nanocrystals were found to give a visible photoresponse on the respective Schottky barrier devices. A summary of all nanocrystal activated devices can be found in Appendix D.

Table 6-1: Summary of nanocrystal activated Schottky barrier cell results.

Section number	Schottky Barrier	NC type deposited	New visible photoresponse due to NC	Amplified M-S barrier visible photoresponse	No extra visible photoresponse features
6.5.1	**Pt/TiO$_2$/Ti**	CdS	X	X	
6.5.2		CdSe			X
6.5.3		CuO		X	
6.5.4		CuInS$_2$			X
6.5.5		CdTe	X		
6.6.1	**Ag-NW/TiO$_2$/Ti**	CdS	X		
6.6.2		CdSe		X	
6.6.4		CuO	X		
6.6.3		CuInS$_2$	X		
6.6.5		CdTe	X	X	

6.1 Yield of devices

A total of 26 NC/Pt/TiO$_2$/Ti devices (NC devices) and 24 NC/NW/TiO$_2$/Ti devices (NC/NW devices) were fabricated. Figure 6-1 and Figure 6-2 display all of the NC devices with respect to the I-V and photoresponse given by each device. Similar to the other device yields given in Figure 4-1 and Figure 5-9 the 'linear', 'exponential' and 'non-ideal' relate to I-V features and 'UV active', 'UV + visible active', 'inactive' represents the photoresponse of the devices. To be grouped in 'linear' or 'exponential' the devices must fit well to this description. The 'non-ideal' I-V features mainly relate to devices with a linear reverse current and shallow forward bias current gradient. 'UV active' indicates that the nanocrystals are not absorbing any visible light and the device is only UV active, as was the case for the Schottky devices presented in 4.5 and 5.2.6. 'UV + visible active' therefore indicates that the nanocrystals are active and absorbing visible light in addition to the UV light that is being absorbed by the TiO$_2$. Only devices with a 'visible active' photocurrent and photovoltage are considered as 'UV + visible active'. There were a few devices that showed either a visible photocurrent or a visible photovoltage, these were considered as 'UV active' only, since both were required to confirm that the device is operating fully.

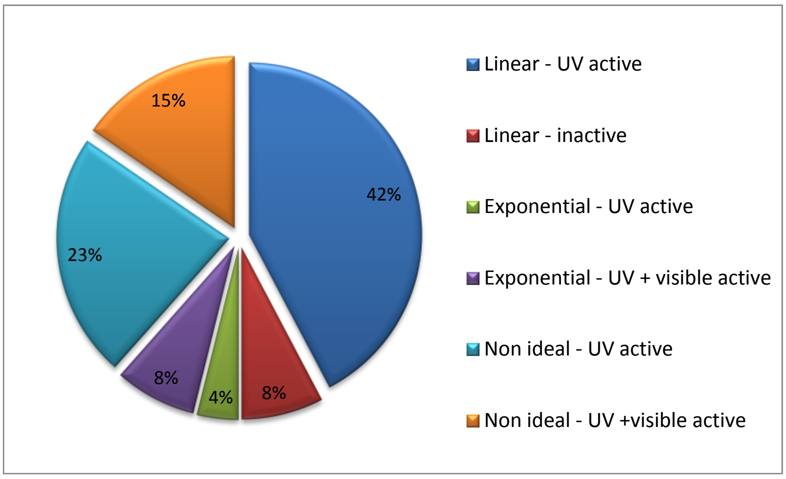

Figure 6-1: Yield of NC/Pt/TiO_2/Ti devices, including all NC varieties. I-V features are described by 'linear', 'exponential' and 'non-ideal'. 'Active' and 'inactive' describe whether the device provided a photocurrent and photovoltage or not.

No 'linear – UV + visible' devices exist either in the NC/Pt or NC/NW devices. This is expected and confirms the need for a Schottky barrier for the architecture to operate. For both architectures, there were approximately 1 in 6 'non ideal – UV + visible' photoresponse devices. The causes for non-ideal I-V features have already been discussed in 4.3 and will not be repeated here since the same mechanisms are expected due to the I-V features still being representative of the Schottky devices regardless of the nanocrystals. Some of the NC devices had exponential forward bias characteristics, but were put in the 'non-ideal' category due to having a defined reverse bias current response.

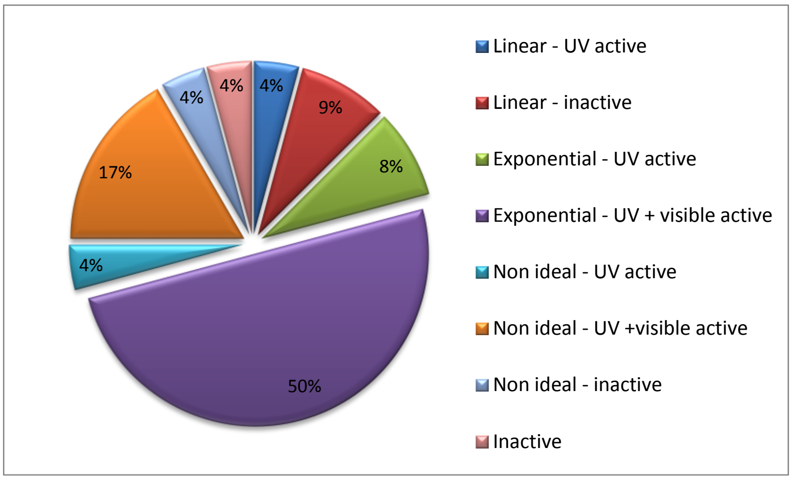

Figure 6-2: Yield of NC/NW/TiO_2/Ti devices, including all NC varieties. I-V features are described by 'linear', 'exponential' and 'non-ideal'. 'Active' and 'inactive' describe whether the device provided a photocurrent and photovoltage or not.

Comparing Figure 6-1 with Figure 6-2 it is evident that the NC/NW devices were overall more successful, with a total of 67% devices giving a UV and visible response. The poor performance of the NC/Pt devices, with only 23% success, appears to be due to the deterioration of the Schottky barrier between the Pt and TiO_2. This is hinted at in Figure 6-1, with only 8% of devices forming a Schottky barrier, compared to the 58% NC/NW devices. I-V characteristics of NC/Pt devices were analysed before and after nanocrystal deposition showing that a Schottky barrier between Pt/TiO_2 device deteriorates post NC treatment, discussed further in 6.5.

6.2 Nanocrystal characterisation

All of the nanocrystals were synthesised by external sources, as described in Table 3-7. Characterisation of the nanocrystals by TEM, fluorescence and absorption spectroscopy were provided by the manufacturers. To confirm the properties of the nanocrystals, or provide a form of characterisation if none were given by the manufacturer, UV visible spectroscopy was carried out in-house. This involved depositing the nanocrystal solution on a glass slide and drying in air before testing in the UV-vis. Nanocrystal solutions were also annealed onto the glass slides and retested to verify the effect of annealing at the temperatures given in Table 3-9.

Characterisation of CdS nanocrystals is presented in Figure 6-3 and Figure 6-4. It is clear from Figure 6-3 that the absorption of the CdS nanocrystals is at 440 nm in both of the absorption plots. This good agreement between the separate characterisations, undertaken by the University of York and in house, confirms the absorption features and also indicates that the nanocrystals are stable over time, since the in-house characterisation was carried out approximately 3 months after receiving the nanocrystals in solution.

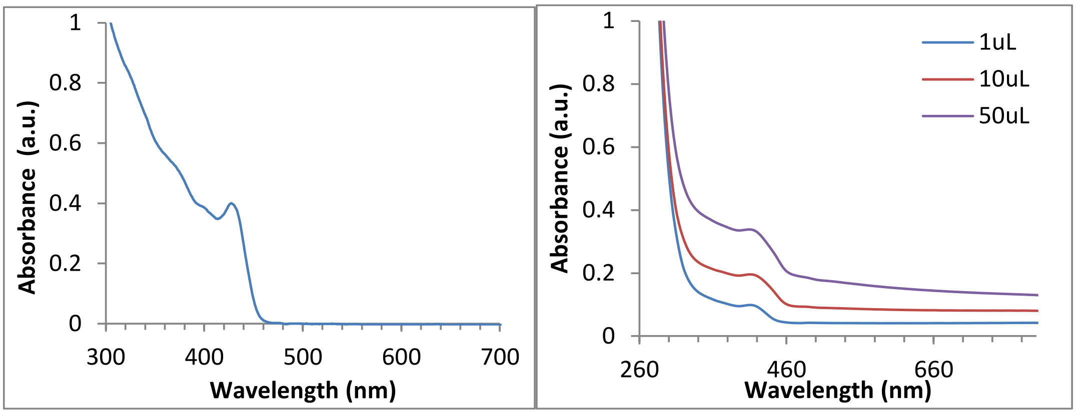

Figure 6-3: Absorbance of CdS nanocrystals showing an excitonic peak at 440 nm, courtesy of Robert Mitchell, University of York, [Left] and UV vis absorption showing an excitonic peak at 440 nm for three mass loadings of CdS nanocrystals [Right].

The TEM image of the CdS and CdSe nanocrystals in Figure 6-4 show that both types of nanocrystals are uniformly dispersed and spherical. Uniformly dispersed nanocrystals are desirable for the device to enable more effective light absorption and transfer to the metal contact. The CdSe nanocrystals are larger than the CdS nanocrystals with diameters of 5 nm and 3 nm respectively.

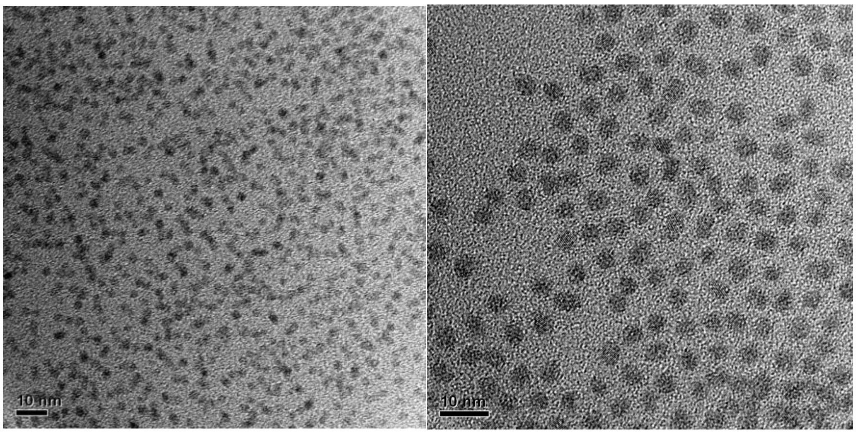

Figure 6-4: TEM images of CdS [left] and CdSe [right] nanocrystals, courtesy of Robert Mitchell, University of York.

The characterisation of CdSe nanocrystals is presented in Figure 6-4 and Figure 6-5. In Figure 6-5 the UV vis of non-annealed CdSe NCs shows a small peak at 600 nm that correlates well with the fluorescence emission which also peaks at 600 nm. There are also some reproducible absorption features at shorter wavelengths which is expected. The excitonic peak of the annealed CdSe-NC device is red shifted in comparison to the non-annealed devices, with an absorption edge at 650 nm. In comparison to the CdS NCs the CdSe NCs show a much shallower and noisier absorption edge. The fact that the CdSe NCs are larger and less uniformly dispersed than the CdS NCs (see Figure 6-4) may account for this.

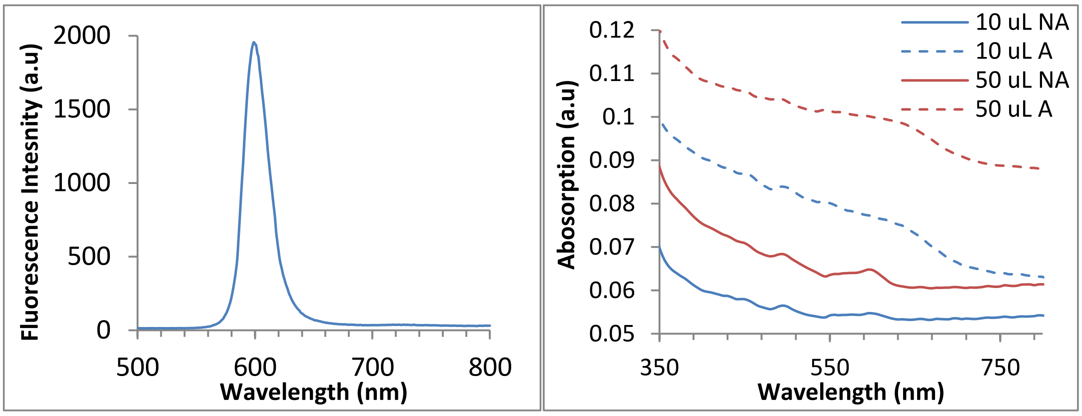

Figure 6-5: Fluorescence intensity against wavelength for CdSe nanocrystals [Left], showing absorption between 570 – 660 nm, courtesy of Robert Mitchell, University of York. UV Vis absorption of CdSe nanocrystals [Right] characterised pre and post annealing (NA – not annealed, A – annealed). The NA excitonic peaks show two distinct peaks, the first at 500 nm and the second at 600 nm.

Figure 6-6 shows the size and absorption of the Cu_2O nanocrystals, given by the manufacturer [277]. The particle size on the provider's website is given as < 350 nm, which is in agreement with the SEM image showing a size of approximately 200 nm. The absorption range of Cu_2O NCs is shown in Figure 6-6 to be quite wide, with a clear excitonic peak at ~520 nm. However UV Vis spectroscopy undertaken in-house showed no clear excitonic peak from the nanocrystals (and hence is not shown here), but did show a vague absorption range between 400 – 600 nm.

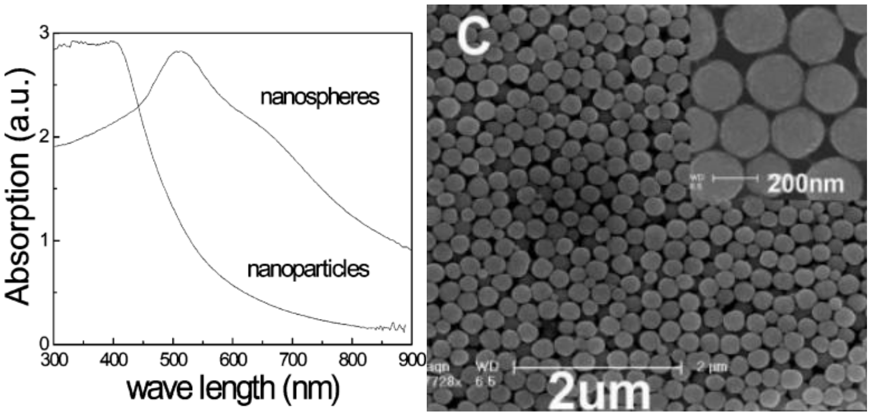

Figure 6-6: Excitonic peak of Cu_2O [left] and SEM of Cu_2O nanospheres [right], sourced from Sigma Aldrich, images taken from [192][1].

Figure 6-7 shows the UV Vis absorption of $CuInS_2$ nanocrystals. Unfortunately no characterisation was provided by the manufacturer. The absorption of the nanocrystals is weak, having only a shallow absorption edge around 560 – 580 nm.

---

[1] As of September 2013 the Cu_2O NCs synthesis reference from Zhang et al 192. Zhang, J., J. Liu, Q. Peng, X. Wang, and Y. Li, *Nearly Monodisperse Cu2O and CuO Nanospheres: Preparation and Applications for Sensitive Gas Sensors.* Chemistry of Materials, 2006. **18**(4): p. 867-871. no longer appears on the Sigma Aldrich website. No explanation has been given, but it is thought that the NCs from this source were discontinued.

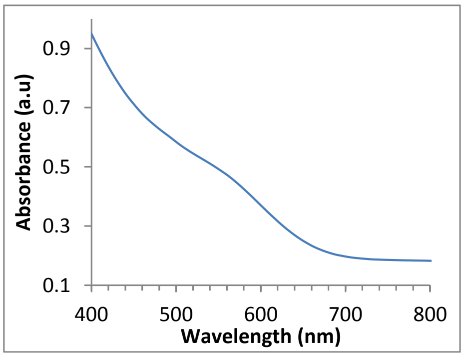

Figure 6-7: $CuInS_2$ NC UV visible absorption. A shallow absorption peak is evident around 560 nm.

Figure 6-8 presents UV Vis absorption for CdTe nanocrystals and correlating luminescence intensity showing the emission peak range for each CdTe NC colour, from the manufacturer. The in-house UV vis shows that the green and yellow CdTe nanocrystals have the most distinctive excitonic peaks and are in agreement with the manufacturer's guidelines of 510 – 550 nm for the green CdTe NCs and 560 – 580 nm for the yellow CdTe NCs. Orange, ruby and red CdTe nanocrystals have weaker excitonic peaks, in comparison to the green and yellow CdTe NCs, but still approximately follow the manufacturer's specification, given in the legend.

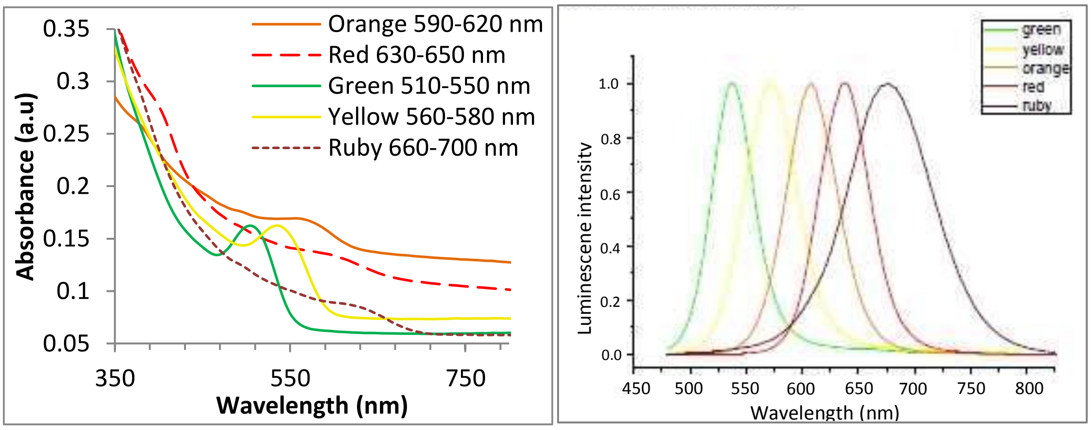

Figure 6-8: UV-vis absorption of CdTe NCs that have not been annealed [Left]. The nanocrystals show good alignment with the given emission wavelength peaks, in the legend, provided by the manufacturer. Typical CdTe luminescence intensity for all CdTe nanocrystals [Right] was also provided by the manufacturer [278].

Table 6-2 summarises the above nanocrystal characterisation. It is evident that the nanocrystal excitonic peaks and absorption ranges are similar to those given by the manufacturers. The CdS NC excitonic peak correlates very well, whereas the excitonic peaks of all of the CdTe nanocrystals occur at the lower wavelengths of the range given by the manufacturer. The excitonic peaks for the CdSe, $CuInS_2$ and Cu_2O NCs are less clear compared to the CdS and CdTe NCs, however the absorption ranges measured still correlate well with manufacturers' guidelines.

Table 6-2: Summary of nanocrystal characterisation from the manufacturers and in-house characterisation.

Nanocrystal	Absorption peak/range external source	Optical absorption features measured (pre annealing)
CdS	440 nm	440 nm
CdSe	575-660 nm	500 and 600 peaks
CdTe – orange	590 – 620 nm	590 nm
CdTe – red	630 – 650 nm	630 nm
CdTe – green	510 – 550 nm	510 nm
CdTe – yellow	560-580 nm	550 nm
CdTe – ruby	660 – 700 nm	640 nm
$CuInS_2$	n/a	560 nm
Cu_2O	~ 520 nm	400 – 600 nm

Figure 6-9 shows the band alignment for the NCs used in this work against TiO_2. The energy gap was calculated from the absorption wavelength using the relationship given in Equation 4-7. In all cases, apart from the Cu_2O NCs, the excitonic peak from in-house UV Vis spectroscopy was used to find the energy gap, over the manufacturers indicated absorption peak/range. Since none of the nanocrystals have been intentionally doped, it was assumed that the Fermi level lies in the centre of the bandgap for the nanocrystals. The position of the TiO_2 is based on the Schottky barrier height calculated in section 4.4. The highest SBH calculated for Pt/TiO_2 and Ag-NW/TiO_2 barriers was 1 eV and 1.02 eV respectively.

The conduction bands of all of the nanocrystals sit above that of TiO_2, which is desirable for electron transport over the barrier into the TiO_2. In some instances the distance between the conduction band of the nanocrystals and the TiO_2 is very small, for example with CdTe red, CdTe ruby and $CuInS_2$ NCs. In these cases we would anticipate more efficient electron transport due to less energy wasted. The valence bands for all of the nanocrystals are over 1 eV, which provides another energy loss mechanism.

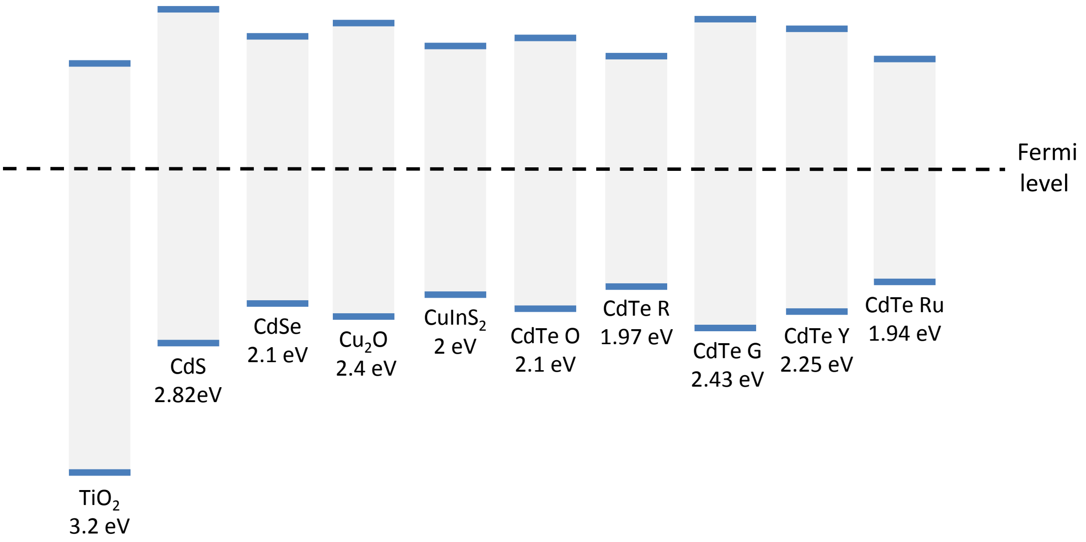

Figure 6-9: Band alignment diagram of TiO_2 in comparison to all nanocrystals used in the nanocrystal-activated device. All energy levels are referenced to the vacuum level, which is assumed to sit in the centre of all nanocrystals.

Table 6-3 presents a comparison of three bandgaps for each of the nanocrystals. The first two columns are NC bandgaps calculated from the manufacturer's information and from in-house UV visible absorption spectroscopy using Equation 4-7. The third column shows the bandgap of the bulk material. It is evident that there are some differences in the calculated bandgap from the manufacturer's information and the UV Vis spectroscopy. However, as expected there is a larger difference between the NC bandgaps and the bulk material bandgap, with the bulk material giving a reduced bandgap.

Table 6-3: Bandgaps of nanocrystals calculated from the manufacturer's information and in-house UV visible absorption spectroscopy compared to the bulk material bandgap.

Nanocrystal	Bandgap (eV)		
	Manufacturer	UV vis spectroscopy	Bulk material
CdS	2.82	2.82	2.42 [279]
CdSe	1.88-2.16	2.1 – 2.48	1.74 [279]
Cu_2O	2.38	2.1 – 3.1	1.9 – 2.0 [280]
$CuInS_2$	n/a	2.14 – 2.2	1.2 [279]
CdTe – orange	2 – 2.1	2.10	1.50 [279]
CdTe – red	1.91 – 1.97	1.97	
CdTe – green	2.25 – 2.43	2.43	
CdTe – yellow	2.14 – 2.2	2.25	
CdTe – ruby	1.77 – 1.88	1.94	

The bandgap for the bulk materials are important since all of the nanocrystals were annealed to evaporate the insulating organic capping agents. As seen below in 6.3 after annealing the nanocrystals agglomerated to form a nanocrystalline film, therefore the bulk bandgap may be more useful to explain nanocrystal photoresponse features in sections 6.5 and 6.6. However this would depend on how intimate the electrical contact is between the nanoparticles and hence is difficult to predict which bandgap is more relevant.

6.3 SEM characterisation

As discussed previously annealing was carried out to remove insulating organic ligands from the nanocrystals, see section 3.5.4 for a full explanation and Table 3-9 for annealing parameters used. A few representative devices were analysed with the SEM to see the effect of annealing the nanocrystals on to the Schottky device. It is known that the removal of organic ligands via heat treatment causes nanocrystal growth or sintering [194]. Figure 6-10 and Figure 6-11 show typical features of a CdS-NC/Pt and CuO-NC/Pt device respectively. The SEM images underwent XRD to confirm that the nanocrystals were the cause of features seen in the images below. Figure 6-10 shows that the CdS-NCs formed an amorphous nanocrystalline layer on top of the Schottky barrier devices. This was expected, since annealing would have evaporated the organic capping agent, allowing the nanocrystals to aggregate into a nanocrystalline film.

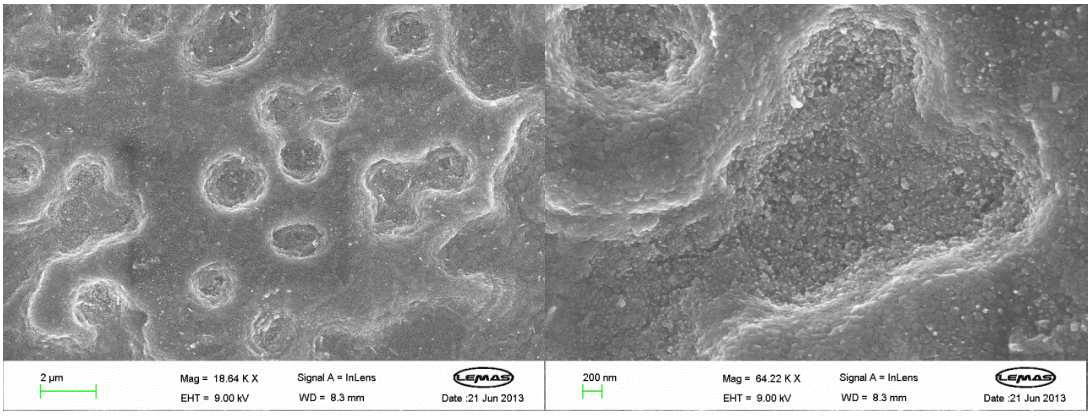

Figure 6-10: Representative SEM images of a CdS-NC/Pt/TiO_2/Ti device (Sample 304).

Unlike the CdS NCs, the CuO NCs formed large faceted agglomerations from lateral nanocrystalline films, see Figure 6-11. The Pt film can clearly be seen under the lateral nanocrystal plates. These images of the CuO nanocrystals are quite different from the manufacturers SEM image in Figure 6-6, despite following the same annealing process. This helps to explain the disparity between the NC absorption and hence different bandgaps found between the in-house and manufacturer’s characterisation outlined in section 6.2.

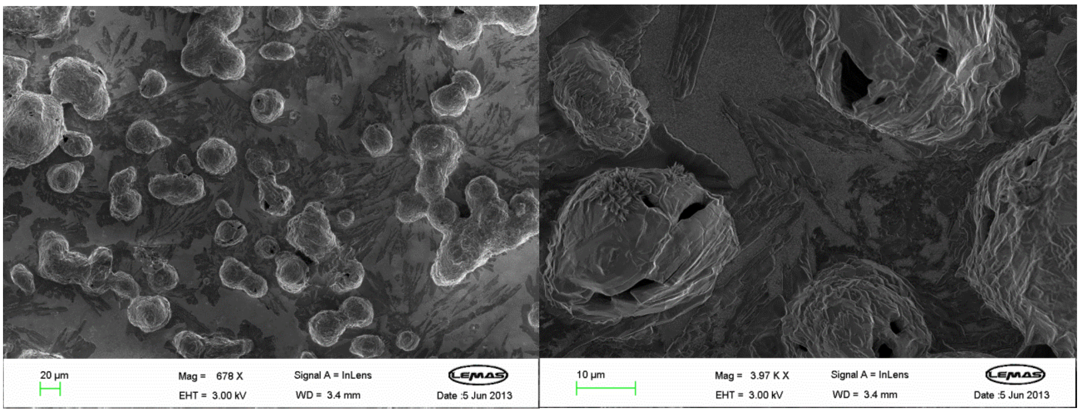

Figure 6-11: Representative SEM images of a CuO-NC/Pt/TiO_2/Ti device (Sample 503).

Figure 6-12 shows a representative SEM image for a NC/NW device. It is clear from the images that the nanocrystals have formed a bulk continuous and planar layer underneath the nanowires. The nanowires have identical features to that previously shown in Figure 5-7. It is evident that the nanowires have adhered mainly to the top of the nanocrystalline film, however diffusion of nanowires into the nanocrystalline film is visible in Figure 6-12 and some nanowires can be seen under the nanocrystal film, despite the nanocrystals being deposited and annealed first. This has implications for the device structure which is discussed further in section 6.6.

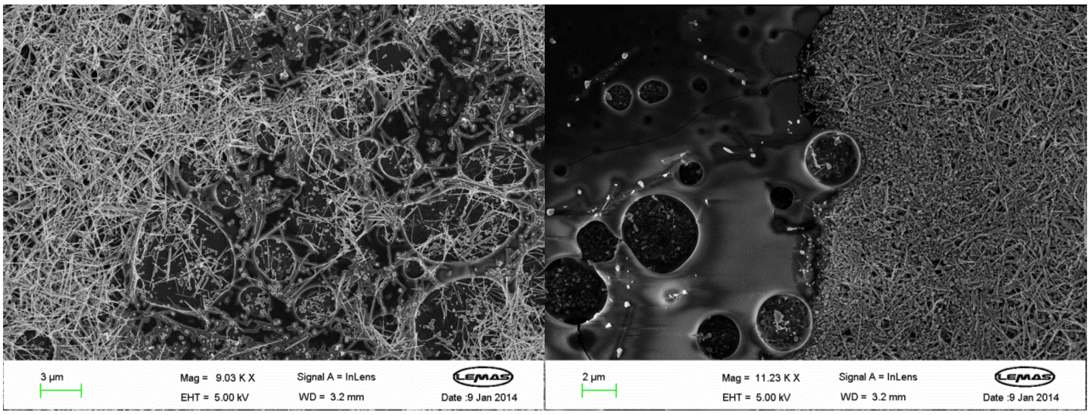

Figure 6-12: SEM image of a $CuInS_2$/Ag-NW/TiO_2/Ti device central location on the sample [left] and silver nanowire deposition edge [right] (sample 801).

In some instances annealing at high temperatures has been shown to remove all excitonic features due to a bulk nanocrystal film being formed. On the other hand, a bulk nanocrystal film has also been shown to result in a very conductive semiconducting film. Therefore, the exact effect of annealing will be nanocrystal dependant [194]. Sections 6.5 and 6.6 will look into the photoresponse of the nanocrystals as part of the Schottky barrier device.

6.4 Photovoltage decay

To ensure that the photovoltage was true to the device and not caused by static charging, photovoltage decay tests were undertaken. Static charging is photo-induced and caused by charging the TiO_2, which results in charge leakage. Some small static charging features were discussed earlier in section 4.5.1. Photovoltage decay tests were routinely undertaken to verify the photoresponse results, a typical result is presented in Figure 6-13.

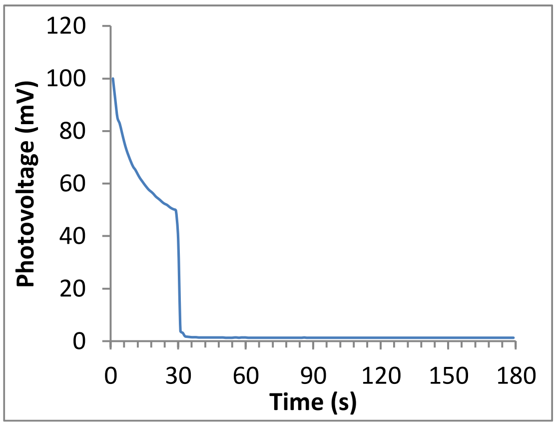

Figure 6-13: Typical photovoltage decay for nanocrystal devices. The device is illuminated with 330 nm light for 30 seconds and the photovoltage during and after illumination is measured, whilst in a black box (Sample 801).

Generally very little or no photovoltage decay was found from the TiO_2 in the NC/metal/TiO_2/Ti devices, which indicated that after illumination the devices very rapidly dissipate charge. In some instances photovoltage decay was an issue, these cases will be outlined in this chapter with the respective photovoltage for the particular device.

6.5 Nanocrystal/Pt/TiO_2/Ti device

This section presents a discussion of the results for all of the NC/Pt devices. A total of 26 devices were fabricated. The method followed for the Pt/TiO_2 device (Pt device) fabrication and characterisation prior to nanocrystal deposition was identical to that used for previous Pt devices in this work, presented in sections 3.4 and 3.6.1. The Pt devices were selected as they reproducibly gave the highest Schottky barrier heights, more regularly gave exponential I-V features and obtained a large UV photoresponse, compared to the other sputtered or evaporated Schottky devices, as discussed in Chapter 4. All varieties of nanocrystals, outlined in Table 3-7, were dropcast on to the Schottky barrier devices under ambient conditions and annealed in line with the information given in Table 3-9. This section analyses the results for each type of NC/Pt device fabricated.

I-V and photoresponse measurements were carried out pre and post nanocrystal deposition to find out if or how the device changes once NCs are deposited. I-V curves for the NC/Pt devices were found to present the same features and variability as those shown in section 4.3 for the Pt devices. This is expected since a Schottky barrier is still required for the device to function after the nanocrystals have been deposited. As explained previously annealing the nanocrystals was thought to be a necessary step to remove the organic ligands surrounding the nanocrystals that would act as an insulating layer. Non-annealed nanocrystal devices were also produced to verify that the annealing stage was essential.

Figure 6-14 displays the impact that the deposition and annealing of nanocrystals has on the I-V characteristics of the devices. It is quite evident that the Schottky barrier at the Pt/TiO_2 interface deteriorates after nanocrystal deposition and annealing, displayed by the reduction in exponential I-V features from 50% before nanocrystal deposition to 6% post nanocrystal deposition and annealing. The percentage of linear and non-ideal I-V characteristics subsequently increases after nanocrystal deposition. The deterioration of the Schottky barrier could be due to a number of mechanisms, previously discussed in section 4.3, including additional resistance in the device due to the nanocrystal layer or Pt interface states in the TiO_2 due to Pt diffusion on annealing the device.

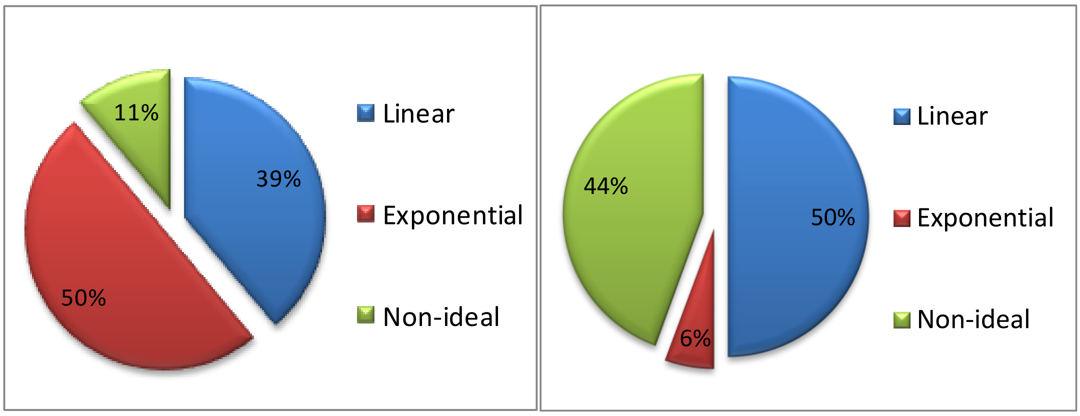

Figure 6-14: Yield of linear, exponential and non-ideal I-V features from the Pt device [left] and respective NC/Pt device [right], across all NC-devices.

Electrical characterisation in the next sections, including I-V, photocurrent and photovoltage are sometimes presented against a normalised axis to emphasise the features obtained from the NC-activated devices. In all instances this relates to normalising the data to the maximum data point for each device, generally found around 330 nm.

6.5.1 CdS-NC/Pt/TiO_2/Ti device

Seven CdS-NC/Pt/TiO_2/Ti devices (CdS-NC/Pt device from here on) were fabricated in total yet only 1 device gave a visible photoactive response, sample 304 displayed in Figure 6-15. Furthermore this device was also the only one to give exponential I-V features. This suggests that the Schottky barrier between the Pt/TiO_2 interfaces had not deteriorated due to the nanocrystal deposition and therefore enabled this device to operate effectively. Figure 6-15 shows that sample 304 has an absorption peak at 470 nm and a small visible response to 800 nm. The Pt/TiO_2/Ti device (Pt device from here on) prior to depositing the CdS NCs showed no visible photoresponse past 400 nm, indicating that the nanocrystals are responsible for producing the visible response. Additionally, the magnitude of the photoresponse from the Pt device is considerably smaller than the CdS-NC/Pt device.

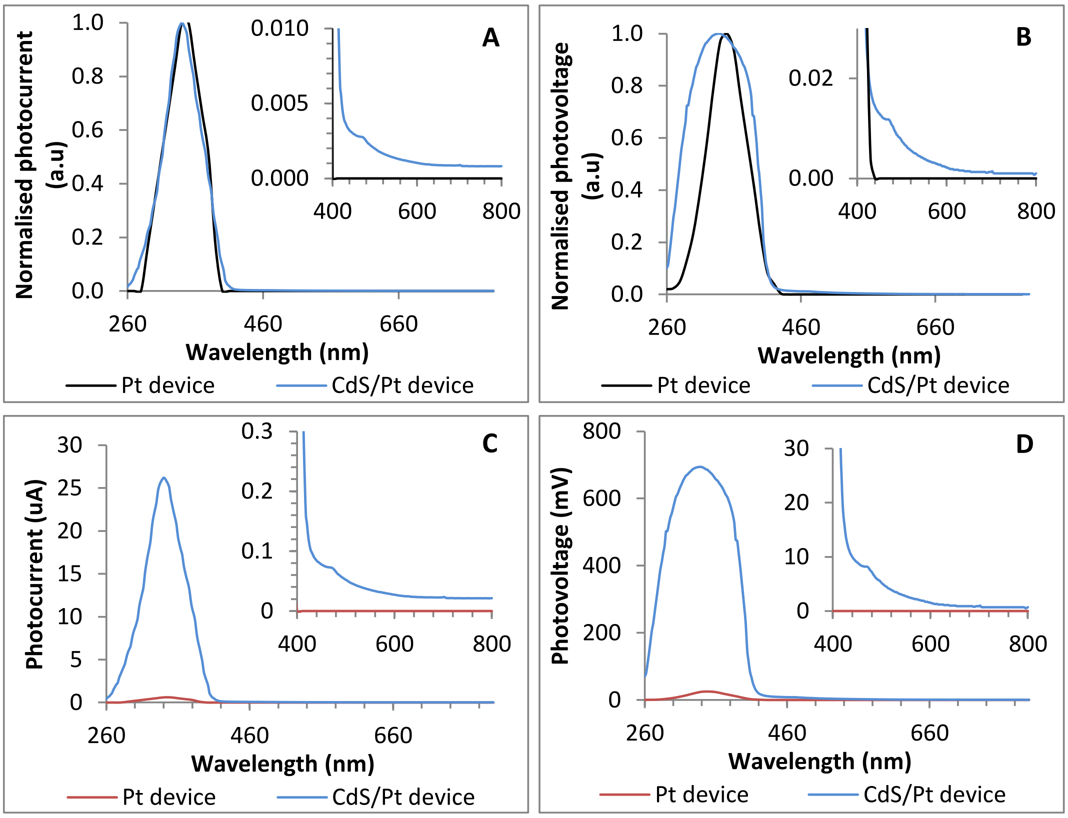

Figure 6-15: Normalised photocurrent [A] and photovoltage [B] comparing a CdS-NC/Pt/TiO_2/Ti device to its base Pt/TiO_2/Ti device. The inset graphs show the photoresponse in the visible range from 400-800 nm. [C] and [D] show the real photocurrent and photovoltage respectively for the same device (Sample 304).

We have assumed that the CdS nanocrystals have no doping or impurities and should be giving a photoresponse relative to their bandgap, hence close to or below the 440 nm excitonic peak found in Figure 6-3. However we can clearly see a red shifted photocurrent and photovoltage giving a response at longer wavelengths above its bandgap. This is thought to be due to the nanocrystals forming a bulk nanocrystalline film, as indicated in the SEM image in Figure 6-10. Hence the optical properties of the NCs would also change to reflect the bulk properties. The bulk bandgap of CdS from Table 6-3 is 2.42 eV which relates to a wavelength of 512 nm. The photoresponse at 470 nm is therefore approximately half way between both the nanocrystal and bulk bandgap for CdS. It was indicated in section 3.5.4 that sintering NCs has been found in the literature to lead to a red shifted photoresponse [80, 194, 199]. Olson et al [80] found similar results to those presented here, with a shift from quantum confinement of untreated nanocrystals to bulk like behaviour due to sintering the NC films, as well as an overall increase in absorption.

The annealing duration was varied to attempt to enhance the magnitude of visible response from the CdS nanocrystals. It was advised by the manufacturers to anneal at 400°C to remove the organic capping agent, which was required to prevent insulating the electrical properties of the nanocrystals, so duration rather than temperature was varied. Figure 6-16 presents the effect of annealing duration on CdS-NC/Pt devices. It is clear that the magnitude of the UV photoresponse is greater for the devices annealed for 3 and 4 hours, whereas the visible response is only highest for the device annealed for 3 hours. Hence 3 hours appears to be the critical point for obtaining the maximum UV and visible photoresponse. Similar to Figure 6-15, a feature at 470 nm is found for these two CdS-NC/Pt devices.

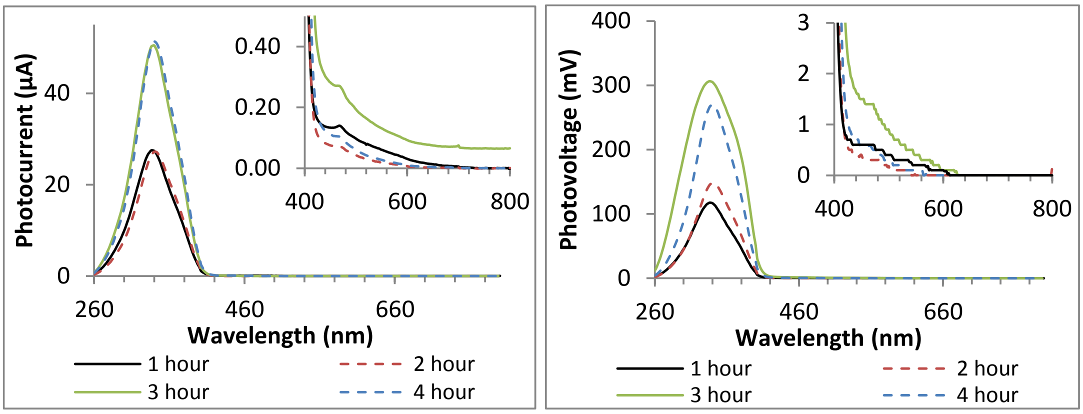

Figure 6-16: Photocurrent [left] and photovoltage [right] of 1 – 4 hour staged annealing of CdS-NC/Pt devices. Insets show a higher resolution photoresponse between 400 – 800 nm. Sample 304R was annealed for 1 and 3 hours and sample 306R was annealed for 2 and 4 hours.

A concern of the CdS-NC/Pt devices was attributing the visible response to the correct component of the cell, i.e. the Pt device or the nanocrystals, since the Pt device was also shown to give a photoresponse at 470 nm, discussed previously in section 4.5.1. It was quite clear in Figure 6-15 that the Pt device had no effect on the visible photoresponse of the complete CdS-NC/Pt device. However, for Sample 306R in Figure 6-17, the visible absorption peak at 470 nm was found for the Pt device prior to NC deposition, as well as the subsequent CdS-NC/Pt device. In this device it is clear that this response is therefore not due to the CdS-NCs.

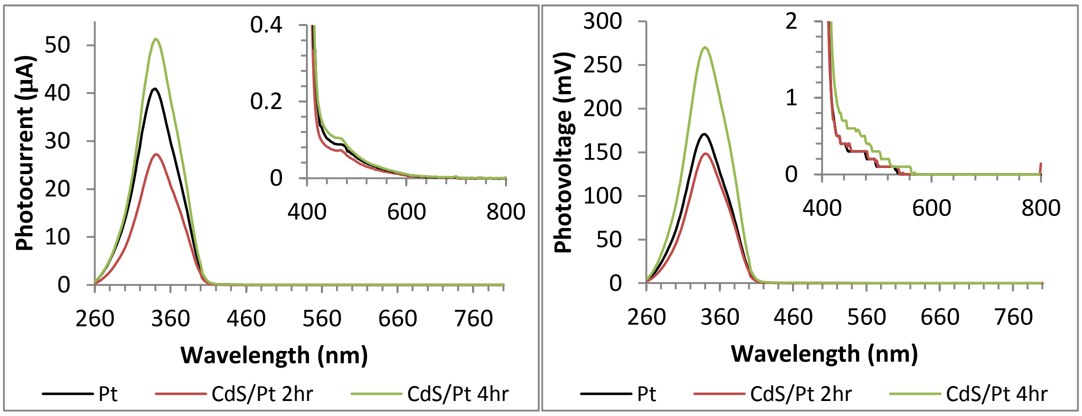

Figure 6-17: Annealing comparison of CdS-NC/Pt device against its base Pt/TiO_2/Ti device, showing the photocurrent [Left] and photovoltage [Right]. The inset graphs show the photoresponse in the visible range from 400 – 800 nm (Sample 306R).

This visible response observed for the Pt devices, previously described in section 4.5.1, was an artefact of the Pt deposited on the TiO_2 and was not due to any subsequent processing. However, in the NC device, the Pt device would have been annealed. To see if annealing affected the visible photoresponse from the Pt device, a Pt device was annealed in stages at the same temperature used for the CdS-NC/Pt device. Figure 6-18 and Figure 6-19 shows the I-V and photoresponse of annealing a Pt device.

Figure 6-18 indicates that sample O17 has become more Ohmic post annealing, with a larger series resistance and a lower leakage resistance. This suggests that either the interface between the Pt/TiO_2 or the TiO_2/Ti has changed due to annealing. It was suggested previously in 4.5.1, that additional Pt interface states could have been created in the TiO_2 which would provide an extra electrical pathway for electrons, therefore making a more Ohmic device. This also indicates the cause for the Schottky barriers degrading between Schottky devices and NC devices, as mentioned previously at the start of this chapter and presented in Figure 6-14.

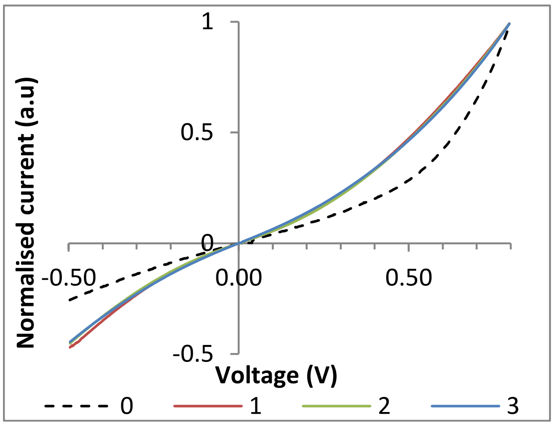

Figure 6-18: Normalised I-V plot of Pt/TiO_2/Ti annealed at 400°C in 1 hour stages up to 3 hours (Sample O17).

The photocurrent of sample O17 presented in Figure 6-19 shows a general trend of reduced response with increasing annealing time. The photovoltage curve suggests that the UV response deteriorates with increasing annealing time; however the visible response between 400 – 700 nm remains largely the same. The photovoltage of sample O17 show a similar absorption feature at 470 nm, as shown by the CdS-NC/Pt device in Figure 6-15 to Figure 6-17. Similar to above, this feature can be attributed to Pt interface states in the TiO_2, as discussed in 4.5.1. However this also causes problems for the analysis of the CdS-NC/Pt device as it remains unclear whether the photoresponse peak at 470 nm is due to the nanocrystals or the Pt interface states. It is noteworthy to highlight that a second Pt device failed to give any electrical or photoresponse after being annealed for only 1 hour, which indicates that in some cases the Pt/TiO_2 barrier completely deteriorates due to annealing. This could be due to Pt film cracking since only a thin, 10 nm Pt layer was deposited, whereas a much thicker layer ~60-80 nm of Pt was deposited on sample O17.

Attributing the visible response at 470 nm to either the NCs or Pt device was done on a case by case basis, by contrasting the photoresponse before and after NC deposition. Hence for sample 304 in Figure 6-15 it is thought that the absorption feature at 470 nm is due to the nanocrystals, since the Pt device prior to nanocrystal deposition gave no visible response. In devices where the Schottky barrier did give a response before the nanocrystal deposition, for example sample 306R in Figure 6-17, the response is considered as a Pt device feature rather than a nanocrystal feature. This outlines the importance of testing the Schottky barrier before depositing nanocrystals.

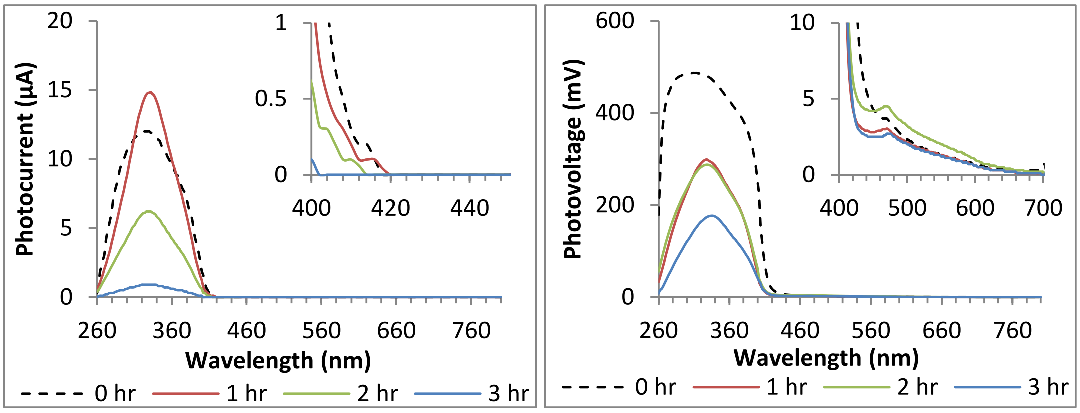

Figure 6-19: Photocurrent [Left] and photovoltage [Right] of a Pt/TiO$_2$/Ti device annealed at 400°C in 1 hour stages up to 3 hours. The inset graphs show the features after 400 nm to a higher resolution (Sample O17).

In summary, it is possible for both the CdS nanocrystals and the Pt interface states to show similar photoresponse features. As discussed above the CdS nanocrystals have formed a nanocrystalline film and therefore have a red-shifted photoresponse due to an extension of the bandgap, nearer to the bulk bandgap energy. For the Pt device, the Pt interface states can effectively provide energy states at a lower energy than that of TiO$_2$. Decreasing the bandgap of TiO$_2$ will lead to a photoresponse at longer wavelengths, since the energy required to excite an electron from the valence band to the interface state is less than that required to excite an electron to the conduction band. Furthermore, only a small change in bandgap is needed for the photoresponse at 470 nm to occur, less than a fifth of the bandgap energy of TiO$_2$. For example reducing the TiO$_2$ bandgap energy from 3.2 eV to 2.6 eV allows excitation of electrons at 470 nm.

Considering that annealing the Pt device leads to deterioration and/or no visible photoresponse enhancement and that only the device with an exponential I-V from the respective M-S interface gave a visible photoresponse, leads to the conclusion that any new or exaggerated visible photoresponse found after characterising the NC device, is attributable to the CdS NCs, despite a similar visible feature found among both the Pt device and the NC device.

Figure 6-20 presents the energy band diagram for the operational CdS-NC/Pt/TiO$_2$/Ti device, showing the calculated energy bandgap for the CdS nanocrystals from Table 6-3, the highest calculated SBH for a Pt/TiO$_2$ Schottky barrier from Table 4-3 and the bandgap of TiO$_2$. The visible EQE measured at 470 nm for the optimum CdS-NC/Pt/TiO$_2$/Ti device was 0.04%.

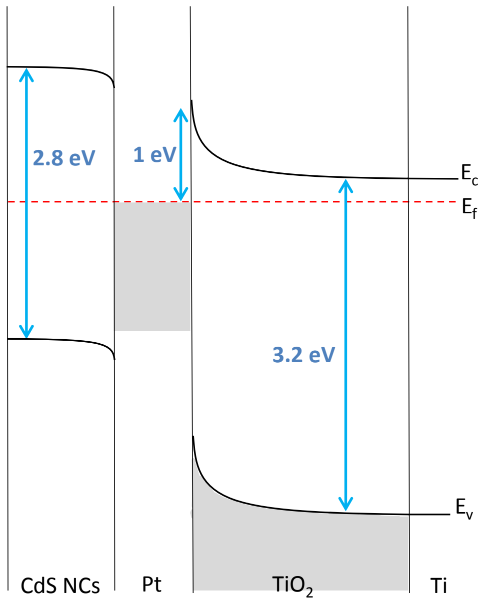

Figure 6-20: Energy band diagram of CdS-NC/Pt/TiO_2/Ti device.

6.5.2 CdSe-NC/Pt/TiO_2/Ti device

Unlike the results presented above in 6.5.1, no visible photoresponse was found for the CdSe-NC/Pt/TiO_2/Ti devices (CdSe-NC/Pt devices). Four CdSe-NC/Pt devices were fabricated with various Pt film thicknesses ranging from 10 nm to a very thick layer of approximately 80 nm to attempt to overcome the problem of a deteriorating Schottky barrier as suggested in Figure 6-14. In two cases an exponential I-V for a Pt device became more linear after annealing the nanocrystals, and in the other two cases a linear I-V was obtained from the Pt device before nanocrystal deposition.

Figure 6-21 and Figure 6-22 show typical results for the CdSe-NC devices. Figure 6-21 shows deterioration of the Pt device once the nanocrystals have been annealed, indicated by the change from the exponential initial I-V to a more resistive linear I-V. The linear I-V here actually represents a short circuit in the device, indicating that the Schottky barrier no longer exists. As discussed previously the deterioration of the Schottky interface may be a cause of the nanocrystals not appearing to give a visible photoresponse, since if the Schottky barrier has failed, the operation of the whole device will also fail.

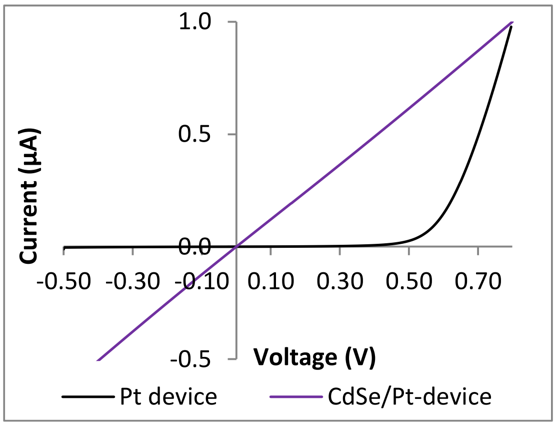

Figure 6-21: I-V of a Pt device and subsequent CdSe-NC/Pt/TiO_2/Ti device. Pt device shows ideal Schottky barrier behaviour, whereas the CdSe-NC/Pt device presents Ohmic behaviour (sample 106).

Figure 6-22 shows that for the CdSe-NC/Pt device the UV photovoltage is a few orders of magnitude smaller than that obtained for the Pt device, whereas the UV photocurrent is slightly higher. However neither shows a visible photoresponse from the CdSe NCs over and above the Pt device. As discussed above it is difficult to determine whether the nanocrystals are working or not since the M-S barrier that is responsible for carrier transport has evidently failed.

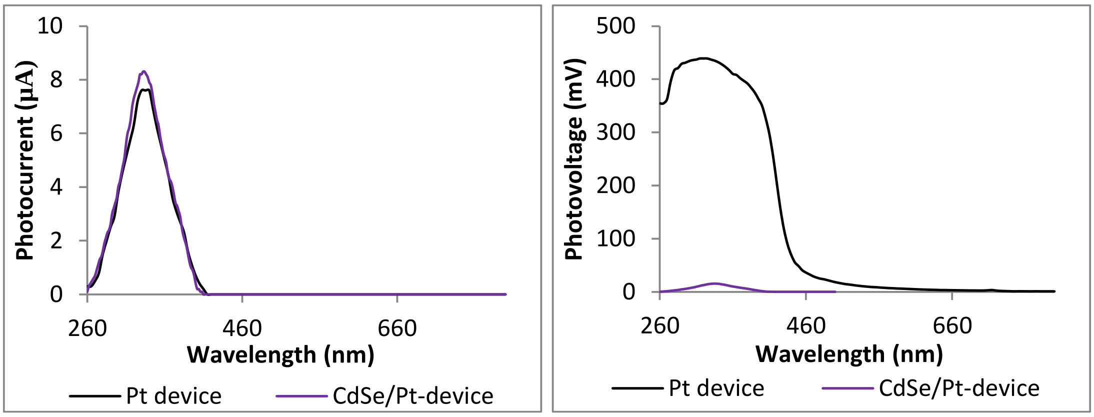

Figure 6-22: Photocurrent [left] and photovoltage [right] comparing the initial testing of a Pt device and the subsequent CdSe-NC/Pt/TiO_2/Ti device (sample 106).

Further work is needed to come to any firm conclusions on the CdSe NC visible response, since none of the devices maintained a Schottky barrier after NC deposition.

6.5.3 CuO-NC/Pt/TiO_2/Ti device

A total of 7 CuO-NC/Pt/TiO_2/Ti devices (CuO-NC/Pt devices) were fabricated. In all of the CuO-NC/Pt devices the M-S interfaces had been compromised, similar to the devices discussed previously, evident from the shift from an exponential I-V to a less ideal I-V with resistive features once the nanocrystals had been annealed, shown in Figure 6-23. In addition, the mass loading of nanocrystals was experimented with in these devices, to see if a higher mass loading could give a better visible response. Initially 1-3 µL of CuO nanocrystals were drop cast and annealed onto the surface, which was increased to 10-30 µL of nanocrystals on the same devices. It is evident from Figure 6-23 that the higher mass loading of nanocrystals has increased resistance, which is expected since the CuO-NC/Pt device would have been annealed twice at this point, and more NC monolayers would be created making a thicker layer for the current to work through before reaching the Schottky barrier.

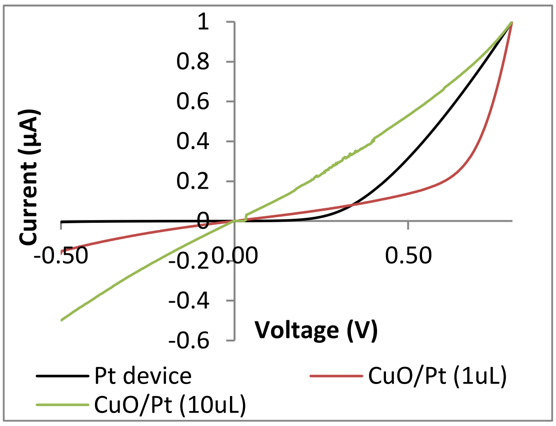

Figure 6-23: Typical I-V features for CuO-NC/Pt/TiO_2/Ti devices against its respective Pt/TiO_2/Ti device. This represents one device which underwent further nanocrystal deposition and annealing to increase the nanocrystal mass loading on the device (sample 501).

The mass loading of CuO NCs provided no benefit to the photoresponse of the CuO-NC/Pt devices, as indicated in Figure 6-24. No visible photocurrent was simultaneously observed with a visible photovoltage for any of the CuO-NC/Pt devices. However 2 out of 7 devices gave a visible photovoltage, as shown in Figure 6-24. The fact that a visible photovoltage is achieved for the CuO-NC/Pt devices suggests that there is a mechanism in place for a visible response, however this is not very efficient and hence has no visible photocurrent. This aligns well with the M-S interface deterioration theory, since we can assume that the excited electrons in the nanocrystals are not being transferred very efficiently across the M-S barrier and instead are being dispersed as heat energy.

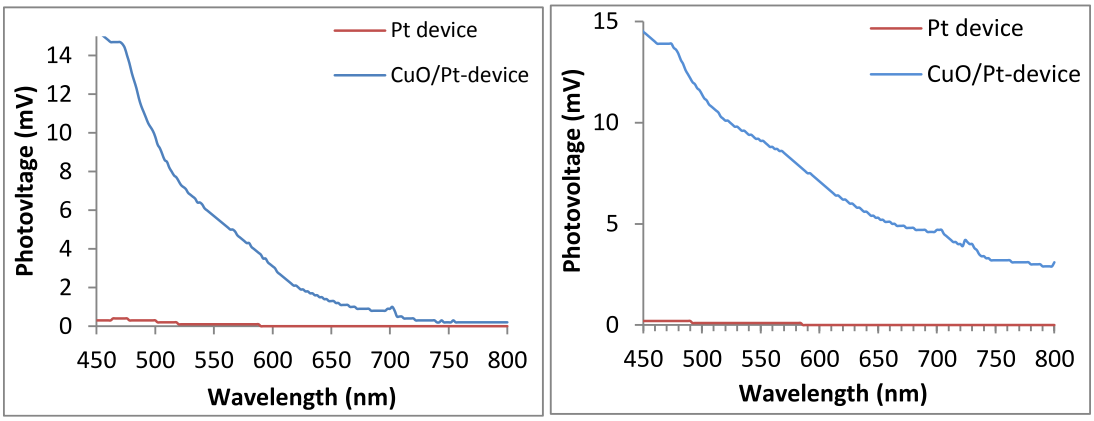

Figure 6-24: Selected photoresponse features for CuO-NC/Pt devices between 450 – 800 nm. Photovoltage comparison between a Pt device and subsequent CuO-NC/Pt device using 1 µL of CuO (sample 501) [left] and 30 µL of CuO (sample 503) [right].

A shallow photovoltage feature between 500 – 600 nm is evident in both photovoltage curves from two different devices in Figure 6-24. This photovoltage feature correlates well to the bandgap estimated for CuO nanocrystals in Table 6-3. The feature at 470 nm, visible in both of the CuO-NC/Pt devices is again due to Pt interface states in the TiO_2. This feature is also evident in the respective Pt device for the same device, but it is not evident in the plots below since the magnitude of the photovoltage is very small compared to the CuO-NC/Pt device.

Unfortunately the visible photoresponse feature in Figure 6-24 can also be seen in Figure 6-25 for a Pt device. This visible feature is not one which is generally observed in Pt devices, see section 4.5.1. However the Pt device in Figure 6-25 was part of a batch, some of which were subsequently used to fabricate the CuO-NC/Pt devices in Figure 6-24. Generally devices would only be compared with their own Pt device for consistency, however it was thought appropriate to outline this Pt device due to the similarity in visible photovoltage and due to being from the same Pt device batch. From this it is difficult to conclude whether the shallow visible feature between 500 – 600 nm is due to the CuO nanocrystals or the Pt device.

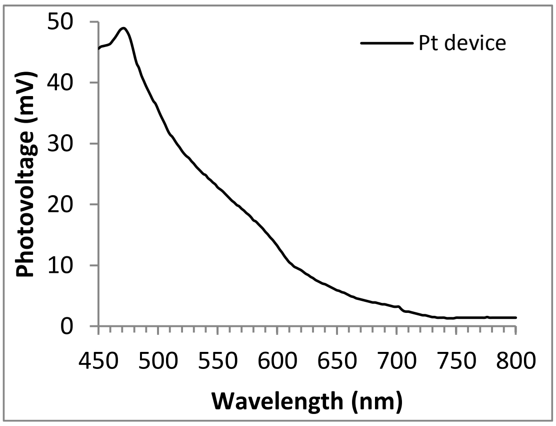

Figure 6-25: Photovoltage of a Pt/TiO_2/Ti device between 450 – 800 nm. This Pt device was fabricated simultaneously to the NC devices in Figure 6-24 (sample 502).

The SEM analysis of the annealed CuO nanocrystals on the Pt device in Figure 6-11, which show large agglomerations rather than a nanocrystalline film, further questions the ability of the nanocrystals to provide a visible response. Moreover, the difficulty in characterising the nanocrystals by UV-vis absorption spectroscopy further points more in the direction that the visible response may be attributable to the Pt device. Overall, the fact that the small feature at 500 – 600 nm is observed in the Pt device, fabricated alongside the Pt device used for the NC devices in Figure 6-24, indicates that the response is not attributable entirely to the CuO nanocrystals.

Similar to the CdS-NC/Pt device, a Pt/TiO_2/Ti device was annealed without CuO nanocrystals, under the same conditions used to anneal CuO nanocrystals, to see if the annealing phase has an effect on the photoresponse of the active device. Figure 6-26 shows that annealing reduces the UV and visible response of a Pt/TiO_2/Ti device.

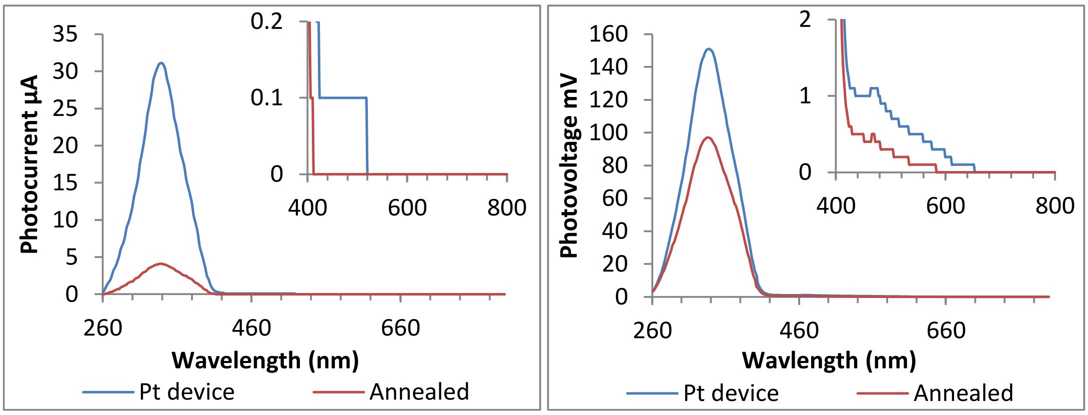

Figure 6-26: Photocurrent [Left] and Photovoltage [Right] of a Pt/TiO_2/Ti device before and after annealing at 500 ºC for 1.5 hours (sample 504).

6.5.4 $CuInS_2$-NC/Pt/TiO_2/Ti device

Due to time restrictions only one $CuInS_2$-NC/Pt/TiO_2/Ti device ($CuInS_2$-NC/Pt device) was fabricated. The results presented below are shown more for reference since significant conclusions cannot be made due to the anticipated low yield of the devices, shown in Figure 6-1, which indicates that a number of the same devices need to be fabricated to draw any firm conclusions. The $CuInS_2$-NC/Pt device did not provide any visible photoresponse, indicating that the nanocrystals are not activating the Schottky barrier. Figure 6-27 and Figure 6-28 show the I-V and photoresponse respectively for the only $CuInS_2$-NC/Pt device fabricated.

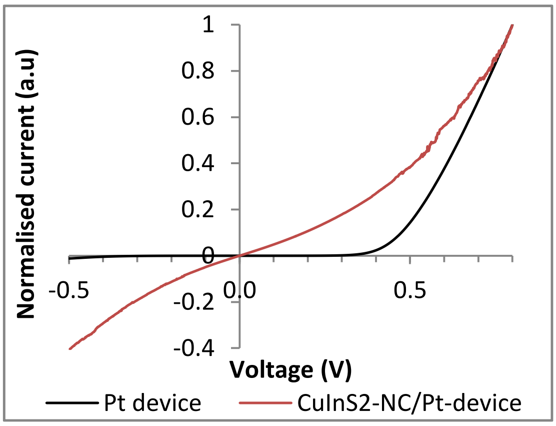

Figure 6-27: Normalised I-V comparison of Pt device and $CuInS_2$-NC/Pt device (sample 505).

Similar to the discussion above, the I-V characteristics of the Schottky barrier have been compromised after deposition and annealing of $CuInS_2$ nanocrystals. Figure 6-27 shows a distinct decrease in leakage resistance in the forward and reverse bias for the $CuInS_2$-NC/Pt device compared to the Pt device. This suggests that a low current pathway exists due to NC deposition and annealing. As discussed previously, the change in the M-S barrier may be the cause of the NC activated device not giving a visible response rather than inactive nanocrystals. However Figure 6-28 suggests that the Schottky barrier is still functioning well with a comparable UV photocurrent and photovoltage obtained after NC annealing.

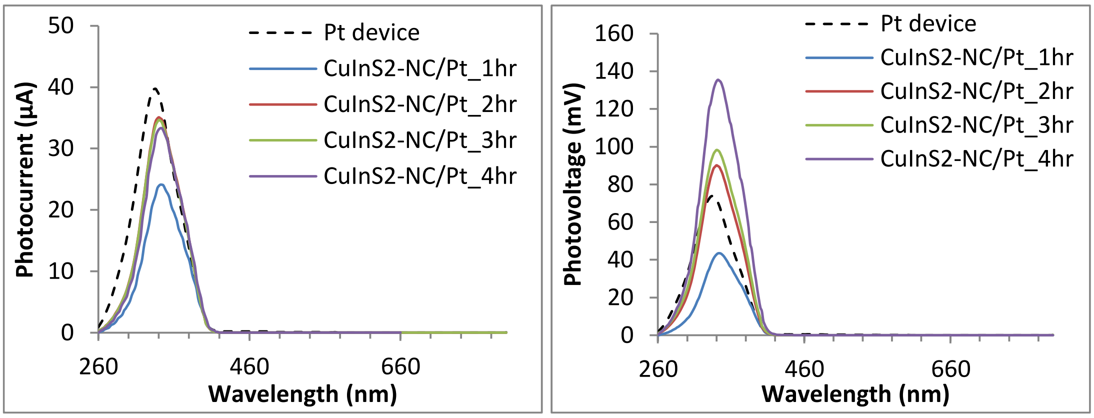

Figure 6-28: Photocurrent [left] and photovoltage [right] for a $CuInS_2$-NC/Pt device. No photoresponse after 420 nm was found (sample 505).

The $CuInS_2$ NCs were annealed onto the Pt device in stages to analyse the effect of annealing duration on nanocrystal properties, since it was less well known how to dissolve the capping agent in the $CuInS_2$ NCs compared to other NCs. Figure 6-28 indicates that none of the $CuInS_2$-NC/Pt devices gained a visible response, despite the annealing duration. The magnitude of UV response from the $CuInS_2$-NC/Pt device appears comparable overall, with a higher response found after 2 hours of annealing. All of the NC devices obtained a comparable UV response to the Pt device, which suggests that despite the change in I-V characteristics, the UV photoresponse is not affected. This suggests that the absorption of UV light in the TiO_2 has not been altered significantly. This may then indicate that the $CuInS_2$ NCs are not photo-active in the device. This could be due to the presence of the organic capping agent insulating the electrical properties of the NCs, or due to destruction of NCs by over heating or annealing for too long.

6.5.5 CdTe-NC/Pt/TiO_2/Ti device

Red and ruby CdTe nanocrystals, with bandgap energies of 1.97 eV and 1.94 eV respectively, were deposited onto the Pt devices. Three devices in total were fabricated, a red CdTe-NC/Pt device (sample 815), a ruby CdTe-NC/Pt device and a third device using ruby-CdTe nanocrystals but depositing the Pt-film after annealing nanocrystals to a TiO_2 substrate (sample 810). The aim of sample 810 was to see if a Schottky barrier could still be fabricated on top of the NCs and hence overcome the problem of damaging the metal layer through NC annealing.

Figure 6-29 shows the electrical characterisation of sample 815 (a red-CdTe-NC/Pt device). To verify the effect of the deposition and annealing of NCs separately on the I-V features, the characterisation was split into three stages – before nanocrystal deposition, after NC deposition and after annealing the NCs. The resultant I-V in Figure 6-29 A and B indicate that dropcasting the nanocrystals on the Pt device does not cause any problems to the Schottky barrier since the I-V curve remains rectifying. It is only when the nanocrystals are annealed that the Schottky barrier then forms more of an Ohmic contact for both forward and reverse biases. The photoresponse also confirms these findings, since after annealing the photocurrent and photovoltage are only in the UV range.

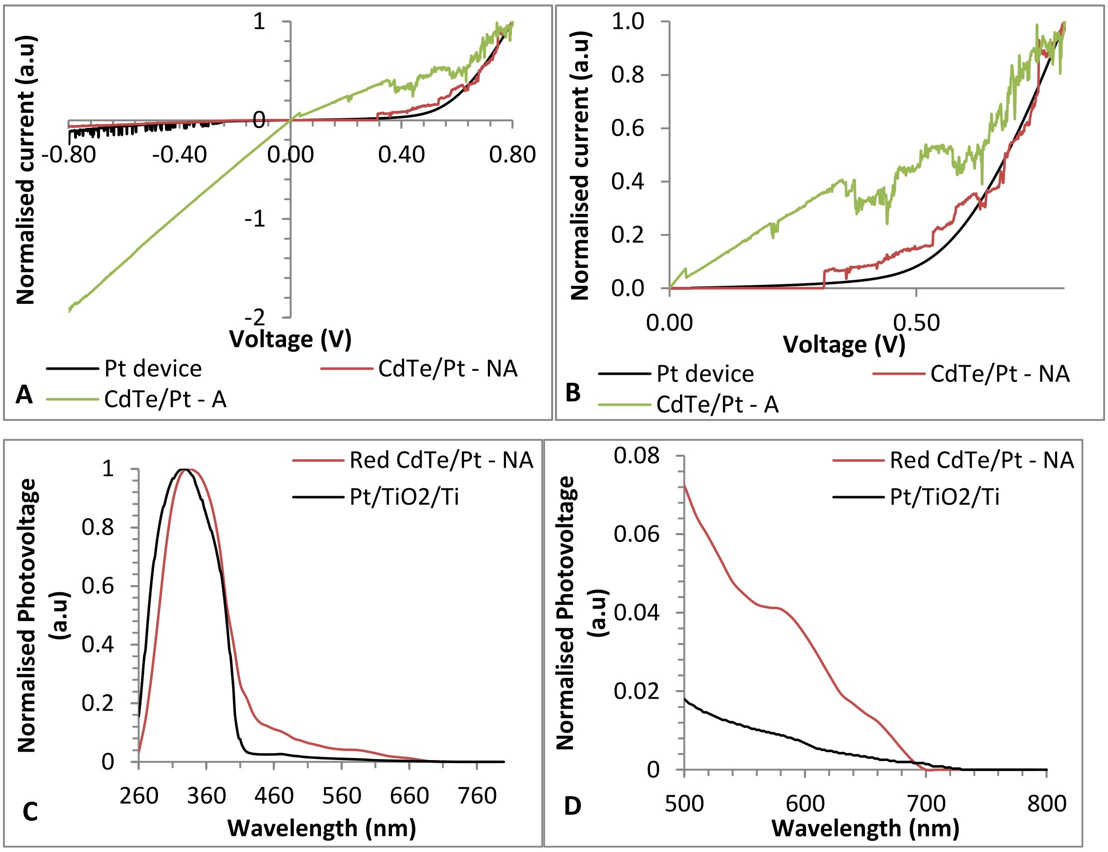

Figure 6-29: Red-CdTe-NC/Pt/TiO_2/Ti device electrical characterisation. [A and B] show normalised I-V features compared to the Pt device before annealing (NA) and after annealing (A). Normalised photovoltage is presented in [C] (the device did not obtain a visible photocurrent). [D] shows an enlarged version of graph [C] between 500 – 800 nm (normalisation on the y-axis is with respect to graph [C]). (Sample 815).

Figure 6-29 C and D show the photovoltage for sample 815, as a Pt device and after NCs have been deposited but not annealed. Prior to annealing no visible photocurrent is obtained, however a visible photovoltage is found, indicating that the red-CdTe NCs worked better without annealing. It is clear from both of the photovoltage curves at different scales that the NC activated device obtains a much higher photovoltage than its respective Pt device. Moreover there is an absorption edge at 580 nm, with a second shallower edge at 650 nm. This distinctive feature at 580 nm has not been seen previously in this work, indicating that the response is due to the red-CdTe-NCs activating the device. The fact that no photocurrent exists implies that the physical transport mechanisms in the NC-activated Schottky barrier device is inefficient.

In an attempt to overcome the problem of the Schottky barrier deteriorating, outlined previously in sections 6.5.2 to 6.5.4, an alternative structure was trailed which involved fabricating the Schottky barrier after depositing and annealing the nanocrystals on to the TiO_2. The altered device architecture will have been more of a ‘hybrid’ NC-activated Schottky barrier. This will be analysed in more detail later in section 6.6 with the nanowire/nanocrystal devices. Figure 6-30 shows the electrical characterisation of the Pt/CdTe-ruby-NC/TiO_2/Ti device (sample 810). It is clear from the I-V curve in A that a rectifying barrier has been formed despite the alteration to the layer deposition order. This shows that depositing the Pt-film after the nanocrystals can still form a Schottky barrier. Moreover it also arguably presents a more enhanced Schottky barrier since an optimum exponential curve has not previously been seen in any other NC activated devices, with the Pt-film deposited first.

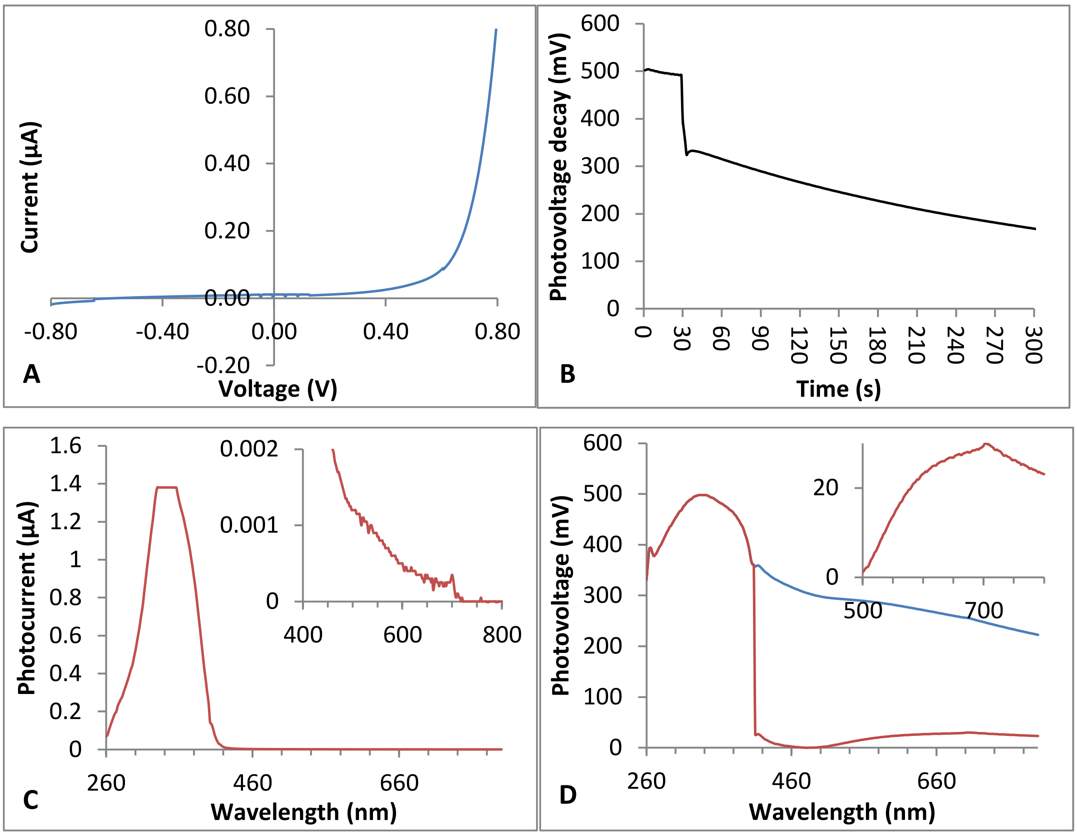

Figure 6-30: Characterisation of a Pt/ruby-CdTe-NC/TiO_2/Ti device, showing the I-V features [A], photovoltage decay [B], photocurrent [C] and photovoltage [D] (Sample 810).

The photoresponse for sample 810 is presented in Figure 6-30. The flat section of the photocurrent curve in C at 330 nm is due to the limits of the transconductance amplifier at

1.5 µA, used to measure the photocurrent. A very small visible photocurrent is evident in the inset graph which suggests that the nanocrystals are absorbing light in this region. From Table 6-3 we would expect to see a distinct response for the ruby CdTe nanocrystals between 640 – 700 nm, however the response here is between 400 – 600 nm. This photocurrent is possibly mainly due to a photocurrent-tail from the UV response, or a response from Pt interface states, similar to the response observed for a Pt device in Figure 6-25.

Sample 810 experienced a large amount of static charging, unlike most of the other NC-devices, as shown in the photovoltage decay curve in B. Hence, it is thought that this was due to the altered device structure. The photovoltage in D reflects this charging in the device. To obtain an accurate photovoltage the decay curve in B was subtracted from the photovoltage to obtain the red line response in D. It is evident from the photovoltage red curve that a good visible response between 500 – 700 nm with a peak at 700 nm has been obtained. This correlates well with the photocurrent found and the bandgap range given for CdTe-ruby nanocrystals in Table 6-3.

6.5.6 Summary

The results displayed above show some promising initial results for the nanocrystal activated Schottky barrier architecture. The most successful device was the CdS-NC/Pt device, as it obtained both a convincing photocurrent and photovoltage. The bandgap of the CdS nanocrystals in the NC/Pt device was found to have decreased due to the nanocrystals forming a bulk layer post annealing. This altered the optical properties of the CdS-NCs to nearer that of bulk CdS, giving a red shift in the photoresponse. The same absorption feature at 470 nm was found between the CdS-NC/Pt devices and the Pt/TiO_2 devices. This feature occurs in Pt devices because of interface states caused by Pt diffusion in to the TiO_2 due to annealing, but was shown to be independent in the CdS-NC/Pt device.

An important discovery was that the Pt/TiO_2 device degraded due to NC annealing, which has the effect of deteriorating the whole NC/Pt device. This was shown in all of the NC devices to some extent. The CuO-NC/Pt device showed a convincing photovoltage but no photocurrent and a deteriorated Schottky barrier, suggesting that the efficiency of transport mechanisms within the device is poor. Both the CdSe-NC/Pt and $CuInS_2$-NC/Pt devices failed to give a photoresponse due to the degradation of the Pt device. To overcome the issue of damaging the Schottky barrier, not annealing the nanocrystals or depositing and annealing the nanocrystals on to the TiO_2 and then sputtering with Pt were trialled. Not annealing the NCs for a red-CdTe-NC/Pt device was shown to maintain the I-V characteristics of the

Schottky barrier and provide a photovoltage, although no photocurrent was obtained suggesting the capping agent was still insulating the current. Depositing the NCs before sputtering the Pt on the device, giving a Pt/red-CdTe-NC/TiO_2/Ti device, was shown to give an optimum rectifying I-V curve and visible photoresponse. However, further NC devices are required to confirm this work.

6.6 Nanocrystal/Ag-NW/TiO_2/Ti device

Section 6.5 highlighted that the Schottky barrier between the TiO_2 and the sputtered Pt film become compromised after the NCs are deposited and annealed on to the Schottky device. To overcome this problem, Ag-NW/TiO_2 devices (Ag-NW device) were trialled. The main advantage of the nanowires over the bulk metal films is that the nanowires form a mesh on the surface rather than a continuous film, allowing the NCs to be in direct electrical contact with the TiO_2, avoiding the requirement for efficient ballistic transport through the noble metal. It was shown in section 5.2 that the Ag-NW devices were comparable to the other Schottky barriers made with sputtered and evaporated metal films, in terms of I-V characteristics and photoresponses, and obtained a higher Schottky barrier height than the optimum Pt device. Hence, Ag-NW devices were thought to provide a good Schottky barrier base to deposit nanocrystals on to.

This section presents a discussion of the results for all of the NC/Ag-NW/TiO_2/Ti devices (NC/Ag-NW devices). A total of 24 devices were fabricated, however only the representative or optimum devices are highlighted here. The NC/Ag-NW device fabrication differed to that of the Ag-NW device, since the nanocrystals had to be deposited and annealed first due to the higher temperature and longer duration required for the nanocrystals compared to the nanowires. This also benefited the device since previously the Schottky barrier had been compromised due to NC annealing, as discussed above. Similar to section 6.5, all varieties of nanocrystals were dropcast on to the substrate under ambient conditions and annealed in line with the information given in Table 3-9. Various quantities and concentrations of nanocrystals were deposited to attempt to find an optimum recipe for a high performing device. After nanocrystal deposition and annealing, the Ag-nanowires were deposited and annealed following the standard method outlined in section 3.4.3.3.

Ultimately the fabrication route used for the NC/NW devices will more than likely have an effect on the device structure. Figure 6-31 outlines the possible device architectures for the NC/NW devices. Rather than the intended NC activated Schottky barrier, the NC/NW device fabricated may now be more of a ‘heterojunction’ design where the nanowires sit on top of the bulk and NC semiconductors, or a 'hybrid' cell, where the nanowires and nanocrystals have mixed so that both the NWs and NCs are in contact with each other and the TiO_2. The 'hybrid' design is the most likely architecture to have been produced, since the NC/NW devices still obtain a Schottky barrier between the TiO_2 and NWs, see Figure 6-32 A, despite the NWs being deposited after the NCs. Furthermore, the SEM images of a NC/NW device in Figure 6-12 verifies the 'hybrid' structure, with the nanowires seemingly above and below the NC layer. A typical Schottky barrier architecture, shown on the left in Figure 6-31, is not likely in the NC/NW device, as it would require all of the nanowires displacing the NCs, which become a bulk nanocrystalline layer after annealing.

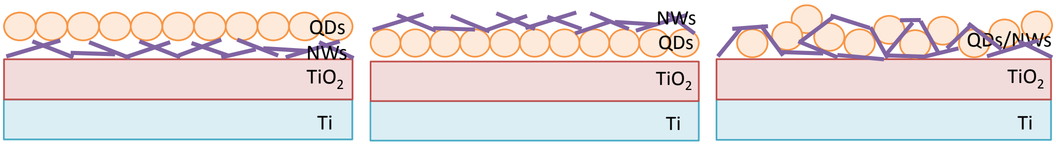

Figure 6-31: Schematics of possible device architectures of the nanocrystal/nanowire devices, showing Schottky barrier [Left], heterojunction [Middle], and hybrid [Right] architectures.

Figure 6-32 presents typical I-V features for the NC/NW-devices. Figure 6-32 A confirms a Schottky barrier between the NW/TiO_2 exists, despite NC deposition and treatment. Moreover, it is clear via a comparison with the I-V characteristics in Figure 5-10 and Figure 5-11 that the I-V features of the NC/NW devices are in fact comparable to those given by the Ag-NW/TiO_2 devices, including the non-ideal features in Figure 6-32 B to D. Compared to the yield of NC/Pt devices in Figure 6-2 it is evident that more NC/NW devices obtained a Schottky barrier, indicating that the NC/NW device is preferential for the nanocrystal activated Schottky barrier solar cell. This is likely due to the fact that the nanocrystals are deposited and annealed first, hence the nanowires do not undergo any additional annealing at high temperatures, so maintain their properties and do not diffuse into the TiO_2.

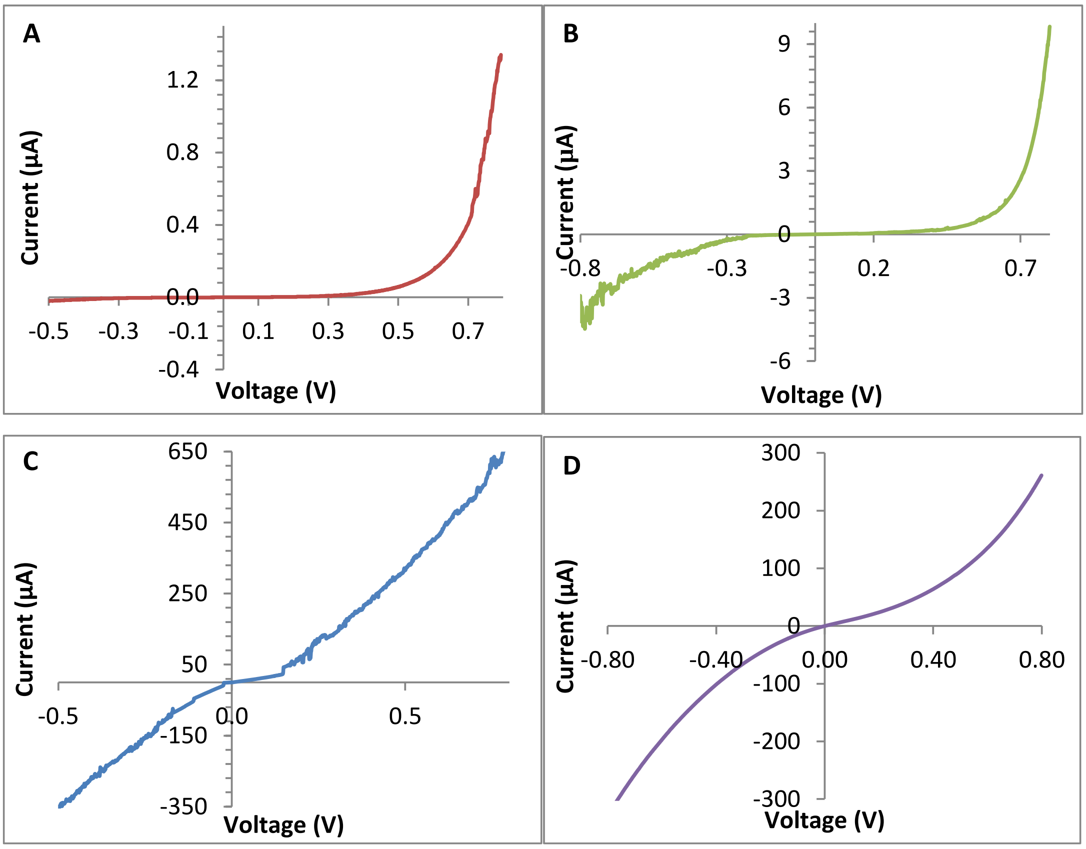

Figure 6-32: Typical ideal [A] and non-ideal [B-D] I-V characteristics of NC/NW-devices. Non-ideal characteristics show reverse saturation current, a lower leakage resistance and higher series resistance compared to the ideal case (A = samples 415, B= sample 804, C = sample 412, D = sample 803).

The rest of this section concentrates on the photoresponse obtained for the NC/NW devices. Similar to the previous section normalised plots for I-V, photocurrent and photovoltage are included to emphasise features obtained by the devices. This relates to normalising the data to the maximum data point for each device, generally found at 330 nm. Unlike the NC/Pt devices, which could easily be compared to its respective Pt device, this was not possible for the NC/NW-devices due to the fabrication technique used. Instead a representative Ag-NW/TiO_2 device I-V, photocurrent and photovoltage is included in the results to act as a comparison. The same Ag/NW device data is used in all of the results for consistency.

6.6.1 CdS-NC/Ag-NW/TiO_2/Ti device

The CdS-NC/Ag-NW/TiO_2/Ti devices (CdS-NC/Ag-NW devices) were more successful than the CdS-NC/Pt devices, with 6 out of 11 devices giving a visible photoresponse, and 5 out of the 6 visibly active devices giving an exponential I-V response. Figure 6-33 presents all of the CdS-NC/Ag-NW devices that gave a distinguishable visible photoresponse against an Ag-NW device. Devices that had a photocurrent with a poor resolution or where no visible photocurrent was found were excluded from Figure 6-33. It is evident that more and larger visible photovoltages, compared to photocurrents, are obtained across the CdS-NC/Ag-NW devices. The difference between the photocurrent and photovoltage highlights the efficiency of the device to transfer charge. The photovoltage shows that the device is operational, whereas the photocurrent suggests that the efficiency of this mechanism is relatively poor, apart from the two devices displayed. A similar observation and discussion can be found for the Ag-NW devices in section 5.2.6. As indicated previously, the NWs need to be refined further to improve the charge transfer mechanics and transparency.

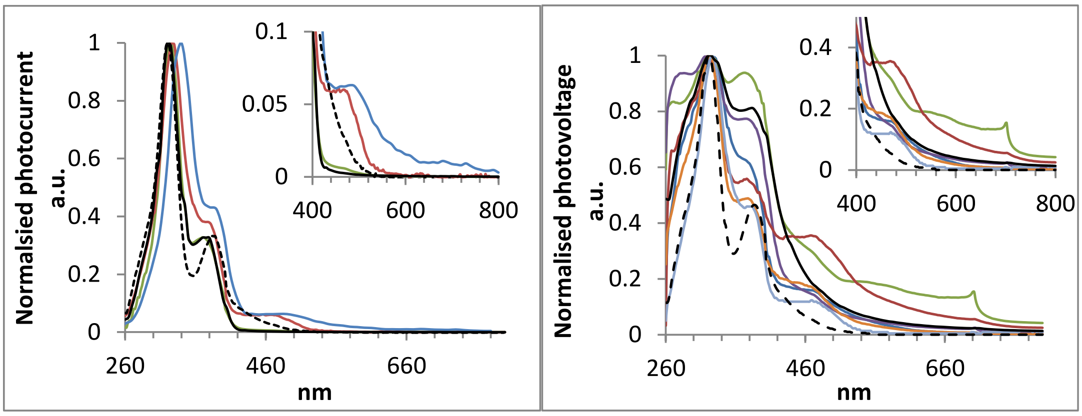

Figure 6-33: Photocurrent [Left] and photovoltage [Right] of CdS/Ag-NW/TiO$_2$/Ti devices (coloured lines), compared with an Ag-NW/TiO$_2$/Ti device (black line). Inset graphs show the photoresponse over the range 400 – 800 nm. All of the lines in the graphs are individual devices which shows the variability across devices.

The typical photoresponse features expected from an Ag-NW device are reflected in all of the CdS-NC/Ag-NW devices, with UV absorption at 330 nm and a distinct second peak at 420 nm, analysed previously in section 5.2.6. The representative Ag-NW devices (black lines) in Figure 6-33 also have a small tail into the visible region, caused by thermal excitation from the UV response and not an additional photoresponse. Many of the CdS-NC/Ag-NW devices also show an enhanced shoulder at 420 nm, indicating that the Ag-NW Schottky barrier response is boosted by the NCs which are expected to be active in this region due to their bandgap. It is clear from Figure 6-33 that an additional peak in the visible range exists at 480 nm for the CdS-NC/Ag-NW devices in both the photocurrent and the photovoltage. This peak has a very distinctive shelf that continues from 420 – 480 nm, which has not previously been observed for the Ag-NW devices. With a bandgap of 2.8 eV, the expected absorption of CdS NC is up to 440 nm. The red shifted photoresponse found up to 480 nm is similar to that observed for the CdS-NC/Pt devices in section 6.5.1. As with the CdS-NC/Pt devices this is thought to be due to a change in the NC properties, bought about by annealing which altered the NCs into a bulk nanocrystalline film. This change in structure has a knock on effect to the bandgap, effectively decreasing it to the bandgap of the bulk CdS at 2.42 eV, allowing the

NC film to absorb up to 512 nm. The EQE for the optimum CdS-NC/Ag-NW device measured at 390 nm was 0.01 and ranged between 0.001 – 0.002% between 430 and 530 nm.

The peak at 700 nm in the photovoltage is thought to be due to poorly filtered second order diffraction from the monochromator, as it is also observed in other nanocrystal devices and is not reproducibly created, hence it is not a specific feature of the CdS NCs. Comparing the photoresponse of the CdS-NC/Ag-NW device in Figure 6-33 to the CdS-NC/Pt device in Figure 6-15 shows that both devices are in good agreement, presenting very similar photoresponses for the CdS NCs. However the photoresponse of the nanocrystals are clearer and more pronounced in the NC/NW devices. This is probably because the NCs are in direct electrical contact with the TiO_2, in the CdS-NC/Ag-NW devices, so there are no losses from the ballistic transport through the noble metal, see Figure 6-34 for band diagram. Further indicating the advantages of the use of NWs in the device over the bulk sputtered films.

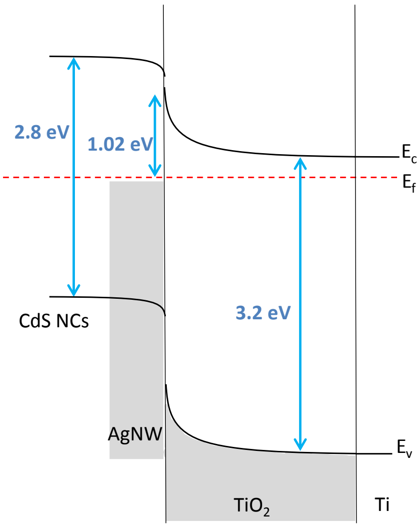

Figure 6-34: Energy band diagram of CdS-NC/Ag-NW/TiO_2/Ti device.

Both CdS-NC devices, on Pt and Ag-NW devices, have shown reproducible and agreeable visible results compared to other NC devices for both Schottky barriers. The main difference between the CdS NCs and all other NCs is that its conduction band sits highest over the TiO_2, see Figure 6-9. This may have the effect of enabling the transport of electrons into the TiO_2. Previously it was stated that NCs with conduction bands closer to the TiO_2 would be more efficient for electron transport, see discussion around Figure 6-9 in section 6.2. On the contrary, it could be that the electrons easily loose energy in this device, due to the device being inefficient and requiring extra refinement. Hence NCs with conduction bands closer to the conduction band of TiO_2 may not be sufficient to transfer electrons. This reasoning also correlates if assuming the bulk CdS bandgap is more likely.

6.6.2 CdSe-NC/Ag-NW/TiO_2/Ti device

Due to the poor characterisation of the CdSe nanocrystals, see Figure 6-5, only three CdSe-NC/Ag-NW devices were fabricated. Two of these devices gave moderate I-V features and a small visible response past 400 nm as depicted in Figure 6-35. A small visible absorption tail is presented in the photocurrent and photovoltage results. CdSe nanocrystal activity should be at approximately 600 nm, due to its absorption edge. Further we might expect a red shift response after earlier discussions on the effect of annealing the nanocrystals into a bulk crystalline layer. The only promising result here is the photocurrent for sample 423, which shows a hint of activity at 600 nm in the photocurrent.

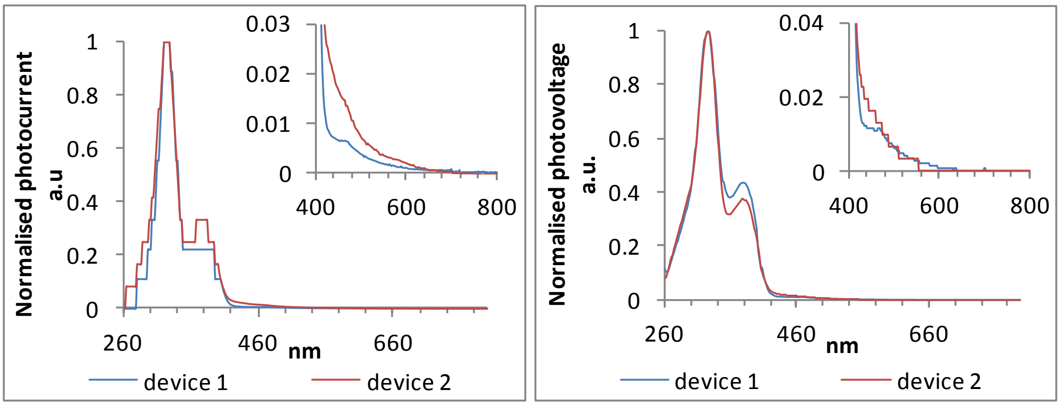

Figure 6-35: CdSe/Ag-NW/TiO_2/Ti photocurrent [Left] and photovoltage [Right]. Resolution of the photocurrent limited to 0.1 µA. Device 1 is sample 413R and device 2 is sample 423.

It was found during characterisation that the absorption edge was not as distinctive as the initial characterisation undertaken by the University of York. This suggests that maybe the nanocrystals degraded between initial characterisation and use.

6.6.3 CuO-NC/Ag-NW/TiO_2/Ti device

Similar to the CdSe NC devices, only two CuO-NC/Ag-NW devices were fabricated due to the fact that the nanocrystal characterisation did not obtain any promising results, as discussed in 6.2. Out of these two devices, one showed a visible photoresponse, presented in Figure 6-36. The device produced a very large visible photovoltage from 400 – 700 nm and the photocurrent reflected this response but at a much smaller comparable magnitude, indicating that the efficiency of the cell is low. It is noteworthy to highlight that this device produced a similar exponential I-V curve to that shown in Figure 6-37, suggesting that a good Schottky barrier was formed, allowing the device to operate effectively.

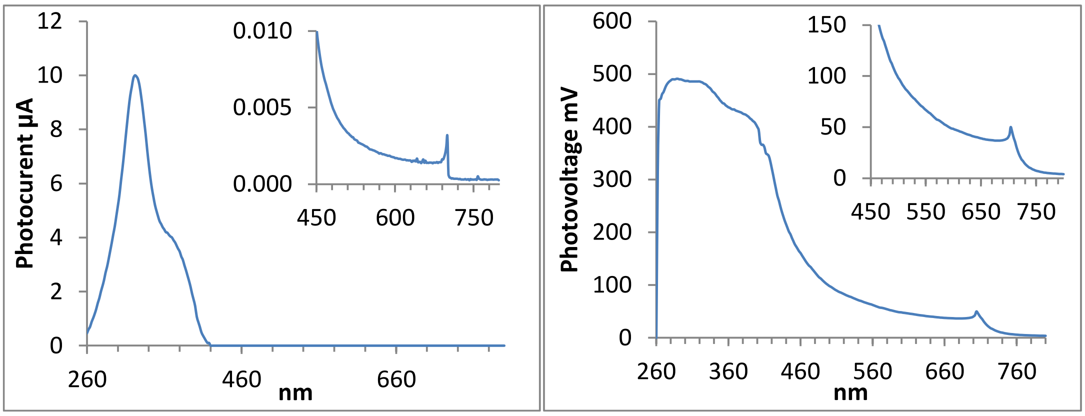

Figure 6-36: Photocurrent [left] and photovoltage [right] for CuO-NC/Ag-NW/TiO_2/Ti device, with inset graphs showing photoresponses between 450 – 800 nm (sample 414).

The absorption peak for CuO nanocrystals from the manufacturer, shown in Figure 6-6, lies between 500 – 600 nm. A more distinct photoresponse peak is anticipated from the results, as is observed in other nanocrystal devices, particularly CdS-NC and $CuInS_2$-NC devices. The fact that no actual peak is evident could suggest that the residual absorption in the visible range could be due to thermal excitation causing a UV tail in the photoresponse. However, this is unlikely due to the fact that no surface charging effects in sample 414 were observed in the photovoltage decay test, outlined in section 6.4. Hence the response displayed in Figure 6-36 is likely to be a NC response. Similar to Figure 6-33, the artefact at 700 nm in the photovoltage is thought to be due to second order diffraction from poorly filtered light from the arc lamp and is present in other nanocrystal devices.

6.6.4 $CuInS_2$/Ag-NW/TiO_2/Ti device

Three $CuInS_2$-NC/Ag-NW devices were fabricated in total. Two of these devices produced a visible photoresponse different to the Ag-NW device and to other types of nanocrystals. However, only one device is presented here because the second device experienced a persistent photovoltage when unilluminated and hence the results are less reliable. Figure 6-37 shows the results for the optimum $CuInS_2$-NC/Ag-NW activated device. The exponential I-V curve in Figure 6-37 A indicates that an optimum Schottky barrier has been created between the Ag-NW and the TiO_2. This again confirms the strength of the NC/NW devices over the NC/Pt devices, since the $CuInS_2$-NC/Pt devices struggled to obtain good Schottky barriers.

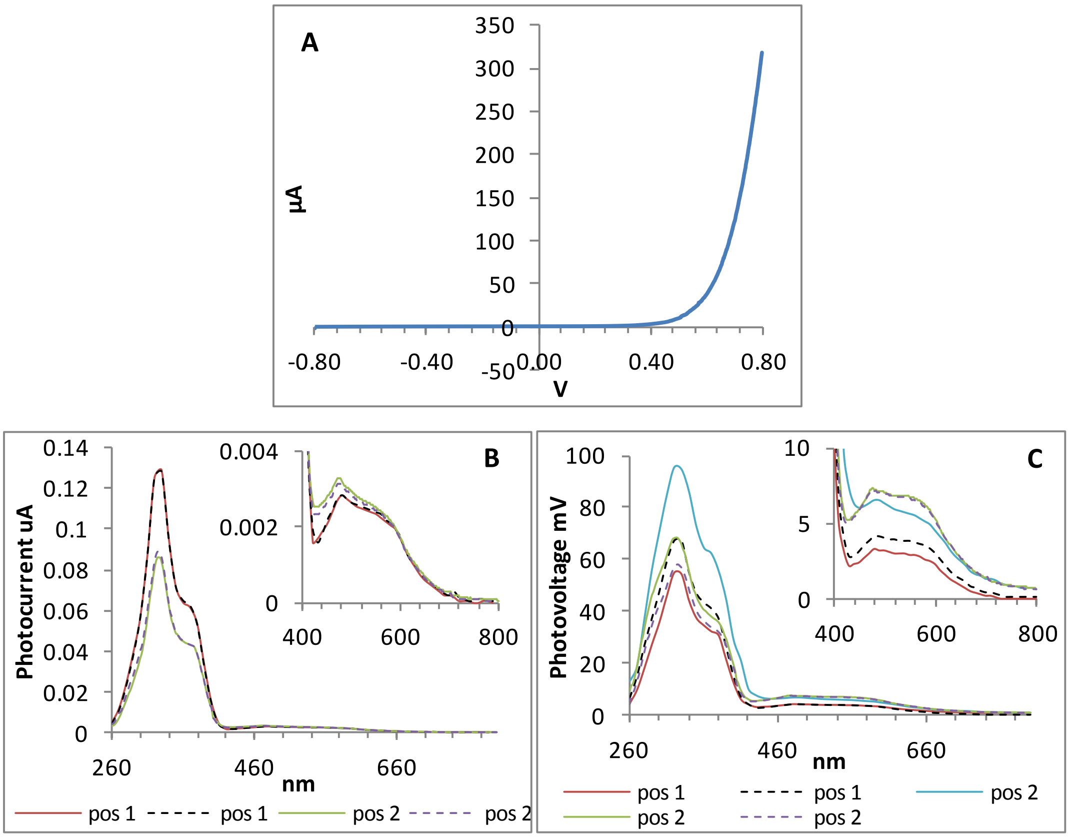

Figure 6-37: I-V [A], photocurrent [B] and photovoltage [C] for a $CuInS_2$/Ag-NW/TiO_2/Ti device. Inset graphs highlight the visible absorption region. The legend refers to the different positions across the same device surface, with position 1 being a central area and position 2 being at the edge of the device (Sample 801).

The photoresponse curves in Figure 6-37 clearly show the Ag-NW device UV response, similar to the other NC/Ag-NW devices so far, with a second shoulder at 420 nm. A visible photoresponse is very distinctive and reproducible in both the photocurrent and the photovoltage, see the inset graphs, with a sharp increase in photoresponse from 440 – 480 nm and an absorption shelf between 480 and 600 nm. The fact that the visible photocurrent was strong in Figure 6-37, suggests that an ideal I-V curve is a good indicator of a successful device. The EQE measured was 0.0004 – 0.0005% between 440-600 nm for sample 801.

The bandgap of the $CuInS_2$ NCs is 2.14 – 2.2 eV (found from UV visible spectroscopy in Figure 6-7) which corresponds to a wavelength of 560 – 580 nm. The bandgap of bulk $CuInS_2$ is 1.2 eV which relates to a wavelength of 1033 nm. The visible photoresponse from sample 801 in Figure 6-37 therefore correlates well with the NC bandgap. This is different to the previous NC devices, in particular the CdS-NC devices, discussed in this chapter where the NC activity is more representative of the bulk material bandgap rather than the NC bandgap. This suggests that the $CuInS_2$ NCs did not form the same bulk crystalline layer that the CdS NCs formed in Figure 6-10. The SEM image in Figure 6-12 hints at this, since the Ag-NWs can be seen below the NCs. This could be due to the fact that the annealing temperature and time for the $CuInS_2$ NCs was less well known compared to the other NCs, and potentially did not completely remove the organic ligands, but reduced the ligands enough to allow conductivity.

Figure 6-38 displays the energy band diagram for the operational $CuInS_2$-NC/Ag-NW device, showing the calculated energy bandgap for the $CuInS_2$ nanocrystals from Table 6-3, the highest calculated SBH for an Ag-NW Schottky barrier from Table 5-4 and the bandgap of TiO_2.

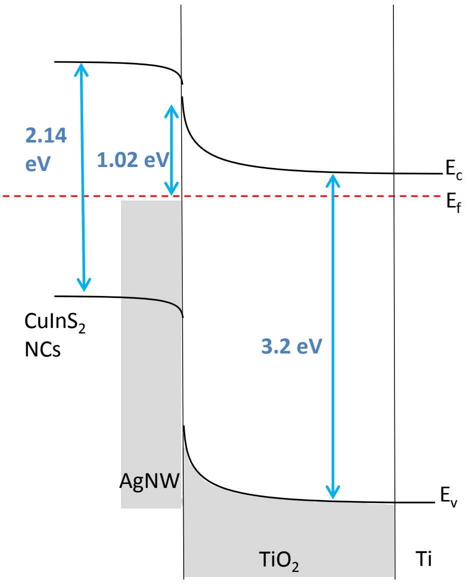

Figure 6-38: Energy band diagram of $CuInS_2$-NC/Ag-NW/TiO_2/Ti device.

The $CuInS_2$-NC/Ag-NW device is comparable to the CdS-NC/Ag-NW device, both achieving convincing and reproducible visible photoresponses which correlate well to the NCs activating the device. Both of these devices also obtained good exponential I-V curves, indicating the importance of a Schottky barrier for the operation of the devices. Furthermore, the $CuInS_2$-NC/Ag-NW device obtained better results than the equivalent $CuInS_2$-NC/Pt device, further confirming the strength of the use of NWs over sputtered Pt films.

6.6.5 CdTe-NC/Ag-NW/TiO_2/Ti device

Five different CdTe nanocrystals (orange, red, green, yellow and ruby) were deposited on to the Ag-NW-devices. Six CdTe-NC/Ag-NW devices were fabricated in total, five of which gave exponential I-V features and a photoresponse extending into the visible range. Some of these visible-active devices experienced surface charging and this is outlined where appropriate. Overall very similar features in the photoresponse across all CdTe-NC/Ag-NW devices were found, the representative devices are shown in Figure 6-39. Similar to all other NC/Ag-NW devices, the Ag-NW features can clearly be seen in the photoresponse results, with a second shoulder in the UV region.

Apart from the red CdTe-NC/Ag-NW device, no distinct absorption peaks were found in any of the devices around the range of CdTe-NC absorption between 510 – 700 nm (see CdTe-NC characterisation in Figure 6-8), as shown in Figure 6-39. Generally an extended photoresponse into the visible range up to 700 nm was found across devices. The red CdTe-NC/Ag-NW device is more promising, however, this device also experienced surface charging, as witnessed from a photovoltage decay scan. The surface charging has been subtracted from the original data to allow for this, shown by 'red 2' in the photovoltage plot. Even after taking into account the photovoltage decay, there is a large sub bandgap feature at 550 nm in the photovoltage.

Unfortunately the photocurrent for the red CdTe-NC/Ag-NW device, shown in Figure 6-39 B, did not match the photovoltage found, which questions the efficiency of the device. A small peak at 470 nm is observed in the photocurrent for four devices, as presented in Figure 6-39 C. This feature at 470 nm has previously been attributed to Pt defect states or CdS nanocrystals, see sections 4.5.1 and 6.5.1 respectively. The presence of this feature in some of the CdTe-NC/Ag-NW devices could be due to the UV photoresponse tail. Similar to other NC-devices, a peak at 700 nm is evident in some of the CdTe-NC/Ag-NW devices. As previously mentioned in section 6.6.1 this is probably due to poorly filtered second order diffraction light, not a real response.

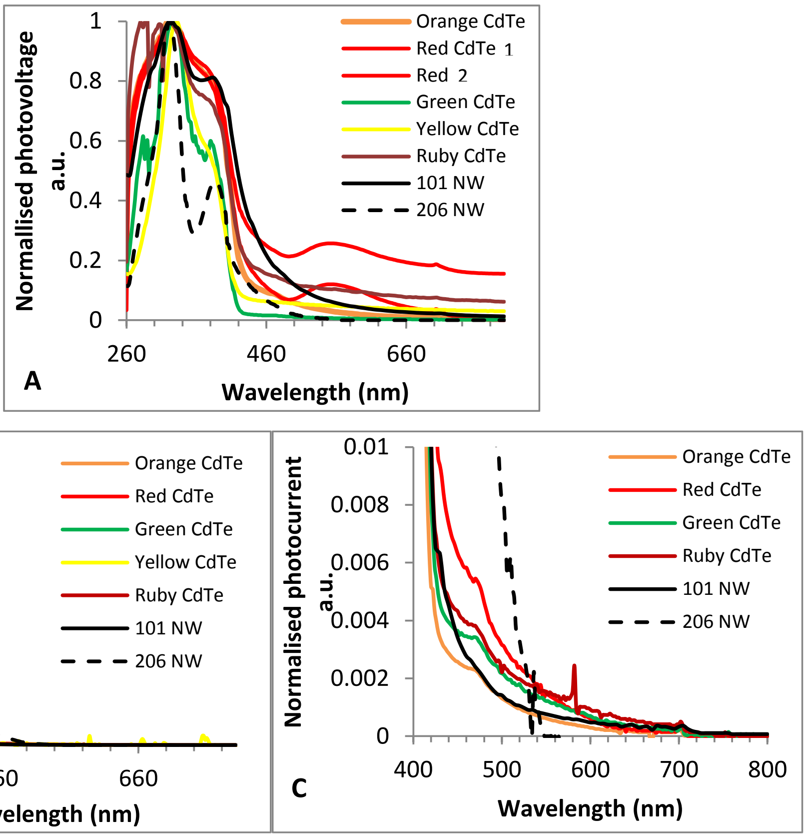

Figure 6-39: Normalised photovoltage [A] photocurrent [B] with an emphasis on 400 – 800 nm [C] for five CdTe-NC/Ag-NW/TiO_2/Ti devices compared to a representative Ag-NW device. Two 'red' lines in the photovoltage are presented to show the effect of charging – 'Red 2' shows the normalised photovoltage after subtracting the photovoltage decay curve. Yellow CdTe is missing from [C] plot due to poor resolution.

Apart from the red CdTe-NC/Ag-NW device photovoltage, the photoresponses obtained for the CdTe-NC/Ag-NW devices did not provide any distinctive peaks that were similar to the absorption properties of the CdTe nanocrystals. The annealing time and temperature used was thought to have affected the photoresponse of the CdTe nanocrystals. As a result UV/vis spectroscopy was carried out on non-annealed and annealed CdTe nanocrystal samples, see Figure 6-8. The absorption peak found for non-annealed nanocrystals was more profound than annealed nanocrystals. Post annealing the nanocrystals still absorbed light in the same range however no clear absorption peak was visible. Various temperatures and durations were trialled but the same results were obtained. Hence it follows that the results presented above do reflect the absorbing capabilities of annealed CdTe nanocrystals. However, not annealing the NCs in the future may enhance the distinctive features and provide confidence in the resultant photoresponses.

6.6.6 Summary

The results displayed above for the NC/Ag-NW devices confirm that a nanocrystal activated Schottky barrier device has been achieved. It was found that a high quality exponential I-V curve is essential to provide the Schottky barrier needed for carrier transport and ultimately an operational NC device. Strong visible photoresponses were generally found for devices with an optimum I-V. The CdS-NC/Ag-NW and $CuInS_2$-NC/Ag-NW devices showed the most convincing results, with large distinctive photocurrents and photovoltages that align well with the absorption properties of the nanocrystals. The CuO, CdTe and CdSe NC/Ag-NW devices produced some visible responses but not as distinctive as that seen for the aforementioned devices. This was probably due to the quality and post deposition treatment of the nanocrystals.

It is evident from a comparison with the NC/Pt devices that the ‘hybrid’ structure used in the NC/Ag-NW devices was advantageous to the nanocrystal activated Schottky barrier solar cell, due to the NCs and NWs both being in direct contact with the TiO_2. This helped to enhance carrier transport, avoiding the requirement for efficient ballistic transport. It also allowed the NWs to be deposited after the NCs which prevented the Schottky barrier from being compromised, as was often seen in section 6.5 due to annealing the NCs on to the Pt film.

6.7 Summary of main findings

This chapter has presented the findings for the nanocrystal activated Schottky barrier solar cell. The NC devices were fabricated by depositing and annealing CdS, CdSe, CuO, $CuInS_2$ and CdTe nanocrystals on to Pt/TiO_2 and Ag-NW/TiO_2 Schottky barriers. Before deposition the nanocrystals were characterised to confirm their excitonic features. I-V and photoresponse tests, identical to those in Chapter 4 and Chapter 5, were undertaken to characterise all of the devices. For the NC/Pt devices the Pt/TiO_2 Schottky barrier was characterised before NC deposition. This was not possible for the NC/Ag-NW devices due to annealing the NCs to the TiO_2 first. Instead two representative photoresponse curves from Ag-NW/TiO_2 devices were used as a comparison. These Schottky barrier base cases was used to contrast against the NC devices to ensure that the visible responses obtained were attributable to the NCs.

The yield of devices show that the NC/NW devices were more successful than the NC/Pt devices, with 67% of NC/NW devices being visibly active compared to 23% of the NC/Pt devices. There are a number of reasons why the NC/NW devices were more successful. Firstly, the altered structure of the NC/NW devices provided advantages since both NCs and

NWs were in contact with the TiO_2, which enhanced carrier transport to the TiO_2 and avoided energy losses. Another cause of the poor performance of the NC/Pt device was the destruction of the Schottky barrier after annealing the NCs, proved by a comparison of I-V features before and after NC deposition and annealing.

The NC/NW devices achieved more visible photoresponses compared to the NC/Pt devices. In some instances for the NC/Pt devices, it was difficult to attribute visible absorption to the nanocrystals since the Pt/TiO_2 device has also been shown to give similar absorption features. The Pt/TiO_2 visible features were explained as Pt diffusion into the TiO_2 which created interface states, hence exciting lower energy electrons. Annealing the NCs was found to give a bulk nanocrystalline film, which presented a red shift in the anticipated photoresponse of the NC devices. This absorption at longer wavelengths was due to the NCs structurally changing and giving optical properties more similar to the smaller bandgap of the bulk material.

The most promising devices were the CdS-NC/PT, CdS-NC/Ag-NW, and the $CuInS_2$-NC/Ag-NW devices. The CdS NCs in both the Pt and Ag-NW Schottky devices gave a distinctive and reproducible visible response that was reflective of the bulk bandgap of CdS. Moreover the same response was evident across both Schottky barriers. The $CuInS_2$ NCs only gave a visible photoresponse in the Ag-NW device, which further confirms the advantage of the Ag-NW Schottky device over the Pt device for the nanocrystal activated cell. The $CuInS_2$-NC/Ag-NW device gave a very distinctive visible photocurrent and corresponding photovoltage feature. This visible response related to the NC bandgap rather than the bulk bandgap, which was thought to be due to the annealing conditions not completely sintering the nanocrystals.

The red CdTe NCs also provided promising results, with a small visible photovoltage feature around 550 nm observed across both of the Schottky barriers. Despite not obtaining a matching photocurrent across the Schottky barriers, the CdTe NCs have the potential to improve with better processing. The annealing process was thought to be too harsh for the CdTe NCs, which was confirmed by the NC characterisation. The UV Vis absorption spectroscopy showed that non-annealed CdTe NCs gave distinctive excitonic features, but these levelled out after annealing. This indicates that the other CdTe NCs can potentially offer better results across both Schottky barriers.

Chapter 7

Conclusion

First generation crystalline silicon solar cells currently dominant the solar cell market. While silicon is a good material for solar cells, it is not ideal, due to the fact that crystalline silicon is an indirect semiconductor, hence optical absorption is low. Although reliable and mature the improvements to this technology are narrowing. Barriers to further development include the high cost of manufacturing high purity silicon wafers and the energy intensive processing causing high life cycle emissions, an important consideration for our future energy mix. Therefore there is a need to research novel, low cost solar cell architectures.

Currently there is vast research into alternative solar cell designs with the overarching aim of reducing the cost. Nanomaterials are a key element to this as they inherently require less materials and can be fabricated using lower cost techniques, such as solution processing. Furthermore, nanocrystal solar cells can lower life cycle emissions, be manipulated to control optical and electrical properties and are potentially able to increase cell efficiency above the Shockley-Quiesser limit due to quantum phenomena. There are many different possible nanocrystal solar cell architectures, however an architecture that has received much less attention is the nanocrystal activated Schottky barrier solar cell. The aim of the work presented in this thesis therefore, was to contribute to the understanding and development of nanocrystal activated Schottky barrier solar cells.

A Schottky barrier solar cell provides a low cost and robust architecture that can be enhanced with nanocrystals to absorb visible light. The concept of activating the Schottky barrier started with McFarland and Tang [34] when they deposited a merbromin dye onto an Au/TiO_2 Schottky barrier solar cell. Tang et al [35] progressed this work by activating an Au/TiO_2 Schottky barrier with CdS/CdSe nanocrystals. However, limited studies have further developed this concept. The work presented in this thesis aims to show that a wide range of semiconducting nanocrystals are suitable for activating a number of different Schottky barrier solar cells. A contribution to the existing knowledge in this field was achieved by experimenting with alternative techniques, testing a variety of semiconducting nanocrystals, experimenting with novel metal electrodes and verifying the key physical mechanisms in the device.

In Chapter 4 Schottky barrier solar cells using gold, silver and platinum on TiO_2/Ti substrates were fabricated via sputtering and evaporating. Chapter 5 expanded on this work by considering alternative and novel metal films of electrodeposited silver and dropcasted silver nanowires and comparing these against the Schottky barriers in Chapter 4. After characterisation of the Schottky barriers, CdS, CdSe, CuO, $CuInS_2$, and CdTe nanocrystals were then dropcast on the Schottky barriers in Chapter 6. Photoresponse and I-V characterisation against the Schottky barrier base were used to infer whether the nanocrystals had activated the device. The remainder of this conclusion will summarise the overall findings from these chapters and outline opportunities for future developments.

7.1 Schottky barrier devices fabricated with sputtered and evaporated metal films

The first part of this research concentrated on fabricating and characterising a Schottky barrier solar cell. To create the Schottky barrier, platinum, gold and silver were sputtered and evaporated on to a TiO_2/Ti substrate. The TiO_2 was formed on a polished Ti substrate by thermal oxidation or chemical anodisation. Analysis of the I-V and photoresponse measurements from the devices enabled an understanding of the physical mechanisms taking place and the effect of preparation and fabrication on the device performance. This stage in the research was important to harness an 'optimum' and reproducible device for eventual use in the nanocrystal activated device.

Comparisons between the three different metals used for the Schottky barriers showed that overall the Pt device outperformed the Au and Ag devices. The Pt device obtained the highest SBH of 1 eV, which is comparable to previous work in this field, and also obtained the highest photocurrent and photovoltage of 390 μAcm^{-2} and 721 mV at 330 nm. The EQE measured at 330 nm was 18% for the optimum Pt device, larger than 1.5% and 11% EQE measured for Au and Ag Schottky devices respectively. The Ag device obtained the second largest UV response of 237 μAcm^{-2} and 282 mV at 330 nm, whilst the Au device maximum photoresponse was 32 μAcm^{-2} and 100 mV at 330 nm.

A small visible response from the Schottky barriers was observed in some cases. This was due to metal induced defect levels in the TiO_2 which allow sub bandgap absorption. The Pt devices gained the highest visible response, the magnitude of which was proportional to the UV response. However, the reproducibility of all of the devices was quite low, with a range of magnitudes of photoresponses and I-V curves obtained across the devices despite repeating the same techniques meticulously. The success of the Pt device may be due to the higher work function of Pt. The Au devices performed poorly due to experimental variables and the Ag devices obtained a low yield due to the low work function of silver which makes it more likely to produce an Ohmic contact.

Thermionic emission was the dominant transport mechanism for most of the ideal Schottky devices created in this work, however, additional series and leakage resistance was often found. Charge hopping transport and tunnelling due to localised states were thought to be dominant in some devices where a departure from ideal I-V characteristics was observed. There are many possible pathways for this departure from ideal Schottky barrier characteristics including low temperature processing, which is known to causes surface defects, inherent impurities and defect levels in the TiO_2 and diffusion of metal particles into the semiconductor. The SBH, ideality factor, as well as the series and leakage resistances calculated by EDM 2, were found to better reproduce the observed I-V curve, compared to the IDM, due to the latter's inherent simplifications. This was expected since the EDM 2 model took account of the additional resistances.

Commercially pure Ti substrates yielded 100% Schottky devices, whereas recycled Ti substrates had a significantly lower yield of <20%, which was thought to be due to a higher impurity level in the Ti which could have extended into the TiO_2 layer. In addition, thermal oxidation of Ti was found to provide a more robust TiO_2 layer, creating less short circuits which were thought to be caused by impurities or etching in the chemical anodisation process.

The reproducibility of the Schottky barriers was the main challenge in this work. Future work should thus concentrate on finding an optimum 'recipe' for creating reproducible Schottky barriers. More control in the fabrication of Schottky barriers will provide greater accuracy and confidence in the results. Better still is the use of alternative, novel metal coatings that could reduce costs if the device was scaled up. Preliminary analysis of the physical mechanisms at play in the Schottky barrier were investigated, however, more detailed analysis is required to confirm these findings. Another potential area of future work includes attempting to enhance the visible absorption of the metals, which result from metal induced defects in the $TiO_{2,}$ to increase the overall device performance.

7.2 Schottky barrier devices fabricated with electrodeposited silver films and silver nanowires

To further develop and add value to the Schottky barrier solar cell, alternative and novel metal coatings of electrodeposited silver and silver nanowires replaced the sputtered and evaporated metals. The main advantage of both of these alternative metal films is that they can be produced via low cost chemical synthesis methods. Silver was electropolished on to the TiO_2/Ti substrates using various silver containing electrolytes via a standard and a strike electrodepositing technique. The silver nanowires, which were synthesised by a polyol method, were filtered and drop cast on to the substrate surface before being annealed.

Silver electrodeposition was found to be unsuccessful in providing an electrically continuous metal film on the TiO_2/Ti substrate and ultimately did not form a Schottky barrier. Dendritic and sporadic silver growth were observed, as observed by other researchers in this area. On the other hand, the silver deposits were found to have a higher surface coverage than previous work, by a comparison of SEM images. Moreover, the strike method was found to deposit more silver and gave an early indication of a continuous layer being formed, however, this was largely uncontrollable, often also forming large silver agglomerations. Adherence was a problem across both electrodepositing techniques since the silver deposits could be easily wiped off the surface.

Future work on silver electrodepositing should concentrate on refining the electrolytes and manipulating the strike technique to control the silver deposits and obtain an electrically continuous layer. The adherence and degradation of electrodeposited silver are important issues since low adherence may prevent the device from operating and oxidisation of the silver may degrade performance. These issues require further research effort. Overall, more experimentation is needed in the area of electrodeposition to provide a feasible method to obtain a reliable silver film for the Schottky barrier solar cell.

The silver nanowires on the other hand, were very successful, forming an electrically continuous mesh on the substrate and outperforming the sputtered and evaporated coatings in terms of obtaining a SBH of 1.02 eV. This may be due to Ag diffusing into the TiO_2 due to annealing. The nanowires worked in the same way as the sputtered and evaporated films, confirmed by the I-V characteristics of the Schottky barrier. The main differences being that the Ag-NW barriers experienced more tunnelling, which is common to nano Schottky barriers, and more ‘noisy’ features, due to nanowire movement during characterisation. The photoresponse of the Ag-NW devices also showed similarities to the other Schottky devices with a large UV peak. However, they also showed a second distinctive shoulder in the UV range extending into the visible region. This additional photoresponse was due to a plasmon effect of the nanowires, which was emphasised by the localised states at the M-S interface. The magnitude of the photovoltage was significantly larger than the photocurrent, which was significantly lower than in the other Schottky devices. This was due to NWs agglomerating on the surface and possibly needing further filtering. In addition the NW devices were much more variable than the other Schottky devices which further indicates that the deposition and production of nanowires requires further refinement. The maximum photocurrent density measured at 330 nm was 18.4 μAcm^{-2}, and the corresponding maximum photovoltage was 397 mV at 330 nm. The EQE measured was 0.43% at 330 nm (significantly lower than the other Schottky barriers) and 0.08% at 390 nm where the second shoulder in the visible region was found.

Further work is therefore required to improve the synthesis of NWs to provide an optimum 'recipe' for producing more consistent, reproducible and transparent NWs. In addition, further work should experiment with alternative, low cost deposition methods, for example spray deposition, spin casting, or printing, to provide a more uniform and well dispersed film. A more precisely deposited NW mesh can lead to better transparency which can enhance the photocurrent. The adherence of the NWs to the TiO_2 surface was not examined in detail, however, the NWs could easily be wiped off the surface, so work is also needed on improving the surface adherence. No obvious signs of degradation were found in the Ag-NW Schottky barriers, however, a more thorough analysis of the degradation of NWs is needed to confirm this.

7.3 Nanocrystal Activated Schottky Barrier Solar Cell

After the Schottky barrier devices had been characterised and confirmed as operational, the device was then activated with nanocrystals to complete the nanocrystal activated Schottky barrier solar cell. Only the Pt and Ag-NW Schottky devices were used in the cell as these showed the most promising results out of all of the Schottky barrier devices. CdS, CdSe, CuO, $CuInS_2$, and CdTe nanocrystals were dropcast on to the Schottky barriers and annealed at a time to suit the reduction of the capping agent. The main difference between the two Schottky barrier devices was that the Ag-NWs had to be drop cast and annealed after the NCs due to the lower temperature required for annealing. A Schottky barrier was still gained for this cell, however, the NCs and NWs were both in direct electrical contact with the TiO_2, which proved advantageous compared to the NC/Pt devices. Overall the NC/Ag-NW devices were found to perform better in terms of I-V and visible photoresponses compared to the NC/Pt devices.

The concept of the NC/Pt device was demonstrated with the CdS-NC/Pt device producing a visible photoresponse. The CdS-NC/Pt device was found to produce a red shifted photoresponse corresponding to the bandgap of bulk CdS. This was prescribed to the fact that annealing structurally changed the NCs into a bulk nanocrystalline film. The EQE measured was 0.04% at 470 nm for the CdS-NC/Pt device (where the visible response was found). The other NC/Pt devices did not show strong or reproducible visible photoresponses.

This was thought to be due to annealing the NCs to the device which degraded the Schottky barrier, indicated by a change in I-V response from rectifying to Ohmic. Evidence for this was observed in the red-CdTe-NC/Pt device where both annealed and non-annealed devices were compared. Some indications of a visible response were found in the red-CdTe-NC/Pt device that had not been annealed, which aligned well with the I-V findings that a Schottky barrier was still operational. Annealing this device led to a more Ohmic I-V response and no visible photoresponse.

Without a fully functioning Schottky barrier it is clear that charge transport is halted, as suggested by the lack of NC visible photoresponse. This was a major issue in the annealed NC devices. Hence, future work should look into lower temperature annealing, chemical ligand replacement methods or using a NC thin film that does not require heating as alternatives to the current annealing process. More detailed work on this device is required to improve the visible response from the NCs and show that it is reproducible across a variety of NCs.

The NC/NW devices proved to be more successful than the NC/Pt devices, with the CdS-NC/Ag-NW and $CuInS_2$-NC/Ag-NW devices giving a clear visible photoresponse and exponential I-V characteristics. The largest EQE measured for the CdS-NC/Ag-NW device was 0.001 – 0.002% between 430 – 530 nm, where the visible feature was found. The EQE measured for the optimum $CuInS_2$-NC/Ag-NW was 0.0004 – 0.0005% between 440-600 nm. The success of the CdS NCs across both Pt and Ag-NW Schottky devices is possibly due to band alignment with the TiO_2, since the conduction band of the CdS NCs sits higher than the other NCs. This would allow for inefficient carrier transport, expected in a proof of concept device and under low temperature processing conditions. The rest of the NC/Ag-NW devices showed good potential with a small indication of a visible photoresponse but without a clear absorption edge or reproducibility, and exponential I-V features. The higher success of these devices is attributable to the use of a NW mesh and the resultant change in structure to a 'hybrid' Schottky barrier design, where the NCs and NWs are both in direct contact with the TiO_2, enhancing carrier transport. Moreover the NWs were deposited and annealed after the NCs, thus avoiding the problems experienced with the NC/Pt devices related to annealing. This was demonstrated with significantly more NC/Ag-NW devices producing exponential I-V characteristics, a good indicator of a Schottky barrier being formed between the NWs and TiO_2 despite the reordering of layers.

Future work should therefore put emphasis on refining the NC/NW devices. This should include refining the synthesis and deposition of the NWs, as described in section 7.2, to provide more reproducible and controllable NW devices as well as an improved mesh. As mentioned previously the post deposition treatment of the NCs requires considerable work to enhance the visible response from the NCs. This design also lends itself well to depositing a variety of NCs with different bandgaps onto the same structure, which could lead to further enhancements in visible photoresponse and overall device performance.

7.4 The impact and future feasibility of the nanocrystal-activated Schottky barrier solar cell

This research has proved the concept of the nanocrystal activated Schottky barrier solar cell and further outlined the potential of a novel nanocrystal activated nanowire Schottky barrier solar cell which has not been shown previously. This is believed to offer a significant contribution to the field of novel, low cost solar cells. The results presented show the initial steps to providing a new route to a low cost solar cell and indicate that this is a viable device worthy of future research.

The promising results shown in this thesis should stimulate research in this area and offer the potential to diversify solar cell technology further. By demonstrating that a variety of bulk and nano materials can produce viable devices, the potential flexibility of future solar cells is increased, which could ultimately lead to cells that are less sensitive to price fluctuations of specific raw materials. Additionally, the use of nanowires in the cell contributes to nanowire research by demonstrating the feasibility of their use in PV applications. This could potentially open up a whole new area of research. Moreover it is feasible that the concept of the NC/NW mesh could be used for other PV applications, for example, BIPV or photoactive coatings.

The cell has used low cost fabrication methods wherever possible providing enhanced opportunities for further research, as well as scaling up of the device. The NC/NW combination, a key component of the device, shows promising potential and future work should explore this further, as well as investigating its use in other PV applications. The NW Schottky barrier is also a prime target for further research due to the potential cost reductions in synthesis and deposition compared to the sputtered films, especially when considering upscaling the device.

7.5 The bigger picture

The underlying theme of this research was to contribute to the field of low cost solar cells. Low cost solar cells are important for our future energy mix across the globe if we are to mitigate against the effects of climate change. In developed countries a lower cost PV panel could encourage and enable homeowners to become prosumers (producer and consumer of energy) of a cleaner and renewable energy source rather than just a consumer of on-grid fossil fuels. Early evidence suggests that prosumers are more energy efficient due to becoming more aware of their own energy use[2]. This may overcome an even bigger battle, since without behavioural change even the lowest cost technologies cannot mitigate against climate change. Other advantages of a higher uptake of PV, enabled by a cost reduction, include the ability to have long-term energy security, ownership of an energy generator and no reliance on the large-scale generators, all top priorities for homeowners in the UK. Further afield, in developing countries, the requirement for low cost PV is threefold, firstly to provide a clean source of energy to replace an ever increasing reliance on cheap fossil fuels, secondly to provide power to the 2 billion that have no access to energy and thirdly to decentralise power in areas where there is over capacity on ageing grid systems which leads to frequent power cuts.

The PV market is currently dominated by silicon cells, in part due to financial incentives and cell price bottoming in China. However, this has led to higher awareness of PV technology and widespread public acceptance, effectively priming the market for alternative, novel and low cost solar cell designs. Current academic and commercial research is focused on increasing the efficiency of cells, effectively reducing the area required for the same amount of power, and reducing the cost of solar cells. The research presented in this thesis has highlighted that the nanocrystal activated Schottky barrier solar cell has the potential to offer a low cost solar cell design. Moreover, nanocrystals hold much promise in boosting the efficiency of solar cells. Hence, with further development the nanocrystal activated Schottky barrier solar cell could provide the powerful combination of a low cost and high efficiency solar cell that is currently being sought.

---

[2] Juliet Davenport founder and CEO of Good Energy. First-hand experience from dealing with prosumers, outlined at the BPVA conference on rooftop PV in June 2014.

References

1. IPCC *Climate Change 2007: The physical science basis*. contribution of working group i to the fourth assessment report of the intergovernmental panel on climate change. Solomon, S., D. Qin, M. Manning, Z. Chen, M.Marquis, K.B. Averyt, M. Tignor and H.L. Miller (eds.), 2007.
2. DECC. *2012 Provisional UK Figures: Statistical release*. 2012 UK greenhouse gas emissions, provisional figures and 2011 UK Greenhouse Gas emissions: final figures by fuel type and end-user. 2013; Available from: https://www.gov.uk/government/publications/provisional-uk-emissions-estimates.
3. HM Government, *The UK Low Carbon Transition Plan*. 2009.
4. Crown, *Climate Change Act 2008*. 2008, The Stationary Office Limited: UK.
5. European Parliament, *Directive 2009/28/EC of the European Parliament and of the Council of 23 April 2009 on the promotion of the use of energy from renewable sources and amending and subsequently repealing Directives 2001/77/EC and 2003/30/EC*, European Commission, Editor. 2009.
6. CCC (Committee on Climate Change), *Building a low-carbon economy – the UK's contribution to tackling climate change,*. 2008.
7. The Royal Society, *Nanoscience and nanotechnologies: opportunities and uncertainties*. Nanotechnology and Nanoscience 2004: The Royal Society & The Royal Academy of Engineering.
8. DECC, *UK Solar PV Strategy Part 1: Roadmap to a brighter future.* 2013.
9. Arnulf Jäger-Waldau, *PV Status Report 2013.* European Commission, JRC Scientific and policy report,, 2013.
10. Emin, S., S.P. Singh, L. Han, N. Satoh, and A. Islam, *Colloidal quantum dot solar cells.* Solar Energy, 2011. **85**(6): p. 1264-1282.
11. Nugent, D. and B.K. Sovacool, *Assessing the lifecycle greenhouse gas emissions from solar PV and wind energy: A critical meta-survey.* Energy Policy, 2014. **65**: p. 229-244.
12. Şengül, H. and T.L. Theis, *An environmental impact assessment of quantum dot photovoltaics (QDPV) from raw material acquisition through use.* Journal of Cleaner Production, 2011. **19**(1): p. 21-31.
13. Barnham, K.W.J., Mazzer, M., and Clive. B,. *Resolving the energy crisis: nuclear or photovoltaics?* Nature Materials [online], 2006. **5** p. 161-164.
14. Goetzberger, A., Hoffmann, V.U., *Photovoltaic solar energy generation*. Optical Sciences ed. W.T. Rhodes. 2005, Germany Springer
15. Surek, T., *Crystal growth and materials research in photovoltaics: progress and challenges.* Journal of Crystal Growth 2004. **275**(1-2): p. 292-304.
16. ENF LTD. *Small Chinese Solar Manufacturers Decimated in 2012*. 2013 06/11/2013] Available from: http://www.enfsolar.com/news/Small-Chinese-Solar-Manufacturers-Decimated-in-2012.
17. DECC, *UK Renewable Energy Roadmap*. 2011.
18. Boyle, G., *Renewable Energy: Power for a Sustainable Future*. 2004, UK: Oxford University Press, The Open University
19. Hillhouse, H.W. and M.C. Beard, *Solar cells from colloidal nanocrystals: Fundamentals, materials, devices, and economics.* Current Opinion in Colloid & Interface Science, 2009. **14**(4): p. 245-259.
20. Shockley, W. and H.J. Queisser, *Detailed balance limit of efficiency of p-n junction solar cells.* Journal of Applied Physics, 1961. **32**(3): p. 510-519.
21. Cartlidge, E., *Bright outlook for solar cells.* Physics world [online]. 2007. **20**(20).
22. Service. R.F., *Solar Energy: Can the upstarts top silicon?* Science AAAS, 2008. **319**(5864): p. 718-720.

23. National Renewable Energy Laboratory (NREL). *Best research cell efficiencies*. 2011.
24. Mary D Archer and Robert Hill, eds. *Clean electricity from photovoltaics* Series on photoconversion of solar energy - Vol. 1. 2001, Imperial College Press: London.
25. Markvart, T. and L. Castaner, eds. *Practical Handbook of Photovoltaics: Fundamentals and Applications*. 2003, Elsevier: Oxford.
26. Dimroth, F., W. Guter, J. Schone, E. Welser, M. Steiner, E. Oliva, A. Wekkeli, G. Siefer, S.P. Philipps, and A.W. Bett. *Metamorphic GaInP/GaInAs/Ge triple-junction solar cells with ≫41 % efficiency*. in *Photovoltaic Specialists Conference (PVSC) 34th IEEE*. 2009.
27. Pattantyus-Abraham, A.G., I.J. Kramer, A.R. Barkhouse, X. Wang, G. Konstantatos, R. Debnath, L. Levina, I. Raabe, M.K. Nazeeruddin, M. Grätzel, and E.H. Sargent, *Depleted-heterojunction colloidal quantum dot solar cells.* ACS Nano, 2010. **4**(6): p. 3374-3380.
28. Goetzberger, A., Hebling, C., Schock, H., , *Photovoltaic materials, history, status and outlook.* Materials Science and Engineering, 2002. **40**: p. 1-46.
29. Seaton, A., Donaldson, K., *Nanoscience, nanotoxicology, and the need to think small.* The Lancet [online], 2005. **365**(9463): p. 923-924.
30. G. N. Tiwari and S. Dubey, *Fundamentals of photovoltaic modules and their applications*. RSC Energy Series, ed. U.C.L. Julian Hunt FRS, London, UK. 2010, Cambridge, UK: The Royal Society of Chemistry.
31. Schaller, R.D., M. Sykora, J.M. Pietryga, and V.I. Klimov, *Seven excitons at a cost of one: redefining the limits for conversion efficiency of photons into charge carriers.* Nano Letters, 2006. **6**(3): p. 424-429.
32. Klimov, V.I., *Detailed-balance power conversion limits of nanocrystal-quantum-dot solar cells in the presence of carrier multiplication.* Applied Physics Letters, 2006. **89**(12): p. -.
33. Choi, J.J., Y.-F. Lim, M.E.B. Santiago-Berrios, M. Oh, B.-R. Hyun, L. Sun, A.C. Bartnik, A. Goedhart, G.G. Malliaras, H.c.D. Abruña, F.W. Wise, and T. Hanrath, *PbSe nanocrystal excitonic solar cells.* Nano Letters, 2009. **9**(11): p. 3749-3755.
34. McFarland, E.W. and J. Tang, *A photovoltaic device structure based on internal electron emission.* Nature, 2003. **421**(6923): p. 616-618.
35. Tang, J., H. Birkedal, E.W. McFarland, and G.D. Stucky, *Self-assembly of CdSe/CdS quantum dots by hydrogen bonding on Au surfaces for photoreception.* Chemical Communications, 2003(18): p. 2278.
36. Nozik, A.J., *Quantum dot solar cells.* Physica E: Low-dimensional systems and nanostructures, 2002. **14**(1-2): p. 115-120.
37. Loef, R., A.J. Houtepen, E. Talgorn, J. Schoonman, and A. Goossens, *Study of electronic defects in CdSe quantum dots and their involvement in quantum dot solar cells.* Nano Letters, 2009. **9**(2): p. 856-859.
38. Rosenberg, H.M., *The Solid State*. 1987, Bristol, UK: Oxford Science Publications
39. Neamen, D.A., *Semiconductor physics and devices : basic principles* ed. T. edition. 2003, Boston, London: McGraw-Hill.
40. Tisdale, W.A., K.J. Williams, B.A. Timp, D.J. Norris, E.S. Aydil, and X.-Y. Zhu, *Hot-electron transfer from semiconductor nanocrystals.* Science, 2010. **328**(5985): p. 1543-1547.
41. Lewis, N.S., *Toward cost-effective solar energy use.* Science, 2007. **315**(5813): p. 798-801.
42. Green, M.A., *Photovoltaic principles.* Physica E: Low-dimensional systems and nanostructures, 2002. **14**(1-2): p. 11-17.
43. Conibeer, G., N. Ekins-Daukes, J.-F. Guillemoles, D. Kőnig, E.-C. Cho, C.-W. Jiang, S. Shrestha, and M. Green, *Progress on hot carrier cells.* Solar Energy Materials and Solar Cells, 2009. **93**(6–7): p. 713-719.

44. König, D., K. Casalenuovo, Y. Takeda, G. Conibeer, J.F. Guillemoles, R. Patterson, L.M. Huang, and M.A. Green, *Hot carrier solar cells: Principles, materials and design.* Physica E: Low-dimensional Systems and Nanostructures, 2010. **42**(10): p. 2862-2866.
45. Conibeer, G.J., D. König, M.A. Green, and J.F. Guillemoles, *Slowing of carrier cooling in hot carrier solar cells.* Thin Solid Films, 2008. **516**(20): p. 6948-6953.
46. Nozik, A.J., *Spectroscopy and hot electron relaxation dynamics in semiconductor quantum wells and quantum dots.* Annual Review of Physical Chemistry, 2001. **52**(1): p. 193-231.
47. Shrestha, S.K., P. Aliberti, and G.J. Conibeer, *Energy selective contacts for hot carrier solar cells.* Solar Energy Materials and Solar Cells, 2010. **94**(9): p. 1546-1550.
48. Würfel, P., *Solar energy conversion with hot electrons from impact ionisation.* Solar Energy Materials and Solar Cells, 1997. **46**(1): p. 43-52.
49. Conibeer, G., R. Patterson, L. Huang, J.-F. Guillemoles, D. Kőnig, S. Shrestha, and M.A. Green, *Modelling of hot carrier solar cell absorbers.* Solar Energy Materials and Solar Cells, 2010. **94**(9): p. 1516-1521.
50. Schaller, R.D., Klimov, V.I., *High efficiency carrier multiplication in PbSe nanocrystals: Implications for solar energy conversion.* Physical Review Letters [online], 2004. **92**(18): pp.186601-186604.
51. Mukai, K. and M. Sugawara, *Slow carrier relaxation among sublevels in annealed self-formed InGaAs/GaAs quantum dots.* Japanese Journal of Applied Physics Part 1-Regular Papers Short Notes & Review Papers, 1998. **37**(10): p. 5451-5456.
52. Gfroerer, T.H., M.D. Sturge, K. Kash, J.A. Yater, A.S. Plaut, P.S.D. Lin, L.T. Florez, J.P. Harbison, S.R. Das, and L. Lebrun, *Slow relaxation of excited states in strain-induced quantum dots.* Physical Review B, 1996. **53**(24): p. 16474-16480.
53. Adler, F., M. Geiger, A. Bauknecht, D. Haase, P. Ernst, A. Dörnen, F. Scholz, and H. Schweizer, *Self-assembled InAs/GaAs quantum dots under resonant excitation.* Journal of Applied Physics, 1998. **83**(3): p. 1631-1636.
54. Conibeer, G.J., C.W. Jiang, D. König, S. Shrestha, T. Walsh, and M.A. Green, *Selective energy contacts for hot carrier solar cells.* Thin Solid Films, 2008. **516**(20): p. 6968-6973.
55. Scheunemann, D., S. Wilken, J. Parisi, and H. Borchert, *Towards depleted heterojunction solar cells with $CuInS_2$ and ZnO nanocrystals.* Applied Physics Letters, 2013. **103**(13).
56. Luther, J.M., J. Gao, M.T. Lloyd, O.E. Semonin, M.C. Beard, and A.J. Nozik, *Stability assessment on a 3% bilayer PbS/ZnO quantum dot heterojunction solar cell.* Advanced Materials, 2010. **22**(33): p. 3704-3707.
57. Ju, T., R.L. Graham, G. Zhai, Y.W. Rodriguez, A.J. Breeze, L. Yang, G.B. Alers, and S.A. Carter, *High efficiency mesoporous titanium oxide PbS quantum dot solar cells at low temperature.* Applied Physics Letters, 2010. **97**(4).
58. Tang, J., K.W. Kemp, S. Hoogland, K.S. Jeong, H. Liu, L. Levina, M. Furukawa, X. Wang, R. Debnath, D. Cha, K.W. Chou, A. Fischer, A. Amassian, J.B. Asbury, and E.H. Sargent, *Colloidal-quantum-dot photovoltaics using atomic-ligand passivation.* Nat Mater, 2011. **10**(10): p. 765-771.
59. Green, M.A., K. Emery, Y. Hishikawa, and W. Warta, *Solar cell efficiency tables (Version 34).* Progress in Photovoltaics, 2009. **17**(5): p. 320-326.
60. Rühle, S., M. Shalom, and A. Zaban, *Quantum-dot-sensitized solar cells.* ChemPhysChem, 2010. **11**(11): p. 2290-2304.
61. Zhao, F., G. Tang, J. Zhang, and Y. Lin, *Improved performance of CdSe quantum dot-sensitized TiO_2 thin film by surface treatment with $TiCl_4$.* Electrochimica Acta, 2012. **62**(0): p. 396-401.

62. Yu, K.H. and J.H. Chen, *Enhancing solar cell efficiencies through 1-D nanostructures.* Nanoscale Research Letters, 2009. **4**(1): p. 1-10.

63. Lee, Y.-L. and Y.-S. Lo, *Highly efficient quantum-dot-sensitized solar cell based on co-sensitization of CdS/CdSe.* Advanced Functional Materials, 2009. **19**(4): p. 604-609.

64. Sun, W.-T., Y. Yu, H.-Y. Pan, X.-F. Gao, Q. Chen, and L.-M. Peng, *CdS quantum dots sensitized TiO_2 nanotube-array photoelectrodes.* Journal of the American Chemical Society, 2008. **130**(4): p. 1124-1125.

65. Parsi Benehkohal, N., V. González-Pedro, P.P. Boix, S. Chavhan, R. Tena-Zaera, G.P. Demopoulos, and I. Mora-Seró, *Colloidal PbS and PbSeS quantum dot sensitized solar cells prepared by electrophoretic deposition.* The Journal of Physical Chemistry C, 2012. **116**(31): p. 16391-16397.

66. Shalom, M., S. Dor, S. Rühle, L. Grinis, and A. Zaban, *Core/Cds quantum dot/shell mesoporous solar cells with improved stability and efficiency using an amorphous TiO_2 Coating.* The Journal of Physical Chemistry C, 2009. **113**(9): p. 3895-3898.

67. Lee, H.J., J.-H. Yum, H.C. Leventis, S.M. Zakeeruddin, S.A. Haque, P. Chen, S.I. Seok, M. Grätzel, and M.K. Nazeeruddin, C*dse quantum dot-sensitized solar cells exceeding efficiency 1% at full-sun intensity.* The Journal of Physical Chemistry C, 2008. **112**(30): p. 11600-11608.

68. Kongkanand, A., K. Tvrdy, K. Takechi, M. Kuno, and P.V. Kamat, *Quantum dot solar cells. tuning photoresponse through size and shape control of CdSe–TiO_2 architecture.* Journal of the American Chemical Society, 2008. **130**(12): p. 4007-4015.

69. Lee, H., H.C. Leventis, S.-J. Moon, P. Chen, S. Ito, S.A. Haque, T. Torres, F. Nüesch, T. Geiger, S.M. Zakeeruddin, M. Grätzel, and M.K. Nazeeruddin, *PbS and CdS quantum dot-sensitized solid-state solar cells: "old concepts, new results".* Advanced Functional Materials, 2009. **19**(17): p. 2735-2742.

70. Lopez-Luke, T., A. Wolcott, L.-p. Xu, S. Chen, Z. Wen, J. Li, E. De La Rosa, and J.Z. Zhang, *Nitrogen-doped and CdSe quantum-dot-sensitized nanocrystalline TiO_2 films for solar energy conversion applications.* The Journal of Physical Chemistry C, 2008. **112**(4): p. 1282-1292.

71. Leschkies, K.S., R. Divakar, J. Basu, E. Enache-Pommer, J.E. Boercker, C.B. Carter, U.R. Kortshagen, D.J. Norris, and E.S. Aydil, *Photosensitization of ZnO nanowires with CdSe quantum dots for photovoltaic devices.* Nano Letters, 2007. **7**(6): p. 1793-1798.

72. Zhu, G., T. Xu, T. Lv, L. Pan, Q. Zhao, and Z. Sun, *Graphene-incorporated nanocrystalline TiO_2 films for CdS quantum dot-sensitized solar cells.* Journal of Electroanalytical Chemistry, 2011. **650**(2): p. 248-251.

73. Chandrasekaran, J., D. Nithyaprakash, K.B. Ajjan, S. Maruthamuthu, D. Manoharan, and S. Kumar, *Hybrid solar cell based on blending of organic and inorganic materials-An overview.* Renewable and Sustainable Energy Reviews, 2011. **15**(2): p. 1228-1238.

74. Shanmugam, M., C.A. Durcan, and B. Yu, *Layered semiconductor molybdenum disulfide nanomembrane based Schottky-barrier solar cells.* Nanoscale, 2012. **4**(23): p. 7399-7405.

75. Li, F.B. and X.Z. Li, *The enhancement of photodegradation efficiency using Pt–TiO_2 catalyst.* Chemosphere, 2002. **48**(10): p. 1103-1111.

76. Liu, S.X., Z.P. Qu, X.W. Han, and C.L. Sun, *A mechanism for enhanced photocatalytic activity of silver-loaded titanium dioxide.* Catalysis Today, 2004. **93-95**: p. 877-884.

77. Pan, C. and L. Dong, *Fabrication of gold-doped titanium dioxide (TiO_2:Au) nanofibers photocatalyst by vacuum ion sputter coating.* Journal of Macromolecular Science, Part B, 2009. **48**(5): p. 919-926.

78. Ma, W., J.M. Luther, H. Zheng, Y. Wu, and A.P. Alivisatos, *Photovoltaic devices employing ternary PbS_xSe_{1-x} nanocrystals.* Nano Letters, 2009. **9**(4): p. 1699-1703.

79. Debnath, R., J. Tang, D.A. Barkhouse, X. Wang, A.G. Pattantyus-Abraham, L. Brzozowski, L. Levina, and E.H. Sargent, *Ambient-processed colloidal quantum dot solar cells via individual pre-encapsulation of nanoparticles.* Journal of the American Chemical Society, 2010. **132**(17): p. 5952-5953.
80. Olson, J.D., Y.W. Rodriguez, L.D. Yang, G.B. Alers, and S.A. Carter, *CdTe Schottky diodes from colloidal nanocrystals.* Applied Physics Letters, 2010. **96**(24): p. 242103.
81. Tang, J., X. Wang, L. Brzozowski, D.A.R. Barkhouse, R. Debnath, L. Levina, and E.H. Sargent, *Schottky quantum dot solar cells stable in air under solar illumination.* advanced materials, 2010. **22**(12): p. 1398-1402.
82. Koleilat, G.I., L. Levina, H. Shukla, S.H. Myrskog, S. Hinds, A.G. Pattantyus-Abraham, and E.H. Sargent, *Efficient, stable infrared photovoltaics based on solution-cast colloidal quantum dots.* ACS Nano, 2008. **2**(5): p. 833-840.
83. Luther, J.M., M. Law, M.C. Beard, Q. Song, M.O. Reese, R.J. Ellingson, and A.J. Nozik, *Schottky solar cells based on colloidal nanocrystal films.* Nano Letters, 2008. **8**(10): p. 3488-3492.
84. Liu, C.-Y. and U.R. Kortshagen, *A silicon nanocrystal schottky junction solar cell produced from colloidal silicon nanocrystals.* Nanoscale Research Letters, 2010. **5**: p. 1253-1256.
85. Klem, E.J.D., D.D. MacNeil, L. Levina, and E.H. Sargent, *Solution processed photovoltaic devices with 2% infrared monochromatic power conversion efficiency: performance optimization and oxide formation.* Advanced Materials, 2008. **20**(18): p. 3433-3439.
86. Zhu, M., J. Zhang, and H. Hou, *Fabrication and electrical characteristics of the Pt/SiNWs/n-Si/Al Schottky diode structure.* Microelectronic Engineering, 2012. **95**(0): p. 112-115.
87. Shah, M., M.H. Sayyad, K.S. Karimov, and M. Maroof-Tahir, *Investigation of the electrical properties of a surface-type Al/NiPc/Ag Schottky diode using I–V and C–V characteristics.* Physica B: Condensed Matter, 2010. **405**(4): p. 1188-1192.
88. Liang, G., T. Cui, and K. Varahramyan, *Fabrication and electrical characteristics of polymer-based Schottky diode.* Solid-State Electronics, 2003. **47**(4): p. 691-694.
89. Johnston, K.W., A.G. Pattantyus-Abraham, J.P. Clifford, S.H. Myrskog, D.D. MacNeil, L. Levina, and E.H. Sargent, *Schottky-quantum dot photovoltaics for efficient infrared power conversion.* Applied Physics Letters, 2008. **92**(15): p. 151115.
90. Cheung, S.K. and N.W. Cheung, *Extraction of Schottky diode parameters from forward current ‐ voltage characteristics.* Applied Physics Letters, 1986. **49**(2): p. 85-87.
91. Güllü, Ö., Ş. Aydoğan, and A. Türüt, *Fabrication and electrical characteristics of Schottky diode based on organic material.* Microelectronic Engineering, 2008. **85**(7): p. 1647-1651.
92. Pattabi, M., S. Krishnan, Ganesh, and X. Mathew, *Effect of temperature and electron irradiation on the I–V characteristics of Au/CdTe Schottky diodes.* Solar Energy, 2007. **81**(1): p. 111-116.
93. Schottky, W., *Semiconductor theory in barrier layers.* Naturwissenschaften, 1938. **26**(52): p. 843-843.
94. Fraser, D.A., *The physics of semiconductors*. Oxford physics series, ed. E.J. Burge, D.J.E. Ingram, and J.A.D. Matthew. 1983, Oxford Clarendon Press.
95. B.L.Sharma, ed. *Metal-semiconductor schottky barrier junctions and their applications*. 1984, Plenum Press: New York and London.
96. Tung, R.T., *Recent advances in Schottky barrier concepts.* Materials Science and Engineering: R: Reports, 2001. **35**(1–3): p. 1-138.

97. Mott, N.F., *Note on the contact between a metal and an insulator or semi-conductor.* Mathematical Proceedings of the Cambridge Philosophical Society, 1938. **34**(04): p. 568-572.

98. Jeong Young Park, J. R. Renzas, Bryan B. Hsu, and Gabor A. Somorjai, *Interfacial and chemical properties of Pt/TiO_2, Pd/TiO_2, and Pt/GaN catalytic nanodiodes influencing hot electron flow.* The Journal of Physical Chemistry C, 2007. **111**: p. 15331-15336.

99. Seah, M.P. and W.A. Dench, *Quantitative electron spectroscopy of surfaces: A standard data base for electron inelastic mean free paths in solids.* Surface and Interface Analysis, 1979. **1**(1): p. 2-11.

100. Koole, R., P. Liljeroth, S. Oosterhout, and D. Vanmaekelbergh, *Chemisorption determines the photovoltage of a Ti/TiO_2/Au/Dye internal electron emission photovoltaic cell.* The Journal of Physical Chemistry B, 2005. **109**(19): p. 9205-9208.

101. Taylor, J.B., L.C. Mayor, J.C. Swarbrick, J.N. O'Shea, and J. Schnadt, *Charge-transfer dynamics at model metal–organic solar cell surfaces.* The Journal of Physical Chemistry C, 2007. **111**(44): p. 16646-16655.

102. Li, R., C. Cai, L. Hu, H. Wu, W. Zhang, and J. Zhu, *Band alignment of ZnO/CdSe quantum dots heterojunction determined by ultraviolet photoelectron spectroscopy using synchrotron radiation.* Applied Surface Science, 2013. **276**(0): p. 258-261.

103. Hanna, M.C., M.C. Beard, and A.J. Nozik, *Effect of solar concentration on the thermodynamic power conversion efficiency of quantum-dot solar cells exhibiting multiple exciton generation.* The Journal of Physical Chemistry Letters, 2012. **3**(19): p. 2857-2862.

104. Pijpers, J.J.H., Hendry, E., Milder, M.T.W., Fanciulli, R., Savolainen, J., Herek, J.L., Vanmaekelbergh, D., Ruhman, S., Mocatta, D., Oron, D., Aharoni, A., Banin, U., and Bonn, M., *Carrier multiplication and its reduction by photodoping in colloidal InAs quantum dots.* Journal of physical chemistry C, 2007. **111**: p. 4146-4152.

105. Rogach, A.L., D. Nagesha, J.W. Ostrander, M. Giersig, and N.A. Kotov, *"Raisin Bun"-type composite spheres of silica and semiconductor nanocrystals.* Chemistry of Materials, 2000. **12**(9): p. 2676-2685.

106. Federation of European Producers of Abrasives (FEPA). *Silicon carbide grains*. FEPA-standard 43-2:2006: Grains of fused aluminium oxide, silicon carbide and other abrasive materials for coated abrasives Microgrits P 240 to P 2500 2013; Available from: http://www.fepa-abrasives.org.

107. Mahé, E. and D. Devilliers, *Surface modification of titanium substrates for the preparation of noble metal coated anodes.* Electrochimica Acta, 2001. **46**(5): p. 629-636.

108. Jumer, J.F., *Electropolishing.* Metal Finishing, 1995. **93**(1, Supplement 1): p. 420-427.

109. Landolt, D., *Fundamental aspects of electropolishing.* Electrochimica Acta, 1987. **32**(1): p. 1-11.

110. Raberto Vidal and A.C. West, *Copper electropolishing in concentrated phosphoric acid.* J. Electrochem. Soc., 1995. **142**(8): p. 2682 - 2688.

111. Kuhn, A., *The electropolishing of titanium and its alloys.* Metal Finishing, 2004. **102**(6): p. 80-86.

112. Piotrowski, O., C. Madore, and D. Landolt, *The mechanism of electropolishing of titanium in methanol-sulfuric acid electrolytes.* Journal of The Electrochemical Society, 1998. **145**(7): p. 2362-2369.

113. Fushimi, K. and H. Habazaki, *Anodic dissolution of titanium in NaCl-containing ethylene glycol.* Electrochimica Acta, 2008. **53**(8): p. 3371-3376.

114. Tajima, K., K.-K.C. M.H., Y. Nagamatsu, H. Kakigawa, and Y. Kozono, *Electropolishing of CP Titanium and its alloys in an alcoholic solution-based electrolyte.* Dent. Mater. J, 2008. **27**: p. 258-265.

115. Piotrowski, C. Madore, and D. Landolt, *The mechanism of electropolishing of titanium in methanol-sulfuric acid electrolytes.* J. Electrochem. Soc, July 1998. **145**(7): p. 2362-2369.
116. Smith, G.X.R., *Energy Research Insitute, Univesity of Leeds*. 2013.
117. Sambur, J.B., T. Novet, and B.A. Parkinson, *Multiple exciton collection in a sensitized photovoltaic system.* Science, 2010. **330**(6000): p. 63-66.
118. Xu, Y. and M.A.A. Schoonen, *The absolute energy positions of conduction and valence bands of selected semiconducting minerals.".* American Mineralogist, 2000. **85**(3-4): p. 543–556.
119. Zhu, W., X. Qiu, V. Iancu, X.-Q. Chen, H. Pan, W. Wang, N.M. Dimitrijevic, T. Rajh, H.M. Meyer, M.P. Paranthaman, G.M. Stocks, H.H. Weitering, B. Gu, G. Eres, and Z. Zhang, *Band gap narrowing of titanium oxide semiconductors by noncompensated anion-cation codoping for enhanced visible-light photoactivity.* Physical Review Letters, 2009. **103**(22): p. 226401.
120. Tang, J., M. White, G.D. Stucky, and E.W. McFarland, *Electrochemical fabrication of large-area Au/TiO_2 junctions.* Electrochemistry Communications, 2003. **5**(6): p. 497-501.
121. Fujishima, A., X. Zhang, and D.A. Tryk, *TiO_2 photocatalysis and related surface phenomena.* Surface Science Reports, 2008. **63**(12): p. 515-582.
122. Hossein-Babaei, F., M.M. Lajvardi, and F.A. Boroumand, *Large area Ag–TiO_2 UV radiation sensor fabricated on a thermally oxidized titanium chip.* Sensors and Actuators A: Physical, 2012. **173**(1): p. 116-121.
123. Seery, M.K., R. George, P. Floris, and S.C. Pillai, *Silver doped titanium dioxide nanomaterials for enhanced visible light photocatalysis.* Journal of Photochemistry and Photobiology A: Chemistry, 2007. **189**(2-3): p. 258-263.
124. Oshida, Y., *Bioscience and bioengineering of titanium materials*. 2007, Oxford: Elsevier.
125. Mo, S.-D. and W.Y. Ching, *Electronic and optical properties of three phases of titanium dioxide: Rutile, anatase, and brookite.* Physical Review B, 1995. **51**(19): p. 13023-13032.
126. Güçlü, F.M., H. Çimenoğlu, and E.S. Kayalı, *The recrystallization and thermal oxidation behavior of CP-titanium.* Materials Science and Engineering: C, 2006. **26**(8): p. 1367-1372.
127. Oshida, Y., *4 - Oxidation and Oxides*, in *Bioscience and Bioengineering of Titanium Materials (Second Edition)*. 2013, Elsevier: Oxford. p. 87-115.
128. Capek, D., M.P. Gigandet, M. Masmoudi, M. Wery, and O. Banakh, *Long-time anodisation of titanium in sulphuric acid.* Surface and Coatings Technology, 2008. **202**(8): p. 1379-1384.
129. Fraunhofer, J.A.V., *Basic Metal Finishing* 1976, London: Elek Science
130. Wernick, S. and R. Pinner, *The surface treatment and finishing of aluminium and its alloys*. Fourth ed. Vol. 1. 1972, Teddington: Robert Draker LTD.
131. Masahashi, N., Y. Mizukoshi, S. Semboshi, and N. Ohtsu, *Enhanced photocatalytic activity of rutile TiO_2 prepared by anodic oxidation in a high concentration sulfuric acid electrolyte.* Applied Catalysis B: Environmental, 2009. **90**(1-2): p. 255-261.
132. Diamanti, M.V., B. Del Curto, and M. Pedeferri, *Interference colors of thin oxide layers on titanium.* Color Research & Application, 2008. **33**(3): p. 221-228.
133. Jaeggi, C., P. Kern, J. Michler, J. Patscheider, J. Tharian, and F. Munnik, *Film formation and characterization of anodic oxides on titanium for biomedical applications.* Surface and Interface Analysis, 2006. **38**(4): p. 182-185.
134. Revie, R.W., ed. *Uhlig's Corrosion Handbook (3rd Edition)*. 2011, John Wiley & Sons.

135. Kozlowski, M.R., P.S. Tyler, W.H. Smyrl, and R.T. Atanasoski, *Photoelectochemical Microscopy of oxide films on metals: Ti/TiO_2 interface* Surface Science 1988. **194**: p. 505-530.
136. Deplancke, J.L., A. Garnier, Y. Massianlt, and R. Winand, *Influence of the anodizing procedure on the structure and the properties of titanium oxide films and its effect on copper nucleation.* Electrochimica Acta, 1994. **39**(8/9): p. 1281-1289.
137. Sul, Y.-T., C.B. Johansson, Y. Jeong, and T. Albrektsson, *The electrochemical oxide growth behaviour on titanium in acid and alkaline electrolytes.* Medical Engineering & Physics, 2001. **23**(5): p. 329-346.
138. Gemelli, E. and N. Camargo, *Oxidation kinetics of commercially pure titanium.* Revista Matéria, 2007. **12**(3): p. 525 - 531.
139. Wen, M., C. Wen, P. Hodgson, and Y. Li, *Thermal oxidation behaviour of bulk titanium with nanocrystalline surface layer.* Corrosion Science, 2012. **59**(0): p. 352-359.
140. Hossein-Babaei, F. and S. Rahbarpour, *Titanium and silver contacts on thermally oxidized titanium chip: Electrical and gas sensing properties.* Solid-State Electronics, 2011. **56**(1): p. 185-190.
141. Hossein-Babaei, F. and S. Rahbarpour, *Separate assessment of chemoresistivity and Schottky-type gas sensitivity in M ‒metal oxide ‒M ′ structures.* Sensors and Actuators B: Chemical, 2011. **160**(1): p. 174-180.
142. Wang, Z., X. Cai, Q. Chen, and P.K. Chu, *Effects of Ti transition layer on stability of silver/titanium dioxide multilayered structure.* Thin Solid Films, 2007. **515**(5): p. 3146-3150.
143. Adachi, M., J.R. Mackert, E.E. Parry, and C.W. Fairhurst, *Oxide Adherence and porcelain bonding to titanium and Ti-6A1-4V alloy.* Journal of Dental Research, 1990. **69**(6): p. 1230-1235.
144. Fang, X., T. Ma, G. Guan, M. Akiyama, T. Kida, and E. Abe, *Effect of the thickness of the Pt film coated on a counter electrode on the performance of a dye-sensitized solar cell.* Journal of Electroanalytical Chemistry, 2004. **570**(2): p. 257-263.
145. Fang, F., Q. Li, and J.K. Shang, *Enhanced visible-light absorption from Ag_2O nanoparticles in nitrogen-doped TiO_2 thin films.* Surface and Coatings Technology, 2011. **205**(8–9): p. 2919-2923.
146. Haynes, W.M., ed. *CRC Handbook of Chemistry and Physics*. 94th Edition (Internet Version 2014) ed. Electron work function of the elements. 2013, CRC Press/Taylor and Francis: Boca Raton, FL.
147. Haynes, W.M., *CRC Handbook of Chemistry and Physics, Electron inelastic mean free paths*, C.J. Powell, Editor. 2013, CRC Press/Taylor and Francis: Boca Raton, FL.
148. Chandra, S.V.J., E. Fortunato, R. Martins, and C.-J. Choi, *Modulations in effective work function of platinum gate electrode in metal-oxide-semiconductor devices.* Thin Solid Films, 2012. **520**(14): p. 4556-4558.
149. Lim, A.E.-J., W.S. Hwang, X.P. Wang, D.M.Y. Lai, G.S. Samudra, D.-L. Kwong, and Y.-C. Yeo, *Metal-gate work function modulation using hafnium alloys obtained by the interdiffusion of thin metallic layers.* Journal of the Electrochemical Society, 2007. **154**(4): p. H309-H313.
150. P. Slepička, V. Švorčík, M. Šlouf, V. Rybka, and M. Špirková, *Characterization of metal nanolayers sputtered on poly(ethyleneterephtalate).* Optoelectronics And Advanced Materials – Rapid Communications, 2008. **2**(3): p. p. 153 - 160.
151. Sawyer, D.T. and J.L. Roberts, *Experimental Electrochemistry for Chemists*. 1974, USA: John Wiley & Sons
152. Pecequilo, C.V. and Z. Panossian, *Study of copper electrodeposition mechanism from a strike alkaline bath prepared with 1-hydroxyethane-1,1-diphosphonic acid through cyclic voltammetry technique.* Electrochimica Acta. **55**(12): p. 3870-3875.

153. Bard, A.J. and L.R. Faulkner, *Electrochemical Methods: Fundamentals and Applications* 2nd edition ed. 2001, United States John Wiley & sons.

154. DoÌˆbeli, M. and et al., *Selective Electrodeposition of Cu nanostructures on focused ion beam sensitized p-Si.* Journal of The Electrochemical Society, 2002. **149**(8): p. C432.

155. Gerko, O. and et al., *Electrodeposition of copper on silicon from sulfate solution.* Journal of The Electrochemical Society, 2001. **148**(11): p. C746.

156. Oskam, G. and et al., *Electrochemical deposition of metals onto silicon.* Journal of Physics D: Applied Physics, 1998. **31**(16): p. 1927.

157. Henau, K. and et al., *The influence of the surface preparation on the electrodeposition of gold particles on silicon.* Journal of Solid State Electrochemistry, 2009.

158. Oskam, G. and P.C. Searson, *Electrochemical nucleation and growth of gold on silicon.* Surface Science, 2000. **446**(1–2): p. 103-111.

159. Allongue, P. and E. Souteyrand, *Metal electrodeposition on semiconductors: Part 2. Description of the nucleation processes.* Journal of Electroanalytical Chemistry, 1993. **362**(1-2): p. 79-87.

160. Boskovic, I., S.V. Mentus, and M. Pjescic, *Electrochemical behavior of an Ag/*TiO_2 *composite surfaces.* Electrochimica Acta, 2006. **51**(14): p. 2793-2799.

161. Lee, C.L. and C.C. Syu, *Electrochemical growth and oxygen reduction property of Ag nanosheet arrays on a Ti/*TiO_2 *electrode.* International Journal of Hydrogen Energy, 2011. **36**(23): p. 15068-15074.

162. Kong, D., J.Z.Y. Tan, F. Yang, J. Zeng, and X. Zhang, *Electrodeposited Ag nanoparticles on* TiO_2 *nanorods for enhanced UV visible light photoreduction CO2 to CH4.* Applied Surface Science, 2013. **277**(0): p. 105-110.

163. Liu, X., Z. Liu, S. Hao, and W. Chu, *Facile fabrication of well-dispersed silver nanoparticles loading on* TiO_2 *nanotube arrays by electrodeposition.* Materials Letters, 2012. **80**(0): p. 66-68.

164. Forment, S., R.L.V. Meirhaeghe, A.D. Vrieze, K. Strubbe, and W.P. Gomes, *A comparative study of electrochemically formed and vacuum-deposited n-GaAs/Au Schottky barriers using ballistic electron emission microscopy (BEEM).* Semiconductor Science and Technology, 2001. **16**(12): p. 975.

165. V.P. Poroshkov and V.S. Gurin, *Surface structures on titanium dioxide electrodes after electrochemical silver deposition.* Surface Science, 1995(331-333): p. 1520-1525.

166. De, S., T.M. Higgins, P.E. Lyons, E.M. Doherty, P.N. Nirmalraj, W.J. Blau, J.J. Boland, and J.N. Coleman, *silver nanowire networks as flexible, transparent, conducting films: extremely high DC to optical conductivity ratios.* ACS Nano, 2009. **3**(7): p. 1767-1774.

167. Misra, S., L. Yu, M. Foldyna, and P. Roca i Cabarrocas, *High efficiency and stable hydrogenated amorphous silicon radial junction solar cells built on VLS-grown silicon nanowires.* Solar Energy Materials and Solar Cells, 2013. **118**(0): p. 90-95.

168. Kayes, B.M., H.A. Atwater, and N.S. Lewis, *Comparison of the device physics principles of planar and radial p-n junction nanorod solar cells.* Journal of Applied Physics, 2005. **97**(11): p. 114302.

169. Krogstrup, P., H.I. Jorgensen, M. Heiss, O. Demichel, J.V. Holm, M. Aagesen, J. Nygard, and A. Fontcuberta i Morral, *Single-nanowire solar cells beyond the Shockley-Queisser limit.* Nature Photonics, 2013. **7**(4): p. 306-310.

170. Reinhard, M., R. Eckstein, A. Slobodskyy, U. Lemmer, and A. Colsmann, *Solution-processed polymer–silver nanowire top electrodes for inverted semi-transparent solar cells.* Organic Electronics, 2013. **14**(1): p. 273-277.

171. Lee, J.-Y., S.T. Connor, Y. Cui, and P. Peumans, S*emitransparent organic photovoltaic cells with laminated top electrode.* Nano Letters, 2010. **10**(4): p. 1276-1279.
172. Gaynor, W., J.-Y. Lee, and P. Peumans, *Fully solution-processed inverted polymer solar cells with laminated nanowire electrodes.* ACS Nano, 2009. **4**(1): p. 30-34.
173. Kang, M.-G., T. Xu, H.J. Park, X. Luo, and L.J. Guo, *Efficiency enhancement of organic solar cells using transparent plasmonic Ag nanowire electrodes.* Advanced Materials, 2010. **22**(39): p. 4378-4383.
174. Gaynor, W., G.F. Burkhard, M.D. McGehee, and P. Peumans, *Smooth nanowire/polymer composite transparent electrodes.* Advanced Materials, 2011. **23**(26): p. 2905-2910.
175. Atwater, H.A. and A. Polman, *Plasmonics for improved photovoltaic devices.* Nature Materials, 2010. **9**: p. 205-213.
176. Garnett, E.C., M.L. Brongersma, Y. Cui, and M.D. McGehee, *Nanowire solar cells.* Annual Review of Materials Research, 2011. **41**(1): p. 269-295.
177. Hutter, E. and J.H. Fendler, *Exploitation of localized surface plasmon resonance.* Advanced Materials, 2004. **16**(19): p. 1685-1706.
178. Korte, K.E., S.E. Skrabalak, and Y. Xia, *Rapid synthesis of silver nanowires through a CuCl- or $CuCl_2$-mediated polyol process.* Journal of Materials Chemistry, 2008. **18**(4): p. 437.
179. Sun, Y., B. Mayers, T. Herricks, and Y. Xia, *Polyol synthesis of uniform silver nanowires: A plausible growth mechanism and the supporting evidence.* Nano Letters, 2003. **3**(7): p. 955-960.
180. Zhang, Z., Y. Zheng, P. He, and Z. Sun, *High yield preparation of silver nanowires by $CuCl_2$-mediated polyol method and application in semitransparent conduction electrode.* Physica E: Low-dimensional Systems and Nanostructures, 2011. **44**(3): p. 535-540.
181. Madaria, A.R., A. Kumar, F.N. Ishikawa, and C. Zhou, *Uniform, highly conductive, and patterned transparent films of a percolating silver nanowire network on rigid and flexible substrates using a dry transfer technique.* Nano Research, 2010. **3**(8): p. 564-573.
182. Lee, J.-Y., S.T. Connor, Y. Cui, and P. Peumans, *Solution-processed metal nanowire mesh transparent electrodes.* Nano Letters, 2008. **8**(2): p. 689-692.
183. Linsebigler, A.L., G. Lu, and J. John T. Yates, *Photocatalysis on TiO_n surfaces: principles, mechanisms, and selected results.* Chem. Rev., 1995. **95**: p. 735-758.
184. Hagfeldt, A. and M. Graetzel, *Light-induced redox reactions in nanocrystalline systems.* Chemical Reviews, 1995. **95**(1): p. 49-68.
185. Zhang, X., F. Liu, Q.-L. Huang, G. Zhou, and Z.-S. Wang, *Dye-sensitized W-doped TiO_2 solar cells with a tunable conduction band and suppressed charge recombination.* The Journal of Physical Chemistry C, 2011. **115**(25): p. 12665-12671.
186. Gratzel, M., *Photoelectrochemical cells.* Nature, 2001. **414**(6861): p. 338 - 344.
187. Ishii, H., K. Sugiyama, E. Ito, and K. Seki, *Energy level alignment and interfacial electronic structures at organic/metal and organic/organic interfaces.* Advanced Materials 1999. **11**(8): p. 605 - 625.
188. Geyer, S., V.J. Porter, J.E. Halpert, T.S. Mentzel, M.A. Kastner, and M.G. Bawendi, *Charge transport in mixed CdSe and CdTe colloidal nanocrystal films.* Physical Review B, 2010. **82**(155201): p. 1-8.
189. Kamat, P.V., *Quantum Dot Solar Cells. Semiconductor nanocrystals as light harvesters†.* The Journal of Physical Chemistry C, 2008. **112**(48): p. 18737-18753.
190. Yu, W.W. and X. Peng, *formation of high-quality cds and other II–VI semiconductor nanocrystals in noncoordinating solvents: tunable reactivity of monomers.* Angewandte Chemie International Edition, 2002. **41**(13): p. 2368-2371.

191. Bailey, R.E. and S. Nie, *Alloyed Semiconductor Quantum Dots: Tuning the optical properties without changing the particle size.* Journal of the American Chemical Society, 2003. **125**(23): p. 7100-7106.
192. Zhang, J., J. Liu, Q. Peng, X. Wang, and Y. Li, *Nearly monodisperse Cu_2O and CuO nanospheres: preparation and applications for sensitive gas sensors.* Chemistry of Materials, 2006. **18**(4): p. 867-871.
193. Luther, J.M., M. Law, Q. Song, C.L. Perkins, M.C. Beard, and A.J. Nozik, *Structural, optical, and electrical properties of self-assembled films of PbSe nanocrystals treated with 1,2-Ethanedithiol.* ACS Nano, 2008. **2**(2): p. 271-280.
194. Law M., Luther Joseph M., Song Qing., B.K. Hughes, Craig L. Perkins, and Arthur J. Nozik, *Structural, optical, and electrical properties of PbSe nanocrystal solids treated thermally or with simple amines.* American Chemical Society, 2008. **130**: p. 5974–5985.
195. Stolle, C.J., T.B. Harvey, and B.A. Korgel, *Nanocrystal photovoltaics: a review of recent progress.* Current Opinion in Chemical Engineering, 2013. **2**(2): p. 160-167.
196. Bucherl, C.N., K.R. Oleson, and H.W. Hillhouse, *Thin film solar cells from sintered nanocrystals.* Current Opinion in Chemical Engineering, 2013. **2**(2): p. 168-177.
197. MacDonald, B.I., A. Martucci, S. Rubanov, S.E. Watkins, P. Mulvaney, and J.J. Jasieniak, *Layer-by-layer assembly of sintered $CdSe_xTe_{1–x}$ nanocrystal solar cells.* ACS Nano, 2012. **6**(7): p. 5995-6004.
198. T.S. Mentzel, V.J.P., S. Geyer, K. MacLean, M.G. Bawendi, M.A. Kastner, *Charge transport in PbSe nanocrystal arrays.* Phys Rev B, 2008. **77**: p. 8.
199. Drndić, M., M.V. Jarosz, N.Y. Morgan, M.A. Kastner, and M.G. Bawendi, *Transport properties of annealed CdSe colloidal nanocrystal solids.* Journal of Applied Physics, 2002. **92**(12): p. 7498-7503.
200. Konstantatos, G., I. Howard, A. Fischer, S. Hoogland, J. Clifford, E. Klem, L. Levina, and E.H. Sargent, *Ultrasensitive solution-cast quantum dot photodetectors.* Nature, 2006. **442**(7099): p. 180- 183.
201. Black, C.T., C.B. Murray, R.L. Sandstrom, and S. Sun, *Spin-dependent tunneling in self-assembled cobalt-nanocrystal superlattices.* Science, 2000. **290**(5494): p. 1131-1134.
202. Huang, W., J. Peng, and L. Wang, *Investigation of annealing effects on microstructure of hybrid nanocrystal–polymer solar cells by impedance spectroscopy.* Synthetic Metals, 2010. **160**(5–6): p. 445-449.
203. Gur, I., N.A. Fromer, M.L. Geier, and A.P. Alivisatos, *Air-stable all-inorganic nanocrystal solar cells processed from solution.* Science, 2005. **310**(5747): p. 462-465.
204. Jasieniak, J., B.I. MacDonald, S.E. Watkins, and P. Mulvaney, *solution-processed sintered nanocrystal solar cells via layer-by-layer assembly.* Nano Letters, 2011. **11**(7): p. 2856-2864.
205. Kelsall, R., Hamley, I., Geoghegan, M., *Nanoscale science and technology*. 2005, Chichester: Wiley.
206. Liu, C.-Y. and U. Kortshagen, *A silicon nanocrystal Schottky junction solar cell produced from colloidal silicon nanocrystals.* Nanoscale Research Letters, 2010. **5**(8): p. 1253-1256.
207. Fuke, N., A. Fukui, A. Islam, R. Komiya, R. Yamanaka, H. Harima, and L. Han, *Influence of TiO_2/electrode interface on electron transport properties in back contact dye-sensitized solar cells.* Solar Energy Materials and Solar Cells, 2009. **93**(6–7): p. 720-724.
208. E.H. Rhoderick and R.H. Williams, *Metal-semiconductor contacts*. 2nd ed. 1988, Oxford: Clarendon Press,.

209. Aydin, M.E., K. Akkiliç, and T. Kiliçoğlu, *The importance of the series resistance in calculating the characteristic parameters of the Schottky contacts.* Applied Surface Science, 2006. **253**(3): p. 1304-1309.

210. Woo Young Park, Gun Hwan Kim, Jun Yeong Seok, Kyung Min Kim, Seul Ji Song, Min Hwan Lee, and Cheol Seong Hwang, *A Pt/TiO_2/Ti Schottky-type selection diode for alleviating the sneak current in resistance switching memory arrays.* Nanotechnology, 2010. **21**(195201).

211. O'Hayre, R., M. Nanu, J. Schoonman, and A. Goossens, *Mott−Schottky and charge-transport analysis of nanoporous titanium dioxide films in air.* The Journal of Physical Chemistry C, 2007. **111**(12): p. 4809-4814.

212. Kim, H., D.-W. Kim, and S.-H. Phark, *Transport behaviours and nanoscopic resistance profiles of electrically stressed Pt/TiO_2/Ti planar junctions.* Journal of Physics D: Applied Physics, 2010. **43**(50): p. 505305.

213. Miller, K., K.S. Nalwa, A. Bergerud, N.M. Neihart, and S. Chaudhary, *Memristive behavior in thin anodic titania.* Electron Device Letters, IEEE, 2010. **31**(7): p. 737-739.

214. Yang, J.J., M.D. Pickett, X. Li, OhlbergDouglas A. A., D.R. Stewart, and R.S. Williams, *Memristive switching mechanism for metal//oxide//metal nanodevices.* Nature Nanotechnology, 2008. **3**(7): p. 429 - 433.

215. Tataroğlu, A. and Ş. Altındal, *The analysis of the series resistance and interface states of MIS Schottky diodes at high temperatures using I–V characteristics.* Journal of Alloys and Compounds, 2009. **484**(1–2): p. 405-409.

216. Chand, S. and J. Kumar, *Effects of barrier height distribution on the behavior of a Schottky diode.* Journal of Applied Physics, 1997. **82**(10): p. 5005-5010.

217. Shockley, W. and W.T. Read, *Statistics of the recombinations of holes and electrons.* Physical Review, 1952. **87**(5): p. 835-842.

218. Hall, R.N., *Electron-hole recombination in germanium.* Physical Review, 1952. **87**(2): p. 387-387.

219. Könenkamp, R. and R. Henninger, *Recombination in nanophase TiO_2 films.* Applied Physics A, 1994. **58**(1): p. 87-90.

220. Daude, N., C. Gout, and C. Jouanin, *Electronic band structure of titanium dioxide.* Physical Review B, 1977. **15**(6): p. 3229-3235.

221. Ekuma, C.E. and D. Bagayoko, *Ab-initio electronic and structural properties of rutile titanium dioxide.* Japanese Journal of Applied Physics, 2011. **50**(10): p. 101103-101110.

222. Landmann, M., E. Rauls, and W.G. Schmidt, *The electronic structure and optical response of rutile, anatase and brookite TiO 2.* Journal of Physics: Condensed Matter, 2012. **24**(19): p. 195503.

223. Saehana, S., P. Arifin, K. Khairurrijal, and M. Abdullah, *A new architecture for solar cells involving a metal bridge deposited between active TiO_2 particles.* Journal of Applied Physics, 2012. **111**(12): p. 123109-123109-7.

224. Mott, N.F., *Conduction in non-crystalline materials.* Philosophical Magazine, 1969. **19**(160): p. 835-852.

225. Nair, K. and S.S. Mitra, *Electrical properties and hopping transport in amorphous silicon carbide films.* Journal of Non-Crystalline Solids, 1977. **24**(1): p. 1-17.

226. Knotek, M.L., M. Pollak, T.M. Donovan, and H. Kurtzman, *Thickness dependence of hopping transport in amorphous-Ge films.* Phys. Rev. Lett., 1973. **30**(18): p. 853--856.

227. Mosbacker, H.L., Y.M. Strzhemechny, B.D. White, P.E. Smith, D.C. Look, D.C. Reynolds, C.W. Litton, and L.J. Brillson, *Role of near-surface states in Ohmic-Schottky conversion of Au contacts to ZnO.* Applied Physics Letters, 2005. **87**(1): p. -.

228. Dittrich, T., V. Zinchuk, V. Skryshevskyy, I. Urban, and O. Hilt, *Electrical transport in passivated Pt/TiO_2/Ti Schottky diodes.* Journal of Applied Physics, 2005. **98**(10): p. 104501.

229. Bardeen, J., *Surface states and rectification at a metal semiconductor contact.* Physical Review, 1947. **71**(10): p. 717-727.
230. Könenkamp, R. and I. Rieck, *Electrical properties of Schottky diodes on nano-porous TiO_2 films.* Materials Science and Engineering: B, 2000. **69–70**(0): p. 519-521.
231. Cowley, A.M. and S.M. Sze, *Surface states and barrier height of metal-semiconductor systems.* Journal of Applied Physics, 1965. **36**(10): p. 3212-3220.
232. Heine, V., *Theory of Surface States.* Physical Review, 1965. **138**(6A): p. A1689-A1696.
233. Thanailakis, A., *Contacts between simple metals and atomically clean silicon.* Journal of Physics C: Solid State Physics, 1975. **8**(5): p. 655.
234. Hope, G.A. and A.J. Bard, *Platinum/titanium dioxide (rutile) interface. Formation of Ohmic and rectifying junctions.* The Journal of Physical Chemistry, 1983. **87**(11): p. 1979-1984.
235. L. Solymar and D. Walsh, *Electrical properties of materials*. 8th ed. 2010, Oxford: Oxford University Press.
236. Lee, H., Y. Keun Lee, T. Nghia Van, and J. Young Park, *Nanoscale Schottky behavior of Au islands on TiO_2 probed with conductive atomic force microscopy.* Applied Physics Letters, 2013. **103**(17): p. 173103.
237. F.A. Padovani and R. Stratton, *Field and thermionic-field emission in Schottky barriers.* Solid-State Electronics, 1966. **9**(7): p. 695–707.
238. Evans-Freeman, J.H., M.M. El-Nahass, A.A.M. Farag, and A. Elhaji, *Current transport mechanisms and deep level transient spectroscopy of Au/n-Si Schottky barrier diodes.* Microelectronic Engineering, 2011. **88**(11): p. 3353-3359.
239. Könenkamp, R., *Carrier transport in nanoporous TiO_2 films.* Physical Review B, 2000. **61**(16): p. 11057-11064.
240. Ye, C., K. Zheng, and G. Chen, *Work function measurement for Ag-TCNQ (TCNQ = Tetracyanoquinodimethane) nanowires.* Journal of Nanoscience and Nanotechnology, 2012. **12**(8): p. 6576-6578.
241. Hossein-Babaei, F., S. Abbaszadeh, and M.S. Esfahani, *Gas sensitive porous silver-rutile high-temperature schottky diode on thermally oxidized titanium.* Sensors Journal, IEEE, 2009. **9**(3): p. 237-243.
242. Konenkamp, R., P. Hoyer, and A. Wahi, *Heterojunctions and devices of colloidal semiconductor films and quantum dots.* Journal of Applied Physics, 1996. **79**(9): p. 7029-7035.
243. Tseng, Y.-H., D.-S. Sun, W.-S. Wu, H. Chan, M.-S. Syue, H.-C. Ho, and H.-H. Chang, *Antibacterial performance of nanoscaled visible-light responsive platinum-containing titania photocatalyst in vitro and in vivo.* Biochimica et Biophysica Acta (BBA) - General Subjects, 2013. **1830**(6): p. 3787-3795.
244. Schierbaum, K.D., S. Fischer, M.C. Torquemada, J.L. de Segovia, E. Román, and J.A. Martín-Gago, *The interaction of Pt with TiO_2(110) surfaces: a comparative XPS, UPS, ISS, and ESD study.* Surface Science, 1996. **345**(3): p. 261-273.
245. Zhao, W., C. Chen, X. Li, J. Zhao, H. Hidaka, and N. Serpone, *Photodegradation of sulforhodamine-B dye in platinized titania dispersions under visible light irradiation: influence of platinum as a functional co-catalyst.* The Journal of Physical Chemistry B, 2002. **106**(19): p. 5022-5028.
246. Gomathi Devi, L. and K. Mohan Reddy, *Photocatalytic performance of silver TiO_2: Role of electronic energy levels.* Applied Surface Science, 2011. **257**(15): p. 6821-6828.
247. Li, X.Z. and F.B. Li, *Study of Au/Au^{3+}-TiO_2 Photocatalysts toward visible photooxidation for water and wastewater treatment.* Environmental Science & Technology, 2001. **35**(11): p. 2381-2387.

248. Chandrasekharan, N. and P.V. Kamat, *Improving the photoelectrochemical performance of nanostructured TiO_2 films by adsorption of gold nanoparticles†.* The Journal of Physical Chemistry B, 2000. **104**(46): p. 10851-10857.
249. Gorzkowska–Sobas, A., E. Kusior, M. Radecka, and K. Zakrzewska, *Visible photocurrent response of TiO_2 anode.* Surface Science, 2006. **600**(18): p. 3964-3970.
250. Ghosh, A.K., F.G. Wakim, and R.R. Addiss, Jr., *Photoelectronic processes in rutile.* Physical Review, 1969. **184**(3): p. 979-988.
251. Houlihan, J.F., R.F. Bonaquist, R.T. Dirstine, and D.P. Madacsi, *Reduction effects on the spectral response of ceramic TiO_2 photoanodes.* Materials Research Bulletin, 1981. **16**(6): p. 659-667.
252. Oskam, G., J.G. Long, M. Nikolova, and P.C. Searson, *Electrochemical deposition of metals on semiconductors*, in *Electrochemical Synthesis and Modification of Materials*, P.C. Andricacos, et al., Editors. 1997. p. 257-266.
253. Cheng, B., Y. Le, and J. Yu, *Preparation and enhanced photocatalytic activity of Ag@TiO_2 core–shell nanocomposite nanowires.* Journal of Hazardous Materials, 2010. **177**(1–3): p. 971-977.
254. Yu, J., J. Xiong, B. Cheng, and S. Liu, *Fabrication and characterization of Ag-TiO_2 multiphase nanocomposite thin films with enhanced photocatalytic activity.* Applied Catalysis B: Environmental, 2005. **60**(3-4): p. 211-221.
255. Wang, Z., M. Zhu, X. Chen, Q. Yan, and J. Zhang, *Defect-assisted tunneling current-transport mechanism for Schottky diodes of Pt thin film on p-SiNWs tips.* Microelectronic Engineering, 2013. **103**(0): p. 36-41.
256. Herrán, J., I. Fernández, R. Tena-Zaera, E. Ochoteco, G. Cabañero, and H. Grande, *Schottky diodes based on electrodeposited ZnO nanorod arrays for humidity sensing at room temperature.* Sensors and Actuators B: Chemical, 2012. **174**(0): p. 274-278.
257. Liu, L., Z. Liu, H. Bai, and D.D. Sun, *Concurrent filtration and solar photocatalytic disinfection/degradation using high-performance Ag/TiO_2 nanofiber membrane.* Water Research, 2012. **46**(4): p. 1101-1112.
258. Veres, Á., T. Rica, L. Janovák, M. Dömök, N. Buzás, V. Zöllmer, T. Seemann, A. Richardt, and I. Dékány, *Silver and gold modified plasmonic TiO_2 hybrid films for photocatalytic decomposition of ethanol under visible light.* Catalysis Today, 2012. **181**(1): p. 156-162.
259. Smit, G.D.J., M.G. Flokstra, S. Rogge, and T.M. Klapwijk, *Scaling of micro-fabricated nanometer-sized Schottky diodes.* Microelectronic Engineering, 2002. **64**(1-4): p. 429-433.
260. Smit, G.D.J., S. Rogge, and T.M. Klapwijk, *Scaling of nano-Schottky-diodes.* Applied Physics Letters, 2002. **81**(20): p. 3852-3854.
261. Hasunuma, R., T. Komeda, and H. Tokumoto, *Electric properties of nanoscale contacts on Si(111) surfaces.* Applied Surface Science Appl. Surf. Sci. 130–132, 84 ~1998, 1998. **130–132**: p. 84-89.
262. Mamedov, R.K., M.A. Yeganehx, S. Rahmatallahpur, and A. Nozad, *Effect of diode size and series resistance on barrier height and ideality factor in nearly ideal Au/n type-GaAs micro Schottky contact diodes.* Chin. Phys. B, 2010. **19**(10): p. 107207.
263. Yeganeh, M.A. and S.H. Rahmatollahpur, *Barrier height and ideality factor dependency on identically produced small Au/p-Si Schottky barrier diodes.* Journal of Semiconductors, 2010. **31**(7).
264. Smit, G.D.J., S. Rogge, and T.M. Klapwijk, *Enhanced tunneling across nanometer-scale metal–semiconductor interfaces.* Applied Physics Letters, 2002. **80**(14): p. 2568-2570.
265. Hasegawa, H., T. Sato, and C. Kaneshiro, *Properties of nanometer-sized metal–semiconductor interfaces of GaAs and InP formed by an in situ electrochemical process.* Journal of Vacuum Science & Technology B, 1999. **17**(4): p. 1856-1866.

266. Yang, L., T. Zhang, H. Zhou, S.C. Price, B.J. Wiley, and W. You, *Solution-processed flexible polymer solar cells with silver nanowire electrodes.* ACS Applied Materials & Interfaces, 2011. **3**(10): p. 4075-4084.
267. Hardin, B.E., W. Gaynor, I.K. Ding, S.-B. Rim, P. Peumans, and M.D. McGehee, *Laminating solution-processed silver nanowire mesh electrodes onto solid-state dye-sensitized solar cells.* Organic Electronics, 2011. **12**(6): p. 875-879.
268. Rahbarpour, S. and M. Purahmad, *Silver-rutile Schottky diode fabricated on oxidized titanium foil.* IOP Conference Series: Materials Science and Engineering, 2011. **17**(1): p. 012016.
269. Elechiguerra, J.L., L. Larios-Lopez, C. Liu, D. Garcia-Gutierrez, A. Camacho-Bragado, and M.J. Yacaman, *Corrosion at the Nanoscale: The case of silver nanowires and nanoparticles.* Chem. Mater., 2005. **17**(24): p. 6042-6052.
270. Landman, U., R.N. Barnett, A.G. Scherbakov, and P. Avouris, *Metal-semiconductor nanocontacts: silicon nanowires.* Phys. Rev. Lett., 2000. **85**(9): p. 1958-1961.
271. Dag, S. and L.-W. Wang, *Atomic and electronic structures of nano- and amorphous CdS/Pt interfaces.* Physical Review B, 2010. **82**.
272. Tsakalakos, L., *Application of Micro- and Nanotechnology in Photovoltaics.* 2012: p. 515-531.
273. Pillai, S., K.R. Catchpole, T. Trupke, and M.A. Green, *Surface plasmon enhanced silicon solar cells.* Journal of Applied Physics, 2007. **101**(9): p. 093105.
274. Derkacs, D., S.H. Lim, P. Matheu, W. Mar, and E.T. Yu, *Improved performance of amorphous silicon solar cells via scattering from surface plasmon polaritons in nearby metallic nanoparticles.* Applied Physics Letters, 2006. **89**(9): p. 093103.
275. Gunawan, C., W.Y. Teoh, C.P. Marquis, J. Lifia, and R. Amal, *Reversible antimicrobial photoswitching in nanosilver.* Small, 2009. **5**(3): p. 341-344.
276. Nolan, N.T., M.K. Seery, S.J. Hinder, L.F. Healy, and S.C. Pillai, *A systematic study of the effect of silver on the chelation of formic acid to a titanium precursor and the resulting effect on the anatase to rutile transformation of* TiO_2*.* Journal of physical chemistry C, 2010. **114**(30): p. 13026-13034.
277. Sigma Aldrich Co. LLC. *Copper (I) Oxide* 2013; Available from: http://www.sigmaaldrich.com/catalog/product/aldrich/678945?lang=en&region=GB.
278. Anon. *Emfutur Technologies*. 2013; Available from: http://www.emfutur.com/12-cadmium-telluride-cdte-.
279. Lide, D.R., ed. *"Properties of semiconductors", in CRC Handbook of Chemistry and Physics, Internet Version* ed. L. I. Berger. 2013: CRC Press, Boca Raton, FL.
280. Nagasubramanian, G., A.S. Gioda, and A.J. Bard, *Semiconductor electrodes: XXXVII . photoelectrochemical behavior of p-type in acetonitrile solutions.* Journal of The Electrochemical Society, 1981. **128**(10): p. 2158-2164.

Appendix A: Summary of Schottky barrier devices fabricated

Device	Sample	Current (I-V max)	I-V curve shape	SBH (eV)	R^2 (IDM)	Photocurrent max @330 nm (µA)	Photocurrent density max (µAcm^{-2})	Photovoltage max @330 nm (mV)	Comments
Au/TiO$_2$/Ti	A2	2.5 mA	L	x	x	x	x	x	Anodised
	A3	1.6 mA	L	x	x	x	x	x	Anodised
	A	1.55 mA	L	x	x	x	x	x	Anodised
	B	4 mA	L	x	x	x	x	x	Anodised
	C	4 mA	L	x	x	x	x	x	Anodised
	R1	4.5 mA	L	x	x	x	x	x	Anodised
	R2	4 mA	L	x	x	x	x	x	Anodised
	R3	4 mA	L	x	x	x	x	x	Anodised
	R4	x	x	x	x	x	x	x	Anodised
	O1	5 mA	L	x	x	x	x	x	Oxidised 400°C for 15 mins
	O2	4.65 mA	L	x	x	x	x	x	Oxidised 400°C for 15 mins
	O3	4.87 mA	L	x	x	x	x	x	Oxidised 400°C for 30 mins
	O4	4.71 mA	L	x	x	x	x	x	Oxidised 400°C for 30 mins
	O5	4.76 mA	L	x	x	x	x	x	Oxidised 400°C for 1 hr
	O6	x	L	x	x	x	x	x	Oxidised 400°C for 1 hr
	O7	60 µA	D	0.78	0.998	3.5	27.8	64	700°C 30 mins
	O8	0.6 mA	L/D	0.83	0.971	4	31.8	4	700°C 30 mins
	O9	4.62 mA	L	x	x	x	x	x	Anodised and annealed 8hr, 550°C
	O10	3 mA	L	x	x	x	x	x	Anodised and annealed 8hr, 550°C
	O11	3.5 mA	L	x	x	x	x	x	550°C for 8 hours

	O12	3 mA	L	x	x	x	x	x	550°C for 8 hours
	O13	125 µA	L/D	0.7	0.999	0.4	3.2	5.4	700°C 30 mins
	O14	S/C	L	x	x	x	x	x	700°C 30 mins
	O15	60 µA	D	0.79	0.999	0.6	4.8	32	700°C 30 mins
	O16	S/C	L	x	x	x	x	x	700°C 30 mins
	O21	120 µA	D	0.78	0.991	0.5	4.0	28	CpTi mp+ep
	O22	200 µA	D	0.81	0.997	0.1	0.8	18	CpTi mp only
	O23	400 µA	L/D	0.67	0.98	0.2	1.6	0.4	CpTi mp only
	O24	140 µA	D	0.78	0.999	0.2	1.6	10	CpTi mp only
	O25	200 µA	SD	0.7	0.985	1	8.0	5	CpTi mp+ep
	O26	160 µA	D	0.83	0.996	0.6	4.8	100	CpTi mp+ep
	T1	2.83 mA	L	x	x	x	x	x	Thick/recycled Ti mp+ep
	T2	3.85 mA	L	x	x	x	x	x	Thick/recycled Ti mp+ep
	T3	250 µA	D	0.76	0.998	0.4	3.2	6	Thick/recycled Ti mp+ep
	T4	120 uA	D	x	x	x	x	x	Thick/recycled Ti mp only
	T5	322 uA	D	x	x	0.2	1.6	x	Thick/recycled Ti mp only
	T6	3.6 mA	L	x	x	x	x	x	Thick/recycled Ti mp only
Pt/TiO$_2$/Ti	O17	150 nA	D	x	x	x	x	x	mp+ep, 40 nm Pt
	O18	150 nA	D	x	x	x	x	x	mp+ep, 40 nm Pt
	O19	90 nA	D	x	x	x	x	x	mp only, 40 nm Pt
	O20	100 nA	D	x	x	x	x	x	mp only, 40 nm Pt
	O17 R	6 µA	L/D	0.79	0.992	18	143	400	Resputtered - 100 nm Pt
	O18 R	5 µA	L	0.79	x	0.9	7.2	90	Resputtered - 100 nm Pt
	O19 R	40 µA	L	0.75	x	4.5	36	40	Resputtered - 100 nm Pt
	O20 R	60 µA	L	0.75	x	10	80	100	Resputtered - 100 nm Pt
	O17 R x1	9 µA	D	0.81	0.994	12	95	487	Retested 6 months later

	O18 R x1	5 µA	L/D	0.78	0.965	1.9	15	308	Retested 6 months later
	O19 R x1	150 µA	L	x	x	23	183	143	Retested 6 months later
	O20 R x1	61 µA	L	x	x	20	159	193	Retested 6 months later
	O17 -1HR	35	D	0.77	x	14.84	118	299	Annealed in 1 hr stages at 400°C
	O17 - 2HR	13.9	D	0.78	x	6.2	49	287	Annealed in 1 hr stages at 400°C
	O17 - 3HR	5.22	D	0.8	x	0.9	7	177	Annealed in 1 hr stages at 400°C
	104	80 µA	D	0.86	0.981	9.5	76	425	10 nm Pt
	105	190 µA	L	x	x	6.5	52	27	10 nm Pt
	106	32 µA	D	0.91	0.985	7.5	60	425	10 nm Pt
	201	25 µA	D	0.92	0.993	x	x	x	thick ~40 - 80 nm Pt
	202	27 µA	D	0.91	0.994	2.7	21	300	thick ~40 - 80 nm Pt
	203	28 µA	D	0.96	0.993	x	x	x	initial test - ~40-80 nm
	203 x1	40 µA	D	0.75	0.989	2.8	22	92	Second test ~40 - 80 nm
	302	172 µA	D	0.86	0.979	20.8	165	473	10 nm Pt
	304	500 µA	L	x	x	15	119	25	10 nm Pt
	306	431 µA	L	x	x	7.6	60	15	10 nm Pt
	307	132 µA	L/D	0.71	0.966	12.1	96	84	10 nm Pt
	308	1.5 mA	L	x	x	3.8	30	2.5	10 nm Pt
	304_20	2 mA	L	x	x	0.7	5.6	0.2	Resputtered, 20 nm Pt total
	306-20	1.5 mA	L	x	x	0.8	6.4	0.5	Resputtered, 20 nm Pt total
	307-20	1 mA	L	x	x	1.2	9.5	1.1	Resputtered, 20 nm Pt total
	308_20	2.8 mA	L	x	x	0.8	6.4	0.3	Resputtered, 20 nm Pt total
	304 R	26.3 µA	D	0.77	0.992	48.96	389	721	Washed in acetone, resputtered 20nm

	306 R	274 µA	L/D	0.68	0.964	40.92	326	170	Washed in acetone, resputtered 20nm
	307 R	4 mA	L	x	x	5.1	41	1.7	Washed in acetone, resputtered 20nm
	308 R	4 mA	L	x	x	3.7	29	1	Washed in acetone, resputtered 20nm
	420	x	x	x	x	x	x	x	new steel mask. No response.
	421	x	x	x	x	x	x	x	new steel mask. No response.
	422	x	x	x	x	x	x	x	new steel mask. No response.
	501	450 µA	D	0.76	0.897	24	191	50	Photovoltage decay tested thoroughly. 10 nm Pt
	502	450 µA	D	0.94	0.973	34	270	455	Photovoltage decay tested thoroughly. 10 nm Pt
	503	450 µA	D	0.85	0.968	30	239	391	Photovoltage decay tested thoroughly. 10 nm Pt
	504	998 µA	L/D	0.66	0.991	21	167	38	Photovoltage decay tested thoroughly. 10 nm Pt
	504	22.6	L	x	x	4.1	33	97	1.30 hr 500°C annealing, similar to CuO
	505	1000 µA	D	0.87	0.93	29.4	234	340	Photovoltage decay tested thoroughly. 10 nm Pt
	506	663 µA	D	0.79	0.984	27	215	393	Photovoltage decay tested thoroughly. 10 nm Pt
	504 R	750 µA	L/D	0.69	0.995	32	255	156	Retested for visible response. Photovoltage decay test
	505 R	800 µA	D	0.73	0.991	39	310	74	Retested for visible response. Photovoltage decay test
	506 R	400 µA	D	0.79	0.961	40	318	450	Retested for visible response. Photovoltage decay test
	811	492 µA	D	0.68	0.981	8.3	66	22	20 nm Pt
	815	424 µA	D	0.77	0.992	39.6	315	355	21 nm Pt

Ag/TiO$_2$/Ti	102	2 mA	D	0.67	0.995	20	159	125	Ag 20nm
	103	4 mA	L	x	x	1.5	12	0.25	Ag 20nm
	Ag1	2 mA	L/D	x	x	x	x	x	Ag 10nm
	Ag2	2 mA	L/D	x	x	x	x	x	Ag 10nm
	Ag3	2 mA	L/D	x	x	x	x	x	Ag 10nm
	Ag1 x1	15 µA	L/D	0.91	0.95	6.5	52	282	re-evaporated 20nm total
	Ag2 x1	x	D	x	x	x	x	x	re-evaporated 20nm total
	Ag3 x1	40 µA	L/D	0.9	0.765	0.9	7	400	re-evaporated 20nm total
	Ag4	3 mA	L/D	0.9	0.966	19	151	88	recycled Ti, Ag 20nm total
	Ag5	4 mA	L/D	0.85	0.917	29.6	235	92	recycled Ti, Ag 20nm total
	Ag6	4 mA	L	x	x	x	x	x	recycled Ti, Ag 20nm total
Ag-NW/TiO$_2$/Ti	101	0.2 µA	D	0.89	0.843	1.4	11.1	397	20 µL NWs
	101x1	250 µA	D	0.95	0.935	0.1	0.8	21	20 µL NWs - retested after 1 week
	101x1 R	200 µA	D	0.77	0.966	0.4	3.2	68	20 µL NWs - retested after 6 months
	204	0.003 µA	D	x	x	x	x	x	20 µL NWs
	205	x	x	x	x	x	x	x	mishandled - rubbed off NWs
	206	2 µA	D	0.93	0.998	0.2	1.6	200	20 µL NWs - initial test
	206x1	3 µA	D	0.91	0.982	0.14	1.1	128	20 µL NWs - retested after 1 week
	206 R	1	D	0.88	0.984	0.8	6.4	255	20 µL NWs - retested after 6 months
	301	0.6 µA	L/d	0.83	0.975	0.3	2.4	0.3	15 µL NWs - poor resolution photoresponse
	303	1.5 mA	L	x	x	0.3	2.4	0.3	20 µL NWs - poor resolution photoresponse
	305	1 mA	L	x	x	1	8.0	1	30 µL NWs - poor resolution photoresponse

	401	x	x	x	x	x	x	x	15 µL NWs
	401 x1	x	x	x	x	x	x	x	Recycled substrate. 6 µL NWs
	401 x2	x	x	x	x	x	x	x	Recycled substrate. 3 µL NWs
	401 x2_15	500 µA	L/D	x	x	0.1	0.8	1.8	Same substrate, deposited more NWs. 15 µL NWs
	402	x	L	x	x	x	x	x	15 µL NWs
	402 x1	25 µA	D	x	x	x	x	x	Recycled substrate. 6 µL NWs
	405	15 µA	D	x	x	x	x	x	9 µL NWs
	406	x	x	x	x	x	x	x	9 µL NWs
	406 x1	x	x	x	x	x	x	x	Recycled substrate. 6 µL NWs
	406 x1_20	2 mA	L	x	x	x	x	x	Same substrate, deposited more. 20 µL NWs
	407	x	L	x	x	x	x	x	9 µL NWs
	407_12	200 µA	L/D	x	x	x	x	90	Same substrate, deposited more. 12 µL NWs
	407 x1	x	x	x	x	x	x	x	Recycled substrate. 9 µL NWs
	407 x1_25	2 mA	L/D	x	x	x	x	x	Same substrate, deposited more. 25 µL NWs
	408	x	x	x	x	x	x	x	9 µL NWs
	408_12	x	x	x	x	x	x	x	Same substrate, deposited more. 12 µL NWs
	409	x	x	x	x	x	x	x	3 µL NWs
	409_15	1.5 mA	L/D	x	x	0.011	0.1	120	Same substrate, deposited more. 15 µL NWs
	410	x	x	x	x	x	x	x	6 µL NWs
	410_20	1 mA	L	x	x	x	x	1	Same substrate, deposited more. 20 µL NWs
	410 x1	x	x	x	x	x	x	x	Recycled substrate. 9 µL NWs
	411	x	x	x	x	x	x	x	9 µL NWs

	411_25	100 µA	L/D	x	x	0.2	2	90	Same substrate, deposited more. 25 µL NWs
	507	1 mA	L/D	0.75	0.906	0.7	5.6	52	25 µL NWs
	508	1 mA	D	0.87	0.983	2.3	18.3	221	30 µL NWs
	509	1 mA	D	0.97	0.98	2.3	18.3	260	35 µL NWs - surface charging on photovoltage
	601	x	S/C	x	x	x	x	x	15 µL NWs
	602	x	S/C	x	x	x	x	x	15 µL NWs
	603	x	S/C	x	x	x	x	x	15 µL NWs
	601 R	500 µA	D	1.05	0.869	0.1	0.8	180	Recycled - 9µL. Washed in acetone, more AgNWs deposited.
	602 R	150 µA	D	1.06	0.835	2.3	18.3	x	Recycled - 9µL. Unable to measure photovoltage. Noisy I-V curve
	809	0.5 mA	L/D	1.09	0.865	2.2	17.5	14.2	40 µL NWs. Noisy I-V
	812	82 µA	D	1.02	0.903	0.12	1.0	230	40 µL NWs. Large differences between I-V curves

Notes: ‘SBH’ – Schottky barrier height, calculated using IDM and ‘R^2’ is therefore the closeness of fit to the linear relationship ; ‘x’ means no response/data obtained; for ‘I-V curve shape’ L = linear, D= diode, L/D= mixture of the too; ‘Current (I-V max)’ is the highest current found at the largest positive voltage, which was 0.5 V in early experiments and 0.8 V in later experiments; ‘comments’ highlight various experimental variables; ‘Photocurrent density’ is calculated directly from the photocurrent.

Appendix B: Matlab code for the extended diode equivalent circuit method (EDM) 1 – iterative error reduction approach

```
%%%%%%%%%%%%
% initiate %
%%%%%%%%%%%%

clear all;

% load data
[Vdevice_raw,Idevice_raw] = textread('Testdata_501_run2.csv','%f %f','delimiter',',');

% select positive data only
j = find(Vdevice_raw>0);
Vdevice = Vdevice_raw(j);
Idevice = Idevice_raw(j);

% guess at device parameters
Rseries = 500; % series resistance
Rleakage = 1e6; % leakage current (not across Rseries)
Isaturation = 1e-7; % reverse saturation current
n = 2; % ideality factor

Rseries_old = Rseries;
Rleakage_old = Rleakage;
Isaturation_old = Isaturation;
n_old = n;

% constants
k = 1.38e-23;
T = 293; % 20 degrees
q = 1.6e-19;
VT = k*T/q;

% initiate vectors
Ilower = zeros(size(Vdevice)); % current through the device
Iupper = zeros(size(Vdevice)); % current through the device
Rmid = zeros(size(Vdevice)); % ratio of Vmid to Vdevice
```

```
%%%%%%%%%%%%%%%%%%%%%%%%%%%
% main curve fitting loop %
%%%%%%%%%%%%%%%%%%%%%%%%%%%

error_old = 1e20; % initiate to a very large number

for factor = 1:6
   switch(factor)
      case 1
         f = 1.05;
      case 2
         f = 1.02;
      case 3
         f = 1.01;
      case 4
         f = 1.005;
      case 5
          f = 1.002;
      case 6
         f = 1.001;
   end

improving_flag = 1;
while improving_flag == 1

   improving_flag = 0;

   for trial = 1:8

   %%%%%%%%%%%%%%%%%%%
   % vary parameters %
   %%%%%%%%%%%%%%%%%%%

   switch(trial)
         case 1
            Rseries = Rseries * f;
         case 2
            Rseries = Rseries / f;
```

```
        case 3
            Rleakage = Rleakage * f;
        case 4
            Rleakage = Rleakage / f;
        case 5
            Isaturation = Isaturation * f;
        case 6
            Isaturation = Isaturation / f;
        case 7
            n = n * f;
        case 8
            n = n / f;
    end

%       disp(['Rseries ' num2str(Rseries) ', Rleakage ' num2str(Rleakage) ', Isaturation ' num2str(Isaturation) ', n ' num2str(n)]);
    disp(['Factor ' num2str(f) ', Rseries ' num2str(Rseries) ', Rleakage ' num2str(Rleakage) ', Isaturation ' num2str(Isaturation) ', n ' num2str(n)]);

    %%%%%%%%%%%%%%%%%%%%%%%%%%%%%%%%%%%%%%%%%%%%%
    % calculate the IV curve for current parameters %
    %%%%%%%%%%%%%%%%%%%%%%%%%%%%%%%%%%%%%%%%%%%%%

    Rmid = 0.5;
    Vmid = Rmid.*Vdevice; % voltage at circuit mid point (to be determined)
    Rstep = 0.25; % increment or decrement step size
    for i = 1:90
        Iupper = (Vdevice-Vmid)/Rseries; % calculate current through upper part of circuit
        Ilower = (Vmid/Rleakage) + Isaturation*(exp(Vmid/(n*VT))-1); % calculate current through lower part of circuit
        Rmid = Rmid - Rstep + 2*Rstep*(Iupper>Ilower); % refine Rmid
        Vmid = Rmid.*Vdevice; % recalculate Vmid
        Rstep = Rstep*0.5; % reduce step size for next iteration
    end


    %%%%%%%%%%%%%%%%%%%%%%%%%%%%%%%%%%%%%%%%%%%%%
    % calculate the residuals and squares error %
```

```
   %%%%%%%%%%%%%%%%%%%%%%%%%%%%%%%%%%%%%%%%%%

   residuals = (Ilower-Idevice).^2;
   error = sum(residuals);
 %   disp(['Error ' num2str(error)]);

   % restore old parameters if there is no reduction in the error
   if error > error_old
      Rseries = Rseries_old;
      Rleakage = Rleakage_old;
      Isaturation = Isaturation_old;
      n = n_old;
      error = error_old;
   end

   if error_old > error
      improving_flag = 1;
   end

   % store the current set of parameters
   Rseries_old = Rseries;
   Rleakage_old = Rleakage;
   Isaturation_old = Isaturation;
   n_old = n;
   error_old = error;

   end % end of for loop
end % end of while loop
end

%%%%%%%%%%%%%%%%%%%%%%%%%%%%%%%%%%
% Recalculate current for output %
%%%%%%%%%%%%%%%%%%%%%%%%%%%%%%%%%%

Rmid = 0.5;
Vmid = Rmid.*Vdevice; % voltage at circuit mid point (to be determined)
Rstep = 0.25; % increment or decrement step size
for i = 1:90
```

```
    Iupper = (Vdevice-Vmid)/Rseries; % calculate current through upper part of circuit
    Ilower = (Vmid/Rleakage) + Isaturation*(exp(Vmid/(n*VT))-1); % calculate current
through lower part of circuit
    Rmid = Rmid - Rstep + 2*Rstep*(Iupper>Ilower); % refine Rmid
    Vmid = Rmid.*Vdevice; % recalculate Vmid
    Rstep = Rstep*0.5; % reduce step size for next iteration
end

residuals = (Ilower-Idevice).^2;
    ssres = sum(residuals);
    devicemean = mean(Idevice);
    sstot = sum((Idevice - devicemean).^2);
    rsquared = 1 - (ssres/sstot);

disp(['*******************************************************************']);
disp(['Factor ' num2str(f) ', Rseries ' num2str(Rseries) ', Rleakage ' num2str(Rleakage) ',
Isaturation ' num2str(Isaturation) ', n ' num2str(n)]);
disp(['R-squared ' num2str(rsquared)]);

figure(1);
plot(Vdevice,Idevice,'r');
hold on;
plot(Vdevice,Ilower,'b');
title('experiment = red, fit = blue');
xlabel('Voltage (V)');
ylabel('Current (A)');


fid = fopen('test2.txt','wt');
fprintf(fid,'%6.3f , %12.3e , %12.3e\n',[Vdevice;Idevice;Ilower]);
fclose(fid);
```

Appendix C: Matlab code for the extended diode equivalent circuit method (EDM) 2 – gradient descent approach

```
%%%%%%%%%%%%
% initiate %
%%%%%%%%%%%%

clear all;

% load data
[Vdevice_raw,Idevice_raw] = textread('505.csv','%f %f','delimiter',',');

% select positive data only
j = find(Vdevice_raw>0);
Vdevice = Vdevice_raw(j);
Idevice = Idevice_raw(j);

% guess at device parameters
Rseries_current = 4e2; % series resistance
Rleakage_current = 1e6; % leakage current (not across Rseries)
Isaturation_current = 1e-10; % reverse saturation current
n_current = 1; % ideality factor

% constants
k = 1.38e-23;
T = 293; % 20 degrees
q = 1.6e-19;
VT = k*T/q;

% initiate vectors
Ilower = zeros(size(Vdevice)); % current through the device
Iupper = zeros(size(Vdevice)); % current through the device
Rmid = zeros(size(Vdevice)); % ratio of Vmid to Vdevice


f1 = 0.9999; % used to calculate the gradient
f2 = 1.0001;

%%%%%%%%%%%%%%%%%%%%%%%%%%%
```

```
% main curve fitting loop %
%%%%%%%%%%%%%%%%%%%%%%%%%%%

for iteration = 1:4000

   f3 = 1;
   if iteration > 2000
      f3 = 0.7;
   end
   if iteration > 3000
      f3 = 0.1;
   end

f_series = 5e8*f3;
f_leakage = 1e10*f3;
f_saturation = 2e-10*f3;
f_n = 4e2*f3;


   for grad_trial = 1:8

   %%%%%%%%%%%%%%%%%%%%%%%%%%%%%%%%%%%%
   % vary parameters to find gradient %
   %%%%%%%%%%%%%%%%%%%%%%%%%%%%%%%%%%%%

   Rseries = Rseries_current;
   Rleakage = Rleakage_current;
   Isaturation = Isaturation_current;
   n = n_current;

   switch(grad_trial)
         case 1
            Rseries = Rseries_current * f1;
         case 2
            Rseries = Rseries_current * f2;
         case 3
            Rleakage = Rleakage_current * f1;
         case 4
```

```
            Rleakage = Rleakage_current * f2;
        case 5
            Isaturation = Isaturation_current * f1;
        case 6
            Isaturation = Isaturation_current * f2;
        case 7
            n = n_current * f1;
        case 8
            n = n_current * f2;
    end

%       disp(['Rseries ' num2str(Rseries) ', Rleakage ' num2str(Rleakage) ', Isaturation '
num2str(Isaturation) ', n ' num2str(n)]);
%    disp(['Factor ' num2str(f) ', Rseries ' num2str(Rseries) ', Rleakage ' num2str(Rleakage) ',
Isaturation ' num2str(Isaturation) ', n ' num2str(n)]);



%%%%%%%%%%%%%%%%%%%%%%%%%%%%%%%%%%%%%%%%%%%%
%%%%%
    % calculate the IV curve for current parameters %

%%%%%%%%%%%%%%%%%%%%%%%%%%%%%%%%%%%%%%%%%%%%
%%%%%

    Rmid = 0.5;
    Vmid = Rmid.*Vdevice; % voltage at circuit mid point (to be determined)
    Rstep = 0.25; % increment or decrement step size
    for i = 1:100
        Iupper = (Vdevice-Vmid)/Rseries; % calculate current through upper part of circuit
        Ilower = (Vmid/Rleakage) + Isaturation*(exp(Vmid/(n*VT))-1); % calculate current
through lower part of circuit
        Rmid = Rmid - Rstep + 2*Rstep*(Iupper>Ilower); % refine Rmid
        Vmid = Rmid.*Vdevice; % recalculate Vmid
        Rstep = Rstep*0.5; % reduce step size for next iteration
    end
```

```
%%%%%%%%%%%%%%%%%%%%%%%%%%%%%%%%%%%%%%%%%%%%%%%%%%
%
   % calculate the residuals and squares error %

%%%%%%%%%%%%%%%%%%%%%%%%%%%%%%%%%%%%%%%%%%%%%%%%%%
%

   residuals = (Ilower-Idevice).^2;
   error = sum(residuals);
 %   disp(['Error ' num2str(error)]);

    switch(grad_trial)
         case 1
            error_series1 = error;
         case 2
            derror_dseries = (error - error_series1)/(Rseries_current*(f2-f1));
         case 3
            error_leakage1 = error;
         case 4
            derror_dleakage = (error - error_leakage1)/(Rleakage_current*(f2-f1));
         case 5
            error_saturation1 = error;
         case 6
            derror_dsaturation = (error - error_saturation1)/(Isaturation_current*(f2-f1));
         case 7
            error_n1 = error;
         case 8
            derror_dn = (error - error_n1)/(n_current*(f2-f1));
    end
   end % end of gradient calculation loop

   Rseries_current = Rseries_current - f_series * derror_dseries;
   Rleakage_current = Rleakage_current - f_leakage * derror_dleakage;
   Isaturation_current = Isaturation_current - f_saturation * derror_dsaturation;
   n_current = n_current - f_n * derror_dn;

 ssres = sum(residuals);
```

```
   devicemean = mean(Idevice);
   sstot = sum((Idevice - devicemean).^2);
   rsquared = 1 - (ssres/sstot);

   if rem(iteration,10) == 1
   disp(['Iteration ' num2str(iteration) ', R-squared ' num2str(rsquared) ', Rseries '
num2str(Rseries_current) ', Rleakage ' num2str(Rleakage_current) ', Isaturation '
num2str(Isaturation_current) ', n ' num2str(n_current)]);
 %   disp(['R-squared ' num2str(rsquared)]);
   end



end % end of iteration

%%%%%%%%%%%%%%%%%%%%%%%%%%%%%%%%%%
% Recalculate current for output %
%%%%%%%%%%%%%%%%%%%%%%%%%%%%%%%%%%

Rseries = Rseries_current;
Rleakage = Rleakage_current;
Isaturation = Isaturation_current;
n = n_current;

Rmid = 0.5;
Vmid = Rmid.*Vdevice; % voltage at circuit mid point (to be determined)
Rstep = 0.25; % increment or decrement step size
for i = 1:90
   Iupper = (Vdevice-Vmid)/Rseries; % calculate current through upper part of circuit
   Ilower = (Vmid/Rleakage) + Isaturation*(exp(Vmid/(n*VT))-1); % calculate current
through lower part of circuit
   Rmid = Rmid - Rstep + 2*Rstep*(Iupper>Ilower); % refine Rmid
   Vmid = Rmid.*Vdevice; % recalculate Vmid
   Rstep = Rstep*0.5; % reduce step size for next iteration
end

residuals = (Ilower-Idevice).^2;
   ssres = sum(residuals);
```

```
    devicemean = mean(Idevice);
    sstot = sum((Idevice - devicemean).^2);
    rsquared = 1 - (ssres/sstot);

disp(['********************************************************************']);
disp(['Rseries ' num2str(Rseries) ', Rleakage ' num2str(Rleakage) ', Isaturation '
num2str(Isaturation) ', n ' num2str(n)]);
disp(['R-squared ' num2str(rsquared)]);

figure();
plot(Vdevice,Idevice,'r');
hold on;
plot(Vdevice,Ilower,'b');
title('experiment = red, fit = blue');
xlabel('Voltage (V)');
ylabel('Current (A)');


fid = fopen('changing_F_variables.txt','wt');
fprintf(fid,'%6.3f , %12.3e , %12.3e\n',[Vdevice;Idevice;Ilower]);
fclose(fid);
```

Appendix D: Summary of Nanocrystal activated Schottky barrier cell

Device	Sample	Current (I-V max)	I-V curve shape	Photocurrent max @330 nm (μA)	Photocurrent density max (μAcm^{-2})	Photovoltage max @330 nm (mV)	Comments
NC/Pt/TiO$_2$/Ti	104	100 μA	L	14	111	50	6 μL CdS
	104 R	200 μA	L	17.3	138	71	7 μL CdS, retest before annealing
	104 A	577 μA	L	12.4	99	19	8 μL CdS, annealed NCs.
	105	192 μA	L	6.4	51	27.4	15 μL CdS
	106	460 μA	L	8	64	17	15 μL CdSe
	202	3.5 mA	L	1.3	10	0.4	15 μL CdS
	203	3 mA	L	1.7	14	0.5	15 μL CdSe
	302	200 μA	L/D	11	88	200	1 μL CuO
	304	18 μA	L/D	26	207	700	1 μL CdS
	304 R	500 μA	L/D	27	215	117	Washed acetone, redeposited 1 μL CdS
	306	250 μA	L	x	x	x	1 μL CdS
	306 R	200 μA	D	28	223	140	Washed acetone, redeposited 1 μL CdS
	307	3 mA	L	x	x	x	1 μL CdSe
	308	3 mA	L	2.1	17	0.7	1 μL CdSe
	501	30 μA	D	30	239	550	1 μL CuO
	502	400 μA	D	32	255	118	2 μL CuO
	503	500 μA	D	34	270	100	3 μL CuO
	501 x1	25 μA	L	4.3	34	150	10 μL CuO
	502 x2	80 μA	L	5	40	68	20 μL CuO
	503 x3	100 nA	D	37	294	250	30 μL CuO
	505	750 μA	D	24	191	43	4 μL CuInS$_2$

	810	0.4 µA	D	2	16	400	10 µL ruby CdTe, Pt on top
	811 NA	150 µA	L/D	0.0025	0.02	5.2	10 µL ruby CdTe
	811	10 µA	L/D	0.25	2	13	10 µL ruby CdTe
	815 NA	150 µA	D	10	80	150	10 µL red CdTe, not annealed NCs
	815	12 µA	L	3.5	28	125	10 µL red CdTe, annealed NCs
NC/Ag-NW/TiO_2/Ti	412	50 nA	D	x	x	1.5	15 µL CdS 15 µL NW
	413	200 nA	D	x	x	x	15 µL CdSe 15 µL NW
	412 R	550 µA	D	6.3	50	167	15 µL CdS 35 µL NW, more NWs deposited
	413 R	500 µA	L	0.9	7	150	15 µL CdSe 35 µL NW, more NWs deposited
	414	800 nA	D	8	64	500	1 µL CuO 20 µL NW
	415	1.5 µA	D	2.5	20	450	1 µL CdS 35 µL NW
	415 x1	800 nA	D	2.1	17	450	1 µL CdS 35 µL NW
	415 x2	0.7 µA	D	1.7	14	450	1 µL CdS 35 µL NW
	415 x3	1 µA	D	1.4	11	437	1 µL CdS 35 µL NW
	416	4.5 µA	D	1.5	12	360	1 µL CdS 35 µL NW
	418	500 µA	L/D	2.4	19	4	1 µL CdS 35 µL NW
	423	400 µA	D	1.2	10	32	1 µL CdSe 35 µL NW
	701	40 µA	D	2	16	300	10 µL CdS 35 µL NW
	702	400 µA	D	2	16	150	10 µL CdS 25 µLNW
	703	2 mA	L	x	x	x	20 µL CdS 20 µL NW
	704	x	x	x	x	x	20 µL CdS 20 µL NW
	705	1 µA	L/D	0.5	4	400*	10 µL $CuInS_2$ 25 µL AgNW. Photovoltage curve very noisy
	705 R	1 µA	L/D	0.87	7	400	10 µL $CuInS_2$ 25 µL AgNW. Photovoltage surface charging
	801	314 µA	D	130	1034	95	10 µL $CuInS_2$ 25 µL AgNW
	802	100 µA	D	0.45	4	31	10 µL CdS 25 µL AgNW. Noisy curve

	803	266 μA	D	0.12	1	0.9	50 μL CdS 25 μL AgNW
	804	10 μA	D	2.6	21	360	10 μL orange CdTe 25 μL AgNW
	805	85 μA	D	1.3	10	270	10 μL red CdTe 25 μL AgNW
	806	400 μA	D	1.4	11	105	10 μL green CdTe 25 μL AgNW
	807	70 μA	D	0.014	0.11	90	10 μL yellow CdTe 25 μL AgNW
	808	40 μA	D	1.1	9	280	10 μL ruby CdTe 25 μL AgNW
	813	150 μA	D	0.25	2	40.7	10 μL red CdTe 25 μL AgNW. NCs not annealed

Notes: An ‘x’ means no response/data obtained; for ‘I-V curve shape’ L = linear, D= diode, L/D= mixture of the too; ‘Current (I-V max)’ is the highest current found at 0.8 V; ‘comments’ highlight the various NC and NW mass loadings; ‘Photocurrent density’ is calculated directly from the photocurrent.